



INVESTIGATING AGGREGATION IN ICE AND SNOW CLOUDS  
USING NOVEL COMBINATION OF TRIPLE-FREQUENCY CLOUD  
RADARS AND RADAR DOPPLER SPECTRA

INAUGURAL-DISSERTATION

ZUR

ERLANGUNG DES DOKTORGRADES

DER MATHEMATISCH-NATURWISSENSCHAFTLICHEN FAKULTÄT

DER UNIVERSITÄT ZU KÖLN

VORGELEGT VON

JOSÉ DIAS NETO

AUS NATAL-RN, BRASILIEN

KÖLN, 21 DECEMBER 2020

BERICHTERSTATTER:  
DR. STEFAN KNEIFEL  
PROF. DR. ROEL NEGGERS

TAG DER MÜNDLICHEN PRÜFUNG:  
01.03.2021



## ABSTRACT

---

Clouds are essential component of the hydrological cycle for transporting of water and distributing precipitation at different parts of the planet. On a global scale, around 63% of the precipitation originates via ice phase. Different ice microphysical processes can lead to growth (e.g. deposition, aggregation, riming) or reduction (e.g. sublimation, breakup) of ice particle sizes. Aggregation, in particular, rapidly increases ice particles sizes and continuously changes the particle size distribution. However, aggregation and other ice microphysical processes are not fully understood.

In order to improve the current knowledge about aggregation and the other microphysical processes, microwave radars are used to observe clouds due to their capability of retrieving information through the different parts of the clouds. Additionally, if Doppler radars operating at different frequencies (multi-frequency setup) are used to observe the same region of clouds, the multi-frequency observations can be used to retrieve information of particles sizes and velocities.

This thesis uses multi-frequency Doppler observations (6 months) to investigate scenarios that intensify aggregation and the impact of increasing aggregate sizes on raindrop sizes. To this end, a multi-frequency data processing framework is introduced to minimize the effect of attenuation (e.g. atmospheric gases, snow, wet radome) and radar miscalibration; it also assigns a set of quality flags to the different correction steps.

The statistical analysis from the observations of the ice part of the clouds indicates that aggregation is intensified in two temperature regions. The first region is between  $-20$  and  $-10$  °C and coincides with the dendritic growth zone (DGZ). Dendritic crystals can favour aggregation due to their branched structure. In addition to the growth of dendrites, the statistical results suggest that an intensification of aggregation in this temperature region correlates with an intensification of updrafts (up to 0.3 m/s). The statistics also show that approximately 25% of the cases where aggregation intensifies an additional mode of small and slow falling particles are present.

The temperature region between  $-10$  and  $0$  °C coincides with the region where the stickiness of ice surfaces increases due to the effect of a quasi liquid layer on the ice surface. Due to this increased stickiness, aggregation intensifies towards the  $0$  °C isotherm. The statistical results indicate that the growth of large aggregates in the DGZ favour, but it is not sufficient to guarantee the presence of even larger aggregates close to  $0$  °C. The results also indicate that an increase in

aggregate sizes close to the 0 °C correlates with an increase in raindrop sizes.

The multi-frequency processing framework and the other filtering processes introduced in this thesis can be used as the foundations for future multi-frequency experiments. The highly qualified multi-frequency dataset and the statistical results from this thesis can be used to evaluate the ice microphysical processes implemented in numerical models.

# CONTENTS

---

1	INTRODUCTION	1
1.1	Motivation	1
1.2	Objectives and outline	6
2	THEORY OVERVIEW	9
2.1	Ice growth microphysical processes	9
2.1.1	Ice nucleation and depositional growth	9
2.1.2	Aggregation	12
2.1.3	Riming	18
2.1.4	Secondary ice production	18
2.2	Radar remote sensing of ice and mixed-phase clouds	22
2.2.1	Scattering properties of a single particle	23
2.2.2	Attenuation and radar reflectivity factor from a particle distribution	27
2.2.3	Doppler spectra and moments	36
3	METHODS	39
3.1	TRIPEX campaign	39
3.2	TRIPEX-Pol campaign	60
3.2.1	Cloud Radars	60
3.2.2	Auxiliary instruments	63
3.2.3	Data processing	64
3.2.4	Improved volume matching and pointing	65
3.3	Evaluating temperature and relative humidity from Cloudnet	70
3.4	Doppler spectra processing	71
3.4.1	Spectra classification	73
3.4.2	Detection of the spectra edges	76
3.5	Detection of the melting layer	78
4	INTENSIFICATION OF AGGREGATION WITHIN DGZ	81
4.1	Review of radar signatures found in the DGZ by previous studies	81
4.2	Case study of DGZ observational features	84
4.3	Statistical analyses of radar variables within DGZ	90
4.4	Aggregation within DGZ and Doppler spectral bimodalities	99
4.5	Aggregation within DGZ and cloud top temperature	102
4.6	Conclusion	103
5	INTENSIFICATION OF AGGREGATION NEAR THE MELTING LAYER	105
5.1	Case study of intense aggregation close to melting layer top	105
5.2	Statistical analyses of aggregation signatures close to ML top	112

5.3	Connecting aggregation at ML top and raindrop characteristic size	122
5.4	Evaluating the one-to-one melting assumption	126
5.5	Conclusion	129
6	CONCLUSIONS AND OUTLOOK	131
	BIBLIOGRAPHY	135

## LIST OF FIGURES

---

- Figure 1.1 Zonal distribution of the mean precipitation rate (Panel a) and fractional dependence of the mean precipitation rate (Panel b) derived from CloudSat/GPM observations. The different colors indicate the different categories of clouds: snow that melts to produce rain (S, cyan), snow that falls to the surface (SS, violet), rain condensation/accretion to the melting ice/snow (R, green), and warm rain (W, red). GPCP stands for Global Precipitation Climatology Project. Taken from Heymsfield et al., (2020). 2
- Figure 2.1 Saturation ratio with respect to water ( $S_w$ ) as a function of the temperature required to obtain a homogeneous nucleation rate of  $1\text{ cm}^{-3}\text{ s}^{-1}$  for water from vapor ( $J_w$ ) and for ice from vapor ( $J_i$ ). The red box indicates the region where the homogeneous nucleation of ice is favourable. Figure adapted from Lohmann, (2016). 10
- Figure 2.2 Onset  $S_i$  and temperatures for heterogeneous nucleation for different INPs. Panel (a) is for mineral dust, Panel (b) is for organic particles and soot, and Panel (c) is for bioaerosol and ammonium. The solid line indicates the  $S_w$ . Figure adapted from Lohmann, (2016). 11
- Figure 2.3 Illustration of the Wegener-Bergeron-Findeisen. Adapted from Lohmann, 2016, but it is originally from <http://www.snowcrystals.com>. 12
- Figure 2.4 Ice particle habit diagram as function of T and  $S_i$  derived from laboratory studies and in-situ observations. The solid line indicates the water supersaturation. Adapted from Bailey and Hallett, (2009). 13
- Figure 2.5 Change of ice particles mass for different growth times under a liquid water content of  $0.1\text{ gm}^{-3}$  and pressure of 1010 hPa. Adapted from Takahashi et al., (1991). 14
- Figure 2.6 Terminal fall velocity of single particles as function of their maximum dimension (Karrer et al., 2020). The continuous and dashed lines are from single crystal and aggregates, respectively. 15

- Figure 2.7 Illustration of the collision between spherical particles. The gray lines indicate the streamline flow. 16
- Figure 2.8 Aggregation collision efficiency of planar branched ice particles. The different curves are from different realisations of the simulation indicated by the legends. Adapted from Böhm, (1992). 16
- Figure 2.9 Variation of the  $E_s$  with temperature. Open diamonds are from Mitchell, (1988) and dark dots are from the parameterization from Phillips et al., (2015). The error bars are the standard deviation obtained by Connolly et al., (2012). Adapted from Phillips et al., (2015). 17
- Figure 2.10 Illustration of rimed ice particles. Panel (a) shows an initially rimed plate, and Panel (b) shows an extremely rimed ice crystal (spherical graupel). Adapted from Wallace and Hobbs, (2006). 18
- Figure 2.11 Increase of the fall velocity of rimed ice particles at  $-10.5$  °C. The continuous line is for liquid water content of  $2$  g/m<sup>3</sup> and the dashed line is for liquid water content less than  $0.5$  g/m<sup>3</sup>. Adapted from Fukuta and Takahashi, (1999). 19
- Figure 2.12 Conceptual illustration of the currently known SIP. Blue color indicates ice phase and red color indicates liquid phase. Adapted from Field et al., 2017. 20
- Figure 2.13 Normalize  $\sigma_b$  from single aggregate of a mix of columns and dendrites calculated using `snowScatt` (Ori et al., 2020b) for X-, Ka-, and W-Band. The vertical lines indicate the diameters equal to 0.5 and 2 mm. 26
- Figure 2.14 Example of attenuation from different components as function of the frequency. The red, green and blue solid lines are the attenuation produced by rain and snow. The brown and blue dotted lines are the attenuation from O<sub>2</sub> and water vapour respectively. The vertical black solid lines indicate the frequency of the X-, Ka- and W-Band radars used in this thesis. Note that the relation between  $\aleph(r, \lambda)$  and  $\alpha(r, \lambda)$  in this figure is  $\aleph(r, \lambda) = [2 \int_0^r \alpha(r, \lambda) dr]^{-1}$ . Adapted from Fabry, 2015. 29

- Figure 2.15 Panel (a) shows the equivalent reflectivity factor ( $Z_e$ ) from a gamma distribution of particles ( $\mu = 0$ ) calculated for X-, Ka- and W-Band. Panel (b) shows three realizations of the gamma distribution with  $\mu = 0$  and three  $\Lambda$  values. 32
- Figure 2.16 Dual wavelength ratio (DWR) from the equivalent reflectivity factors shown in figure Figure 2.15-a: a) as function of  $\Lambda$  and b) as function of  $D_0$  (Equation 2.23). 33
- Figure 2.17 Triple-frequency plot of the simulated DWR-XKa and DWR-KaW of dendrite rimed aggregates (Leinonen and Szyrmer, 2015). The blue, green, red, and purple curves are from 0, 0.1, 0.5 and 10 kg/m<sup>2</sup> effective liquid water path. The gray and black curves are for gamma distribution with  $\mu$  equal to 0 and 4, respectively. 34
- Figure 2.18 Time-height plots of the DWR-KaW (Panel (a)) and the DWR-XKa (Panel (b)) from November 10<sup>th</sup>, 2018. The red box highlights the regions where the DWR values are negative. 35
- Figure 2.19 Conceptual illustration of the effect of attenuation (Panel (a)), vertical air motion (Panel (b)) and turbulence (Panel (c)). 37
- Figure 2.20 Simulated spectrum from a distribution of aggregates of mix of columns and dendrites for X-, Ka- and W-Band. The vertical dashed lines indicate the mean Doppler velocity from each spectrum. 38
- Figure 3.1 Sketch (not to scale) of the horizontal separation between the radars and their height. The height of JOYCE-CF platform is also indicated. This platform is 111 m above mean sea level. 61
- Figure 3.2 Picture of the JOYCE-CF platform. The labels indicate the position from each radar and from the auxiliary sensors operated during the campaign. 61
- Figure 3.3 Histograms of the  $Z_e$  from the Level-2 data from the entire TRIPEX-Pol. The red curve is the vertical profile of the minimum measured  $Z_e$ . Panels a, b and c are the histograms for X-, Ka and W-Band, respectively; all the error flags were applied to filter the data. 65

- Figure 3.4 Illustration of the vertical mismatch between X- and Ka-Band radars (Panel a) and Ka- and W-Band radars for the different chirp sequence (Panels b-e) during TRIPEX. 67
- Figure 3.5 As in Figure 3.5, but for TRIPEX-Pol. 68
- Figure 3.6 Time-height plot of the DDV-KaW from November 20<sup>th</sup>, 2015 (observed during TRIPEX). 69
- Figure 3.7 Time-height plot of the DDV-XKa (a) and DDV-KaW (b) from November 26<sup>th</sup>, 2018 (TRIPEX-Pol). 69
- Figure 3.8 Panels a, c, and e are two dimensional histograms of T, RHw and RH<sub>i</sub> from Cloudnet products versus the corresponding radiosonde measurements. Panels b, d and f are two dimensional histograms of error of the T, RHw and RH<sub>i</sub> from Cloudnet over the range of values measured by the radiosonde. 72
- Figure 3.9 Conceptual illustration of the Doppler spectra classification. The numbers on top of each mode are the ordering indexes. 74
- Figure 3.10 Panel a is a bi-modal spectrum from January 22<sup>nd</sup>, 2019, at 15 : 07, from an altitude of  $\approx 3$  km. The measured and the interpolated spectrum are indicated by the green and orange curve, respectively. The dots indicate the retrieved velocity-power pairs for the Peak-0 and Peak-1. Panel b is the spectra from the same day and same time. The circles and crosses indicate Peak-0 and Peak-1, respectively. 75
- Figure 3.11 Time-height map of the number of identified peaks from January 22<sup>nd</sup>, 2019. The vertical gray dashed line indicates the time of the spectra from Figure 3.10. 75
- Figure 3.12 Observed Ka-Band spectra from the same time as Figure 3.10. The green and orange curves are the retrieved fast slow edges, respectively. 77
- Figure 3.13 Illustration of the main (black) and secondary (green and red) transmitted (continuous) and received chirps (dashed) of a distant target; the yellow region indicates the frequency range of the band-pass filter. 77



- Figure 3.14 Observed W-Band spectra from the same time as Figure 3.10. The fast and slow edges retrieved from the Ka-Band spectra are indicated by the green and orange curves, respectively. The spurious signal are laying outside of the Ka-Band edges at  $\approx 1$ ,  $\approx 3.2$  and  $\approx 6.5$  km. 78
- Figure 3.15 Time-height of the Ze from the W-Band from January 22<sup>nd</sup>, 2019. Panel a is the observed data affected by the spurious signal. Panel b is the same data after filtering the spurious data using the retrieved edges from the Ka-Band. 79
- Figure 3.16 Time-height plot of the LDR observed by the Ka-Band on December 23<sup>rd</sup>, 2018. The top and bottom of the ML are indicated by the blue and orange curves, and the isotherm of 0 °C is indicated by the grey dashed curve. 80
- Figure 4.1 Conceptual illustration of the radar signatures within DGZ found by previous studies. Radar reflectivity factor Ze (a), differential reflectivity ZDR (b), specific differential phase KDP (c), dual wavelength ratios DWR (d), mean Doppler velocity MDV (e). The horizontal dashed line indicates the isotherm of  $-15$  °C. The gray strip indicates the region where updraft or bi-modal spectra were observed. 85
- Figure 4.2 Time-height displays of several radar variables obtained at JOYCE on January 22<sup>nd</sup>, 2019: radar reflectivity factor Ze (a), mean Doppler velocity MDV (b) and the negative values indicate downward motion, dual wavelength ratios DWR-XKa (c) and DWR-KaW (d), differential reflectivity ZDR (e), specific differential phase KDP (f). The polarimetric variables are from 30° elevations and projected to the zenith. The vertical dashed gray line indicates 15 : 07 UTC and the horizontal line indicates the  $-15$  °C isotherm. 88

- Figure 4.3 Ten minutes averaged profiles of the radar variables on January 22<sup>nd</sup>, 2019 centred at 15 : 07 UTC. In panel (a) the blue, green and red curves are  $Z_e$  profiles from W-, Ka- and X-Band, respectively. Panel (b) shows the MDV profile from Ka-Band. In Panel (c), the red and blue curves are from the DWR-XKa and DWR-KaW, respectively. Panels (d) and (e) show the ZDR and KDP profiles, respectively.  $Z_e$ , DWRs, ZDR are average from the profiles in log units. The standard deviation is indicated by the contour along each profile. The horizontal gray dashed lines indicate the separation between the different regions as described in the text. 90
- Figure 4.4 Histograms of the DWR-KaW profiles stratified with temperature for the mDWR-KaW classes defined in Table 4.1. Panels a) to e) are for the class-1 to class-5. The continuous and dashed lines are the median and the quartiles of the distribution, respectively. Panel f) is the intercomparison between the median profiles from the different classes. The horizontal and vertical dashed lines indicate the isotherm of  $-15$  °C and DWR-KaW equal to 0 dB, respectively. 93
- Figure 4.5 Similar as Figure 4.4 but for DWR-XKa profiles. 94
- Figure 4.6 Similar as Figure 4.4 but for MDV profiles. The vertical dashed line at  $-1$  m/s indicates the typical fall velocity of snowflakes. 96
- Figure 4.7 Similar as Figure 4.4 but for the slow and fast edges of the Doppler spectra. The vertical dashed lines at the fast and slow edge panels indicate the fall velocities of  $-1$  m/s and 0 m/s, respectively. 98
- Figure 4.8 Histogram of the height separation between the mDWR-KaW and mSLOW as a function of mDWR-KaW. The continuous and dashed white lines are the median and quantiles of the distribution. The horizontal grey lines indicate the separation height at 0 and 0.4 km. The vertical gray line at 2 dB indicates the point where the median height separation reverses. 100

- Figure 4.9 Panels a) and c) are the probability distributions of the mDWR-KaW within DGZ and the co-located DWR-XKa of the mono- and multi-peak classes, respectively. Panels b) and d) are the differences between the probability distributions of the mono- and multi-peak classes of the mDWR-KaW and the co-located DWR-XKa, respectively. The vertical dashed grey line in Panel b) indicates the mDWR-KaW of 2 dB. 101
- Figure 4.10 Probability distribution curves (PDC) of the CTT grouped according to the mDWR-KaW in the DGZ. Each distribution is normalized by its total number of counts. 103
- Figure 5.1 Time-height plots of radar reflectivity factor  $Z_e$  (a), mean Doppler velocity (b) and negative values indicate downward motion, dual wavelength ratios DWR-KaW (c) and DWR-XKa (d), linear depolarization ratio LDR (e). The DWR-XKa is limited to a maximum altitude of 7 km because of less sensitive of the X-Band used during TRIPEX. The vertical dashed grey line indicates 06 : 50 UTC and the horizontal line indicates the  $-15\text{ }^\circ\text{C}$  isotherm. 107
- Figure 5.2 Ten minutes averaged profiles of the radar variables on December 31<sup>st</sup>, 2015 centred at 06 : 50 UTC. In panel (a) the blue, green, and red curves are  $Z_e$  profiles from W-, Ka- and X-Band, respectively. In Panel (b), the red and blue curves denote DWR-XKa and DWR-KaW, respectively. Panels (c) and (d) shows the MDV and LDR profiles from Ka-Band. The standard deviation is indicated by the contour along each profile. The numbers indicate the different defined regions. 110
- Figure 5.3 Triple-frequency plot of all DWR-XKa and DWR-KaW pairs. Panel (a) is from the observed DWR pairs from the temperature region between  $-5$  and  $0\text{ }^\circ\text{C}$  in Figure 5.2-b, the color code indicates temperature. Panel (b) is from simulated DWR pairs of three unrimed aggregate models using a gamma distribution for  $\mu$  equal to 0 and 4, and the color code indicates  $D_0$ . See Table 5.1 for the list of the used models. 111

- Figure 5.4 Histograms of the DWR-KaW profiles stratified with temperature for the mDWR-XKa classes defined in Table 5.2. Panels a) to e) are for the class-1 to class-5. The continuous and dashed lines are the median and the quartiles of the distribution, respectively. Panel f) is the inter-comparison between the median profiles from the different classes. The horizontal and vertical dashed lines indicate the isotherm of  $-15\text{ }^{\circ}\text{C}$  and DWR-KaW equal to 0 dB, respectively. 115
- Figure 5.5 Similar as Figure 5.4 but for DWR-XKa profiles. The horizontal line indicates the isotherm of  $-15\text{ }^{\circ}\text{C}$ . 117
- Figure 5.6 Similar as Figure 5.4 but for MDV-Ka profiles. The vertical dashed line at  $-1\text{ m/s}$  indicates the typical fall velocity of snowflakes and the horizontal line indicates the isotherm of  $-15\text{ }^{\circ}\text{C}$ . 119
- Figure 5.7 Histograms of the slow and fast edges of the spectra as in Figure 5.4. The vertical dashed lines at the fast and slow edge panels indicate the fall velocities of  $-1\text{ m/s}$  and  $0\text{ m/s}$ , respectively. 121
- Figure 5.8 Two-dimensional histogram of the pairs rain  $D_m$  and DWR-XKa in the snow aloft.  $D_m$  is from one range gate below the identified ML bottom and DWR-XKa is from four range gates above the identified ML top. Panel (a) is for the entire dataset. Panel (b) is for the data where MDV-Ka four range gates above the ML is slower than  $-1.5\text{ m/s}$  (unrimed), and Panel (c) is for MDV-Ka faster than  $-1.5\text{ m/s}$  (rimed). The dashed line and the continuous line are the median and the fit, respectively. The fitting equation is indicated on the top of each Panel. Panel (d) shows the intercomparison between the fits from (a) to (c). 125
- Figure 5.9 Scatter plot of the simulated  $D_m$  from raindrops and the DWR-XKa from snow for increasing riming mass fraction of dendrite aggregates with various degree of riming (Leinonen and Szyrmer, 2015). The blue, green, red, and purple curves are from 0, 0.1, 0.5 and  $10\text{ kg/m}^2$  effective liquid water path. 126

- Figure 5.10 Histograms of the Ze flux ratio (ZFR). The blue and red histograms are from the data where the MDV-Ka at four range gates above the ML top is faster and slower than  $-1.5$  m/s, respectively. The vertical dashed line indicates the theoretical ZFR ( $\mu = 0.23$ ), and the vertical continuous lines indicates the uncertainty range in case of vertical air motion of  $\pm 0.5/\pm 1$  m/s in the rain/snow region (Drummond et al., 1996). 128
- Figure 5.11 Statistical results of the Ze flux ratio from the data where the MDV-Ka at four range gates above the ML top is slower than  $-1.5$  m/s. Panel (a) shows the histograms of ZFR and Panel (b) shows the cumulative probability distribution from the profiles classified according to the mDWR-XKa. Additionally, Panel (b) shows the cumulative probability distribution from the profiles where the MDV-Ka is faster than  $-1.5$  m/s (orange line). 129

## LIST OF TABLES

---

- Table 2.1 Frequencies of interest for various meteorological radar applications adapted from Raghavan, (2003). 24
- Table 2.2 List of the typical mean Doppler velocities observed using vertically pointing radars (Khain and Pinsky, 2018; Lohmann, 2016; Pruppacher and Klett, 1997; Wallace and Hobbs, 2006) 25
- Table 3.1 Technical specifications and settings of the three vertically pointing radars operated during TRIPEX-Pol at JOYCE-CF. 63
- Table 3.2 Configuration parameters of the chirp sequence of the W-Band (vertically pointing) during the TRIPEX-Pol. 63
- Table 3.3 Coefficients a and b of the sensitivity equation retrieved for the X-, Ka-, and W-Band using the Level-2 data. All values flagged as error are excluded from the fitting calculation. 65

Table 3.4	Statistics of the comparison between the T, RHw, and RHi data from Cloudnet products and the corresponding data measured by the radiosonde. <a href="#">73</a>
Table 4.1	mDWR-KaW intervals defined to represent aggregates at the different growth stage inside of the DGZ. <a href="#">91</a>
Table 5.1	List of the of the aggregate scattering models used to simulate the DWRs pairs in <a href="#">Figure 5.3-b</a> . <a href="#">112</a>
Table 5.2	mDWR-XKa intervals defined to represent aggregates at the different growth stage close to the ML top. <a href="#">112</a>

## INTRODUCTION

---

### 1.1 MOTIVATION

Clouds cover around 73% of the planet surface according to a climatological study based on satellite observation (Stubenrauch et al., 2013). Clouds also play an essential role in the hydrological cycle by transporting water and distributing precipitation across the planet, which has a direct impact on society by filling up water reservoirs, inducing floods, increasing the amount of ice on glaciers, agriculture and thereby food security (Boucher et al., 2013; Lohmann, 2016; Wallace and Hobbs, 2006). Several studies indicate that on a global scale the majority of the precipitation originates via ice phase (Behrangi et al., 2014; Field and Heymsfield, 2015; Heymsfield et al., 2020; Mülmenstädt et al., 2015). Heymsfield et al., (2020) combined precipitation estimates from global precipitation measurement (GPM) and Cloud-Sat, and calculated the fractional contribution of different processes which lead to precipitation (Figure 1.1). In this analysis they found that around 63% of the precipitation originates via ice phase. Their results also indicate that on average for all latitudes, the ice phase is the main contributor to the precipitation (Figure 1.1).

Despite the great importance of clouds, our current understanding of the different processes (microphysical, dynamical, and thermodynamical) that may take place during their lifetime is still limited (Boucher et al., 2013; Eliasson et al., 2011; Stephens, 2005). In particular, the microphysical processes related to the formation of ice particles and the dependency of the processes on the temperature and water/ice supersaturation are far beyond to be fully understood (Libbrecht, 2005; Pruppacher and Klett, 1997). These limitations lead to misrepresentations of the different microphysical processes in numerical models, which in turn affect forecasts from numerical weather prediction models and climate projections (Boucher et al., 2013; Zelinka et al., 2017). Furthermore, the microphysical processes are extremely complex, and they cannot be resolved on the required scale (Morrison et al., 2020). Therefore, those processes are represented by complex parameterizations.

Different microphysical processes can take place during the lifetime of clouds, for example, nucleation, depositional growth, aggregation, riming, and melting (Khain and Pinsky, 2018; Lohmann, 2016; Pruppacher and Klett, 1997). Aggregation is known for producing a rapid increase in the size of the ice particles (Lawson et al., 1993, 1998), which produces a direct impact on precipitation by forming larger

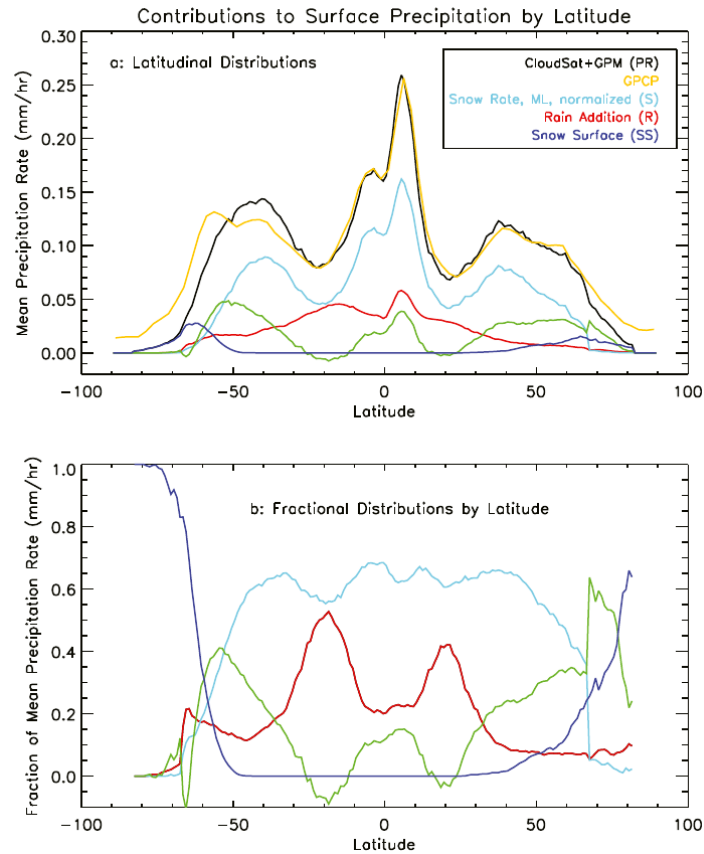


Figure 1.1: Zonal distribution of the mean precipitation rate (Panel a) and fractional dependence of the mean precipitation rate (Panel b) derived from CloudSat/GPM observations. The different colors indicate the different categories of clouds: snow that melts to produce rain (S, cyan), snow that falls to the surface (SS, violet), rain condensation/accretion to the melting ice/snow (R, green), and warm rain (W, red). GPCP stands for Global Precipitation Climatology Project. Taken from Heymsfield et al., (2020).



snowflakes or raindrops (Heymsfield, 1986; Sölch and Kärcher, 2011). Precipitation of large snowflakes can produce a large amount of accumulated snow on the ground, which may impose a problem for public mobility (Moisseev et al., 2015). The raindrop size determines e.g., how much the surface precipitation is decreased by evaporation because larger raindrops will fall faster through subsaturated layers and evaporate slower than smaller raindrops (Seifert, 2008) Since aggregation is a result of collisions between different particles that stick to each other, it produces a continuous change in the particle size distribution (Field and Heymsfield, 2003), where larger and faster particles collect the small and slower ones. This process is particularly challenging because it can occur over a broad temperature range, from temperatures smaller than 0 down to  $-60$  °C (Connolly et al., 2005; Crosier et al., 2011; Field and Heymsfield, 2003; Kajikawa and Heymsfield, 1989) and between a large variety of ice crystals types. Although aggregation can happen in such large temperature range, results from in-situ observation, laboratory investigations, and computational experiments have indicated that aggregation preferentially enhances at around  $-15$  °C due to the growth of dendrite-like crystals and close to 0 °C due to formation of a quasi liquid layer on the ice surface (Connolly et al., 2012; Hobbs et al., 1974; Lawson et al., 1998; Stewart, 1992).

In order to improve our current knowledge about ice and mixed-phase clouds and to evaluate different microphysical parameterizations and models, detailed observations of the evolution of microphysical processes in ice and mixed-phase clouds are extremely important. To this end, a significant effort has been made to increase the number of in-situ (Hobbs et al., 1974; Kajikawa and Heymsfield, 1989; Krüger et al., 2014; Lawson et al., 1998; Matrosov et al., 2001; McFarquhar et al., 2011; Verlinde et al., 2007) and remote sensing observations (Hoose and Möhler, 2012; Lobl et al., 2007; Löhnert et al., 2011; Lubin et al., 2020; Macke et al., 2017; Petäjä et al., 2016).

In-situ observations of ice and mixed-phase clouds are challenging; most of the time, these clouds populate regions far above the ground. Therefore, in-situ observations are often restricted to ground base stations at high mountains or to airborne campaigns. Although in-situ measurements are extremely valuable for models and parameterization evaluations due to all the details of the cloud particles that they can provide, this kind of observations are restricted to a specific time or place and only sample a small part of the clouds and cannot provide continuous profiles. In particular, aircraft based experiments can not be used as a source of long term observations due to the large number of resources required for it. Additionally, aircraft-based observations are often affected by artificial offset, for example, measurements of ice nucleating particles (INP) could be underestimated because the probes may miss a larger amount of INP, and measurements of ice

concentration could be overestimated due to artificial ice shattering produced by the probes (Baumgardner et al., 2012; Korolev et al., 2020; Schwarzenboeck et al., 2009).

A complementary observational approach is to use radar remote sensing. It gives the advantage to retrieve information along the path travelled by the signal, while it is propagating through the clouds. Since the late 90s and thanks to enormous technological development, radars have been installed in satellites and used to monitor precipitation on a global scale and provide information from regions where ground-based observations are not readily available (e.g. over the ocean). Thanks to spaceborne radars, it was possible to identify the importance of ice and mixed-phase clouds to the precipitation (Heymsfield et al., 2020; Mülmenstädt et al., 2015). Although spaceborne radars can provide 3-D observations of the clouds on a global scale, they have a coarse vertical resolution (250-500 m), are affected by ground clutter at altitudes lower than 1 km above the surface, and their signals are strongly attenuated.

Ground-based radars have been used to study and monitor clouds and precipitation. Since meteorological radars were introduced, they went through several technological developments adding the capability to use polarimetry which, for example, allows to retrieve additional information from the bulk shape of the particles. Several studies have used polarimetric radars to improve our understanding of the microphysical processes that take place in ice and mixed-phase clouds. One example is the identification of regions populated by pristine and asymmetric ice crystals (e.g. plate, dendrites needles) (Kumjian, 2013; Wolde and Vali, 2001a,b), indicating the predominance of depositional growth and nucleation. In particular, at temperature regions around  $-15\text{ }^{\circ}\text{C}$  several studies have found polarimetric signatures that suggest vigorous growth of dendrites by deposition (Andrić et al., 2013; Bechini et al., 2013; Griffin et al., 2018; Kennedy and Rutledge, 2011; Schrom et al., 2015; Trömel et al., 2019). Another example is the better identification of the region where the ice particles start to melt (melting layer). Polarimetric observations show enhanced signatures due to continuous change in the dielectric properties of the melting particle (Baldini and Gorgucci, 2006; Kumjian, 2013; Ryzhkov and Zrníc, 1998; Trömel et al., 2013, 2014). This improved characterization of the melting layer has been used to improve the representation of melting in numerical models (Fabry and Szyrmer, 1999; Szyrmer and Zawadzki, 1999; Trömel et al., 2014; Zawadzki et al., 2005).

Although polarimetric radar provided an essential contribution to the understanding of some of the microphysical processes mentioned previously, two other processes, namely riming and aggregation, cannot be unambiguously identified using polarimetric radars alone; both processes reduce the asymmetry of the ice particles producing similar polarimetric signatures (Kumjian, 2013; Ryzhkov et al., 2016; Trömel

et al., 2019). However, aggregates and rimed particles with equivalent sizes when melted, form raindrops with different sizes. The sizes of the melted rimed particles are larger than the melted aggregates. Therefore, identification of aggregation and better separation from riming is needed to improve our understanding of aggregation.

The most innovative way of using radar for remote sensing is to combine observations from nearby placed vertically pointing radars that operate at different frequencies. The data obtained by the radars from this kind of setup can be used, for example, to retrieve liquid water content and ice water content (Gaussiat et al., 2003; Yoshida et al., 2006) and to estimate the snow differential attenuation (Hogan et al., 2005; Tridon et al., 2020). Another possible application for multi-frequency observation is to retrieve information about particles sizes (Hogan et al., 2000; Matrosov, 1992). The combination of two or more radars with one radar operating at low frequency, ensuring that all particles scatter in Rayleigh regime, and the other radars operating at well chosen higher frequencies, ensuring that the particles transit from Rayleigh to non-Rayleigh scattering regime at different sizes, allows tracking the growth of ice particles along their path towards the ground (Sekelsky et al., 1999). A theoretical study by Kneifel et al., (2011) using different scattering models to simulate the triple-frequency observations indicated that this approach could be used to distinguish between different particle types. Another theoretical study, from Leinonen and Szyrmer, (2015), suggested that the triple-frequency observations could be affected by the changing in the density of ice particles. Kneifel et al., (2015) also verified this behaviour using data from a triple-frequency experimental campaign; the authors identified a distinct behaviour between rimed and unrimed aggregates. The capability to obtain information about the particles growth and their change in density gives the possibility to use multi-frequency radar observation to study aggregation and riming.

If the vertically pointing multi-frequency radars are also Doppler capable, it adds the possibility to use the Doppler velocity as an indicator of the particles fall velocity. Barthazy and Schefold, (2006) and Mosimann, (1995) indicated that the increase in density due to riming could be verified by an increase in the Doppler velocities. While the Doppler velocity of unrimed aggregates increases up to 1 m/s, the occurrence of riming can further increase the Doppler velocities, for example, up to 3 m/s (Kneifel and Moisseev, 2020). This additional source of information of changing in particles density combined with the multi-frequency observation can be used for improving our knowledge about aggregation and riming.

## 1.2 OBJECTIVES AND OUTLINE

Despite the fundamental importance of aggregation to the formation of large precipitating particles, few works have been dedicated to studying aggregation in clouds. This thesis uses the state-of-art of radar remote sensing technique based on multi-frequency observation from vertically pointing Doppler radars to investigate the conditions that intensify aggregation in temperature regions around  $-15\text{ }^{\circ}\text{C}$  and  $0\text{ }^{\circ}\text{C}$  and how this affects the raindrop sizes, which is an important parameter to estimate surface precipitation rates. To this end, this thesis introduces a novel methodology for correcting the multi-frequency observations.

[Chapter 2](#) provides a brief introduction to the theory of the cloud microphysical processes related to the formation and growth of ice particles. Additionally, this chapter gives a short introduction to the theory of radar remote sensing and introduces the basic concepts of multi-frequency observation.

[Chapter 3](#) describes the experimental setup and technical specifications of the radars used during the triple-frequency and polarimetric radar experiment for improving process observation of winter precipitation (TRIPEX, 2015/2016) and (TRIPEX-Pol, 2018/2019) campaigns. It also highlights the improvements applied to TRIPEX-Pol based on the knowledge obtained during TRIPEX campaign. The data from TRIPEX and TRIPEX-Pol is used in this thesis as the primary source of information of aggregation. This chapter additionally describes the methodology developed to process the data collected during both campaigns. The data processing minimizes the effect of attenuation, miscalibration, remaining offsets, removes spurious data and assigns quality flags for each processing step.

In [Chapter 4](#), the triple-frequency observations from TRIPEX and TRIPEX-Pol are combined to provide the longest available dataset (6 months long) to study the formation of aggregation in temperature regions between  $-20$  and  $-10\text{ }^{\circ}\text{C}$  (DGZ). The maximum dual wavelength ratio Ka-W (mDWR-KaW) within DGZ is used as an indicator of increase in snowflake sizes. The radar profiles from the combined dataset are then classified according to the mDWR-KaW. This classification is used to investigate if the intensification of aggregation within DGZ is favoured by the occurrence of upward motion or microphysical processes.

[Chapter 5](#) also uses the combined triple-frequency observations from TRIPEX and TRIPEX-Pol, but for studying the intensification of aggregation in temperatures between  $-10$  and  $0\text{ }^{\circ}\text{C}$ . Similarly to the approach used in [Chapter 4](#), the profiles from this longterm dataset are classified according to the maximum dual wavelength ratio X-Ka (mDWR-XKa) within this temperature region to identify conditions that favour the formation of large aggregates. As most of the global

precipitation reaches the ground as rain but is formed via the ice phase (Figure 1.1), it is important to investigate the effect of ice microphysical processes (e.g. aggregation) on the properties (e.g. size) of the rain. This chapter investigates if the increase of aggregate sizes above the melting layer favours the increase of raindrop sizes and if this increase of aggregate sizes favours additional aggregation or break up while aggregates are melting.

Finally, Chapter 6 summarizes the main results and draws conclusions regarding the conditions that favour the intensification of aggregation. Additionally, it also provides an outlook for future research.



This chapter introduces the theoretical bases of the microphysical processes from ice mixed-phase clouds, and it presents the basic theory of radar remote sensing. [Section 2.1.1](#) describes the conditions needed for the formation and growth of a single ice crystal and the influence of these conditions on the shape of ice crystals. An overview of the growth by aggregation is given in [Section 2.1.2](#). An introduction to the formation of ice fragments is provided in [Section 2.1.4](#). [Section 2.2.1](#) introduces the concepts related to the scattering of a single particle, and [Section 2.2.2](#) describes attenuation and radar reflectivity factor from a distribution of particles. Finally, [Section 2.2.3](#) introduces the Doppler spectra and other related concepts.

## 2.1 ICE GROWTH MICROPHYSICAL PROCESSES

During the lifetime of the clouds, several microphysical processes can take place leading to the formation of, for example, solid- and liquid-phase particles. Each one of these processes require different conditions to take place. Here, an introductory description of the microphysical processes related to the formation of ice crystals and snow is given, and a more in-depth description can be found in Lohmann, (2016) and Pruppacher and Klett, (1997).

### 2.1.1 *Ice nucleation and depositional growth*

The formation of the initial ice particles can take place via two different processes. The first process is homogeneous nucleation, where those particles are formed in the absence of ice nucleating particles (INP). The direct transition from vapour to ice phase requires colder temperatures and ice supersaturation ( $S_i$ ) that are rarely observed, suggesting that this transition is a rare phenomenon in the atmosphere (Lohmann, 2016). [Figure 2.1](#) provides an example of the homogeneous nucleation rate for water and ice from vapour ( $J_w$  and  $J_i$ ). One can see that the homogeneous nucleation of ice becomes favourable at temperatures smaller than  $\approx 226$  K ( $-47$  °C) and for water supersaturation  $S_w$  larger than 21, which is much higher than the observed in the atmosphere (Lohmann, 2016). In contrast, the formation of ice particles due to spontaneous freezing of the water droplets is observed in the atmosphere. Experimental results show that pure water droplets freeze spontaneously at temperatures around  $-38$  °C (Pruppacher and Klett, 1997). The second process is heterogeneous nucleation (e.g. im-

mersion freezing, condensation freezing, contact freezing, deposition nucleation), where ice particles can form on the surface of aerosols even in conditions where homogeneous nucleation would not be possible; however, not all aerosols serve as INP (Khain and Pinsky, 2018; Lohmann, 2016). The reasons why some aerosols serve as INP and others not are not completely known, but it is known that the surface of INPs provides an ice-like structure which favour water molecules bonds. Examples of INP are bacterias, pollen, dust particles, organic aerosols and soot particles. Figure 2.2 shows, for different aerosols types, the onset of ice supersaturation ( $S_i$ ) and temperatures where ice nucleation is observed (Hoose and Möhler, 2012; Lohmann, 2016).

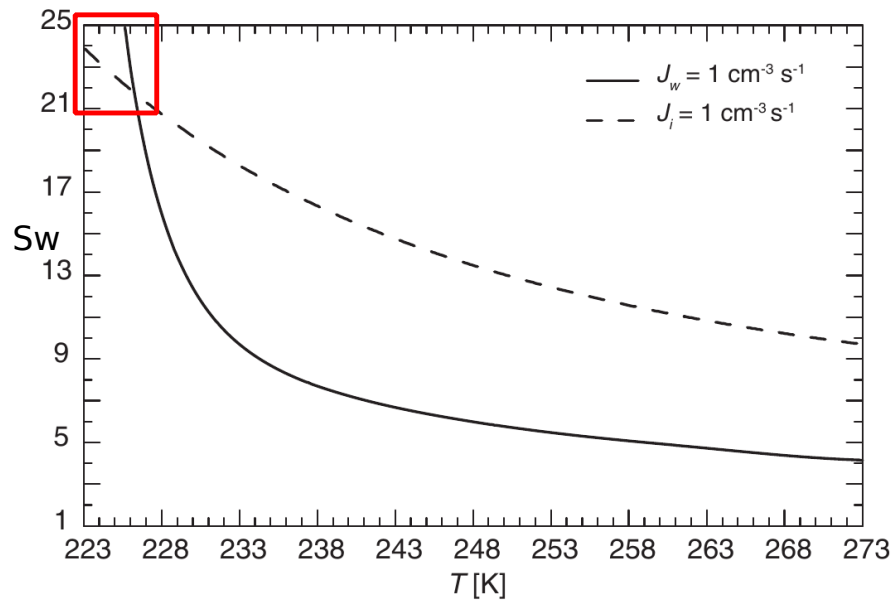


Figure 2.1: Saturation ratio with respect to water ( $S_w$ ) as a function of the temperature required to obtain a homogeneous nucleation rate of  $1\text{cm}^{-3}\text{s}^{-1}$  for water from vapor ( $J_w$ ) and for ice from vapor ( $J_i$ ). The red box indicates the region where the homogeneous nucleation of ice is favourable. Figure adapted from Lohmann, (2016).

During the early stage of the initially generated ice particle, depositional growth is the most efficient growth process (Lohmann, 2016; Pruppacher and Klett, 1997), where water vapour molecules deposit on the surface of ice particles increasing their masses and sizes. If the new-formed ice particles are in a region of the cloud where the environment is supersaturated with respect to ice and water, these ice particles and the co-existing droplets grow competing with each other for the available water vapour (Korolev, 2007). However, if those new ice particles are in a region supersaturated with respect to ice and sub-saturated with respect to water, a diffusion process known as Wegener-Bergeron-Findeisen (WBF) takes place and the ice particles grow on the expense of the water droplets (Korolev, 2007). Figure 2.3



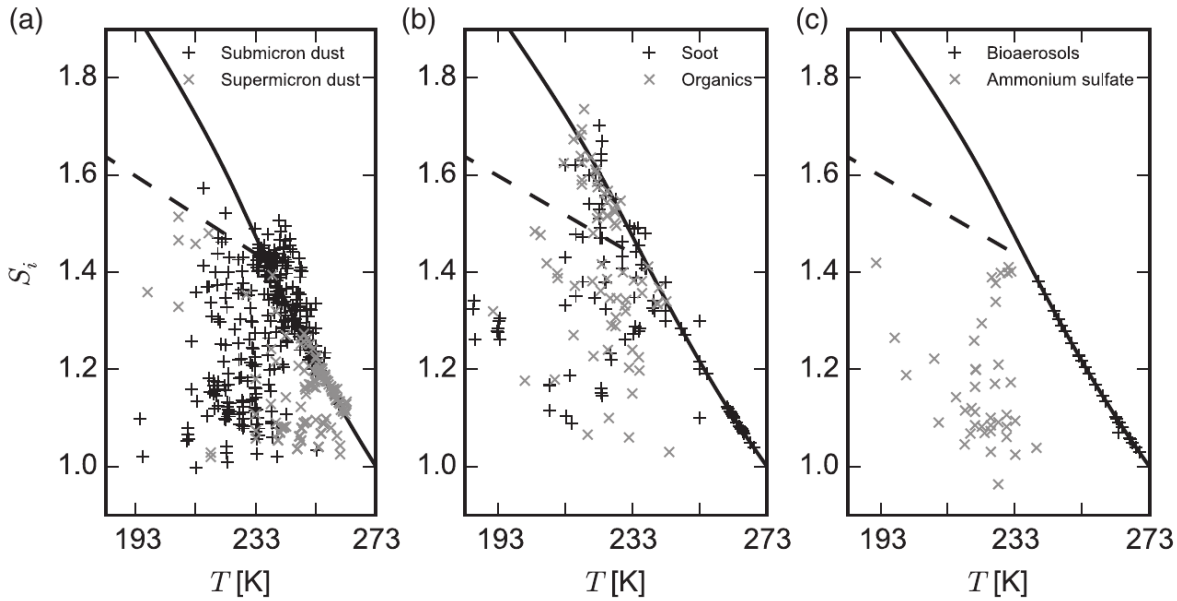


Figure 2.2: Onset  $S_i$  and temperatures for heterogeneous nucleation for different INPs. Panel (a) is for mineral dust, Panel (b) is for organic particles and soot, and Panel (c) is for bioaerosol and ammonium. The solid line indicates the  $S_w$ . Figure adapted from Lohmann, (2016).

illustrates the WBF process. The void region surrounding the crystal indicates that the nearby droplets were consumed during the growth of the crystal.

During the depositional growth, the water molecules attach to each other via the hydrogen bonds giving a hexagonal structure to the ice lattice (Lohmann, 2016; Pruppacher and Klett, 1997). However, the shape of the ice crystals is dependent on  $T$  and  $S_i$  (Fukuta, 1969; Hallett and Mason, 1958; Keller, 1980; Takahashi, 2014; Takahashi et al., 1991). Another factor that plays a role in the formation of the particle shape is the time that water molecules have to arrange themselves on the crystalline structure. Different combinations of those parameters lead to a large variety of habits, from simple structures as plates to complex ones as dendrites and rosettes. A comprehensive habit diagram based on several laboratory studies and in-situ observations proposed by Bailey and Hallett, 2009 shows the large variety of habits observed in the atmosphere for  $T$  between  $-70$  and  $0$  °C and  $S_i$  between  $0$  and  $0.6$  (Figure 2.4). The diagram indicates, for example, that at temperatures between  $-20$  and  $-10$  °C branched crystals, such as sector and dendrites, are formed in an environment supersaturated with respect to water; however, if the water saturation is not reached, the ice crystals grow plate-like. The temperature regime, between  $-20$  and  $-10$  °C, is commonly addressed as dendrite growth zone (DGZ).

The growth rate of a single particle by diffusion is described by Equation 2.1.  $m$  is the mass of the ice crystal,  $\alpha_m$  is the accommodation

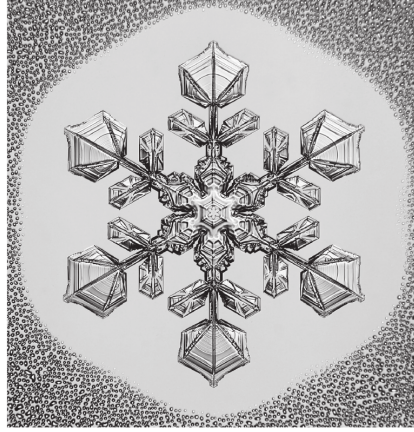


Figure 2.3: Illustration of the Wegener-Bergeron-Findeisen. Adapted from Lohmann, 2016, but it is originally from <http://www.snowcrystals.com>.

coefficient,  $C$  is the capacitance, and it is proportional to the particle size,  $L_s$  is the latent heat of sublimation,  $T$  is the temperature,  $R_v$  is the gas constant of water vapour,  $K$  is the thermal conductivity of the air,  $D_v$  is the molecular diffusion coefficient of water vapour in the air and  $e_{s,i}$  is the saturation vapour pressure with respect to ice. From the electrostatic theory,  $C$  is dependent on the geometry of the particle; however, the shape of the ice particles are dependent on  $T$  and  $e_{s,i}$  as indicated in Figure 2.4. A laboratory study from Takahashi et al., (1991) showed that this change in capacitance with  $T$  and  $e_{s,i}$  leads to a growth rate that is enhanced in two temperature regimes. Figure 2.5 shows the change in the mass of ice crystals for different growth periods. One can see that there are two temperature regions where the growth rate is enhanced; one is between  $-8$  and  $-2$  °C where needles preferentially grow, and the other is between  $-20$  and  $-10$  °C (within DGZ) where the growth rate is strongly enhanced.

$$\frac{dm}{dt} = \alpha_m 4\pi C (S_i - 1) \left[ \left( \frac{L_s}{R_v T} - 1 \right) \frac{L_s}{KT} + \frac{R_v T}{e_{s,i}(T) D_v} \right]^{-1} \quad (2.1)$$

### 2.1.2 Aggregation

Aggregation is the process where different particles remain attached after a collision between them. Several in-situ experimental campaigns observed aggregation taking place at temperatures between  $-60$  and  $0$  °C (Connolly et al., 2012; Crosier et al., 2011; Field and Heymsfield, 2003). From the hydrodynamic theory, the growth rate by aggregation between different particles is described by the statistical growth equation (Equation 2.2) (Pruppacher and Klett, 1997).  $f(m_i)$  is the number distribution of particles with mass  $m_i$ .  $i$  and  $j$  are indexes of

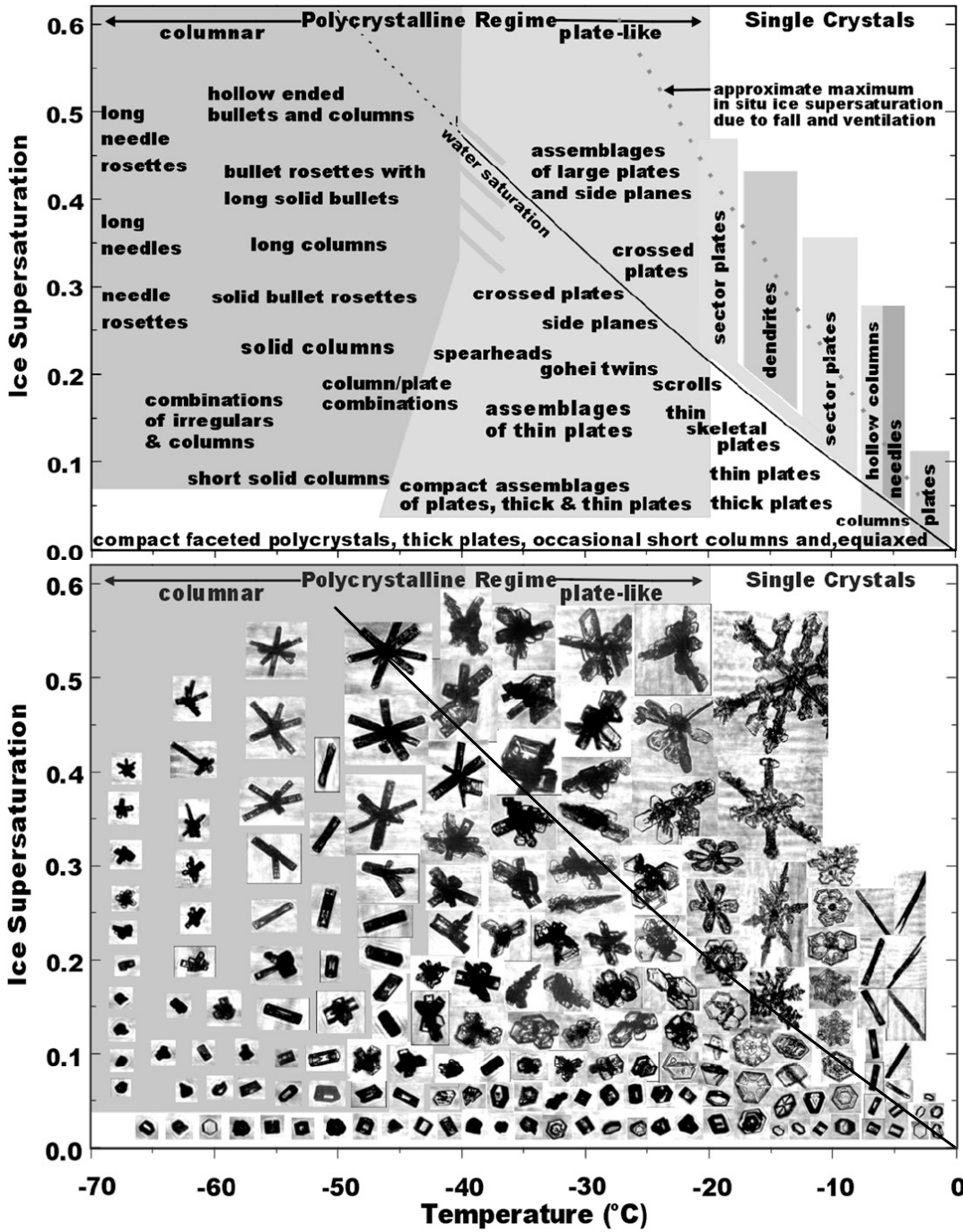


Figure 2.4: Ice particle habit diagram as function of T and Si derived from laboratory studies and in-situ observations. The solid line indicates the water supersaturation. Adapted from Bailey and Hallett, (2009).

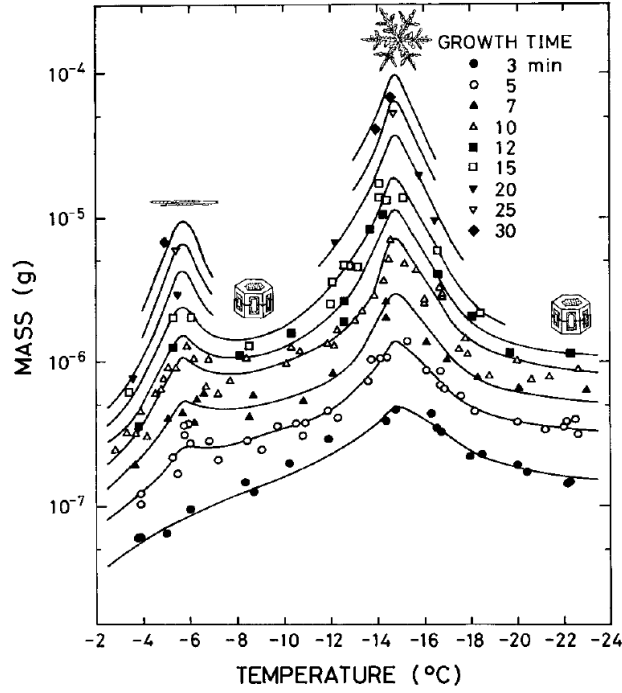


Figure 2.5: Change of ice particles mass for different growth times under a liquid water content of  $0.1 \text{ gm}^{-3}$  and pressure of 1010 hPa. Adapted from Takahashi et al., (1991).

two distinct particles.  $K$  is the collision kernel (Equation 2.3) (Pruppacher and Klett, 1997), which gives the probability of two particles aggregate. Since the ice particles do not have a well defined radius, the time-average projected area of the particles normal to the fall direction  $A$  is used to characterize their sizes.  $v$  is the terminal velocity.  $E_{agg}$  represents the aggregation efficiency, and it is the product of two other parameters, the collision efficiency  $E_c$  and the sticking efficiency  $E_s$ .

$$\left. \frac{df(m_i)}{dt} \right|_{agg} = \int_0^{m_i/2} f(m_j)f(m_i - m_j)K(i, j)dm_j - \int_0^\infty f(m_i)f(m_j)K(i, j)dm_j \quad (2.2)$$

$$K(i, j) = (A_i^{0.5} + A_j^{0.5})^2 |v_i - v_j| E_{agg} \quad (2.3)$$

An immediate result from Equation 2.3 is that the probability of collision increases with the increase of the size of both particles. It also indicates that this probability increases with the increase in the difference between particles terminal velocities; particles with the same terminal velocity have a null probability of aggregation. Figure 2.6 shows the terminal fall velocity from different ice particles obtained by Karrer et al., (2020) using the hydrodynamic theory and an aggregation model. One can see that there is a large variability of the

terminal velocity for a different type of particles and sizes, favouring the collision between them.

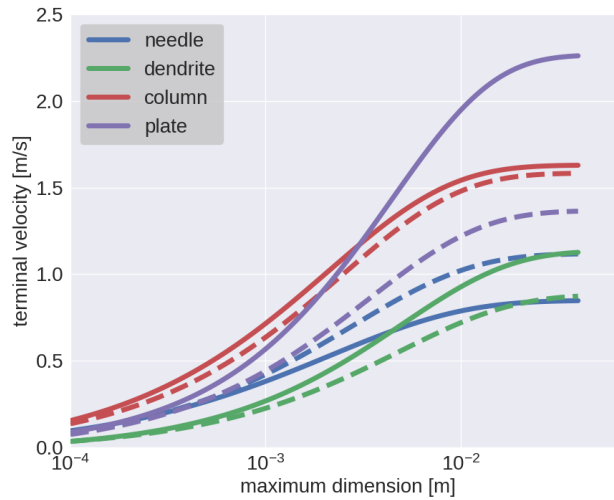


Figure 2.6: Terminal fall velocity of single particles as function of their maximum dimension (Karrer et al., 2020). The continuous and dashed lines are from single crystal and aggregates, respectively.

$E_c$  is a measure of the tendency for collision, which represents the fact that some of the collisions may not happen because one of the particles can be deflected by the flow (Lohmann, 2016; Pruppacher and Klett, 1997). Figure 2.7 illustrates the collision between small spherical particles P1, P2, P3. P2 and P3 have the same diameter  $d$  smaller than the diameter  $D$  of P1. P2 and P3 have the same fall velocity  $v$  slower than velocity  $V$  of P1. P2 follows a streamline closer to the centre of P1 than P3, leading to a collision between P1 and P2, while P1 and P3 do not collide. Although pristine ice crystals and snowflakes are mostly not spherical, similar behaviour also happens to them (Pruppacher and Klett, 1997). Based on the hydrodynamic theory and combined with the theories of boundary-layers, Böhm, (1992) introduced a semi-empirical solution of  $E_c$  for different kinds of particles and sizes. Figure 2.8 shows  $E_c$  calculated for planar branched ice particles and indicates that  $E_c$  strongly changes for different collision setups. One can see that there are two possibilities for increasing  $E_c$ . One possibility is increasing the dimensions of the colliding particles indicated by the general increase of  $E_c$  for different curves. Another possibility is having collisions between particles with comparable sizes indicated by the maximum of each curve.

$E_s$  is the temperature dependent probability of particles to stick after collision. This temperature dependency is related to two different factors. One factor is the shape of the ice particles; as shown in Section 2.1.1, the shape of the ice crystals is dependent on the environmental temperature. At temperature range between  $-20$  and  $-10$  °C dendrites grow, and due to their branched structure, this type of

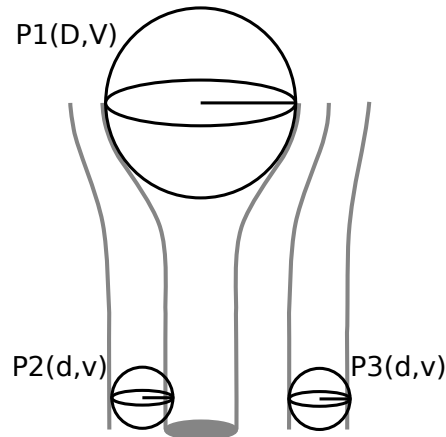


Figure 2.7: Illustration of the collision between spherical particles. The gray lines indicate the streamline flow.

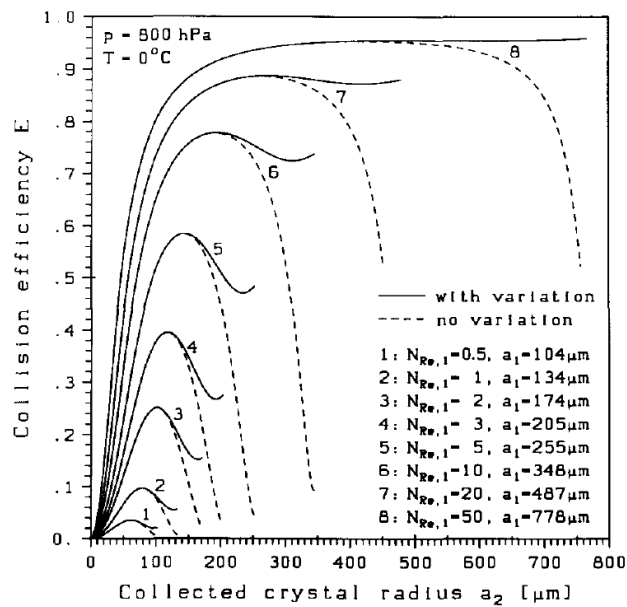


Figure 2.8: Aggregation collision efficiency of planar branched ice particles. The different curves are from different realisations of the simulation indicated by the legends. Adapted from Böhm, (1992).



ice crystals interlock with each other which is not possible for plates or needles (Connolly et al., 2012). The second factor is the presence of quasi-liquid layer (QLL) on the surface of the ice particles, where the water molecules are not random structured as a liquid nor do they fixed structured as crystal (Li and Somorjai, 2007). The QLL forms at temperatures colder than 0 °C, and it starts to be distinguishable from the crystalline structure at around  $-33$  °C (Slater and Michaelides, 2019). This QLL gets thicker with increasing temperature, which increases  $E_s$  by enhancing the sintering between ice particles.

It is not easy to measure  $E_s$  (Phillips et al., 2015), and only a few studies about the variation of  $E_s$  with temperature are available (Connolly et al., 2012; Hosler and Hallgren, 1960; Kajikawa and Heymsfield, 1989; Mitchell, 1988). Often in-situ and laboratory investigation using diffusion chambers investigate  $E_s$  indirectly by studying the  $E_{agg}$  as a function of temperature and assuming  $E_c = 1$ . Figure 2.9 shows the  $E_s$  values from available parameterization (Phillips et al., 2015) and measurements (Mitchell, 1988) and indicates that  $E_s$  enhances at a temperature range between  $-20$  and  $-10$  °C, which represents the fact that dendrites grow in this region and they efficiently interlock each other.

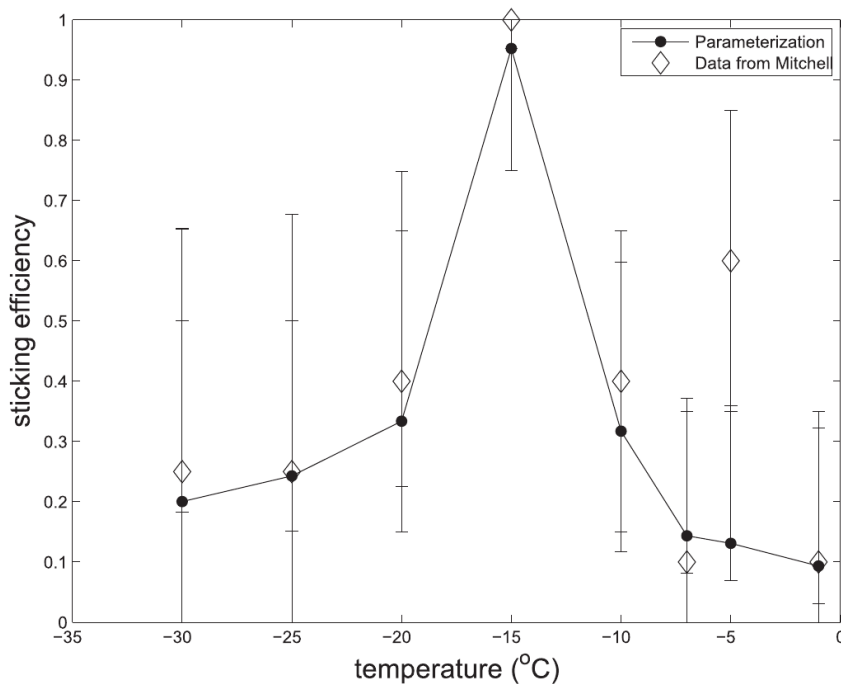


Figure 2.9: Variation of the  $E_s$  with temperature. Open diamonds are from Mitchell, (1988) and dark dots are from the parameterization from Phillips et al., (2015). The error bars are the standard deviation obtained by Connolly et al., (2012). Adapted from Phillips et al., (2015).

### 2.1.3 Riming

Riming is the process in which particles grow by accretion of supercooled liquid water (SLW). During this process, the collected water droplets freeze onto the surface of the ice particles leading to a rapid increase of their masses while their sizes remain almost constant (Pruppacher and Klett, 1997). The size of the particles only increases after their surfaces are filled in with rimed ice (Heymsfield, 1982), which indicates that rimed particles experience a rapid increase in density. Figure 2.10(a-b) show examples of rimed particles in two different stages. One can see that the more the crystal is affected by riming, the less of its initial characteristics remain generating a spherical like particle (graupel).

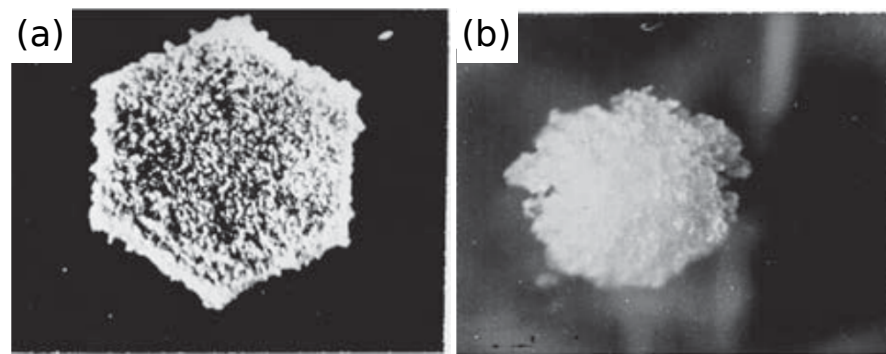


Figure 2.10: Illustration of rimed ice particles. Panel (a) shows an initially rimed plate, and Panel (b) shows an extremely rimed ice crystal (spherical graupel). Adapted from Wallace and Hobbs, (2006).

Due to this rapid increase in density, the particles fall velocities rapidly increase. This change in velocities was verified by Fukuta and Takahashi, (1999) and Takahashi and Fukuta, (1988) as a response to the riming enhancement in a windy tunnel experiment. Figure 2.11 shows the results obtained by Takahashi, and one can see that the more the particles grow by riming, the faster they get. Observational studies reported rimed particles with fall velocities up to 3 m/s (Barthazy and Schefold, 2006; Mosimann, 1995).

Riming can play an important role in the precipitation cycle by enhancing the precipitation rate. Harimaya and Sato, (1989) found that in the coastal area of Japan, riming contributed to 40 to 63% of the snow mass. In the Sierra Nevada, Mitchell et al., (1990) found that this contribution was between 30 and 40%.

### 2.1.4 Secondary ice production

Secondary ice production (SIP) represents a class of atmospheric production ice where pre-existing ice particles are required, which differ from the primary formation (homogeneous and heterogeneous nucle-



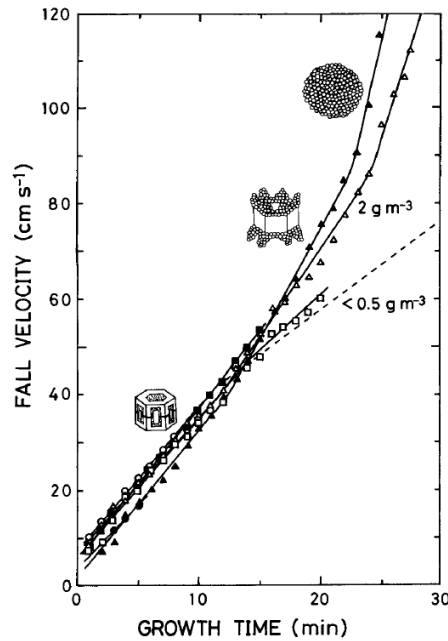


Figure 2.11: Increase of the fall velocity of rimed ice particles at  $-10.5\text{ }^{\circ}\text{C}$ . The continuous line is for liquid water content of  $2\text{ g m}^{-3}$  and the dashed line is for liquid water content less than  $0.5\text{ g m}^{-3}$ . Adapted from Fukuta and Takahashi, (1999).

ation) where the ice particles are formed by spontaneous formation of the ice germs in extremely cold temperatures ( $T < -40\text{ }^{\circ}\text{C}$ ) or in the presence of INP. SIP is of particular importance during the life-time of the clouds because it can enormously increase the concentration of ice particles. Several studies (Crawford et al., 2012; Crosier et al., 2011; Heymsfield and Willis, 2014; Korolev et al., 2020; Lawson et al., 2017) reported that the concentration of ice particles often exceeds the concentration of INP, and the likely explanation for this fact is the presence of SIP. For example, in-situ observations in the Arctic indicate that at least 18% of the fragmented stellar like crystals result from natural processes (Schwarzenboeck et al., 2009), while the remaining 82% could result from not proved natural fragmentation or from the measurements methodology. The production of secondary ice in the DGZ could favour the production of branched like crystals and then enhance the formation of aggregates. A laboratory study conducted by Mignani et al., (2019) where the dendrite crystals were individually melted and refrozen, indicated that  $\approx 81\%$  of the crystals did not have active INP in temperatures between  $-12$  and  $-20\text{ }^{\circ}\text{C}$  suggesting that they are likely to result from SIP.

A recent extensive review from the literature by Korolev and Leisner, (2020) listed six identified SIP. Those processes are conceptually illustrated in Figure 2.12, and they are briefly described in the following text. For a detailed description of SIP see Field et al., (2017) and Korolev et al., (2020).

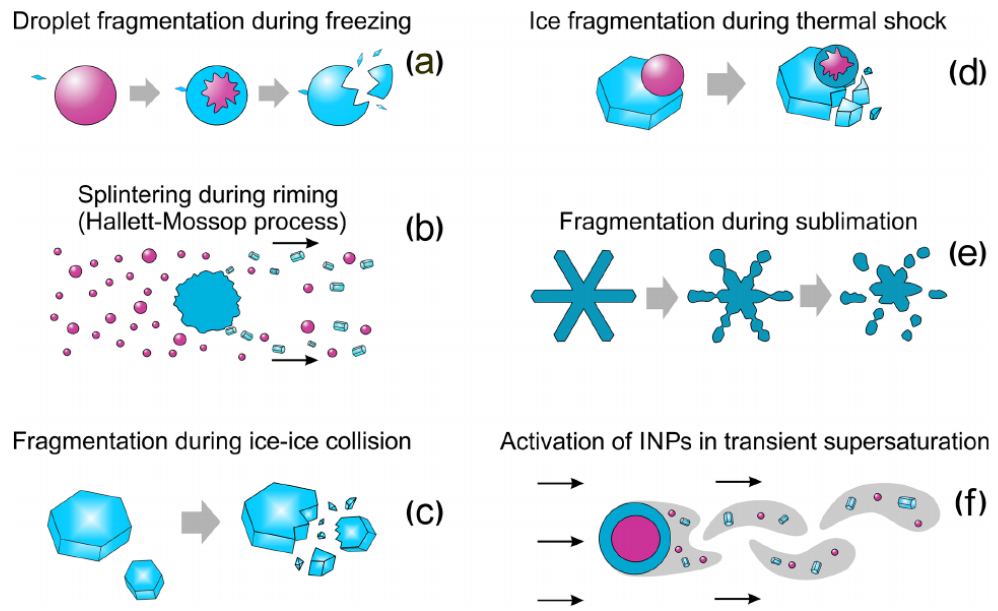


Figure 2.12: Conceptual illustration of the currently known SIP. Blue color indicates ice phase and red color indicates liquid phase. Adapted from Field et al., 2017.

The first process is droplet fragmentation during freezing. This process was initially proposed by several studies as the likely explanation for SIP (Mason and Maybank, 1960). It can occur during freezing of water droplets, as their outermost part freezes creating an ice shell and trapping the liquid water in the inner part. As the droplets freeze inward, the pressure inside the ice shell increases rapidly. At a certain point, the internal pressure reaches its maximum, and after that, any additional increase in pressure produces two possible results (Leisner et al., 2014). Either the frozen surface of the droplet cracks producing splinters, or it forces a spicule to form through the surface. Laboratory studies indicate that this process can take place in a wide temperature range (from 0 to  $-30$  °C). Additional studies suggest that this process could be one of the main sources of secondary ice (Korolev et al., 2004, 2020; Lawson et al., 2017; Rangno, 2008).

The second process is the production of splinters during riming; it is also referred to as Hallett-Mossop. This process was initially verified by different laboratory studies (Aufdermaur and Johnson, 1972; Hobbs and Burrows, 1966) where they identified the production of ice splinters while riming was taking place in temperatures between  $-5$  and  $-20$  °C. Later, Hallett and Mossop, (1974) and Mossop and Hallett, (1974) using a cloud chamber, found that this process requires specific conditions to take place. The environmental temperature should be between  $-8$  and  $-3$  °C, and the diameter of the colliding supercooled water droplet should be larger than  $25$   $\mu\text{m}$ . Additionally, Mossop, (1985) and Saunders and Hosseini, (2001) found that the collision velocities should be between 0.2 and 6 m/s. Heymsfield and Mossop,

1984 suggested that during Hallett-Mossop the surface of the colliding droplet freezes during contact with ice particles, and after that, the internal pressure increases until the droplet shell bursts producing splinters.

The third process is fragmentation during a collision between ice particles. This process was supported by ground-based and in-situ measurements (Jiusto and Weickmann, 1973; Takahashi, 1993). Takahashi et al., (1995) and Vardiman, (1978) in laboratory investigation found that ice fragments were produced when colliding rimmed particles. Khain and Pinsky, (2018) and Schwarzenboeck et al., (2009) also indicate that Collisions between branched ice crystals like dendrites are likely to produce fragments due to their structure. The current literature does not indicate a preferential temperature range for this process to occur.

The fourth process is the ice fragmentation during thermal shock. Koenig, (1963) proposed that while riming is taking place, a fraction of latent heat is transferred from the supercooled droplet to the ice particle and due to differential deformation the particle cracks. This process was verified in laboratory studies by (Dye and Hobbs, 1968) where ice crystals shattered into several pieces after getting in contact with supercooled droplets. King and Fletcher, (1976a,b) based on the thermoelastic theory and experiments, suggested that thermal shock is unlikely to be relevant for producing secondary ice in temperatures smaller than  $-5$  °C.

The fifth process is the ice fragmentation during sublimation. This process was identified in the laboratory when the ice crystals were submitted to an environment sub-saturated over ice (Bacon et al., 1998; Dong et al., 1994; Oraltay and Hallett, 1989). The few available studies indicate that this process happened at temperatures between  $-30$  and  $0$  °C and for relative humidity over ice between 50 and 100%.

The last known process is the activation of INP in transient supersaturation regions. This mechanism was suggested by Gagin, (1972) where a freezing drop would create a supersaturated transient region and activate INP that usually are not active. This process requires that the temperature at the drop surface should be higher than the temperature in the surrounding environment, and under this condition, the water molecules diffuse from the frozen surface to the environment (Dye and Hobbs, 1968). Fukuta and Lee, (1986) found that for a 2 mm falling graupel at  $-10$ ,  $-20$  and  $-30$  °C, the water supersaturation reached approximately 10, 40, 100%, respectively. However, the supersaturation reduced to 5.5, 23 and 35% when a 6 mm graupel was used.

## 2.2 RADAR REMOTE SENSING OF ICE AND MIXED-PHASE CLOUDS

One of the first usages of radars (Radio Detection and Ranging) for meteorological applications is from Marshall et al., (1947), where radars were used to estimate precipitation and since that time the usage of radars for meteorological applications rapidly increased. Radars brought the possibility to monitor the weather at almost real-time. Around the world, the number of radars dedicated to monitor the weather also increased, which in turn allowed, for example to observe and study thunderstorms, tornados and avoid natural disasters. Besides, radars allow observing a much larger portion of the clouds when compared to in situ methods (e.g. radiosondes, airborne sensors).

Radars transmit and receiving electromagnetic signals (pulses). Those signals are characterized by different physical properties of the electromagnetic waves such as frequency, amplitude, polarization, pulse width, pulse repetition frequency and phase. After the transmission, the signal propagates through the atmosphere interacting with its gaseous constituents and other liquid or solid targets (e.g. cloud droplets, snowflakes, ice crystals and insects), which absorb and scatter part of the energy of the transmitted signal. The signal scattered towards the radar (backscattered) can be received and recorded by the radars, allowing to relate the properties of the received signal (frequency, power, phase and polarization) with the properties of the hydrometeors which scattered the signal. The received power ( $P_r$ ) is described by Equation 2.4, where  $c$  is the speed of light,  $P_t$  is the pulse transmitted power, and  $\delta$  is the width of  $P_t$ ,  $G$  is the gain of the antenna,  $f$  is the radar frequency,  $\theta$  and  $\phi$  are the horizontal and vertical beamwidths,  $\alpha$  is the attenuation along the path travelled by the signal,  $r$  is the distance between the radar and the scatterers,  $|K|^2$  is the dielectric constant from the scatterers, and  $Z$  is the reflectivity factor of the scatterers. The derivation of the Equation 2.4 can be found in Bringi and Chandrasekar, (2001), Doviak and Zrnic, (2014), and Raghavan, (2003). Equation 2.4 shows that the  $P_r$  decreases with increasing distance and enhances with the increasing frequency.

$$P_r = \underbrace{\frac{\pi^3}{1024 \ln(2) c}}_{\text{constants}} \underbrace{P_t \delta G^2 f^2 \theta \phi}_{\text{radar parameters}} \underbrace{\frac{\alpha}{r^2}}_{\text{path properties}} \underbrace{|K|^2 Z}_{\text{scatterer properties}} \quad (2.4)$$

An important characteristic of the radars is the operating frequency. It determines for which meteorological application the radars can be best used. The different applications are based on the fact that the backscattering and attenuation are frequency-dependent. Table 2.1 lists the available radar frequency bands and the main meteorological application. Two other characteristics of some of the currently available

radars are polarimetry and Doppler capability. Polarimetric radars transmit and receive signals with a different polarization orientation (most common horizontal and vertical) which allow accessing information of the shape of the particles. Doppler radars allow, additionally, to retrieve information related to the radial velocity of the particles. In case Doppler radars are operated vertically pointing, the retrieved Doppler velocity is closely related to the particles fall velocity and gives the possibility to identify classes of hydrometeor. [Table 2.2](#) gives examples of the typical fall velocities of some classes of hydrometeor.

In case a particle with a specific size is illuminated by radar signals with different frequencies, the scattering regime can be different, and it is determined by the relation between the size of the particle and the frequency. The combination of observations from radars operating at different frequencies can provide additional information about the microphysical processes (e.g. aggregation, riming, melting) and improve retrievals of snow properties (Hogan et al., 2000; Kneifel et al., 2015; Matrosov, 1998). However, this method requires that the different radars observe the same volume.

### 2.2.1 Scattering properties of a single particle

From a classical electrodynamics perspective, when an electromagnetic wave propagates through a dielectric material, one part of the energy carried by the wave is absorbed and converted into thermal energy (absorption) and another part is dissipated in all directions (scattering) (Jackson, 1999; Liou, 2002). This combined loss of energy is called extinction. For a radar signal propagating through the atmosphere, the extinction produced by each atmospheric component (e.g. aerosols, water vapour molecules, droplets, ice particles) can be related to a quantity called extinction cross-section ( $\sigma_{ext}$ , [Equation 2.5](#)), and it represents the extinction produced by one particle from a given atmospheric component.  $\sigma_a$  and  $\sigma_s$  are the absorption cross-section and the scattering cross-section, respectively. These quantities ( $\sigma_a$  and  $\sigma_s$ ) are dependent on both the electromagnetic wave properties (i.e. the wavelength  $\lambda$  and the polarization state), as well as the properties of the particle such as the dielectric constant  $|K|^2$ , the illuminated surface area, the shape and orientation (Raghavan, 2003).

$$\sigma_{ext} = \sigma_a + \sigma_s \quad (2.5)$$

$\sigma_s$  represents the amount of radiation scattered in all directions; however for radar applications, only the amount scattered towards the radar contributes to the received signal, and it is represented by  $\sigma_b$  (backscattering cross-section). If the transmitted signal is vertically or horizontally polarized, the received signal is also polarized, and  $\sigma_b$  is proportional to the amplitudes of the backscattered signal ([Equa-](#)

Table 2.1: Frequencies of interest for various meteorological radar applications adapted from Raghavan, (2003).

Band designation	Frequency range	Range of wavelengths	Main application
VHF	30-300 MHz	10-1 m	Observation of clear air phenomena in the troposphere and stratosphere, wind-profiling, turbulence, refractive index structure
UHF	300-1000 MHz	1-0.3 m	
L	1-2 GHz	30-15 cm	Clear air and precipitation phenomena
S	2-4 GHz	15-7.5 cm	Precipitation measurement, tropical cyclone observation, local severe storms, radio wave propagation
C	5-7 GHz	6-4.5 cm	Local severe storms, precipitation measurement, tropical cyclone observation, radio wave propagation, use on aircraft
X	9-11 GHz	3.3-2.7 cm	Thunderstorm and gust front detection, radio wave propagation, use on aircraft
Ku	12-18 GHz	2.5-1.7 cm	Cloud physics, cloud boundaries, air- and space-borne radar
Ka	27-40 GHz	1.1-0.75 cm	Sea surface studies, precipitation measurement from attenuation, tornado observation
W	94 GHz	3.2 mm	Cloud boundaries, cloud microphysics and dynamics, tornado observation
F	140 GHz	2.14 mm	
G	220 GHz	1.30 mm	

Table 2.2: List of the typical mean Doppler velocities observed using vertically pointing radars (Khain and Pinsky, 2018; Lohmann, 2016; Pruppacher and Klett, 1997; Wallace and Hobbs, 2006)

hydrometeor class	fall velocity [m/s]
snow	0.5 - 1.5
hail	0.6 - 10
super cooled water	0
light rain	0.5 - 2
heavy rain	4 - 6

tion 2.6).  $S$  is the matrix of amplitudes of the backscattered linear polarized signal (Equation 2.7) (Sinclair, 1950). The indexes H (horizontal) and V (vertical) are used to indicate the polarization of the transmitted and received signals. The elements  $S_{HV}$  and  $S_{VH}$  are the depolarization components, which arises from the interaction between the linear polarized wave and the particles that are not vertically or horizontally aligned (Andronache, 2018).

$$\sigma_b = 4\pi|S|^2 \quad (2.6)$$

$$S = \begin{bmatrix} -S_{HH} & S_{HV} \\ S_{VH} & S_{VV} \end{bmatrix} \quad (2.7)$$

If the size of the illuminated particle is much smaller compared to the wavelength, it can be assumed that each point of the scatterer is instantaneously experiencing the same forcing electric field. This means that the individual induced dipoles oscillate in phase with each other. Under this condition, the scattering effects are considered to be in the Rayleigh regime and  $\sigma_b$  can be calculated using the Rayleigh approximation (Equation 2.8).

$$\sigma_b = \frac{\pi^5}{\lambda^4} |K|^2 D^6 \quad (2.8)$$

where  $D$  is the diameter of an equivalent sphere with the same diameter of the particle. The dielectric factor  $|K|^2$  accounts for the dielectric properties of the material constituting the scatterer and is related to the complex refractive index  $m(\lambda)$  as follows:

$$|K|^2 = \left| \frac{m(\lambda)^2 - 1}{m(\lambda)^2 + 2} \right|^2 \quad (2.9)$$



On the other hand, if the particle size is larger or comparable to the wavelength, the induced dipoles oscillate out of phase with one another, radiating waves that interfere constructively or destructively. In this case, the amount of backscattered radiation differs from the Rayleigh approximation, and the scattering is said to be in the non-Rayleigh regime. As an illustration of the transition to different scattering regimes with increasing  $D$ , Figure 2.13 shows the  $\sigma_b$  of simulated aggregates of a mix of columns and dendrites for X- (9.4 GHz), Ka- (35 GHz), and W-Band (94 GHz). One can see, for example, that a particle with a diameter of  $\approx 0.5$  mm scatters in the Rayleigh regime for all the three frequencies, while a particle with a diameter of  $\approx 2$  mm scatters in the non-Rayleigh regime for Ka- and W-Band, but it is still in the Rayleigh regime for X-Band.

*"snowScatt is a python package that provides scattering and microphysical properties of realistically shaped snowflakes developed at University of Cologne."*

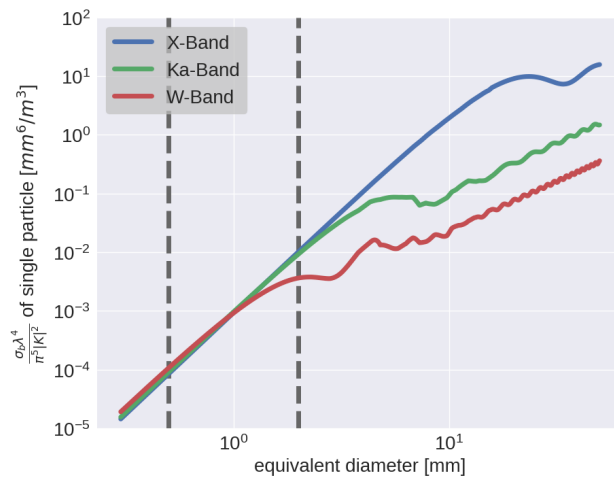


Figure 2.13: Normalize  $\sigma_b$  from single aggregate of a mix of columns and dendrites calculated using `snowScatt` (Ori et al., 2020b) for X-, Ka-, and W-Band. The vertical lines indicate the diameters equal to 0.5 and 2 mm.

In addition to the amount of backscattered radiation that is related to the particle size, the frequency of the returned signal can provide information about the radial velocity of the particle ( $v_r$ ) due to the Doppler shift of the frequency. This frequency change ( $\Delta f$ ) is quantified by Equation 2.10, where  $c$  is the speed of light and  $f$  is the frequency of the incident wave.

$$\Delta f = \frac{2v_r}{c} f \quad (2.10)$$

For example, if a radar transmits a signal at a frequency of 35 GHz and it illuminates a particle moving towards the radar with  $v_r = 1$  m/s, the  $\Delta f$  of the backscattered signal is approximately 233.3 Hz, which is  $10^9$  times smaller than the frequency of the transmitted signal. Some of the currently available radars can retrieve the Doppler velocity, but this order of magnitude of  $\Delta f$  is difficult to measure by the current



radars systems. Therefore, the Doppler velocity  $v_D$  is estimated from the temporal change in the phase ( $\varphi$ ) of the consecutive backscattered signals (Andronache, 2018; Doviak and Zrnic, 2014; Fabry, 2015), and it is given by Equation 2.11.  $m_{\text{air}}$  is the average refractive index of the air along the path.

$$\frac{d\varphi}{dt} = \frac{-4\pi f m_{\text{air}}}{c} v_D \quad (2.11)$$

However, this method leads to a limitation of the detectable velocity range, because the maximum absolute detectable phase difference is limited to  $\pm\pi$  (Andronache, 2018; Fabry, 2015; Raghavan, 2003), as shown by Equation 2.12. PRF is the pulse repetition frequency.

$$\max(v_D) = \left| \frac{c \text{PRF}}{4f} \right| \quad (2.12)$$

## 2.2.2 Attenuation and radar reflectivity factor from a particle distribution

### 2.2.2.1 Attenuation

The extinction of the radar signal is not a result of a single particle only, but it results from the extinction caused by all particles (e.g. aerosols, water vapour, ice particles, atmospheric gases) that are distributed along the path travelled by the signal. From a theory perspective, the extinction caused ( $\beta_{\text{ext}}$ , extinction coefficient) by an atmospheric component over an infinitesimal path is represented by the summation of the extinction caused by each particle with a specific diameter  $D$  that is illuminated by the transmitted signal Equation 2.13.  $\sigma_{\text{ext}}(D)$  is the extinction cross-section from a particle with a diameter  $D$ , and  $N(D)$  is the particle size distribution.

$$\beta_{\text{ext}}(s, \lambda) = \int \sigma_{\text{ext}}(D, \lambda) N(D) dD \quad (2.13)$$

The optical path of a particular atmospheric component is given by Equation 2.14, where the multiplicative factor 2 represents the double path that the signal travels between the transmission and reception and  $r$  is the range between the radar and the scatterer. The cumulative loss of the energy after the signal propagates through the optical path is called attenuation.

$$\tau_i(r, \lambda) = 2 \int_0^r \beta_{\text{ext}}(s, \lambda) ds \quad (2.14)$$

The two-way attenuation coefficient can be derived as Equation 2.15, where the total optical path ( $\tau_{\text{tot}}$ ) that the signal travels between the

transmission and reception is equal to the summation of all individual optical paths.

$$\begin{aligned} \mathfrak{K}(r, \lambda) &= \exp(-\tau_{\text{tot}}(r, \lambda)) \\ \tau_{\text{tot}}(r, \lambda) &= \tau(\text{water vapour}) + \tau(\text{O}_2) + \tau(\text{other gases}) \\ &\quad + \tau(\text{snow}) + \dots + \tau(\text{rain}) + \tau(\text{radome}) \end{aligned} \quad (2.15)$$

The radars used for atmospheric remote sensing operate in the microwave range of the electromagnetic spectrum. At this range, the O<sub>2</sub> and water vapour are the gases that mainly attenuate the radar signal. As indicated in [Figure 2.14](#), the attenuation by O<sub>2</sub> slowly increases for frequencies between 0.1 and 20 GHz, while for frequencies between 20 and 100 GHz the attenuation sharply increases and it has a maximum of 10 dB/km around 60 GHz. The attenuation by water vapour continuously increases between 3 and 100 GHz, and its maximum attenuation is around 22 GHz. Other atmospheric components also attenuate the radar signal. For example, rain and snow produce frequency-dependent attenuation and is, in addition, also proportional to the intensity of the precipitation. As indicated in [Figure 2.14](#), the attenuation produced by extreme rainfall ( $\approx 50$  mm/h) is more significant than the attenuation produced by lighter rainfall ( $\approx 2$  mm/h). The vertical lines from [Figure 2.14](#) indicate the frequencies of the radars used in this thesis, and one can see that the W-Band is the most affected by attenuation. Other possible sources of attenuation related to the impact of precipitation, not shown in the figure, are wet antenna and wet radome.

#### 2.2.2.2 Radar reflectivity factor

Similarly to extinction, the backscattered signal results from the contribution of all particles that are within the sampled volume. Analogous to the backscattering of single particles ([Section 2.2.1](#)), the amount of radiation backscattered by the sampled volume can be represented by the volume-averaged backscattering cross-section ( $\eta$ , [Equation 2.16](#));  $\eta$  is also known as reflectivity.  $n$  is the number concentration of particles, and it has units of  $\text{m}^{-3}$ . The angle brackets  $\langle \rangle$  indicate the ensemble average.

$$\eta = \langle n\sigma_b \rangle = \langle n4\pi|S|^2 \rangle \quad (2.16)$$

Considering that those particles are scattering in the Rayleigh regime,  $\eta_{\text{Ray}}$  is given by [Equation 2.17a](#).  $Z$  is the radar reflectivity factor, and this quantity is exclusively dependent on the properties of the particles.  $D$  is the particle diameter [mm], and  $N(D)dD$  is the num-

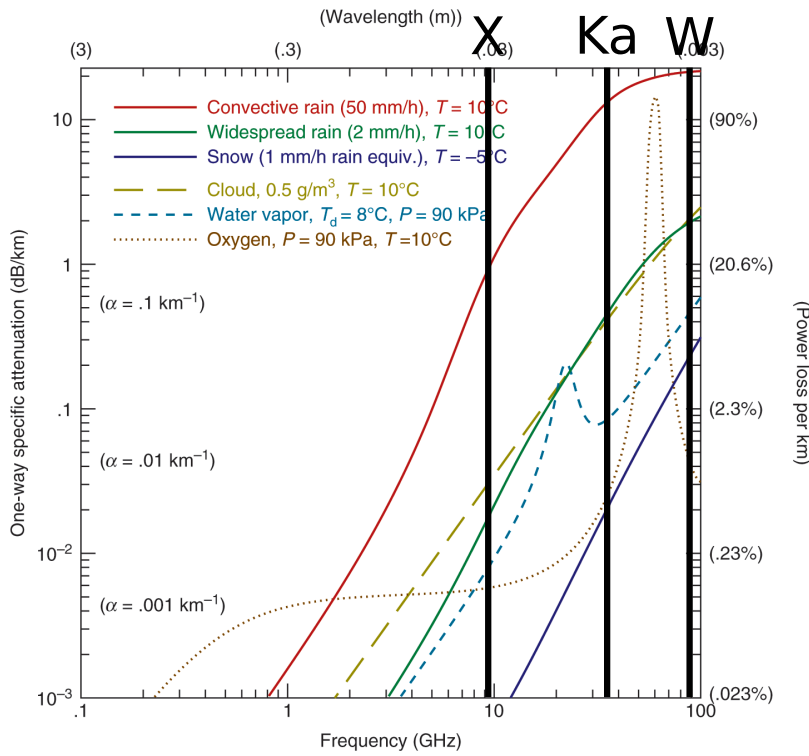


Figure 2.14: Example of attenuation from different components as function of the frequency. The red, green and blue solid lines are the attenuation produced by rain and snow. The brown and blue dotted lines are the attenuation from O<sub>2</sub> and water vapour respectively. The vertical black solid lines indicate the frequency of the X-, Ka- and W-Band radars used in this thesis. Note that the relation between  $\mathfrak{K}(r, \lambda)$  and  $\alpha(r, \lambda)$  in this figure is  $\mathfrak{K}(r, \lambda) = [2 \int_0^r \alpha(r, \lambda) dr]^{-1}$ . Adapted from Fabry, 2015.

ber of particles per cubic meter in the diameter interval  $(D, D + dD)$  (Bringi and Chandrasekar, 2001).

$$\eta_{\text{Ray}} = \frac{\pi^5}{\lambda^4} |\mathbf{K}|^2 \langle nD^6 \rangle \quad (2.17a)$$

$$= \frac{\pi^5}{\lambda^4} |\mathbf{K}|^2 \int D^6 N(D) dD \quad (2.17b)$$

$$= \frac{\pi^5}{\lambda^4} |\mathbf{K}|^2 Z \quad (2.17c)$$

$$Z \equiv \int D^6 N(D) dD \quad (2.18)$$

However, not all particles may be scattering in the Rayleigh regime, and not all particles have the same dielectric factor  $|\mathbf{K}|^2$ . Therefore, for meteorological purposes, all the particles within the sampled volume are assumed to be Rayleigh scatters and have the water dielectric factor  $|\mathbf{K}_w|^2$ . Based on those assumptions, the Equation 2.19a gives the definition of the radar equivalent reflectivity factor ( $Z_e$ ).

$$Z_e(\lambda) \equiv \frac{\lambda^4}{\pi^5 |\mathbf{K}_w|^2} \eta \quad (2.19a)$$

$$= \frac{\lambda^4}{\pi^5 |\mathbf{K}_w|^2} \langle n\sigma_b \rangle \quad (2.19b)$$

$$= \frac{\lambda^4}{\pi^5 |\mathbf{K}_w|^2} \int \sigma_b(D, \lambda) N(D) dD \quad (2.19c)$$

As introduced in Section 2.2.2.1, the radar signal is attenuated while it propagates through the atmosphere and the  $Z_e$  received by the radar is given by Equation 2.20.

$$Z_e(r, \lambda) = \mathfrak{K}(r, \lambda) \frac{\lambda^4}{\pi^5 |\mathbf{K}_w|^2} \int \sigma_b(D, \lambda) N(D) dD \quad (2.20)$$

For linear polarized waves, the  $Z_e$  can be written as Equation 2.21. Where the indices  $i$  and  $j$  are received and transmitted polarization directions respectively;  $i$  and  $j$  can be H or V.

$$Z_e(r, \lambda)_{ij} = \mathfrak{K}(r, \lambda) \frac{\lambda^4}{\pi^5 |\mathbf{K}_w|^2} \int \sigma_b(D, \lambda)_{ij} N(D) dD \quad (2.21)$$

Several studies (Greco et al., 2004; Heymsfield et al., 2004; Mitchell, 2002; Petty et al., 2011; Rose and Chandrasekar, 2006) showed that the size distribution of hydrometers in the atmosphere is well represented by a gamma distribution (Equation 2.22), where  $\Lambda$  and  $\mu$  are the

shape parameters, and  $N_0$  is the scaling parameter (Petty et al., 2011).  $N_0$  has dimensions  $L^{-(\mu+4)}$ , and  $\Lambda$  has dimensions  $L^{-1}$ . From this distribution, two additional parameters are defined ( $D_0$  and  $D_m$ ), and they are used to characterize the particle size distribution.  $D_0$  is the diameter that divides the volume in two equal parts (Equation 2.23), and  $D_m$  is the mass-weighted mean diameter (Equation 2.24).

$$N(D) = N_0 D^\mu \exp(-\Lambda D) \quad (2.22)$$

$$D_0 = \frac{3.67 + \mu}{\Lambda} \quad (2.23)$$

$$D_m = \frac{4 + \mu}{\Lambda} \quad (2.24)$$

The combination of Equation 2.21 and Equation 2.22 gives the final form of  $Z_e$ , which is the received  $Z_e$  from scatters at a range  $r$  far from the radar. Hereafter if the index  $i$  and  $j$  are not indicated, it will mean that  $Z_e$  is transmitted and received with the same polarization.

$$Z_e(r, \lambda)_{ij} = \mathfrak{K}(r, \lambda) \frac{\lambda^4 N_0}{\pi^5 |K_w|^2} \int \sigma_b(D, \lambda)_{ij} D^\mu \exp(-\Lambda D) dD \quad (2.25)$$

From this last equation, the linear depolarization ratio (LDR) of a distribution of particles can be defined as Equation 2.26.

$$\text{LDR}_{ij} \Big|_{i \neq j} = 10 \log \left( \frac{Z_{e_{ij}}}{Z_{e_{jj}}} \right) \quad (2.26)$$

LDR is dependent on the shape of the particle and the dielectric constant of the particles, and is independent of the particles concentration and attenuation (Andronache, 2018; Fabry, 2015; Raghavan, 2003). Very symmetric hydrometeors like small droplets can produce LDR around  $-35$  dB while needles can produce LDR larger than  $-10$  dB. The LDR is strongly enhanced during the melting process, which can be used to identify the melting layer.

### 2.2.2.3 Dual wavelength ratio

An advanced technique to remote sensing clouds with radars is to combine  $Z_e$  observations from different frequencies. This methodology is based on the fact that  $Z_e$  is a monotonic function of  $\Lambda$  (assuming  $Z_e$  defined by Equation 2.25) and that  $Z_e$  is different from different frequencies. Figure 2.15-a shows  $Z_e$  from X-, Ka- and W-Band radars simulated using an inverse exponential function (Equation 2.22,  $\mu = 0$ )

without taking attenuation into account. One can see that for large values of  $\Lambda$   $Z_e$  from the different frequencies is the same, while for decreasing  $\Lambda$   $Z_e$  curves deviate from each other. This deviation happens because, with decreasing  $\Lambda$ , the concentration of large scatters increases (Figure 2.15-b), and they transit from Rayleigh to non-Rayleigh scattering regime with increasing frequency.

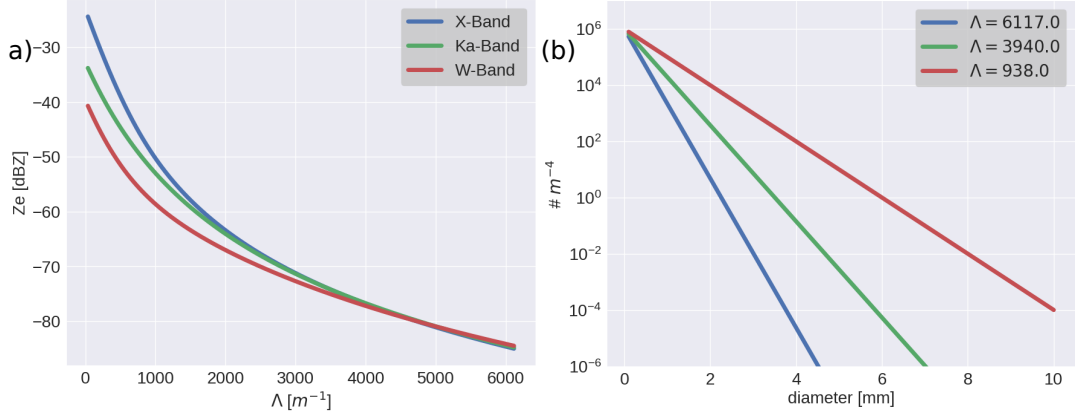


Figure 2.15: Panel (a) shows the equivalent reflectivity factor ( $Z_e$ ) from a gamma distribution of particles ( $\mu = 0$ ) calculated for X-, Ka- and W-Band. Panel (b) shows three realizations of the gamma distribution with  $\mu = 0$  and three  $\Lambda$  values.

The dual wavelength ratio (DWR) is defined as Equation 2.27, where  $\lambda_1$  is larger than  $\lambda_2$ . From the definition, one can see that DWR is a monotonic function of Lambda and independent of  $N_0$  (Matrosov, 1992).

$$\text{DWR}(\lambda_1, \lambda_2) \Big|_{\lambda_1 > \lambda_2} = 10 \log \left( \frac{Z_e(\lambda_1)}{Z_e(\lambda_2)} \right) \quad (2.27)$$

Figure 2.16-(a,b) shows two different combinations of the DWRs, one for the pair X and Ka (DWR-XKa) and another for the pair Ka and W (DWR-KaW) for the same  $Z_e$ s used in Figure 2.15. One can see that for  $\Lambda$  larger than  $5000 \text{ m}^{-1}$  ( $D_0$  smaller than 1 mm) both DWRs are around 0 dB indicating that small ice crystals produce the same  $Z_e$  (Hogan et al., 2006). For  $\Lambda$  smaller than  $5000 \text{ m}^{-1}$  ( $D_0$  larger than 1 mm) the DWR-KaW continuously increases and reaches a maximum around 7 dB ( $\Lambda = 500 \text{ m}^{-1}$ ,  $D_0 = 6 \text{ mm}$ ), while the DWR-XKa, first slowly increases and then, around the region where DWR-KaW reaches its maximum, the DWR-XKa rapidly increases up to  $\approx 14 \text{ dB}$ . From this example, one can see that the combination of DWRs from three different frequencies can be used as a proxy for identifying different kinds of ice particles or growth processes (e.g. aggregation, riming) (Kneifel et al., 2011, 2015). From a study combining in situ observation and triple frequency observation (X-, Ka-, W-Band), Kneifel et al., (2015) suggested that DWR-KaW is sensitive to the

initial aggregation and riming, while DWR-XKa is sensitive to the later growth by aggregation.

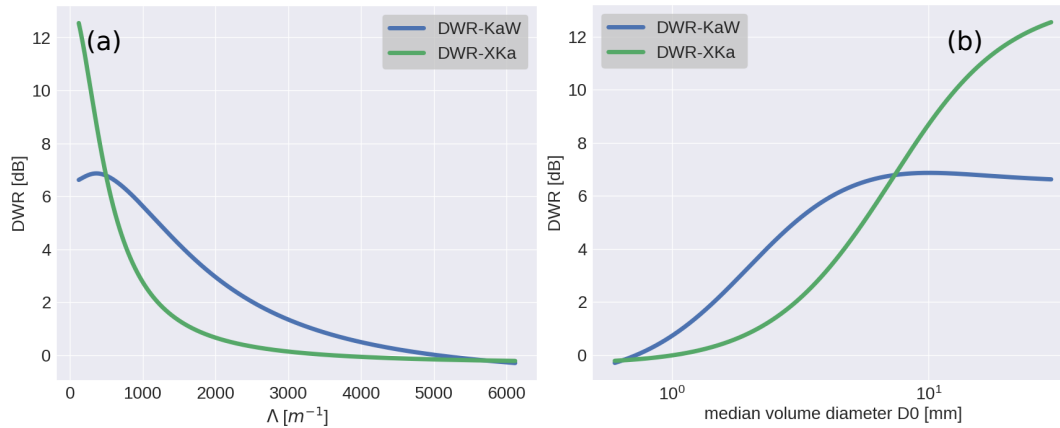


Figure 2.16: Dual wavelength ratio (DWR) from the equivalent reflectivity factors shown in figure Figure 2.15-a: a) as function of  $\Lambda$  and b) as function of  $D_0$  (Equation 2.23).

Combing the DWR pairs (XKa and KaW) it is possible to create a two-dimensional diagram of the DWRs (triple-frequency plot). Kneifel et al., (2015) suggest that two basic signatures could be identified in the triple-frequency plot; the increase of  $D_0$  would stretch the curves, while the density of the particles would control the bending of the curves. The authors suggested that in the triple-frequency plot, particles with low density (e.g. unrimed aggregates) produce a hook signature, while particles with high density (e.g. rimed aggregates) produce a flat signature. Lately, Mason et al., (2019) suggested that the  $\mu$  parameter also controls the bending signature suggesting that the shape of the particle size distribution also modulates the triple-frequency signatures. Figure 2.17 shows the triple-frequency plot of subsequently rimed aggregates (Leinonen and Szyrmer, 2015) and illustrates the conceptual behaviour of the increasing density of aggregates and increasing  $\mu$ . One can see that the density of the particles and the shape of the distribution ( $\mu$  parameter) can produce similar signatures (Mason et al., 2019). It indicates that the signatures in triple-frequency plot need to be carefully interpreted and preferentially associated with another variable. For example, the MDV would help to identify the occurrence of riming (Mosimann, 1995).

Equation 2.28 gives the complete form of the DWR. One can see that besides the contribution from the scattering components the attenuation also contributes to the DWR (Kneifel et al., 2011; Tridon et al., 2013). It also indicates that the contribution to the DWR from the scattering component is locally dependent, while the contribution

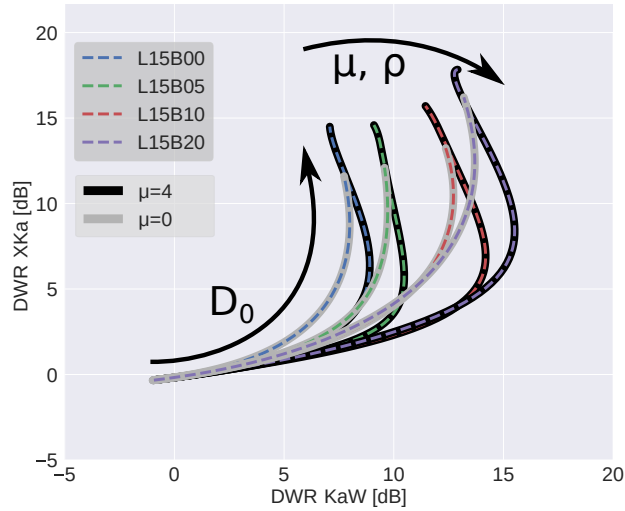


Figure 2.17: Triple-frequency plot of the simulated DWR-XKa and DWR-KaW of dendrite rimed aggregates (Leinonen and Szyrmer, 2015). The blue, green, red, and purple curves are from 0, 0.1, 0.5 and 10  $\text{kg}/\text{m}^2$  effective liquid water path. The gray and black curves are for gamma distribution with  $\mu$  equal to 0 and 4, respectively.

from the attenuation is cumulative along the path traveled by the signal.

$$\text{DWR}(\lambda_1, \lambda_2) = 10 \log \left( \underbrace{\frac{\mathfrak{K}(\tau, \lambda_1)}{\mathfrak{K}(\tau, \lambda_2)}}_{\text{attenuation component}} \underbrace{\frac{\lambda_1^4 \int \sigma_b(D, \lambda_1) D^\mu \exp(-\Lambda D) dD}{\lambda_2^4 \int \sigma_b(D, \lambda_2) D^\mu \exp(-\Lambda D) dD}}_{\text{scattering component}} \right) \quad (2.28)$$

As introduced in Section 2.2.2.1 and pointed out by Kneifel et al., (2011), the attenuation of Zes increases with an increasing frequency indicating that the DWR-KaW is more affected by attenuation than DWR-XKa. The attenuation component of the DWR can be minimized by estimating the attenuation produced by some of the atmospheric components (e.g.  $\text{O}_2$ , water vapor, other gases) combining model analyses (e.g. Cloudnet products Illingworth et al., (2007)) and radiative transfer models (e.g. PAMTRA, Mech et al., 2020). The attenuation components from other sources (e.g. snow, rain, supercooled liquid water, wet radome) are not trivial to estimate, but it can be minimized by assuming that Ze from small particles in the uppermost part of the cloud is the same (see Section 3.1). However, this approach also introduces spurious DWR because the same attenuation correction is applied to the entire DWR profiles.

Figure 2.18 shows an example of corrected DWRs combining the assumptions that small ice particles produce the same Ze and the



that the DWR correction is constant within a certain time window. Section 3.1 provides a detailed description of the DWR corrections applied to the dataset used in this thesis. Figure 2.18-(a,b) show that the corrected data is affected by spurious DWRs indicated by the continuous vertical stripes. Additionally, one can see that DWR-KaW (Figure 2.18-a) is more affected by spurious DWRs than the DWR-XKa (Figure 2.18-b). One possible explanation is that attenuation produced by the hydrometeors (e.g. rain, snow) affects Ze-W more than Ze-Ka and due to the size of the time window used in the statistical correction approach, the rapid fluctuation of the attenuation can not be corrected using the mean value. Another example of the misestimation of the DWR correction is the negative values below the melting layer (indicated by a red box). Those negative DWR values arise from the fact that the offset correction estimated at the uppermost part of the cloud is applied to the entire profile leading to overcorrection of the Zes below the melting layer.

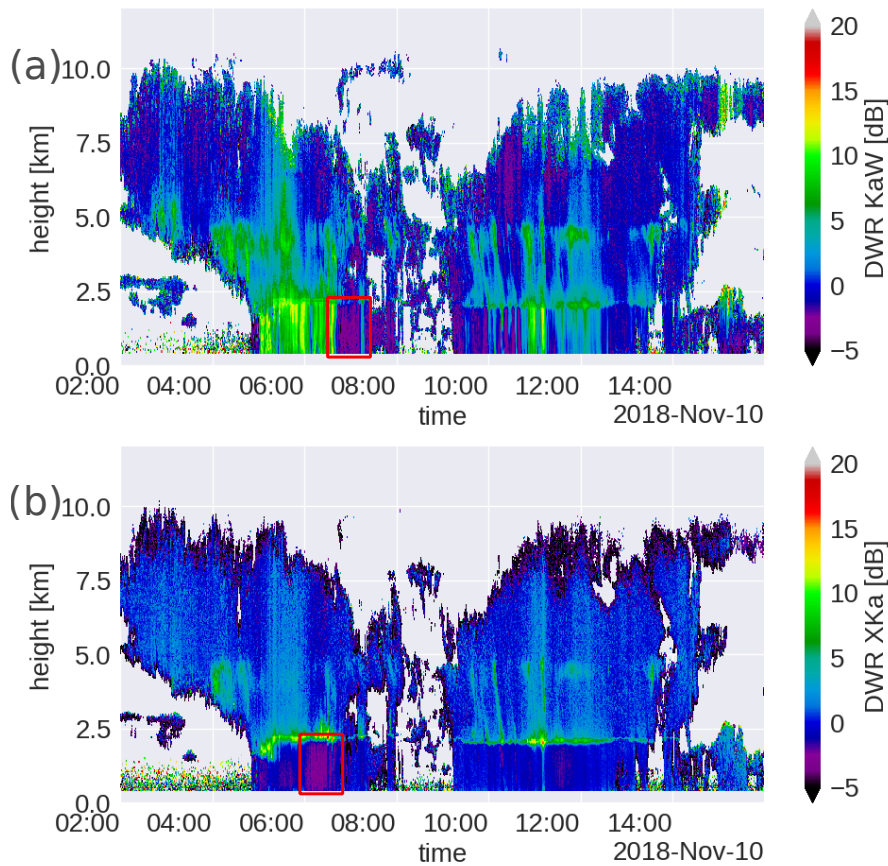


Figure 2.18: Time-height plots of the DWR-KaW (Panel (a)) and the DWR-XKa (Panel (b)) from November 10<sup>th</sup>, 2018. The red box highlights the regions where the DWR values are negative.

### 2.2.3 Doppler spectra and moments

As introduced [Section 2.2.1](#), the received signal carries information about the radial velocity of the particles, which appears as fluctuation in the frequency of the received signal due to Doppler shift. By applying the fast Fourier transform to the received signal, the Doppler radars map the frequency shift  $f + \Delta f$  into a velocity range  $v + \Delta v$  and provide a distribution of power as a function of the Doppler velocity ( $v$ ). Similarly to  $Z_e$  from a distribution of scatterers sizes ([Equation 2.20](#)),  $Z_e$  can also be described as a distribution of the scatterer velocities ([Equation 2.29](#)), where  $\sigma_b(v, \lambda)$  is the backscattering cross-section for a particle with velocity  $v$  observed using a wavelength  $\lambda$ .

$$Z_e(r, \lambda) = \aleph(r, \lambda) \frac{\lambda^4}{\pi^5 |K_w|^2} \int \sigma_b(v, \lambda) N(v) dv \quad (2.29)$$

Since the signal received by the radars is coming from a sampled volume with a distribution of sizes  $N(D)$  which also has a distribution of velocities  $N(v)$ , the [Equation 2.20](#) can be made equal to [Equation 2.29](#) and from that one can define the spectra as [Equation 2.30](#). The  $dD/dv$  is the transformation factor from the velocity space to the diameter space. In this thesis, negative velocities indicate that the particles move towards the radar, while positive velocities indicate that the particles move away from the radar.

$$S_r(r, \lambda) = \aleph(r, \lambda) \frac{\lambda^4}{\pi^5 |K_w|^2} \int \sigma_b(D, \lambda) N(D) \frac{dD}{dv} \quad (2.30)$$

*By definition,  $\aleph$  is equal to or smaller than one*

[Equation 2.30](#) indicates that attenuation equally affects the spectra by reducing the amplitude by a factor  $\aleph$ ; the conceptual effect of attenuation is illustrated in [Figure 2.19-a](#). Additionally, the spectra can be affected by random air motion produced by turbulence at scales smaller than the sampled volume, leading to a broadening of the spectra, as shown in [Figure 2.19-c](#). In the case of vertically pointing radars, vertical air motions also affect the spectra by adding a velocity offset and shifting the spectra towards positive or negative radial velocities ([Figure 2.19-b](#)).

Based on the spectra, one can define the mean Doppler velocity (MDV), which represents the mean motion of the particles within the sampled volume ([Equation 2.31](#)) where each  $v$  is weighted by the received signal. The variance of spectra characterizes the broadening, and its root square defines the spectrum width (SW, [Equation 2.32](#)).

$$MDV(r, \lambda) = \frac{\int v S_r(r, \lambda) dv}{Z_e(r, \lambda)} \quad (2.31)$$

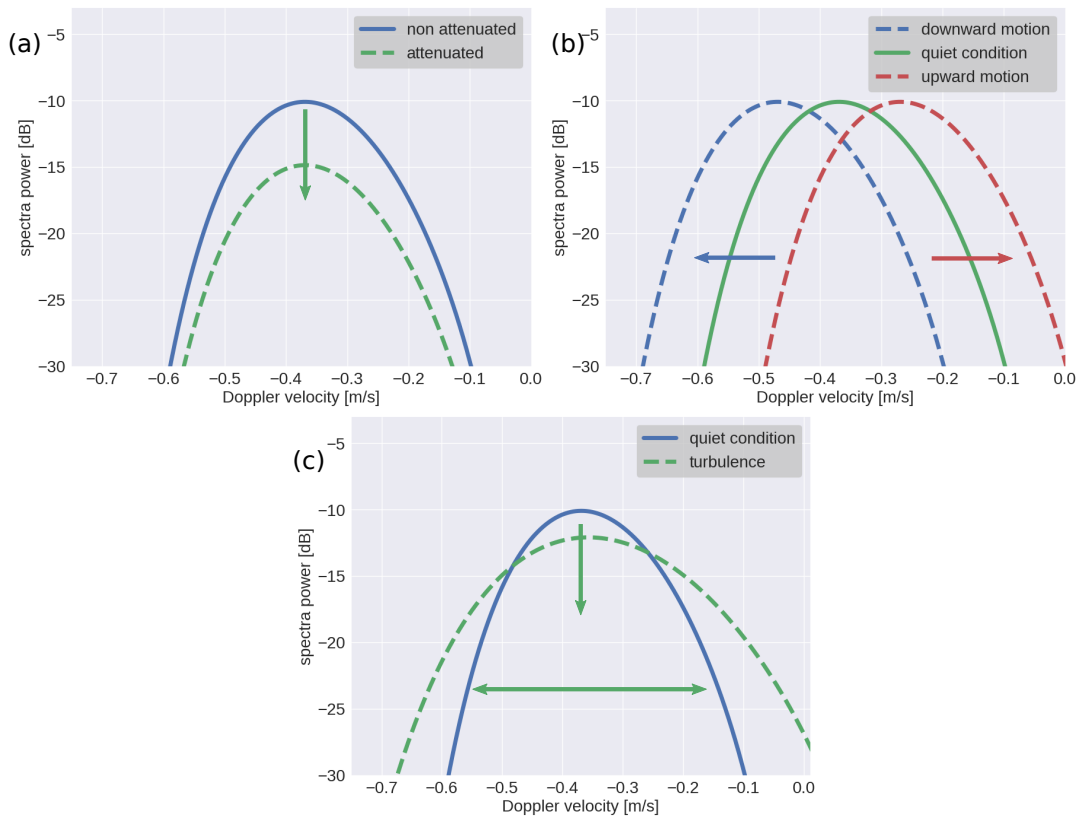


Figure 2.19: Conceptual illustration of the effect of attenuation (Panel (a)), vertical air motion (Panel (b)) and turbulence (Panel (c)).

$$SW(r, \lambda) = \left( \frac{\int (v_r - MDV(r, \lambda))^2 S_r(r, \lambda) dv}{Ze(r, \lambda)} \right)^{\frac{1}{2}} \quad (2.32)$$

Figure 2.20 shows the spectra from the same distribution of particles simulated for vertically pointing X-, Ka- and W-Band radars. One can see that the spectra deviate from each other with increasing fall velocities, which results from the transition from Rayleigh to the non-Rayleigh regime with increasing particle sizes and increasing frequency. Consequently, the MDV from different frequencies can also differ from each other, as indicated by the vertical lines. This differences in the MDV can be used, for example, to retrieve  $D_m$  from raindrops (Mróz et al., 2020b) and it will be exploited in section Section 5.3.

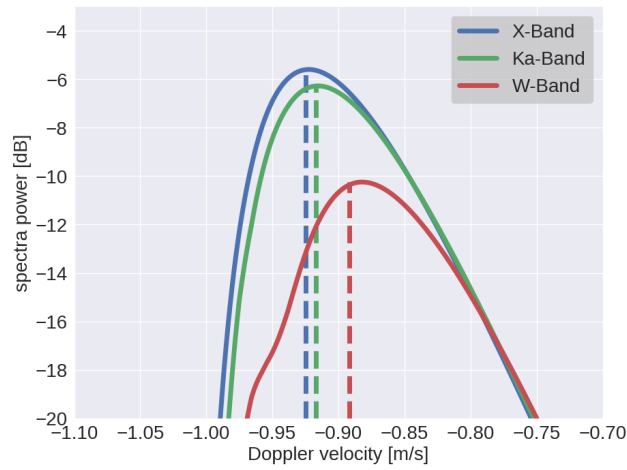


Figure 2.20: Simulated spectrum from a distribution of aggregates of mix of columns and dendrites for X-, Ka- and W-Band. The vertical dashed lines indicate the mean Doppler velocity from each spectrum.

This chapter describes the instruments and their respective dataset used in this thesis. It also introduces a novel multi-frequency data processing framework that applies different correction steps and assigns quality flags to each processing step. Additionally, this chapter describes the methods and techniques developed/applied for filtering out spurious signals that affected the dataset. [Section 3.1](#) describes the first TRIPLE-frequency and Polarimetric radar Experiment for improving process observation of winter precipitation (TRIPEX) and the dataset obtained during the initial statistical results. This campaign provided the basis for the development of the multi-frequency data processing, which is also described in [Section 3.1](#). In order to provide reliable statistical results, the data from the second TRIPLE-frequency and Polarimetric radar Experiment for improving process observation of winter precipitation (TRIPEX-Pol) is combined with the data from the first campaign. [Section 3.2](#) introduces the TRIPEX-Pol and highlights the difference between both campaigns. Temperature and relative humidity from Cloudnet are two essential variables needed as input for the multi-frequency data processing. For this reason, in [Section 3.3](#), both variables are compared to the radiosonde measurements to assess their quality. Two additional variables derived from the Doppler spectra are introduced in [Section 3.4](#). These variables are the time-height map of the spectra modes and the spectra edges; they are used in the statistical analyses combined with the radar moments. The spectra edges are also used for filtering spurious signals. Since this thesis is mainly focused on the ice part of the clouds, [Section 3.5](#) introduces the methodology used for detecting the top and bottom of the melting layer.

### 3.1 TRIPEX CAMPAIGN

The Triple-frequency and polarimetric radar experiment for improving process observation of winter precipitation (TRIPEX) took place at the Jülich Observatory for Cloud Evolution Core Facility (JOYCE-CF, Löhnert et al., (2015)) during the winter from 2015 – 2016. Dias Neto et al., (2019) provides a detailed description of this experimental campaign and introduces a methodology developed for correcting multi-frequency observations. The authors show, for the first time, statistical results from longterm triple-frequency observations. The publication is included in this section, and a summary of the main achievements is provided in the following text.

Dias Neto et al., (2019) introduced the first triple-frequency experimental campaign ever conducted in Germany, which besides providing observations also served as a reference for planning future multi-frequency campaigns. The paper also introduced a two-level multi-frequency processing system that is used to resample the dataset from the different radars to a common time-height grid producing the Level-1 data; then, it applies several other processing steps to correct for possible radar miscalibration, attenuation due to atmospheric gases, melting and hydrometeors to generate the Level-2 data. Additionally, in the Level-2 processing, a set of quality flags is defined, allowing to identify regions where the quality of corrections cannot be ensured. This approach brings flexibility while using the dataset because it allows activating or deactivating specific flags according to the needs.

This dataset allowed, for the first time, to calculate longterm statistical analyses of triple-frequency observations and point out its dependency on temperature. The statistical results of the Level-2 data indicated that aggregation is the predominant process and that it is most pronounced in two preferential regions. One region is between  $-20$  and  $-10$  °C, and another region is between  $-10$  and  $0$  °C (Figures 9 a and b from the paper). The scatterplot of the DWRs pairs from this last temperature region showed a bending up signature similar to found by Kneifel et al., (2015) and Stein et al., (2015). The statistical analyses also showed that for some cases extreme aggregation took place close to the melting layer top, which is indicated by DWR-XKa as large as 20 dB. This study revealed that in contrast to aggregation, riming did not happen so often. The results based on the Level-2 data indicated that riming occurred only in short periods which correspond to approximately 1% of the dataset.

Thanks to the careful corrections applied to this dataset and identification of regions possibly affected by remaining issues, Ori et al., (2020a) used the TRIPEX dataset as a reference to evaluate the growth of ice particles in Icosahedral Nonhydrostatic Model (ICON; Heinze et al., (2017) and Zängl et al., (2015)).



# The TRiple-frequency and Polarimetric radar Experiment for improving process observations of winter precipitation

José Dias Neto<sup>1</sup>, Stefan Kneifel<sup>1</sup>, Davide Ori<sup>1</sup>, Silke Trömel<sup>2</sup>, Jan Handwerker<sup>3</sup>, Birger Bohn<sup>4</sup>,  
Normen Hermes<sup>5</sup>, Kai Mühlbauer<sup>2</sup>, Martin Lenefer<sup>2</sup>, and Clemens Simmer<sup>2</sup>

<sup>1</sup>Institute for Geophysics and Meteorology, University of Cologne, Cologne, Germany

<sup>2</sup>Institute for Geosciences and Meteorology, University of Bonn, Bonn, Germany

<sup>3</sup>Institute of Meteorology and Climate Research (IMK), Karlsruhe Institute  
of Technology (KIT), Karlsruhe, Germany

<sup>4</sup>Institute of Energy and Climate Research (IEK-8), Research Centre Jülich, Jülich, Germany

<sup>5</sup>Institute of Bio- and Geosciences Agrosphere (IBG-3), Research Centre Jülich, Jülich, Germany

**Correspondence:** José Dias Neto (jdiasnet@uni-koeln.de)

Received: 16 November 2018 – Discussion started: 21 December 2018

Revised: 28 March 2019 – Accepted: 7 May 2019 – Published: 14 June 2019

**Abstract.** This paper describes a 2-month dataset of ground-based triple-frequency (X, Ka, and W band) Doppler radar observations during the winter season obtained at the Jülich Observatory for Cloud Evolution Core Facility (JOYCE-CF), Germany. All relevant post-processing steps, such as re-gridding and offset and attenuation correction, as well as quality flagging, are described. The dataset contains all necessary information required to recover data at intermediate processing steps for user-specific applications and corrections (<https://doi.org/10.5281/zenodo.1341389>; Dias Neto et al., 2019). The large number of ice clouds included in the dataset allows for a first statistical analysis of their multifrequency radar signatures. The reflectivity differences quantified by dual-wavelength ratios (DWRs) reveal temperature regimes where aggregation seems to be triggered. Overall, the aggregation signatures found in the triple-frequency space agree with and corroborate conclusions from previous studies. The combination of DWRs with mean Doppler velocity and linear depolarization ratio enables us to distinguish signatures of rimed particles and melting snowflakes. The riming signatures in the DWRs agree well with results found in previous triple-frequency studies. Close to the melting layer, however, we find very large DWRs (up to 20 dB), which have not been reported before. A combined analysis of these extreme DWR with mean Doppler velocity and a linear depolarization ratio allows this signature to be separated, which is most likely related to strong aggregation, from the triple-frequency characteristics of melting particles.

## 1 Introduction

The combined observation of clouds and precipitation at different radar frequencies is used to improve retrievals of hydrometeor properties. All methods exploit frequency-dependent hydrometeor scattering and absorption properties governed by their microphysical characteristics.

Multifrequency retrievals are already well developed for liquid hydrometeors. For example, Hogan et al. (2005) used differential radar attenuation at 35 and 94 GHz to retrieve

vertical profiles of cloud liquid water. Improved precipitation rate retrievals on a global scale are provided by the core satellite of the Global Precipitation Mission which operates a Ku–Ka band dual-frequency radar (Hou et al., 2014). For frequencies below  $\approx 10$  GHz, attenuation effects are negligible (except for heavy rainfall or hail), and the sensitivity to non-precipitating particles, such as ice crystals, is relatively weak. Therefore, the majority of multifrequency applications for cold clouds focus on cloud radar systems operating at 35 or 94 GHz. At these frequencies, the radars are sensitive



enough to detect even sub-millimeter ice particles and cloud droplets. The sizes of large ice crystals, snowflakes, graupel, and hail are on the order of the wavelengths used to observe them (3 mm, 8 mm, and 3 cm for W, Ka, and X band, respectively). Thus, non-Rayleigh scattering becomes important and can be used to constrain particle size distributions, improving ice and snow water content retrievals (Matrosov, 1998; Hogan et al., 2000; Leinonen et al., 2018; Grecu et al., 2018).

Recent modeling studies (Kneifel et al., 2011b; Tyynelä and Chandrasekar, 2014; Leinonen and Moisseev, 2015; Leinonen and Szyrmer, 2015; Gergely et al., 2017) revealed that different ice particle classes like graupel, single crystals, or aggregates can be distinguished using a combination of three radar frequencies (13, 35, and 94 GHz). Triple-frequency radar datasets from airborne campaigns (Leinonen et al., 2012; Kulie et al., 2014) and satellites (Yin et al., 2017) confirmed distinct signatures in the triple-frequency space. Ground-based triple-frequency radar measurements in combination with in situ observations (Kneifel et al., 2015) provided the first experimental evidence for a close relation between triple-frequency signatures and the characteristic particle size, as well as the bulk density of snowfall. These early results were corroborated and refined by coinciding in situ observations in aircraft campaigns (Chase et al., 2018) as well as by ground-based observations (Gergely et al., 2017). A better understanding of the relations between triple-frequency signatures and snowfall properties is key for triple-frequency radar retrieval development. The connection between scattering and microphysical properties is currently addressed by novel ground-based in situ instrumentation (Gergely et al., 2017) and triple-frequency Doppler spectra (Kneifel et al., 2016). Long-term triple-frequency datasets from various sites and radar systems are, however, needed to better understand the relations between triple-frequency signatures and clouds.

We present a first analysis of triple-frequency (X, Ka, and W band) radar observations collected over two winter months at the Jülich Observatory for Cloud Evolution Core Facility, Germany (Löhnert et al., 2015). The data were corrected for known offsets and attenuation effects and re-gridded for multifrequency studies. Section 2 describes the experimental setup and the characteristics of the X, Ka, and W band radars. Section 3 details the data processing and corrections applied. Section 4 gives a general overview of the dataset and its limitations. Section 5 presents a statistical analysis of the data with a focus on the temperature dependency of the triple-frequency properties, signatures of riming, intense aggregation, and melting snow particles. We summarize and discuss our results in Sect. 6.

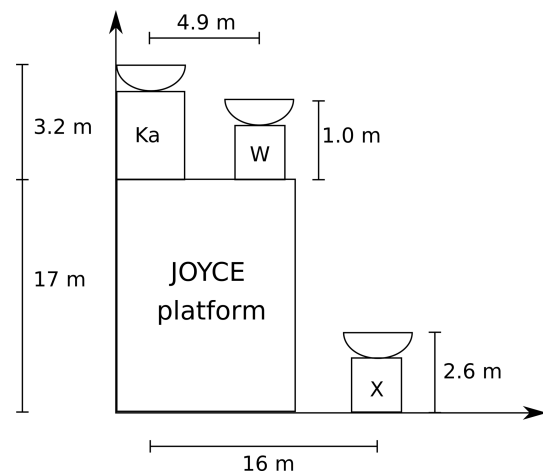


**Figure 1.** Sketch (not to scale) of the horizontal and vertical distances between the three zenith-pointing radars operated during TRIPEX. The JOYCE-CF platform with all auxiliary instruments is located on the roof of a 17 m tall building. The mobile X band radar was placed on the ground close to the other two radars.

## 2 Measurement site and instruments

The TRiple-frequency and Polarimetric radar Experiment for improving process observation of winter precipitation (TRIPEX) was a joint field experiment of the University of Cologne, the University of Bonn, the Karlsruhe Institute of Technology (KIT), and the Jülich Research Centre (Forschungszentrum Jülich, FZJ). TRIPEX took place at the Jülich Observatory for Cloud Evolution Core Facility (JOYCE-CF 50°54′31″ N, 6°24′49″ E; 111 m above mean sea level) from 11 November 2015 until 4 January 2016. The core instruments deployed during TRIPEX were three vertically pointing radars providing a triple-frequency (X, Ka, and W band) column view of the hydrometeors aloft. All three radars were calibrated by the manufacturers before the campaign. Figure 1 sketches the positions of the instruments relative to each other and the ground surface. A large number of additional permanently installed remote sensing and in situ observing instruments are available at the JOYCE-CF site (see Löhnert et al., 2015, for a detailed overview).

### 2.1 Precipitation radar KiXPol (X band)

KiXPol, hereafter referred to as the X band, is a pulsed 9.4 GHz Doppler precipitation radar, usually integrated into the KITcube platform (Kalthoff et al., 2013). The mobile Meteor 50DX radar, manufactured by Selex ES (Gematronik), is mounted on a trailer and placed next to the JOYCE-CF building in order to position it as close as possible to the other two radars, which were installed on the JOYCE-CF roof platform (see Fig. 1). The radar operates in a simultaneous transmit and receive (STAR) mode and is thus capable of measuring standard polarimetric variables like differential reflectivity



$Z_{dr}$  and differential phase shift  $\Phi_{dp}$ . The linear depolarization ratio (LDR) is not provided because it requires the emission of single-polarization pulses in order to allow for independent measurements of the cross-polarized component of the returning signal. During the campaign, the X band was set to a pulse duration of  $0.3 \mu\text{s}$ ; a slight oversampling was applied to achieve a radial resolution of 30 m in order to match the resolution of the other radars as close as possible (see Table 1). The X band radar is designed for operational observations of precipitation via volume scans (series of azimuth scans at several fixed elevation angles). KiXPol was operated at JOYCE in this mode during the HOPE campaign (Xie et al., 2016; Macke et al., 2017). The standard software requires the antenna to be rotated in azimuth in order to record data. Hence, we constantly rotated the antenna at zenith elevation with a slow rotation speed ( $2^\circ \text{s}^{-1}$ ) in order to enhance the sensitivity through longer time averaging. After each complete rotation, the radar stops the measurements for a few seconds before the next scan starts, thus introducing a small measurement gap in each scan routine. Further technical specifications of the X band are listed in Table 1.

## 2.2 Cloud radar JOYRAD-35 (Ka band)

JOYRAD-35, hereafter referred to as the Ka band, is a scanning 35.5 GHz Doppler cloud radar of the type MIRA-35 (Görsdorf et al., 2015) manufactured by Metek (Meteorologische Messtechnik GmbH), Germany. An overview of its main technical characteristics and settings used during TRIPEX is provided in Table 1. The radar transmits linearly polarized pulses at 35.5 GHz and receives the co- and cross-polarized returns simultaneously. This allows derivation of the LDR, which is used by the Metek processing software to filter out signals from insects and to detect the melting layer. From the measured Doppler spectra, standard radar moments such as the effective reflectivity factor  $Z_e$ , mean Doppler velocity (MDV) and Doppler spectral width (SW) are computed. Since March 2012, the Ka band radar has been a permanent component of JOYCE-CF (Löhnert et al., 2015), and its zenith observations are used as input for generating CloudNet products (Illingworth et al., 2007). The radar was vertically pointing most of the time because the major scientific focus during TRIPEX was to collect combined triple-frequency observations. Every 30 min, a sequence of range height display (RHI) scans in different azimuth directions (duration  $\approx 4$  min) was performed in order to capture a snapshot of the spatial cloud field and also to derive the radial component of the horizontal wind inside the cloud. The scanning data have not been processed yet; thus, the dataset described here only includes the zenith observations; the RHI scans will be included in a future release. The Ka band radar operated almost continuously during the TRIPEX campaign, except for a gap from 25 November to 2 December 2015 due to a failure of the storage unit.

**Table 1.** Technical specifications and settings of the three vertically pointing radars operated during TRIPEX at JOYCE-CF.

Specifications	X band	Ka band	W band
Frequency (GHz)	9.4	35.5	94.0
Pulse repetition frequency (kHz)	1.2	5.0	5.3–12 <sup>b</sup>
Doppler velocity bins	1200	512	512
Number of spectral average	1	20	8–18 <sup>b</sup>
3dB beam width ( $^\circ$ )	1.3	0.6	0.5
Sensitivity at 5 km (dBZ) <sup>a</sup>	−10	−39	−33
Nyquist velocity ( $\pm \text{m s}^{-1}$ )	9	10	4.2–9.7 <sup>b</sup>
Range resolution (m)	30.0	28.8	16–34.1 <sup>b</sup>
Temporal sampling (s)	1	2	3
Lowest clutter-free range (m)	700	400	370
Radome	Yes	No	Yes

<sup>a</sup> Minimum sensitivities have been derived from the reflectivity histograms shown in Fig. 8. <sup>b</sup> Pulse repetition frequency, number of spectral average, Nyquist velocity, and range resolution depend on the chirp definition; those values are indicated in Table 2.

## 2.3 Cloud radar JOYRAD-94 (W band)

JOYRAD-94, hereafter referred to as the W band, is a 94 GHz frequency-modulated continuous-wave (FMCW) radar, combined with a radiometric channel at 89 GHz. The instrument is manufactured by Radiometer Physics GmbH (RPG), Germany. Unlike the X and Ka band radar, the W band radar is a non-polarimetric, non-scanning, and non-pulsed system. The W band started measurements at JOYCE-CF in October 2015; a detailed description of the radar performance, hardware, signal processing, and calibration can be found in Küchler et al. (2017). The W band radar has a similar beam width, range, and temporal resolution as the Ka band (Table 1). The FMCW system allows the user to set different range resolutions for different altitudes by acting on the frequency modulation settings (chirp sequence). During TRIPEX the standard chirp sequence (Table 2) was used. After correcting the Doppler spectra for aliasing using the method described in Küchler et al. (2017), standard radar moments such as the equivalent  $Z_e$ , MDV, and SW are derived.

## 3 Data processing

The full TRIPEX dataset is structured on three processing levels. Level 0 contains the original data from the X, Ka, and W band. For Level 1, the measurements are corrected for known instrument problems and sampled into a common time–height grid. At this stage, the data can still be considered raw; further processing steps that are either dependent on radar frequency or atmospheric conditions are applied to the Level 2 dataset. These processing steps include the detection and removal of measurements affected by ground clutter, an offset correction of the radars based on independent sources, the compensation for estimated differential attenuation caused by atmospheric gases, adjustment of the DWRs by cross calibrations between the three radars and the addi-

**Table 2.** Main settings of the chirp sequence used during TRIPEX for the W band radar. See Küchler et al. (2017) for a detailed description.

Attributes	Chirp sequence			
	1	2	3	4
Integration time (s)	0.338	0.402	0.530	1.769
Range interval (m)	100–400	400–1200	1200–3000	3000–12 000
Range resolution (m)	16.0	21.3	26.9	34.1
Nyquist velocity ( $\pm \text{m s}^{-1}$ )	9.7	8.1	6.2	4.2
Doppler velocity bins	512	512	512	512
Number of spectral average	8	8	8	18
Chirp repetition frequency (kHz)	12.2	10.2	7.8	5.3

tion of data quality flags. These steps are meant to remove spurious multifrequency signals that are not produced by cloud properties. The processing is performed to the best of our knowledge; however, intermediate steps are included in the dataset in order to allow the original data to be recovered at any stage and different processing techniques to be applied. Figure 2 illustrates the work chain from Level 0 to Level 2. The following sections provide a detailed description of each step.

### 3.1 Spatiotemporal re-gridding and offset correction

Since the range and temporal resolutions of the three radars are slightly different (Table 1), the data are re-gridded at a common time and space resolution in order to allow for the calculation of dual wavelength ratios (DWRs) defined for two wavelengths  $\lambda_1$  and  $\lambda_2$  as

$$\text{DWR} = Z_{e_{\lambda_1}} - Z_{e_{\lambda_2}}, \quad (1)$$

with  $Z_{e_{\lambda}}$  in dBZ. The reference grid has a temporal resolution of 4 s and a vertical resolution of 30 m, which is the resolution of the W band. The data are interpolated using a nearest-neighbor approach, with the maximum data displacement limited to  $\pm 17$  m in range and  $\pm 2$  s in time. This method preserves the high-resolution information of the original radar observations. Limiting the interpolation displacement avoids spurious multifrequency features that may result from nonmatching radar volumes. Residual volume mismatches may occur at cloud boundaries where heterogeneities are largest. For the Ka band, two corrections are applied to the original reflectivity as suggested by the manufacturer (Matthias Bauer-Pfundstein, Metek GmbH, personal communication, 2015). An offset of 2 dB is added to account for power loss caused by the finite receiver bandwidth; another 3 dB offset is added to correct for problems in the digital signal processor used in older MIRA systems. These corrections are applied for processing of the Level 1 data.

### 3.2 Clutter removal

Following the corrections for radar offsets and re-gridding, the first step in the Level 2 processing is the removal of the

range gates affected by ground clutter. Considering the different radar installation locations (roof mount or ground surface) and antenna patterns, the clutter contamination affects each type of radar data differently. The thresholds for the lowest usable range gates are determined empirically and are reported in Table 1.

### 3.3 Evaluation of the Ka band calibration with PARSIVEL disdrometer measurements

The three radars have been individually calibrated by their respective manufacturers; however, radar components might experience drifts over time, which can lead to biases of several dB. The JOYCE site is equipped with a PARSIVEL optical disdrometer (Löffler-Mang and Joss, 2000), which provides the drop size distribution (DSD) with a temporal resolution of 1 min. For rainfall events, the DSD can be used to calculate the associated radar reflectivity factor. In this study, the scattering properties of raindrops are calculated using the T-matrix approach (Leinonen, 2014) with a drop shape model that follows Thurai et al. (2007) and assuming drop canting angles that follow a Gaussian distribution with zero mean and  $7^\circ$  standard deviation (Huang et al., 2008). Unfortunately, the lowest usable radar range gates are 500–600 m above the PARSIVEL; thus we have to assume a constant DSD over this altitude range in order to compare with the radar reflectivities. Time lags and wind shear effects raise further problems in the direct comparisons between radar-measured  $Z_e$  and the one calculated with PARSIVEL. For this reason, we only compare the statistical distribution of reflectivities at the lowest range gates measured over several hours with the corresponding distribution calculated at the ground level. Of course, systematic differences caused by rain evaporation, drop breakup, or drop growth due to accretion towards the ground may affect such comparisons. However, the changes in the  $Z_e$  profile are very close to the ones predicted by attenuation and constant DSD from three light rainfall cases. The reflectivity distributions from PARSIVEL and the Ka band (Fig. 3) of those periods are very similar but differ by approximately 3.6 dB, with the Ka band having the lower reflectivities. For these comparisons, periods before and after

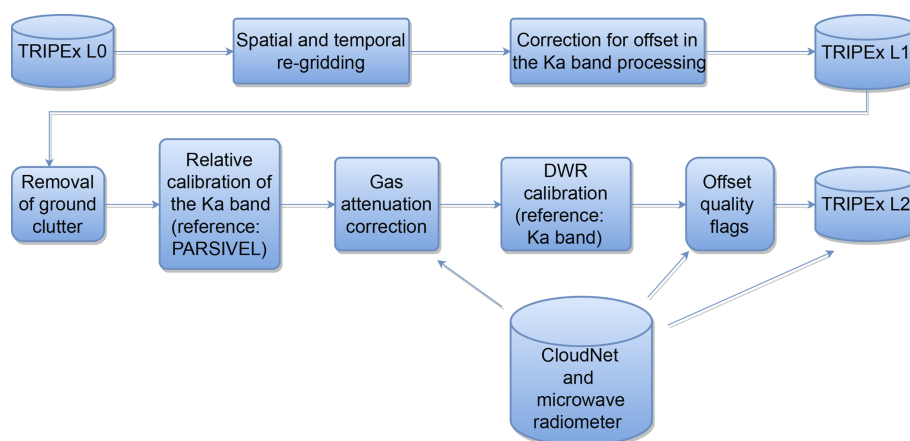


**Figure 2.** Flowchart of the TRIPEX data processing. The upper part describes the steps producing data Level 1 and the bottom part those producing data Level 2.

the TRIPEX campaign had to be used because PARSIVEL had a hardware failure during the campaign. The similarity of the results gives us an indication that this method is reliable; however, a large number of cases are still needed in order to draw a final conclusion on this method. Unfortunately, only the Ka band was available because the other two radars did not measure during the selected rainfall events.

### 3.4 Correction for atmospheric gas attenuation

Hydrometeors and atmospheric gases cause considerable attenuation at cloud radar frequencies. The reflectivities from the X, Ka, and W band are corrected for estimated attenuation due to atmospheric gases (Fig. 2) by means of the Passive and Active Microwave TRANSfer model (PAMTRA) (Maahn et al., 2015). PAMTRA calculates specific attenuation due to molecular nitrogen, oxygen, and water vapor based on the gas absorption model from Rosenkranz (1993, 1998, 1999). Input parameters are the vertical profiles of atmospheric temperature, pressure, and humidity provided by the CloudNet products (Illingworth et al., 2007), which are generated operationally at the JOYCE-CF site. The two-way path-integrated attenuation (PIA) at the radar range gates is derived from the specific attenuation integrated along the vertical. Table 3 lists the minimum and maximum two-way attenuation values at  $\approx 12$  km (height of the maximum range gate in Level 2 data) for the three radars during the entire campaign. The highest attenuation of  $\approx 2.6$  dB occurs at 94 GHz and is mainly caused by water vapor. Conversely, the 9.4 GHz maximum attenuation of  $\approx 0.1$  dB is the lowest among the three radars, and it is mainly produced by oxygen continuum absorption. At 35.5 GHz, attenuation is governed by both oxygen and water vapor. The maximum attenuation value found at this frequency is  $\approx 0.7$  dB.

**Table 3.** Calculated minimum and maximum two-way path-integrated attenuation (PIA) at a height of  $\approx 12$  km for the X, Ka, and W band during TRIPEX.

Frequency (GHz)	Minimum attenuation (dB)	Maximum attenuation (dB)
9.4	0.077	0.104
35.5	0.365	0.728
94	0.650	2.675

### 3.5 DWR calibration and generation of quality flags

Spurious multifrequency signals can arise from attenuation effects due to particulate atmospheric components (e.g., liquid water, melting layer, and snow) but also from instrument-specific effects such as a wet radome, snow on the antenna, and remaining relative offsets due to radar miscalibration. With this processing step, the reflectivity measurements are adjusted in order to take into account the cumulative effects of the aforementioned bias mechanisms at the top of the clouds. By doing so, the effects of the cloud microphysical processes on the DWR signals are recovered.

The Ka band is used as a reference because of its better sensitivity level and larger dynamic range compared to the other radars (up to high altitudes) and its lower signal attenuation compared to the W band. Moreover, the Ka band is the only system not equipped with a radome which might collect raindrops on its surface and cause additional attenuation. The signal attenuation due to antenna wetness on the Ka band is expected to be lower compared to other radars' radome attenuation because of the periodic antenna tilts during RHI scans (every 30 min). The processing is complemented by the generation of quality flags categorized as errors and warnings. Error flags mark data of poor quality based on the applied correction procedure, while warnings indicate the detection

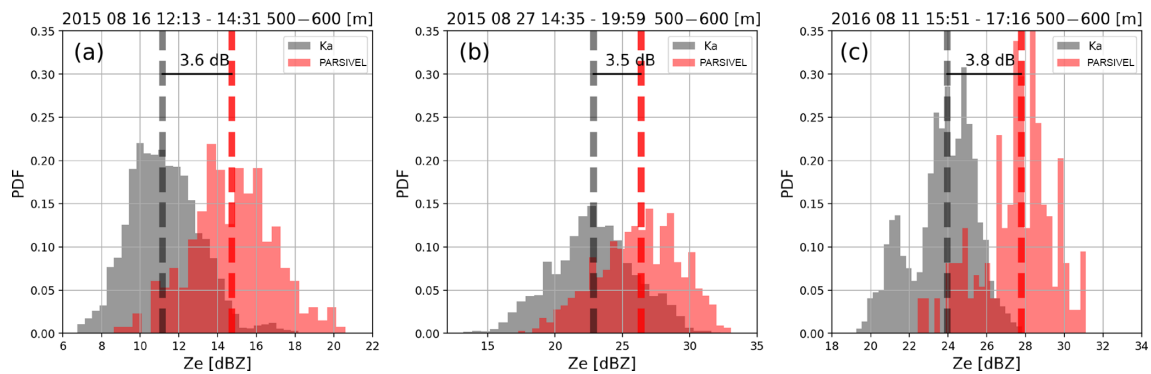


**Figure 3.** Histograms of radar reflectivities from the Ka band (gray) and results from T-matrix calculations with the raindrop size distribution provided by PARSIVEL (red) for three long-lasting stratiform rain cases before and after the TRIPEx campaign (**a** 16 August 2015, **b** 27 August 2015, **c** 11 August 2016). Ka band reflectivities are taken from the lowest clutter-free range gates between 500 and 600 m. The vertical dashed line indicates the median of the distribution; the offset is calculated as the difference between Ka band and T-matrix results.

of potential sources of DWR offsets that have not been accounted for in the procedures described below. An additional error flag is raised if spurious multifrequency signals due to radar volume mismatch are suspected. A list of all the quality flags (both errors and warnings) is provided in Table 4.

The small ice particles in the upper parts of clouds are mostly Rayleigh scatterers (Kneifel et al., 2015; Hogan et al., 2000); thus, their reflectivities should not be frequency-dependent (Matrosov, 1993). The reflectivity range, at which the Rayleigh approximation can be assumed, is estimated by investigating the behavior of the observed DWRs as a function of  $Z_{e_{Ka}}$ . Within the Rayleigh regime, the measured DWRs are expected to remain constant at a value that accounts for all the integrated differential attenuation and radar miscalibration effects. As the ice particles grow larger, the DWRs start to deviate from that constant value, and this deviation affects the higher-frequency radars first. Because of that, the Rayleigh data have been isolated by means of two different reflectivity thresholds for X and W band radars. In addition, the sensitivity of the X band is much lower; thus, a higher reflectivity threshold is accepted for the offset estimate between the X and Ka band compared to the Ka and W band. For the determination of the relative offset for the W band, we found an optimal range of  $-30 < Z_{e_{Ka}} < -10$  dBZ and  $-20 < Z_{e_{Ka}} < -5$  dBZ for the X band. In order to safely exclude partially melted particles, only reflectivities from at least 1 km above the  $0^{\circ}\text{C}$  isotherm are used.

The relative offset correction is estimated for each measuring time from the data inside a moving time window of 15 min. The selected data are restricted to the reflectivity pairs, which are within threshold values defined above. The mean value of the DWR computed for these reflectivity pairs constitutes the DWR offset. The quality of this offset estimation strongly depends on the quality and quantity of the reflectivity data included in the average. Empirical analysis showed that at least 300 data points spanning a wide reflectivity range are required in order to have acceptable sampling

**Table 4.** Quality flags included in the data Level 2 product (bit coded in a 16-bit integer value). The flags indicate the reliability of the data and in relation to the quality of the relative offset estimate for X-Ka and W-Ka band reflectivities. Note that offsets are not calculated when the number of reflectivity pairs is below 300.

	Bits	Criteria
Warning	0–5	Reserved for future warning flags
	6	$LWP > 200 \text{ g m}^{-2}$
	7	Rain detected by CloudNet
Errors	8–12	Reserved for future error flags
	13	Variance in time of DWR $> 2 \text{ dB}^2$
	14	Correlation of data points is poor ( $< 0.7$ )
	15	Number of valid measurements $< 300$

errors. The data that present smaller sampling statistics are marked with an error flag.

Whenever cloud edges are included in the sampling volume, and/or when the measured  $Z_e$  is close to the sensitivity limits of the instruments, the correlation between the reflectivities of two radars might strongly deteriorate. In order to help the user identify these potential sources of errors, the data profiles presenting a correlation lower than 0.7 are marked with an additional error flag.

Despite the matching procedure of the different frequency radar volumes (Sect. 3.1), mismatches are unavoidable due to the horizontal distances between the radars (Fig. 1) and the different radar range resolutions and beam widths (Table 1). At cloud edges and close to the melting layer, where the largest spatial cloud inhomogeneities are expected, the effects of the remaining radar volume mismatches will be maximized. The temporal DWR variability during 2 min moving windows is used as an indicator for a potential volume mismatch; cloud regions with variances above  $2 \text{ dB}^2$  are flagged accordingly.



The described adjustment technique accounts for all processes that affect relative offsets of the radars in the upper and frozen part of clouds. These processes include possible frequency-dependent attenuation effects from lower levels, radar miscalibration, and radome and antenna attenuation. Since the estimated correction is applied to the entire profile, inevitably overcompensations might occur in the lower, possibly rainy parts of clouds. This limitation is necessary in order to increase the quality of the data in the ice part of the clouds, which is the main focus area of the presented study.

The lack of information about vertical hydrometeor distribution prevents reliable reflectivity corrections by differential attenuation. As a consequence of the presented DWR calibration and the fact that hydrometeor attenuation is hitting the higher frequencies more, the computed DWRs are expected to be increasingly underestimated towards the ground. A refined correction should be applied for rain and melting layer studies. Possible sources of information about the amount and position of supercooled liquid water could be collocated lidar or analysis of radar Doppler spectra measurements. Those data are available at JOYCE-CF, but they are not included in the current dataset. However, an additional warning flag indicates periods with large liquid water paths derived from the collocated microwave radiometer. Lastly, the occurrence of rainfall and/or a melting layer from the CloudNet classification and indicated by the precipitation gauge is marked with an additional warning flag (Table 4).

## 4 Overview of the dataset

The Level 2 of the TRIPEx dataset contains radar moments, polarimetric variables, integrated attenuation, and atmospheric state variables. The polarimetric variables are included as they are provided by the radar software, and no additional processing or quality check is applied to them.  $Z_{dr}$ ,  $\phi_{dp}$ , and  $\rho_{hv}$  from the X band might be a useful additional source of information for melting layer studies (Zrnić et al., 1994; Baldini and Gorgucci, 2006). We are not confident about the quality of  $K_{dp}$  provided by the X band software, and therefore, this variable is not included in the dataset but can be calculated by the user. Table 5 lists all variables available in Level 2.

The dataset contains 47 days of measurements. For each day, Table 6 lists the atmospheric conditions such as temperature at 2 m ( $T_{2m}$ ), rain rate (RR), accumulated rain (AR), liquid water path (LWP), and integrated water vapor (IWV). The duration of four empirically classified predominant types of cloud and precipitation is provided for each day (Table 6). The two most frequent cloud types are ice clouds (IC) with 377 h and shallow mixed-phase clouds with 222 h of observations. Stratiform rainfall (SR) occurred during 137 h, while rain showers (SR) were only observed during 137 h. The average rain rate (RR) for all rainy periods over the whole period (mean rain intensity) is  $0.078 \text{ mm h}^{-1}$ , with a maximum in-

stantaneous RR of  $8.07 \text{ mm h}^{-1}$ . DWR signatures and radar Doppler information suggest that the ice part of clouds is dominated by depositional growth and aggregation. Riming only seems to occur during a few short events. Although the dataset spans the main winter season, no snowfall was recorded at the surface. In the following, we will demonstrate the effect of applying data quality flags and discuss remaining limitations as well as the effects of the different radar sensitivities.

### 4.1 Effects of data filtering based on quality flags

The effects of data filtering on  $DWR_{XKa}$  and  $DWR_{KaW}$  are demonstrated for clouds observed on 20 November 2015 in Figs. 4 and 5. In order to give a better visual impression of these effects, the filtering steps are applied sequentially and cumulatively. Figure 4a–c show the unfiltered Level 2 data. The time–height plots (Fig. 4a and b) reveal a stratiform cloud passing over the site from 01:00 to 17:00 UTC, followed by a series of low-level, shallow, most likely mixed-phase clouds. The short periodic gaps result from interruptions of zenith observations caused by range-height indicator (RHI) scans of the Ka band, and the large gap in  $DWR_{KaW}$  between 09:00 and 10:00 UTC is caused from missing W band observations. The  $-15^\circ\text{C}$  isotherm (dashed line in the time–height plots) separates DWRs around 0 dB for temperatures below  $-15^\circ\text{C}$  from rapid increases with reflectivity for higher temperatures.

Figure 4c displays a scatter density plot of  $DWR_{XKa}$  versus  $DWR_{KaW}$  (hereafter called the triple-frequency plot). The position in the triple-frequency plot is mainly driven by the respective hydrometeors' bulk density  $\rho$  and their mean volume diameter  $D_0$  (Kneifel et al., 2015). This plot allows discrimination between the two processes: rimed particles follow the flat curve (low  $DWR_{XKa}$ ) due to their higher density, while aggregated particles give rise to a bending-up signature (increase in  $DWR_{XKa}$ , while  $DWR_{KaW}$  saturates or even decreases) due to their lower density, which is nicely shown in Fig. 4c.

A large number of points in Fig. 4c populate areas which are unrealistic from a microphysical point, such as negative DWRs. Some of those originate from time periods when the offset cannot be calculated properly or when the correlation between the three radars is poor. Figure 4d and e show the results after removing those points (bits 14 and 15 in the quality flag; see Table 4), an effect best visible between 17:00 and 20:00 for  $DWR_{KaW}$  and between 17:00 and 23:00 for  $DWR_{XKa}$ . The triple-frequency plot (Fig. 4f) shows a strong reduction of outliers when compared to the unfiltered triple-frequency plot (Fig. 4c).

Despite the data filtering described in the previous paragraph, the scatter around the main signature is still large. Figure 5a and b show the time–height plots after removing observations flagged with the DWR 2 min temporal variance flag (bit 13 in the quality flag; see Table 4). This filtering

**Table 5.** Variables available in the TRIPEX dataset Level 2.

Radar variables	X band	Ka band	W band
Reflectivity (dBZ)	x	x	x
Mean Doppler velocity ( $\text{m s}^{-1}$ )	x	x	x
Spectral width ( $\text{m s}^{-1}$ )	x	x	x
Differential reflectivity (dB)	x	—	—
Differential propagation phase shift ( $^{\circ}$ )	x	—	—
Co-polar correlation coefficient	x	—	—
Linear depolarization ratio (dB)	—	x	—
Two-way path-integrated attenuation (dB)	x	x	x
Atmospheric variables	CloudNet		
Air temperature ( $^{\circ}\text{C}$ )		x	
Air pressure (Pa)		x	
Relative humidity (%)		x	

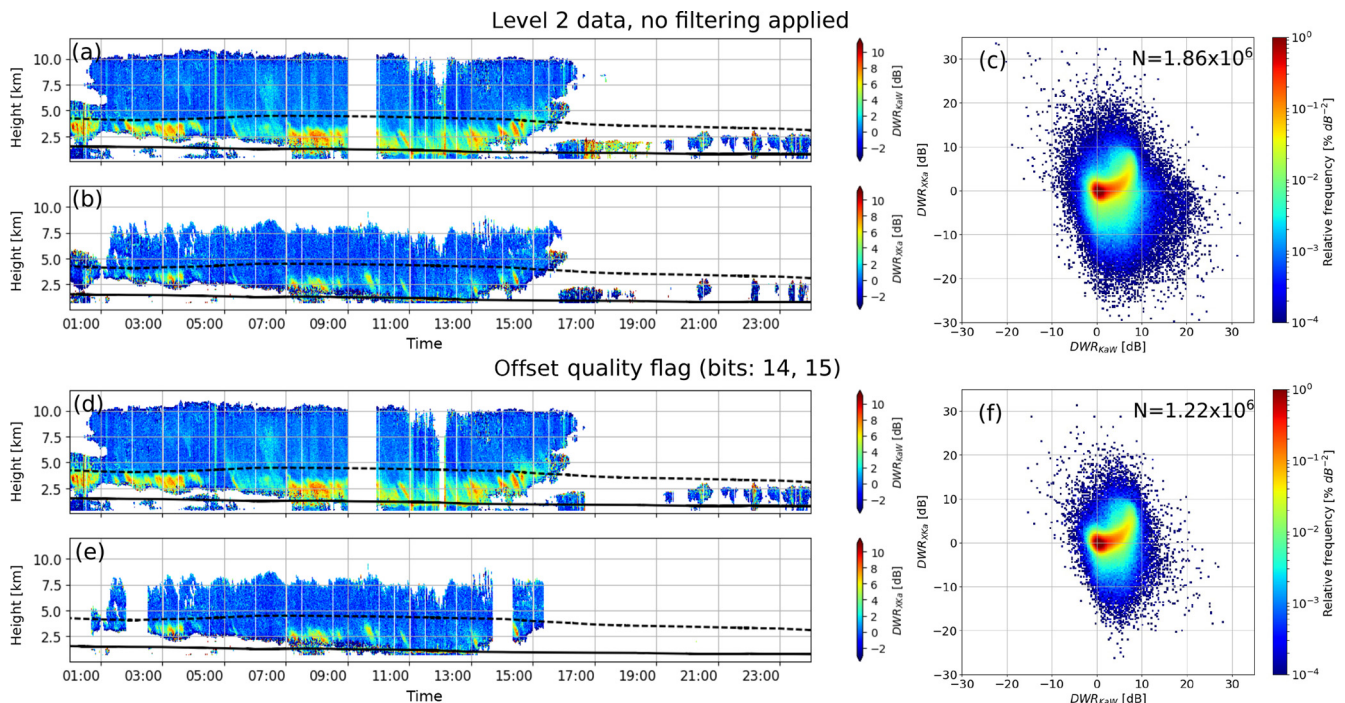


**Figure 4.** Time–height plots of  $\text{DWR}_{\text{KaW}}$  (a) and  $\text{DWR}_{\text{XKa}}$  (b) using the Level 2 data of 20 November 2015 without applying any filtering. The continuous line and dashed line are the 0 and  $-15^{\circ}\text{C}$  isotherms (provided by the CloudNet products), respectively. The triple-frequency signatures for the ice part of the clouds are shown in (c). Panels (d–f) show the remaining data after applying the offset quality flags and the restriction to data pairs with sufficient correlation.  $N$  in (c, f) indicates the respective number of data pairs in the ice part of the clouds. Note the log scale on the color bars in (c, f).

step removes most of the outliers from the aggregation signature in the triple-frequency plot (Fig. 5c). It is worth noting that the removal of such data reduces the scatter in the triple-frequency space but might also remove interesting measurements from regions with strong reflectivity gradients. Additional 3 min running-window averaging of the reflectivities keeps the most stable signatures (Fig. 5d and e), further removes scatter, and thus accentuates the aggregation signature

in triple-frequency plot (Fig. 5f). The averaged reflectivities calculated in this procedure are not included in the TRIPEX dataset because it would not be possible to retrieve the original data. The last two quality flags (bits 7 and 6; see Table 4) mark data acquired during rainfall according to the CloudNet product and times with total liquid water path larger than  $200\text{ g m}^{-2}$  as estimated by the microwave radiometer. The latter filtering significantly reduces the amount of usable data

**Table 6.** Characterization of the atmospheric conditions and estimated duration of cloud and precipitation events during TRIPEX.  $T_{2m}$  is the air temperature at 2 m from a nearby weather station. RR and AR are the rain rate and the accumulated rain measured by a Pluvio disdrometer; mean RR is calculated using all RR values larger than  $0 \text{ mm h}^{-1}$ . Liquid water path (LWP) and integrated water vapor (IWV) are derived from the collocated 14-channel microwave radiometer; mean LWP is calculated using all LWP values larger than  $0.03 \text{ kg m}^{-1}$  in order to exclude clear-sky periods. The columns with IC, SR, RS, and MP indicate the approximate duration in hours of non-precipitating ice clouds, stratiform rain, rain showers, and shallow mixed-phase clouds, respectively.

Date (yyyy.mm.dd)	$T_{2m}$ (°C) max/min	RR ( $\text{mm h}^{-1}$ ) max/mean	AR (mm)	LWP ( $\text{kg m}^{-2}$ ) max/mean	IWV ( $\text{kg m}^{-2}$ ) max/mean	IC (h)	SR (h)	RS (h)	MP (h)
2015.11.11	12.85/11.13	0.00/0.00	0.00	0.42/0.10	25.76/17.50	9	0	0	24
2015.11.12	12.81/10.25	0.00/0.00	0.00	0.29/0.07	20.58/17.34	18	0	0	18
2015.11.13	13.89/7.52	0.66/0.27	0.59	1.61/0.15	23.72/15.82	13	0	8	6
2015.11.14	10.86/6.46	0.33/0.12	0.79	0.38/0.10	19.34/12.23	12	10	0	0
2015.11.15	15.99/10.15	0.15/0.05	0.08	0.63/0.11	28.27/20.87	11	0	0	21
2015.11.16	13.74/11.45	2.16/0.40	2.16	2.64/0.15	28.65/18.99	4	4	3	12
2015.11.17	15.83/11.94	5.97/0.82	8.31	1.68/0.16	29.39/19.23	10	0	10	0
2015.11.18	14.60/11.41	8.07/1.88	4.40	1.65/0.13	27.71/15.02	6	0	0	14
2015.11.19	11.76/8.41	5.64/1.16	12.82	1.70/0.20	23.51/17.22	13	12	2	0
2015.11.20	9.45/4.87	1.08/0.27	1.02	0.98/0.13	19.02/13.63	10	3	0	6
2015.11.21	5.66/2.17	0.30/0.11	0.23	1.38/0.12	15.38/8.820	4	0	7	6
2015.11.22	5.33/−0.09	7.35/3.80	2.54	0.84/0.07	11.11/8.17	4	0	5	2
2015.11.23	5.32/−0.42	0.00/0.00	0.00	0.52/0.08	9.81/7.83	7	0	0	2
2015.11.24	4.51/0.19	1.26/0.28	1.30	0.53/0.17	16.71/12.57	10	12	0	0
2015.12.03	11.90/6.63	0.00/0.00	0.00	0.03/0.03	15.38/13.59	10	0	0	5
2015.12.04	11.39/5.87	2.67/0.56	3.38	0.57/0.21	24.09/10.98	4	4	0	2
2015.12.05	10.20/4.47	0.00/0.00	0.00	–	9.77/7.19	16	0	0	0
2015.12.06	12.86/3.34	0.00/0.00	0.00	0.39/0.11	24.14/15.63	2	0	0	12
2015.12.07	14.53/8.74	0.03/0.03	0.00	0.51/0.13	24.31/18.81	9	0	4	8
2015.12.08	14.66/7.92	2.67/0.84	4.06	0.84/0.18	23.01/14.67	2	5	0	0
2015.12.09	9.34/2.20	0.06/0.03	0.04	0.48/0.08	18.89/8.96	0	4	0	1
2015.12.10	8.81/0.77	0.00/0.00	0.00	–	11.86/6.49	7	0	0	0
2015.12.11	8.61/4.77	2.16/0.57	9.34	0.41/0.17	19.81/16.18	2	20	0	0
2015.12.12	10.42/4.7	0.03/0.03	0.02	0.36/0.09	21.10/15.73	16	0	0	0
2015.12.13	10.08/6.18	3.09/0.37	5.50	1.07/0.38	22.73/19.10	7	0	0	8
2015.12.14	9.24/3.36	0.03/0.03	0.02	0.17/0.08	16.00/12.95	6	0	0	0
2015.12.15	10.3/3.89	0.39/0.16	0.16	0.57/0.15	23.55/17.51	12	2	3	0
2015.12.16	13.04/8.90	2.49/0.39	6.02	–	–	0	10	0	7
2015.12.17	16.28/12.53	3.60/0.48	0.72	1.12/0.15	25.61/20.01	8	0	0	6
2015.12.18	13.11/8.74	0.27/0.17	0.08	0.71/0.12	26.64/16.45	10	0	1	2
2015.12.19	13.21/9.93	0.00/0.00	0.00	0.27/0.09	25.11/22.70	8	0	0	0
2015.12.20	13.22/11.31	0.00/0.00	0.00	0.44/0.10	23.15/20.99	22	1	0	0
2015.12.21	12.17/9.52	0.72/0.18	0.45	0.84/0.13	23.52/14.49	3	3	1	6
2015.12.22	14.75/10.41	2.19/0.41	1.45	0.61/0.08	26.53/22.00	16	2	0	8
2015.12.23	13.00/4.38	0.45/0.21	0.42	0.23/0.07	14.21/11.24	4	0	0	8
2015.12.24	14.51/4.38	5.34/0.68	1.82	1.14/0.11	22.91/15.40	6	0	1	3
2015.12.25	13.35/7.78	3.27/0.81	4.72	0.60/0.13	24.76/18.32	15	8	0	4
2015.12.26	15.78/7.17	0.00/0.00	0.00	0.20/0.08	22.51/17.55	4	0	0	4
2015.12.27	14.40/6.13	0.00/0.00	0.00	–	18.71/14.20	12	0	0	0
2015.12.28	11.07/5.12	0.00/0.00	0.00	–	9.56/8.57	11	0	0	0
2015.12.29	11.87/4.35	0.00/0.00	0.00	0.34/0.08	19.78/13.80	2	3	0	0
2015.12.30	9.40/3.77	0.00/0.00	0.00	0.05/0.04	17.80/10.93	3	0	0	0
2015.12.31	10.31/3.53	0.69/0.20	0.47	1.01/0.22	24.39/11.82	4	3	2	0
2016.01.01	8.45/3.46	0.30/0.13	0.10	0.83/0.13	15.42/9.85	13	0	0	6
2016.01.02	5.94/4.11	2.88/0.72	4.69	0.42/0.14	17.80/12.89	6	7	0	8
2016.01.03	8.29/4.84	1.86/0.44	2.95	0.93/0.23	19.85/14.45	6	14	0	4
2016.01.04	7.74/3.66	3.57/0.81	7.06	–	–	0	10	0	9
Total						377	137	47	222

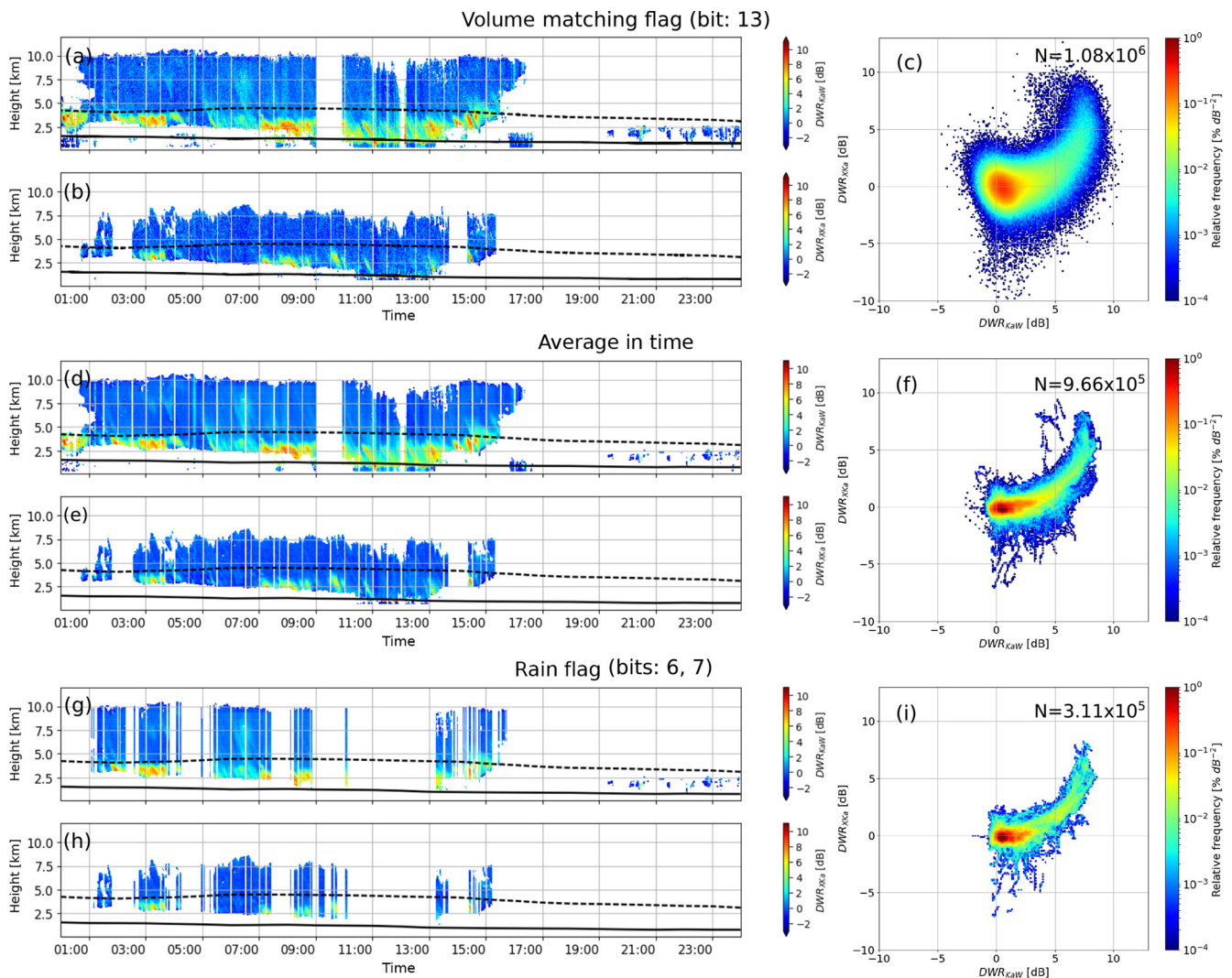


**Figure 5.** Same as Fig. 4, but here the effects of cumulative data filtering subject to different quality flags and averaging are illustrated. Panels (a–c) display the effect of filtering based on the DWR variance in time, which removes areas potentially affected by poor radar volume matching. The effect of the additional temporal averaging over 3 min is shown in (d–f). The effects of the removal of time periods with rain as identified by CloudNet or large liquid water paths measured by the nearby microwave radiometer are displayed in (g–i). Note the log scale on the color bars in (c, f, i).

(Fig. 5g and h) but preserves the main aggregation signature surprisingly well (Fig. 5i).

#### 4.2 Limitations of the current dataset

Despite the filtering steps discussed in Sect. 3.5, some limitations remain. As an example, on 23 November 2015 between 16:00 and 23:00 UTC we observe enhanced values of  $Z_{eX}$  (−20 up to 10 dBZ) (Fig. 6a), while  $Z_{eKa}$  and  $Z_{eW}$  remain very low. The mean Doppler velocity of that structure is very small (MDV between 0 and  $0.5 \text{ m s}^{-1}$ ) and is associated with a strongly enhanced LDR from the Ka band (Fig. 6b). Large  $Z_{dr}$  values are observed by the nearby weather polarimetric X band radars JuXPol and BoXPol (see Diederich et al.,

2015, for a detailed characterization of the radars) that were performing RHI scans over the TRIPEX site at that time. The most likely explanation based on the polarimetric signature and the fall velocity is fall streaks of chaff deployed by military aircraft during a training session. We recommend avoiding this period in cloud microphysical studies.

As described in Sect. 2.1, the X band was operated vertically pointing while rotating the antenna. Figure 7 illustrates effects related to imperfect vertical antenna pointing. When looking at the differences between vertical Doppler velocities observed from low-frequency and high-frequency radars (dual Doppler velocity, DDV), increases are expected in the presence of large scatterers (Matrosov, 2011; Kneifel et al., 2016). Large particles, which usually also have greater termi-



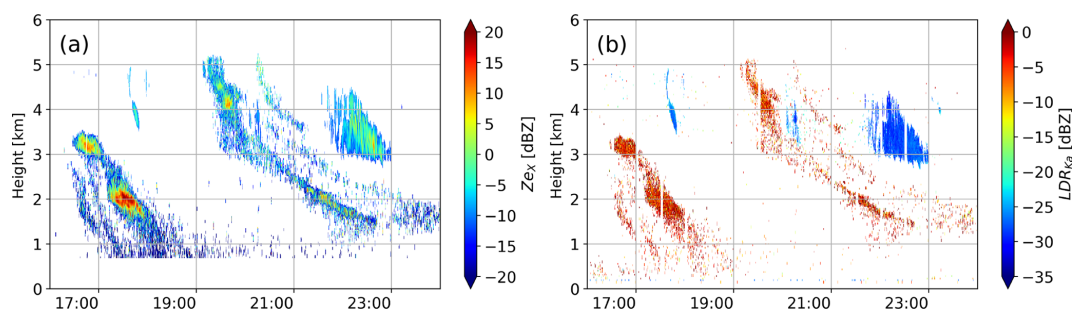


**Figure 6.** Time–height plots of the  $Z_{eX}$  and  $LDR_{Ka}$  of 23 November 2015 between 16:00 and 23:59. The region where the LDR is  $\approx -5$  dB is most probably the result of chaff. The Ka band software applies a filtering for non-meteorological targets which removes most of the chaff; only the filtered Ka band data are included in the TRIPEX dataset. Note that no such filtering is applied to the X band and W band data.

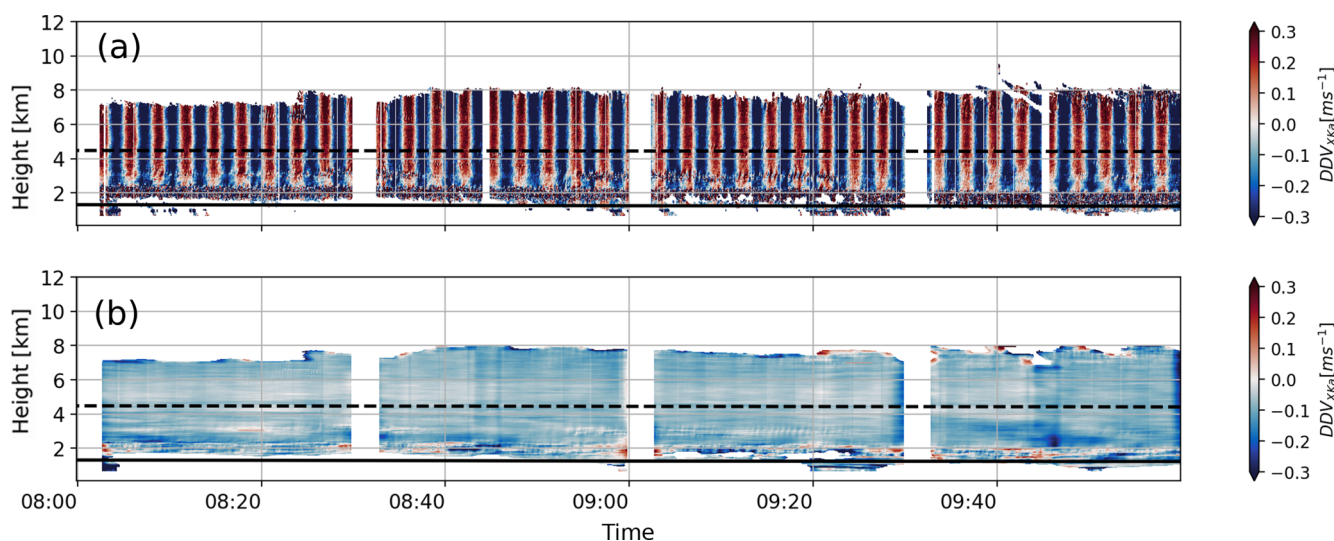


**Figure 7.** Time–height plots of the dual mean Doppler velocity using the Level 2 data of 20 November 2015. The dashed line and the continuous line are the  $-15$  and  $0^\circ\text{C}$  isotherms, respectively. Panel (a) shows the  $DDV_{XKa}$  using the original data from Level 2. Panel (b) shows the  $DDV_{XKa}$  after applying a 3 min moving average.

nal velocities, give a lower reflectivity signal at high frequencies due to non-Rayleigh scattering. This effect also leads to a lower MDV ( $MDV_X > MDV_{Ka} > MDV_W$ ). Since the ice particles in the uppermost part of the clouds are expected to be Rayleigh scatterers, the DDV should be zero. However,  $DDV_{XKa}$  (Fig. 7a) shows a periodic variation along the entire vertical range, with the period matching the X band scan duration of 3 min. Obviously, a non-perfect zenith pointing of the X band antenna introduces these periodic shifts in the mean Doppler velocity due to the contamination of the vertical Doppler signal by the horizontal wind component. A temporal average over 3 min minimizes the standard deviation of  $DDV_{XKa}$  relative to other averaging window sizes (Fig. 7b). Note that the averaged data are not included in the Level 2 data product because the optimal averaging window might depend on the prevailing atmospheric, height-dependent wind conditions, and original data cannot be recovered after averaging. We can also not completely

rule out a slight mispointing of the other two radars because their DDVs sometimes show deviations, especially in regions with strong horizontal winds with maximum DDVs. However, these DDVs are found to be below  $0.4 \text{ m s}^{-1}$ . An ad hoc estimate of the related relative radar mispointing of the two radars using the horizontal wind information from radiosondes for a few extreme cases suggests a potential mismatching of  $0.5^\circ$ . A correction of the shift requires reliable horizontal wind profiles, which will be investigated in more detail in the future.

### 4.3 Radar sensitivity

Figure 8 shows the distribution of reflectivity values measured by the three radars during the entire campaign filtered with the error flags (bits 13, 14, and 15 in Table 4) and stratified by height above the site. As already mentioned, the Ka band and W band show higher sensitivities compared to the X band up to high altitudes. The Ka band (Fig. 8b) ex-

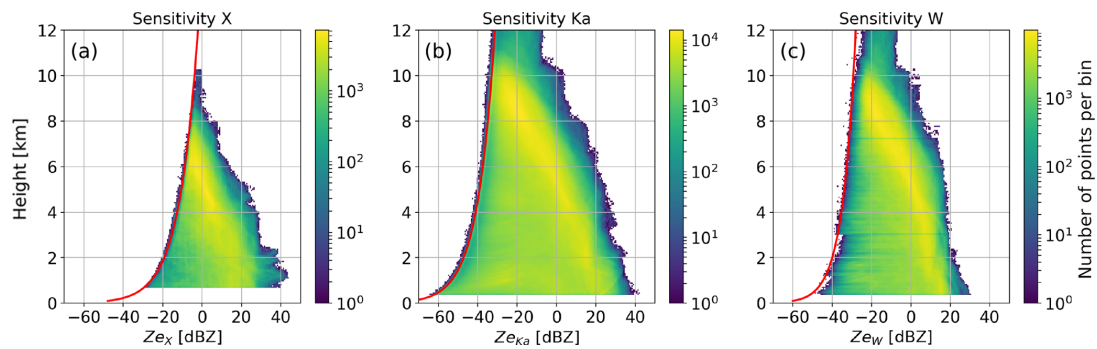


**Figure 8.** Histograms of reflectivities from the entire TRIPEX campaign Level 2 data for each radar. The red curve is the profile of the minimum retrieved reflectivity (Eq. 2). Panels (a), (b), and (c) show the histograms for the X, Ka, and W band, respectively; all error flags (see Table 4) were applied to filter the data. Note the log scale on the color bars.

**Table 7.** Coefficients  $a$  and  $b$  for the sensitivity fit (Eq. 2) obtained for the X, Ka, and W band. The coefficients were calculated using the Level 2 dataset with filtering according to the error flags applied (see Table 4).

Radar	$a$	$b$
X band	$6.25 \times 10^{-10}$	2.19
Ka band	$3.41 \times 10^{-12}$	2.04
W band	$8.36 \times 10^{-10}$	1.53

hibits the largest dynamic range (Fig. 8a and c). The step-like shape of the lowest altitude reflectivities from the W band is caused by different chirp settings (Table 2). A polynomial fit to the minimum retrieved linear reflectivities ( $Z_{e,lin}$ , in units of  $\text{mm}^6 \text{m}^{-3}$ ) as a function of altitude  $z$  (units of m),

$$Z_{e,lin}(z) = a \cdot z^b, \quad (2)$$

results for the X and Ka band in the expected nearly quadratic decrease with range (Table 7). The slower decrease (smaller exponent) for the W band results from the altitude-dependent sensitivity associated with the height-varying chirp settings.

The melting layer was mostly observed at altitudes between 1 and 2 km, where it causes a sharper increase in the reflectivity distribution and the largest values measured for the X band reflectivities. The X band  $Z_e$  distribution shows an enhancement of the largest recorded values at 2 km from  $\approx 30$  to  $\approx 40$  dBZ. The X band sensitivity limitations did not allow signals above 7 km with reflectivities below  $-10$  dBZ to be observed; however, dual-wavelength studies of clouds in this region are still possible with the W band and Ka band included in the Level 2 data. Nonetheless, ice aggregation and riming, which are most relevant for triple-frequency studies, usually occur at lower levels and larger reflectivities where all three radars provide sufficient sensitivity.

## 5 Triple-frequency characteristics of ice and snow clouds

Longer time series of observations are required in order to reliably estimate the occurrence probabilities of process signatures in the triple-frequency space. Those statistics might be useful for the development of microphysical retrievals and to constrain snow particle scattering models. Currently available datasets are restricted to short time periods or specific cases. Kulie et al. (2014) and Leinonen et al. (2012) used observations from airborne Ku, Ka, and W band radars data collected during the Wakasa Bay campaign (Lobl et al., 2007) to evaluate aggregate and spheroidal snowflake models. Their  $DWR_{KaW}$  and  $DWR_{KuKa}$  values reach up to 10 and 8 dB, respectively. Although their data are rather noisy due to volume mismatch and attenuation effects, they were the first observations which confirmed triple-frequency signatures predicted by complex aggregate scattering models (Kneifel et al., 2011a). The first triple-frequency signatures from ground-based radars (S, Ka, and W band) were presented by Stein et al. (2015) for two case studies. Similar to the Wakasa Bay studies, they found deviation from predictions based on simpler spheroidal-based scattering models, but their aggregates showed a  $DWR_{KaW}$  saturation around 8 dB and not the “hook” or “bending back” feature found in the previous studies. They attributed this behavior to a snow aggregate fractal dimension of 2. Kneifel et al. (2015) combined triple-frequency ground-based radar (X, Ka and W band) with in situ observations and analyzed three cases characterized by falling snow particles with different degrees of riming. For low-density aggregates, their  $DWR_{KaW}$  also did not exceed the 8 dB limit reported by previous studies but exhibited a strong bending back feature (i.e., reduction of  $DWR_{KaW}$  for larger particles) with large  $DWR_{XKa}$  up to 15 dB. During riming periods, the triple-frequency signatures showed a distinctly different behavior:  $DWR_{KaW}$  increases up to 10 dB, while  $DWR_{XKa}$  remains constant or slowly increases up to 3 dB, which appears in triple-frequency plots as an almost horizontal line.

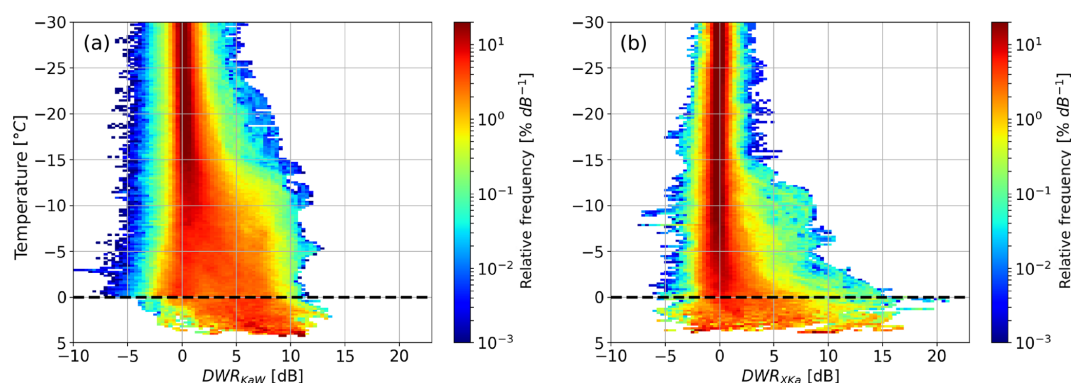


**Figure 9.** Two-dimensional histograms (contoured frequency by altitude diagram, CFAD; see Yuter and Houze, 1995, for more details) of DWR against air temperature for the entire TRIPEX dataset. The dashed line indicates the 0 °C isotherm. The data below the dashed line are only collected from the cases in which a melting layer is observed. The DWRs were filtered using the error flags and averaged in time using a 3 min moving window. Panels (a) and (b) show  $DWR_{KaW}$  and  $DWR_{XKa}$ , respectively. Note the log scale of the color bars.

The TRIPEX dataset is, to the best of our knowledge, one of the longest, quality-controlled triple-frequency datasets currently available, which allows for reliable estimations of the occurrence of several triple-frequency signatures in mid-latitude winter clouds. In the following sections, we use the Level 2 data filtered only with the error quality flag (see Table 4) to analyze the temperature dependence of the triple-frequency signatures and signatures of riming and melting snow particles. The extension of the filtering to the warning flags would remove all melting layer cases and/or observations with larger amounts of supercooled liquid water, which portray particularly interesting signatures of partially melted or rimed particles.

### 5.1 Temperature dependence of triple-frequency signatures

The relatively large dataset allows us to stratify the occurrence probability of  $DWR_{KaW}$  (Fig. 9a) and  $DWR_{XKa}$  (Fig. 9b) according to air temperature, which results in four main regimes. The regime in which the temperature is smaller than  $-20$  °C exhibits small DWR values, mostly below 3 dB.

Between  $-20$  and  $-10$  °C, we find a widening of the distribution to higher values in both DWRs. This DWR increase becomes very rapid at temperatures warmer than  $-15$  °C, which suggests an increasing number of larger aggregates caused by stronger aggregation due to preferential growth of dendritic particles in the  $-20$  to  $-10$  °C temperature range (Kobayashi, 1957; Pruppacher and Klett, 1997). Dendrites are well known to favor snow aggregation due to their branched crystal structure. In accordance with previous studies,  $DWR_{KaW}$  saturates around 7 dB at  $-10$  °C, with only a small fraction reaching up to 10 dB.  $DWR_{XKa}$  approaches maximum values of 5 to 8 dB; however, the occurrence probability of enhanced  $DWR_{XKa}$  is smaller compared to those found for  $DWR_{KaW}$ . This is an expected behavior since early

aggregation is likely to first enhance the  $DWR_{KaW}$  because particle growth affects the high frequencies early which first transition out of the Rayleigh regime. Thus the W band radar is the first influenced by this transition which enhances  $DWR_{KaW}$ .

At temperatures between  $-10$  and  $0$  °C, the distribution of  $DWR_{KaW}$  remains almost constant, with the exception of a small peak with higher values around  $-5$  °C and a widening of the DWR distributions towards negative values. The latter effect might relate to two causes. The first is the DWR calibration (Sect. 3.5), derived for the upper part of the clouds (ice part), which, when applied to the entire profile, leads to the overestimation of  $Z_{eW}$ . The second possible contributor is the radar volume mismatch, which becomes worse for observations closer to the radars due to reduced overlap of the radar beams.

Interestingly,  $DWR_{XKa}$  grows continuously up to 12 dB for temperatures warmer than  $-5$  °C, which is in line with intensified aggregation of the snow particles towards lower heights. The very large  $DWR_{XKa}$  in this regime can be explained by increasing particle stickiness when approaching the 0 °C level. In the fourth regime between 0 °C and the LDR maximum,  $DWR_{KaW}$  tends to further increase, while  $DWR_{XKa}$  remains constant or even decreases.  $DWR_{KaW}$  reaches values up to 10 dB, while  $DWR_{XKa}$  attains values up to 15 dB, which could be produced by persistent aggregation.

Figure 10 shows the triple-frequency plots for the temperature ranges  $-20 < T < -10$  °C (panel a) and  $-10 < T < -1$  °C (panel b). Between  $-20$  and  $-10$  °C (panel a), we find the typical bending signature in the triple-frequency space saturating at about a  $DWR_{KaW}$  of 8 dB, similar to Stein et al. (2015). This temperature regime includes the dendritic growth zone (DGZ), which is usually defined by cloud chamber experiments in the range of temperatures  $-17$  to  $-12$  °C (Kobayashi, 1957; Yamashta et al., 1985; Takahashi, 2014). It is worth reminding the reader that the temperature infor-

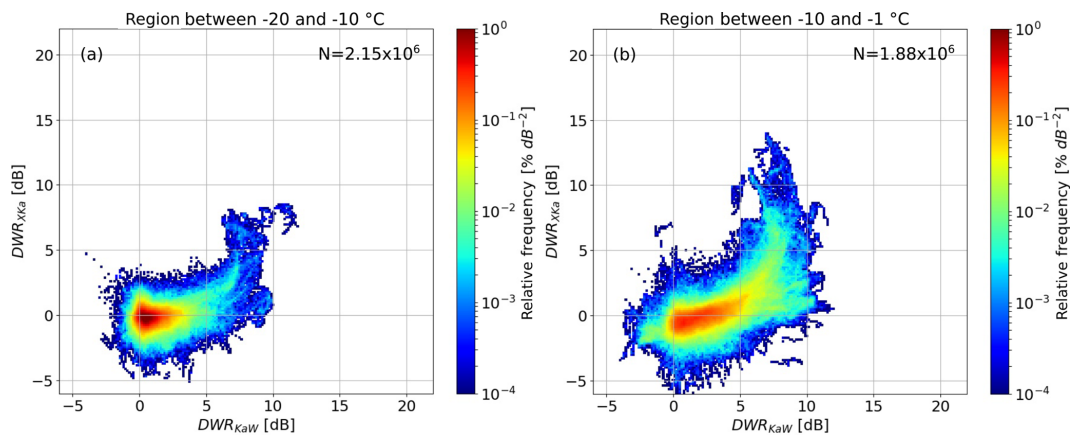


**Figure 10.** Two-dimensional histogram of the triple-frequency signatures for different temperature regions normalized by the total number of points  $N$ . The color shows the relative frequency. Panel (a) is for temperatures between  $-20$  and  $-10$  °C. Panel (b) shows the region between  $-10$  and  $-1$  °C. Note the log scale on the color bars.

mation included in the TRIPEX dataset has not been obtained from a direct measurement, but it has been taken from CloudNet. Consequently, it is not surprising that the growth regimes that we have identified using the signatures observed in the DWR profiles do not perfectly correspond in temperature to the ones determined in cloud chamber experiments.

Although we combine observations from different clouds, the variability of the triple-frequency signatures is relatively small. For warmer temperatures ( $-10$  to  $-1$  °C, panel b), needle aggregates are likely to be generated, and ice particles start to become more sticky, leading to a more pronounced bending feature. For  $DWR_{XKa}$  reaching up to 12 dB, the hook (or bending back) signature (Kneifel et al., 2015) also becomes visible for parts of the dataset ( $DWR_{XKa}$  decreases, while  $DWR_{KaW}$  is still increasing). This panel also reveals a secondary mode with  $DWR_{XKa}$  below 3 dB and  $DWR_{KaW}$  reaching up to 12 dB. Following Kneifel et al. (2015), this mode could hint at rimed particles, which are still too small to enhance  $DWR_{XKa}$ , but due to their increased density and hence larger refractive index, the  $DWR_{KaW}$  increases. We will investigate this feature in more detail in the next subsection.

The dataset contains particularly large DWR signatures close to 0 °C and at higher temperatures, which are probably caused by melting snowflakes or simply by enhanced aggregation. To further investigate this signature we generated the triple-frequency plot for the data between the 0 °C and the height of the LDR maximum (Fig. 11), which we consider to be a proxy for the center of the melting layer (Le and Chandrasekar, 2013). In this region,  $DWR_{XKa}$  reaches maximum values up to 20 dB already at low  $DWR_{KaW}$ . Overall, the data points are much more scattered than those in the colder temperature regions. This larger variability might result from effects of the radar volume mismatch caused by strong vertical gradients near the melting layer. Another possible explanation is the much lower amount of data. Latent heat release by

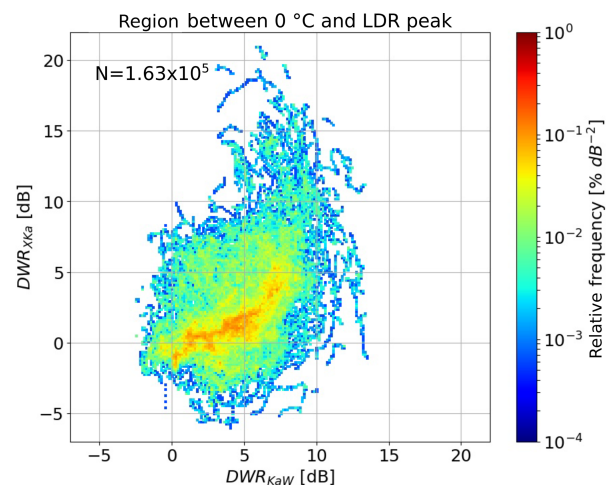


**Figure 11.** Two-dimensional histogram of the triple-frequency signatures for the region between 0 °C and the LDR maximum in the melting layer normalized by the total number of points  $N$ . The color shows the relative frequency, and the binning matches what was used for Fig. 10. Note the log scale on the color bar.

melting increases turbulent motion, which might further enhance the detrimental effects of volume mismatch. We need to be careful in interpreting these features as triple-frequency signatures of the melting layer because the temperature information is based on CloudNet products taken from ECMWF analyses which cannot be expected to represent small-scale variations of the 0 °C isotherm. Moreover, melting can be delayed depending on the profiles of temperature and humidity and on the density and size of the particles themselves (Matsuo and Sasyo, 1981; Rasmussen and Pruppacher, 1982). A sagging of the melting layer has been repeatedly observed with the scanning polarimetric X band radar in Bonn (BoX-Pol, also part of JOYCE-CF) for dominant riming processes



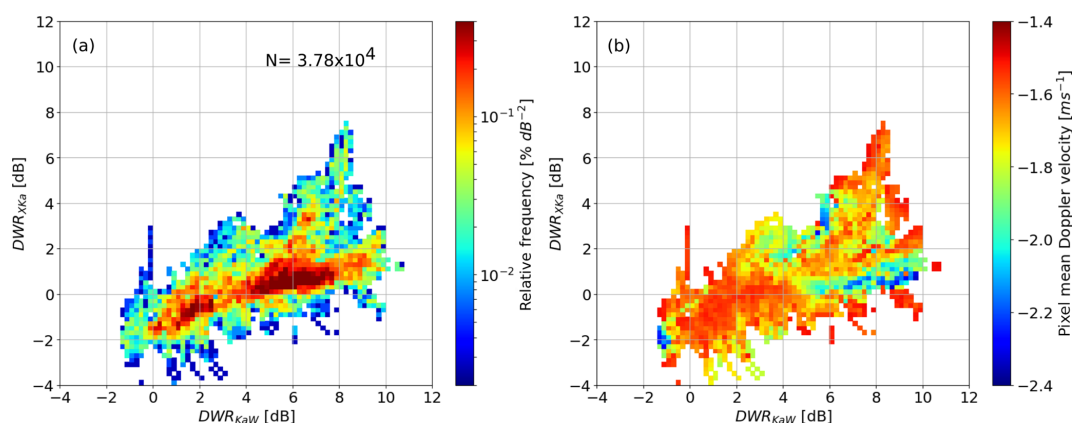


**Figure 12.** Triple-frequency signatures for Level 2 data with temperatures between  $-20$  and  $-1$  °C and a mean Doppler velocity (MDV) above  $1.5 \text{ m s}^{-1}$  in order to select potentially rimed particles. Panel (a) shows the relative frequency of the observations. Panel (b) indicates the average MDV of each pixel in the histogram. Note the log scale on the color bar in (a).

(Xie et al., 2016; Trömel et al., 2019). Rimed particles fall with higher terminal velocities and consequently take more time to melt. In the following subsection, we will use the LDR and the mean Doppler velocity to better separate non-melted from melted snow particles.

## 5.2 Signatures of riming and melting snow particles

During riming, supercooled liquid water droplets freeze onto the ice particles. This strongly increases the particle mass, while its size grows more slowly, especially during the onset of riming. Since the terminal velocity is mainly governed by the relation between particle mass (gravitational force) and its cross section perpendicular to the air stream (drag force), its terminal velocity observed by the mean Doppler velocity (MDV) increases due to riming (Mosimann, 1995). MDVs above  $1.5 \text{ m s}^{-1}$  can be used as a simple indicator of rimed particles as long as vertical air velocities are small (Mosimann, 1995). About 1 % of triple-frequency data in the temperature range between  $-20$  and  $-1$  °C have a MDV above  $1.5 \text{ m s}^{-1}$  (Fig. 12). Interestingly, we find one mode very similar to a sloped line found for rimed particles in Kneifel et al. (2015), which coincides with large MDVs up to  $2.4 \text{ m s}^{-1}$  and  $DWR_{KaW}$  up to 10 dB. However, the correlation between enhanced  $DWR_{KaW}$  and MDV is less clear than in the case shown in Kneifel et al. (2015). A more detailed investigation showed that TRIPEX only contains short riming periods of a few minutes' duration, while the period analyzed by Kneifel et al. (2015) was considerably longer ( $\approx 20$  min). In general,  $DWR_{KaW}$  is expected to increase for larger particles and strong riming, but detailed sensitivity studies which clearly characterize these dependencies are still missing. Another mode in Fig. 12 with larger  $DWR_{XKa}$  of about 3 dB suggests mean particle sizes exceeding 8 mm according to Kneifel et al. (2015). We speculate that this mode might be related to only slightly rimed aggregates. A larger number of

riming events are required to better investigate the sensitivities of MDV and triple-frequency signatures to various degrees of riming, which would also be a very valuable basis on which to constrain theoretical particle models, as developed, for example, by Leinonen and Szyrmer (2015).

A particularly interesting signature shown in Fig. 11 is the very large  $DWR_{XKa}$  close to the melting layer. To the best of our knowledge, these features have not yet been described. It is not clear to us whether these signatures are caused by very large aggregates or melting particles. A pure melting of snowflakes should enhance the MDV because of their decrease in size (and thus cross-sectional area) as well as drag in the airflow. Early melting can, however, be better detected by the LDR: the much larger refractive index of liquid water compared to ice and the initially still asymmetric melting snowflakes result in a much larger depolarization signal as compared to dry snowflakes. Hence, we replot Fig. 11 to better see the transition from dry snowflakes with a typical MDV of  $1 \text{ m s}^{-1}$  and a LDR around  $-15$  dB to larger MDV coinciding with a rising LDR as expected for melted snow (Fig. 13). Interestingly, the very large  $DWR_{XKa}$  mostly shows MDV and LDR values associated with unmelted snowflakes. Once the MDV and LDR indicate the onset of melting, the DWRs, especially  $DWR_{XKa}$ , rapidly decrease. As  $DWR_{XKa}$  is strongly related to the mean particle size, the results indicate that the largest snowflake sizes occur before the melting starts. Once snowflakes are completely melted,  $DWR_{KaW}$  will still be enhanced due to Mie scattering by the raindrops, while  $DWR_{XKa}$  will remain close to 0 dB (Tridon et al., 2017). However, our corrections for attenuation within the melting layer are certainly incomplete; thus we leave a deeper analysis of that feature to future studies.

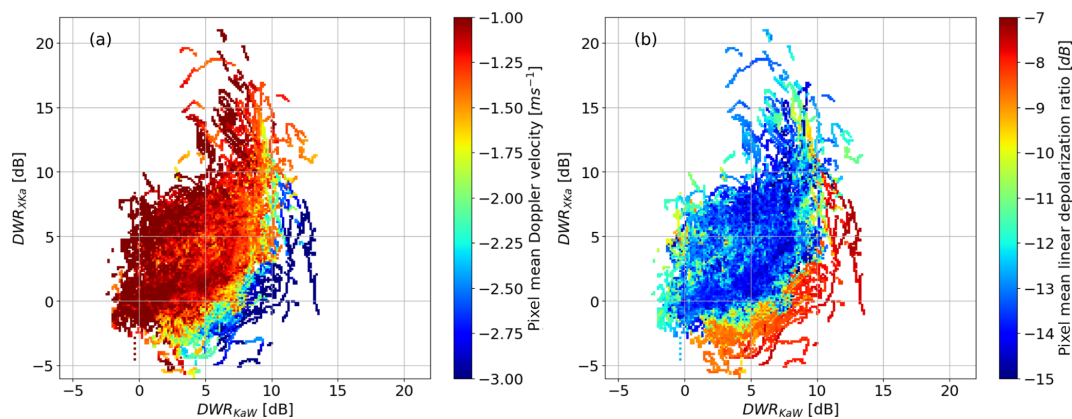


**Figure 13.** Triple-frequency diagrams of observations between  $0^{\circ}\text{C}$  and the LDR maximum in the melting layer (same as Fig. 10c), but the color in (a) indicates the average MDV, while in (b) the color shows the average LDR.

## 6 Data availability

The TRIPEX Level 2 data are available for download at the ZENODO platform (<https://doi.org/10.5281/zenodo.1341389>; Dias Neto et al., 2019). Quicklooks of the TRIPEX dataset are freely accessible via a data quicklook browser ([http://gop.meteo.uni-koeln.de/~Hatpro/dataBrowser/dataBrowser1.html?site=TRIPEX&date=2015-11-20&UpperLeft=3radar\\_Ze](http://gop.meteo.uni-koeln.de/~Hatpro/dataBrowser/dataBrowser1.html?site=TRIPEX&date=2015-11-20&UpperLeft=3radar_Ze)). The raw and Level 1 data and  $K_{dp}$  can be requested from the corresponding author.

## 7 Conclusions

We present the first 2-month-long dataset of vertically pointing triple-frequency Doppler radar (X, Ka, and W band) observations of winter clouds at a midlatitude site (JOYCE-CF, Jülich, Germany). The dataset includes spatiotemporal re-gridded data including offset and attenuation corrections. Several quality flags allow the dataset to be filtered according to the needs of the specific application. The quality flags have been separated into error and warning flags; we recommend always applying the error flags, while the warning flags might not be necessary depending on the application. All corrections applied are stored separately in the data files in order to allow the user to recover and also work with data at intermediate processing steps and to potentially apply individual corrections. This might be necessary because the campaign focus was on the ice and snow part of the cloud. Consequently, the correction for path-integrated attenuation might be inappropriate, for example, for studies investigating the melting layer or rainfall.

The statistical analysis of the ice part of the clouds revealed dominant triple-frequency signatures related to aggregation (hook or bending up feature). In agreement with previous studies,  $DWR_{KaW}$  mostly saturates around 7 dB, while  $DWR_{XKa}$  reaches values of up to 20 dB in regions of presum-

ably intense aggregation close to the melting layer. Due to the large dataset, we were able to investigate the relation between the DWRs and temperature. The first significant increase of aggregation starts around  $-15^{\circ}\text{C}$ , where dendritic crystals are known to grow efficiently and favor aggregation. In this zone,  $DWR_{KaW}$  mostly increases up to its saturation value of 7 dB.  $DWR_{XKa}$  increases mainly below  $-10^{\circ}\text{C}$ . Close to the melting layer,  $DWR_{XKa}$  massively increases up to 20 dB, which has not been reported so far. A deeper investigation using the LDR and MDV revealed that these extreme  $DWR_{XKa}$  are indeed due to large dry aggregates rather than melting particles. Once melting is indicated by larger MDV and LDR values,  $DWR_{XKa}$  appears to rapidly decrease. Clearly, combined observational and scattering modeling studies are needed to further investigate this transition. Although the dataset only contains a few short riming periods (approximately 1 % of the data between  $-20$  and  $-1^{\circ}\text{C}$ ), a simple MDV threshold reveals the typical riming signature (flat horizontal line in the triple-frequency space) reported for riming case studies in Kneifel et al. (2015). The statistical analysis of riming is more challenging compared to aggregation. Riming is often connected to larger amounts of supercooled liquid water, larger vertical air motions, and turbulence, which deteriorate the signal due to liquid water attenuation and enhance effects of imperfect radar volume matching. Riming could be further investigated with this dataset by focusing on single cases, for which it is possible to apply specific corrections and filtering.

The synergy with nearby polarimetric weather radar observations will be investigated in future studies by including the vertical polarimetric profiles matching the JOYCE-CF site based on quasi-vertical profiles (QVPs) (Trömel et al., 2014; Ryzhkov et al., 2016) or columnar vertical profiles (CVPs) (Murphy et al., 2017; Trömel et al., 2019). Also a data release including the W and Ka band Radar Doppler spectra is planned.

**Supplement.** The supplement related to this article is available online at: <https://doi.org/10.5194/essd-11-845-2019-supplement>.

**Author contributions.** JDN wrote the paper, developed the data processing, and analyzed the data. SK, ST, JH, and CS designed the experiment. SK also supervised the analysis and writing of the paper. DO helped in developing data processing, radar calibration, and analysis. ST, JH, BB, SK, NH, KM, ML, and CS carried out the various radar measurements, set up specific measurement modes, and contributed to the paper.

**Competing interests.** The authors declare that they have no conflict of interest.

**Acknowledgements.** The authors acknowledge the funding provided by the German Research Foundation (DFG) under grant KN 1112/2-1 as part of the Emmy-Noether Group OPTIMIce. José Dias Neto also acknowledges support by the Graduate School of Geosciences of the University of Cologne. We thank the departments S, G and IEK-7 for the technical and administrative support during the field experiment. The majority of data for this dataset were obtained at the JOYCE Core Facility (JOYCE-CF) co-funded by the DFG under DFG research grant LO 901/7-1. Major instrumentation at the JOYCE site was funded by the Transregional Collaborative Research Center TR32 (Simmer et al., 2015) funded by the DFG and JuXPol by the TERENO (Terrestrial Environmental Observatories) program of the Helmholtz Association (Zacharias et al., 2011). For this work, we used products obtained within the Cloud-Net project (part of the EU H2020 project ACTRIS, European Research Infrastructure for the observation of Aerosol, Clouds, and Trace Gases) and developed during the High Definition Clouds and Precipitation for advancing Climate Prediction HD(CP)<sup>2</sup> project funded by the German Ministry for Education and Research under grants 01LK1209B and 01LK1502E.

**Review statement.** This paper was edited by Giulio G. R. Iovine and reviewed by five anonymous referees.

## References

- Baldini, L. and Gorgucci, E.: Identification of the Melting Layer through Dual-Polarization Radar Measurements at Vertical Incidence, *J. Atmos. Ocean. Tech.*, 23, 829–839, <https://doi.org/10.1175/JTECH1884.1>, 2006.
- Chase, R. J., Finlon, J. A., Borque, P., McFarquhar, G. M., Nesbitt, S. W., Tanelli, S., Sy, O. O., Durden, S. L., and Poellot, M. R.: Evaluation of Triple-Frequency Radar Retrieval of Snowfall Properties Using Coincident Airborne In Situ Observations During OLYMPEX, *Geophys. Res. Lett.*, 45, 5752–5760, <https://doi.org/10.1029/2018GL077997>, 2018.
- Dias Neto, J., Kneifel, S., and Ori, D.: The TRiple-frequency and Polarimetric radar Experiment for improving process observation of winter precipitation (version 2) [Data set], Zenodo, <https://doi.org/10.5281/zenodo.1341390>, 2019.
- Diederich, M., Ryzhkov, A., Simmer, C., Zhang, P., and Trömel, S.: Use of Specific Attenuation for Rainfall Measurement at X-Band Radar Wavelengths. Part I: Radar Calibration and Partial Beam Blockage Estimation, *J. Hydrometeorol.*, 16, 487–502, <https://doi.org/10.1175/JHM-D-14-0066.1>, 2015.
- Gergely, M., Cooper, S. J., and Garrett, T. J.: Using snowflake surface-area-to-volume ratio to model and interpret snowfall triple-frequency radar signatures, *Atmos. Chem. Phys.*, 17, 12011–12030, <https://doi.org/10.5194/acp-17-12011-2017>, 2017.
- Görsdorf, U., Lehmann, V., Bauer-Pfundstein, M., Peters, G., Vavriv, D., Vinogradov, V., and Volkov, V.: A 35-GHz polarimetric doppler radar for long-term observations of cloud parameters-description of system and data processing, *J. Atmos. Ocean. Tech.*, 32, 675–690, <https://doi.org/10.1175/JTECH-D-14-00066.1>, 2015.
- Greco, M., Tian, L., Heymsfield, G. M., Tokay, A., Olson, W. S., Heymsfield, A. J., Bansemer, A., Greco, M., Tian, L., Heymsfield, G. M., Tokay, A., Olson, W. S., Heymsfield, A. J., and Bansemer, A.: Nonparametric Methodology to Estimate Precipitating Ice from Multiple-Frequency Radar Reflectivity Observations, *J. Appl. Meteorol. Clim.*, 57, 2605–2622, <https://doi.org/10.1175/JAMC-D-18-0036.1>, 2018.
- Hogan, R. J., Illingworth, A. J., and Sauvageot, H.: Measuring crystal size in cirrus using 35- and 94-GHz radars, *J. Atmos. Ocean. Tech.*, 17, 27–37, [https://doi.org/10.1175/1520-0426\(2000\)017<0027:MCSICU>2.0.CO;2](https://doi.org/10.1175/1520-0426(2000)017<0027:MCSICU>2.0.CO;2), 2000.
- Hogan, R. J., Gaussiat, N., and Illingworth, A. J.: Stratocumulus Liquid Water Content from Dual-Wavelength Radar, *J. Atmos. Ocean. Tech.*, 22, 1207–1218, <https://doi.org/10.1175/JTECH1768.1>, 2005.
- Hou, A., Kakar, R., Neeck, S., Azarbarzin, A., Kummerow, C., Kojima, M., Oki, R., Nakamura, K., and Iguchi, T.: The Global Precipitation Measurement Mission, *B. Am. Meteorol. Soc.*, 95, 701–722, <https://doi.org/10.1175/BAMS-D-13-00164.1>, 2014.
- Huang, G.-J., Bringi, V. N., and Thurai, M.: Orientation Angle Distributions of Drops after an 80-m Fall Using a 2D Video Disdrometer, *J. Atmos. Ocean. Tech.*, 25, 1717–1723, <https://doi.org/10.1175/2008JTECHA1075.1>, 2008.
- Illingworth, A. J., Hogan, R. J., O'Connor, E. J., Bouniol, D., Brooks, M. E., Delanoë, J., Donovan, D. P., Eastment, J. D., Gaussiat, N., Goddard, J. W. F., Haeffelin, M., Klein Baltinik, H., Krasnov, O. A., Pelon, J., Piriou, J. M., Protat, A., Russchenberg, H. W. J., Seifert, A., Tompkins, A. M., van Zadelhoff, G. J., Vinit, F., Willen, U., Wilson, D. R., and Wrench, C. L.: Cloudnet: Continuous evaluation of cloud profiles in seven operational models using ground-based observations, *B. Am. Meteorol. Soc.*, 88, 883–898, <https://doi.org/10.1175/BAMS-88-6-883>, 2007.
- Kalthoff, N., Adler, B., Wieser, A., Kohler, M., Träumner, K., Handwerker, J., Corsmeier, U., Khodayar, S., Lambert, D., Kopmann, A., Kunka, N., Dick, G., Ramatschi, M., Wickert, J., and Kottmeier, C.: KITcube – a mobile observation platform for convection studies deployed during HyMeX, *Meteorol. Z.*, 22, 633–647, 2013.
- Kneifel, S., Kulie, M. S., and Bennartz, R.: A triple-frequency approach to retrieve microphysical snowfall parameters, *J. Geophys. Res.*, 116, D11203, <https://doi.org/10.1029/2010JD015430>, 2011a.

- Kneifel, S., Maahn, M., Peters, G., and Simmer, C.: Observation of snowfall with a low-power FM-CW K-band radar (Micro Rain Radar), *Meteorol. Atmos. Phys.*, 113, 75–87, <https://doi.org/10.1007/s00703-011-0142-z>, 2011b.
- Kneifel, S., von Lerber, A., Tiira, J., Moisseev, D., Kollias, P., and Leinonen, J.: Observed relations between snowfall microphysics and triple-frequency radar measurements, *J. Geophys. Res.-Atmos.*, 120, 6034–6055, <https://doi.org/10.1002/2015JD023156>, 2015.
- Kneifel, S., Kollias, P., Battaglia, A., Leinonen, J., Maahn, M., Kalesse, H., and Tridon, F.: First observations of triple-frequency radar Doppler spectra in snowfall: Interpretation and applications, *Geophys. Res. Lett.*, 43, 2225–2233, <https://doi.org/10.1002/2015GL067618>, 2016.
- Kobayashi, T.: Experimental Researches on the Snow Crystal Habit and Growth by Means of a Diffusion Cloud Chamber, *J. Meteorol. Soc. Jpn., Ser. II*, 35A, 38–47, [https://doi.org/10.2151/jmsj1923.35A.0\\_38](https://doi.org/10.2151/jmsj1923.35A.0_38), 1957.
- Küchler, N., Kneifel, S., Löhnert, U., Kollias, P., Czekala, H., and Rose, T.: A W-band radar-radiometer system for accurate and continuous monitoring of clouds and precipitation, *J. Atmos. Ocean. Tech.*, 34, 2375–2392, <https://doi.org/10.1175/JTECH-D-17-0019.1>, 2017.
- Kulie, M. S., Hiley, M. J., Bennartz, R., Kneifel, S., and Tanelli, S.: Triple-Frequency Radar Reflectivity Signatures of Snow: Observations and Comparisons with Theoretical Ice Particle Scattering Models, *J. Appl. Meteorol. Clim.*, 53, 1080–1098, 2014.
- Le, M. and Chandrasekar, V.: Hydrometeor profile characterization method for dual-frequency precipitation radar onboard the GPM, *IEEE T. Geosci. Remote*, 51, 3648–3658, <https://doi.org/10.1109/TGRS.2012.2224352>, 2013.
- Leinonen, J.: High-level interface to T-matrix scattering calculations: architecture, capabilities and limitations, *Opt. Express*, 22, 1655–1660, <https://doi.org/10.1364/OE.22.001655>, 2014.
- Leinonen, J. and Moisseev, D.: What do triple-frequency radar signatures reveal about aggregate snowflakes?, *J. Geophys. Res.*, 120, 229–239, <https://doi.org/10.1002/2014JD022072>, 2015.
- Leinonen, J. and Szyrmer, W.: Radar signatures of snowflake riming: a modeling study, *Earth and Space Science*, 2, 346–358, <https://doi.org/10.1002/2015EA000102>, 2015.
- Leinonen, J., Kneifel, S., Moisseev, D., Tyynelä, J., Tanelli, S., and Nousiainen, T.: Evidence of non-spheroidal behavior in millimeter-wavelength radar observations of snowfall, *J. Geophys. Res.*, 117, D18205, <https://doi.org/10.1029/2012JD017680>, 2012.
- Leinonen, J., Lebsock, M. D., Tanelli, S., Sy, O. O., Dolan, B., Chase, R. J., Finlon, J. A., von Lerber, A., and Moisseev, D.: Retrieval of snowflake microphysical properties from multi-frequency radar observations, *Atmos. Meas. Tech.*, 11, 5471–5488, <https://doi.org/10.5194/amt-11-5471-2018>, 2018.
- Lobl, E. S., Aonashi, K., Murakami, M., Griffith, B., Kummerow, C., Liu, G., and Wilheit, T.: Wakasa bay, Organization, 551–558, <https://doi.org/10.1175/BAMS-88-4-551>, 2007.
- Löffler-Mang, M. and Joss, J.: An optical disdrometer for measuring size and velocity of hydrometeors, *J. Atmos. Ocean. Tech.*, 17, 130–139, [https://doi.org/10.1175/1520-0426\(2000\)017<0130:AODFMS>2.0.CO;2](https://doi.org/10.1175/1520-0426(2000)017<0130:AODFMS>2.0.CO;2), 2000.
- Löhnert, U., Schween, J. H., Acquistapace, C., Ebell, K., Maahn, M., Barrera-Verdejo, M., Hirsikko, A., Bohn, B., Knaps, A., O’Connor, E., Simmer, C., Wahner, A., and Crewell, S.: JOYCE: Jülich Observatory for Cloud Evolution, *B. Am. Meteorol. Soc.*, 96, 1157–1174, <https://doi.org/10.1175/BAMS-D-14-00105.1>, 2015.
- Maahn, M., Löhnert, U., Kollias, P., Jackson, R. C., and McFarquhar, G. M.: Developing and evaluating ice cloud parameterizations for forward modeling of radar moments using in situ aircraft observations, *J. Atmos. Ocean. Tech.*, 32, 880–903, <https://doi.org/10.1175/JTECH-D-14-00112.1>, 2015.
- Macke, A., Seifert, P., Baars, H., Barthlott, C., Beekmans, C., Behrendt, A., Bohn, B., Brueck, M., Bühl, J., Crewell, S., Damian, T., Deneke, H., Düsing, S., Foth, A., Di Girolamo, P., Hammann, E., Heinze, R., Hirsikko, A., Kalisch, J., Kalthoff, N., Kinne, S., Kohler, M., Löhnert, U., Madhavan, B. L., Maurer, V., Muppa, S. K., Schween, J., Serikov, I., Siebert, H., Simmer, C., Späth, F., Steinke, S., Träumner, K., Trömel, S., Wehner, B., Wieser, A., Wulfmeyer, V., and Xie, X.: The HD(CP)2 Observational Prototype Experiment (HOPE) – an overview, *Atmos. Chem. Phys.*, 17, 4887–4914, <https://doi.org/10.5194/acp-17-4887-2017>, 2017.
- Matrosov, S. Y.: Possibilities of cirrus particle sizing from dual-frequency radar measurements, *J. Geophys. Res.*, 98, 20675–20683, <https://doi.org/10.1029/93JD02335>, 1993.
- Matrosov, S. Y.: A dual-wavelength radar method to measure snowfall rate, *J. Appl. Meteorol.*, 37, 1510–1521, [https://doi.org/10.1175/1520-0450\(1998\)037<1510:ADWRMT>2.0.CO;2](https://doi.org/10.1175/1520-0450(1998)037<1510:ADWRMT>2.0.CO;2), 1998.
- Matrosov, S. Y.: Feasibility of using radar differential Doppler velocity and dual-frequency ratio for sizing particles in thick ice clouds, *J. Geophys. Res.*, 116, D17202, <https://doi.org/10.1029/2011JD015857>, 2011.
- Matsuo, T. and Sasyo, Y.: Melting of Snowflakes below Freezing Level in the Atmosphere, *J. Meteorol. Soc. Jpn., Ser. II*, 59, 10–25, [https://doi.org/10.2151/jmsj1965.59.1\\_10](https://doi.org/10.2151/jmsj1965.59.1_10), 1981.
- Mosimann, L.: An improved method for determining the degree of snow crystal riming by vertical Doppler radar, *Atmos. Res.*, 37, 305–323, [https://doi.org/10.1016/0169-8095\(94\)00050-N](https://doi.org/10.1016/0169-8095(94)00050-N), 1995.
- Murphy, A., Ryzhkov, A., Zhang, P., McFarquhar, G., Wu, W., and Stechman, D.: A Polarimetric and Microphysical Analysis of the Stratiform Rain Region of MCSs, in: 38th Conference on Radar Meteorology, Chicago, Illinois, USA, 28 August–1 September 2017.
- Pruppacher, H. R. and Klett, J. D.: *Microphysics of Clouds and Precipitation*, Springer, Dordrecht, 547–567, <https://doi.org/10.1007/978-0-306-48100-0>, 1997.
- Rasmussen, R. and Pruppacher, H. R.: A wind tunnel and theoretical study of the melting behavior of atmospheric ice particles I: A wind tunnel study of frozen drops of radius < 500  $\mu\text{m}$ , [https://doi.org/10.1175/1520-0469\(1982\)039<0152:AWTATS>2.0.CO;2](https://doi.org/10.1175/1520-0469(1982)039<0152:AWTATS>2.0.CO;2), 1982.
- Rosenkranz, P. W.: *Atmospheric Remote Sensing by Microwave Radiometry*, chap. 2, Wiley, New York, 1993.
- Rosenkranz, P. W.: Water vapor microwave continuum absorption: A comparison of measurements and models, *Radio Sci.*, 33, 919–928, <https://doi.org/10.1029/98RS01182>, 1998.
- Rosenkranz, P. W.: Correction [to “Water vapor microwave continuum absorption: A comparison of measurements and models” by Philip W. Rosenkranz], *Radio Sci.*, 34, 1025–1025, <https://doi.org/10.1029/1999RS900020>, 1999.



- Ryzhkov, A., Zhang, P., Reeves, H., Kumjian, M., Tschallener, T., Trömel, S., and Simmer, C.: Quasi-vertical profiles—A new way to look at polarimetric radar data, *J. Atmos. Ocean. Tech.*, 33, 551–562, <https://doi.org/10.1175/JTECH-D-15-0020.1>, 2016.
- Simmer, C., Thiele-Eich, I., Masbou, M., Amelung, W., Bogena, H., Crewell, S., Diekkrüger, B., Ewert, F., Hendricks Franssen, H.-J., Huisman, J. A., Kemna, A., Klitzsch, N., Kollet, S., Langensiepen, M., Löhnert, U., Rahman, A. S. M. M., Rascher, U., Schneider, K., Schween, J., Shao, Y., Shrestha, P., Stiebler, M., Sulis, M., Vanderborcht, J., Vereecken, H., van der Kruk, J., Waldhoff, G., and Zerenner, T.: Monitoring and Modeling the Terrestrial System from Pores to Catchments: The Transregional Collaborative Research Center on Patterns in the Soil–Vegetation–Atmosphere System, *B. Am. Meteorol. Soc.*, 96, 1765–1787, <https://doi.org/10.1175/BAMS-D-13-00134.1>, 2015.
- Stein, T. H., Westbrook, C. D., and Nicol, J. C.: Fractal geometry of aggregate snowflakes revealed by triple-wavelength radar measurements, *Geophys. Res. Lett.*, 42, 176–183, <https://doi.org/10.1002/2014GL062170>, 2015.
- Takahashi, T.: Influence of Liquid Water Content and Temperature on the Form and Growth of Branched Planar Snow Crystals in a Cloud, *J. Atmos. Sci.*, 71, 4127–4142, <https://doi.org/10.1175/JAS-D-14-0043.1>, 2014.
- Thurai, M., Huang, G. J., Bringi, V. N., Randeu, W. L., and Schönhuber, M.: Drop Shapes, Model Comparisons, and Calculations of Polarimetric Radar Parameters in Rain, *J. Atmos. Ocean. Tech.*, 24, 1019–1032, <https://doi.org/10.1175/JTECH2051.1>, 2007.
- Tridon, F., Battaglia, A., Luke, E., and Kollias, P.: Rain retrieval from dual-frequency radar Doppler spectra: validation and potential for a midlatitude precipitating case-study, *Q. J. Roy. Meteor. Soc.*, 143, 1364–1380, <https://doi.org/10.1002/qj.3010>, 2017.
- Trömel, S., Ryzhkov, A. V., Zhang, P., and Simmer, C.: Investigations of backscatter differential phase in the melting layer, *J. Appl. Meteorol. Clim.*, 53, 2344–2359, <https://doi.org/10.1175/JAMC-D-14-0050.1>, 2014.
- Trömel, S., Ryzhkov, A., Hickman, B., Mühlbauer, K., and Simmer, C.: Climatology of the vertical profiles of polarimetric radar variables at X band in stratiform clouds, *J. Appl. Meteorol. Clim.*, submitted, 2019.
- Tyynelä, J. and Chandrasekar, V.: Characterizing falling snow using multifrequency dual-polarization measurements, *J. Geophys. Res.–Atmos.*, 119, 8268–8283, <https://doi.org/10.1002/2013JD021369>, 2014.
- Xie, X., Evaristo, R., Simmer, C., Handwerker, J., and Trömel, S.: Precipitation and microphysical processes observed by three polarimetric X-band radars and ground-based instrumentation during HOPE, *Atmos. Chem. Phys.*, 16, 7105–7116, <https://doi.org/10.5194/acp-16-7105-2016>, 2016.
- Yamashtta, T., Asano, A., and Ohno, T.: Comparison of Ice Crystals Grown from Vapour in Varying Conditions, *Ann. Glaciol.*, 6, 242–245, <https://doi.org/10.3189/1985AoG6-1-242-245>, 1985.
- Yin, M., Liu, G., Honeyager, R., and Joseph Turk, F.: Observed differences of triple-frequency radar signatures between snowflakes in stratiform and convective clouds, *J. Quant. Spectrosc. Ra.*, 193, 13–20, <https://doi.org/10.1016/J.JQSRT.2017.02.017>, 2017.
- Yuter, S. E. and Houze, R. A.: Three-Dimensional Kinematic and Microphysical Evolution of Florida Cumulonimbus. Part II: Frequency Distributions of Vertical Velocity, Reflectivity, and Differential Reflectivity, *Mon. Weather Rev.*, 123, 1941–1963, [https://doi.org/10.1175/1520-0493\(1995\)123<1941:TDKAME>2.0.CO;2](https://doi.org/10.1175/1520-0493(1995)123<1941:TDKAME>2.0.CO;2), 1995.
- Zacharias, S., Bogena, H., Samaniego, L., Mauder, M., Fuß, R., Pütz, T., Frenzel, M., Schwank, M., Baessler, C., Butterbach-Bahl, K., Bens, O., Borg, E., Brauer, A., Dietrich, P., Hajnsek, I., Helle, G., Kiese, R., Kunstmann, H., Klotz, S., Munch, J. C., Papen, H., Priesack, E., Schmid, H. P., Steinbrecher, R., Rosenbaum, U., Teutsch, G., and Vereecken, H.: A Network of Terrestrial Environmental Observatories in Germany, *Vadose Zone J.*, 10, 955, <https://doi.org/10.2136/vzj2010.0139>, 2011.
- Zrníc, D. S., Raghavan, R., and Chandrasekar, V.: Observations of Copolar Correlation Coefficient through a Bright Band at Vertical Incidence, *J. Appl. Meteorol.*, 33, 45–52, [https://doi.org/10.1175/1520-0450\(1994\)033<0045:OOCCT>2.0.CO;2](https://doi.org/10.1175/1520-0450(1994)033<0045:OOCCT>2.0.CO;2), 1994.

### 3.2 TRIPEX-POL CAMPAIGN

As a follow-on campaign of the TRIPEX campaign (Section 3.1), the TRIPEX-Pol took place at JOYCE-CF from November 11<sup>th</sup>, 2018 to February 21<sup>st</sup>, 2019, thanks to the collaboration between the University of Cologne (Germany) and the Research Centre Jülich (Germany). TRIPEX-Pol was intended to be an improved campaign where the knowledge learned from the previous campaign was applied. For example, one of the essential improvement of this campaign was the permanent installation of an X-Band radar with much higher sensitivity when compared with X-Band used during TRIPEX. As a result of the PROM-IMPRINT project, the Radiometer Physics GmbH (RPG, Germany) temporarily installed a prototype polarimetric W-Band. Due to additional collaboration with the University of Granada (Spain) it was possible to install another W-Band radar temporarily. In total, four cloud radars operated on top of the JOYCE-CF platform (one X-, one Ka-, and two W-Band). The X-, Ka-, and one W-Band operated vertically pointing continuously, while the polarimetric W-Band operated with elevation different than 90° (non-vertically pointed) and performed different scan patterns. Figure 3.1 depicts the layout of the radars during the TRIPEX-Pol. Additionally, Figure 3.2 shows a picture of the JOYCE-CF platform equipped with four radars and the auxiliary sensors operated during TRIPEX-Pol.

*PROM-IMPRINT:  
Understanding Ice  
Microphysical  
Processes by  
combining  
multi-frequency and  
spectral Radar  
polarimetry and  
super-particle  
modelling*

Several improvements were made based on the knowledge gained from the TRIPEX campaign. The pointing accuracy of the Ka-Band radar was carefully verified, and a relative comparison between the pointing of the X- and W-Band (vertically pointing one) using the Ka-Band as reference was also performed. In order to reduce the cumulative displacement of the centre of each range bin among the vertically pointing radars, an effect observed during TRIPEX campaign, the vertical range resolution from each radar was carefully adjusted.

#### 3.2.1 Cloud Radars

JOYRAD-10, hereafter referred to as the X-Band, is a 9 GHz pulsed vertically pointing non-polarimetric Doppler radar (type MIRA 10) that uses a solid state amplifier manufactured by Metek (Meteorologische Messtechnik GmbH), Germany. Metek developed this radar to retrieve high-quality Doppler spectra of hydrometeors aloft, and to provide high-quality spectral moments such as reflectivity factor ( $Z_e$ ), mean Doppler velocity (MDV) and Doppler spectral width (SW). Since October 2018, X-Band became a permanent installation of the JOYCE-CF. During TRIPEX-Pol, X-Band operated continuously. Table 3.1 gives an overview of the technical characteristics and settings of the X-Band used during the campaign.

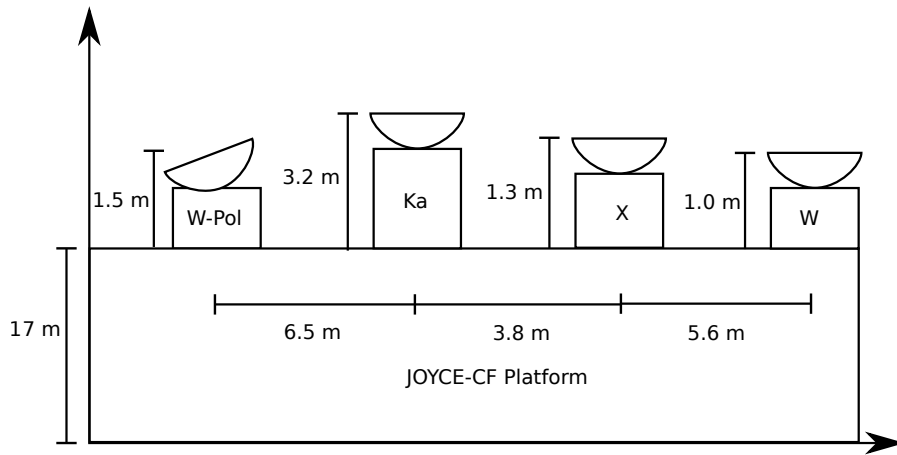


Figure 3.1: Sketch (not to scale) of the horizontal separation between the radars and their height. The height of JOYCE-CF platform is also indicated. This platform is 111 m above mean sea level.

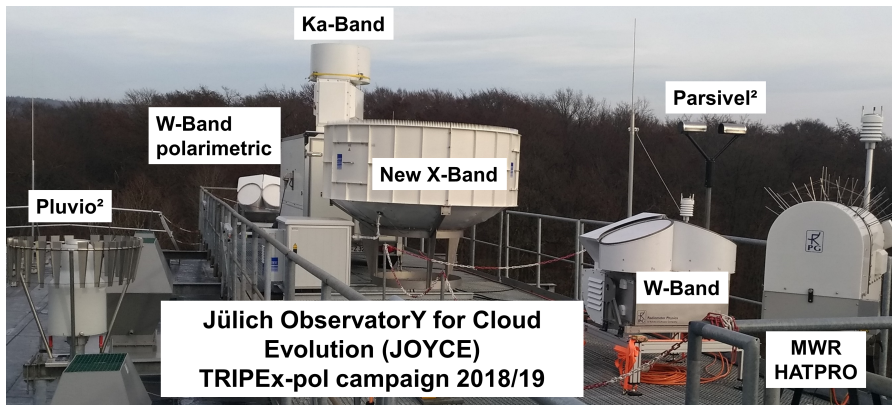


Figure 3.2: Picture of the JOYCE-CF platform. The labels indicate the position from each radar and from the auxiliary sensors operated during the campaign.

JOYRAD-35 is the same radar used during the TRIPEX campaign. Section 2.2 from Dias Neto et al., (2019) gives a detailed description of the Ka-Band and the configuration settings used during that campaign. The configuration settings used during TRIPEX-Pol (listed in Table 3.1) differ from those used in the previous campaign; the new settings were planned to provide a better agreement with the observed volume and temporal sampling from the X- and W-Band. In Table 3.1, one can see that the X-Band has much higher Nyquist velocity (78 m/s) compared to the Ka- and W-Band and in order to obtain similar Doppler resolution the number of velocity bin is also much higher (4096).

GRARAD-94, hereafter referred to as the W-Band, is a 94 GHz frequency-modulated continuous-wave (FMCW) Doppler radar manufactured by Radiometer Physics GmbH (RPG, Germany) (Küchler et al., 2017). This radar transmits a single polarized signal and receives the co- and cross-polarized signal providing the possibility to retrieve the linear depolarization ratio (LDR) besides the other radar moments ( $Z_e$ , MDV, SW). An additional characteristic of the radar is the possibility of defining different range resolution for different range intervals. W-Band integrates the observational site of the University of Granada (Spain). This radar was temporarily mounted on JOYCE-CF site and continuously operated from November 31<sup>st</sup>, 2018 to February 20<sup>th</sup>, 2019. Table 3.1 gives additional information about the technical specifications used during the campaign, and the Table 3.2 lists the configuration parameters of each chirp sequence. The chirp settings used during TRIPEX-Pol differ from that used during TRIPEX (Table 2 in Section 3.1); the settings used during TRIPEX-Pol were adjusted to match as close as possible the temporal resolution, the centre of each range bin, and Doppler resolution from the other vertically pointing radar.

RPGRADPol-94, hereafter referred to as the W-Pol, is a 94 GHz frequency-modulated continuous-wave (FMCW) polarimetric Doppler radar also manufactured by Radiometer Physics GmbH (RPG), Germany. As the GRARAD-94 the W-Pol also allows defining different range resolution for different range intervals. During TRIPEX-Pol, W-Pol periodically performed three scans patterns, which are range height indicator (RHI, azimuth: 235.11°, elevation: 30 - 85°), plan position indicator (PPI, azimuth: 0 - 354°, elevation: 85.02°) and constant elevation (CEL, azimuth: 235.11°, elevation: 30.02°).

Looking at Figure 3.1 and Figure 3.2, one can see that W-Band and W-Pol radars were mounted close to each other, which arose an issue for the operation of both radars during the experimental campaign. If both radars were operated using the same frequency the signal transmitted by one radar would produce interferences in the signal received by the other radar. In order to avoid interferences, the operating frequency from the W-Band was adjusted to 94.11960

GHz while the W-Pol was operated at the standard frequency for RPG radars that is 93.99969 GHz.

Table 3.1: Technical specifications and settings of the three vertically pointing radars operated during TRIPEX-Pol at JOYCE-CF.

Specifications	X Band	Ka Band	W Band
Frequency [GHz]	9.4	35.5	94.0
Pulse Repetition [kHz]	10	5	2.2-12.8
Doppler velocity bins	4096	512	128-512
Number of Spectral Average	10	19	11-13
3dB Beam Width [°]	1.0	0.6	0.5
Sensitivity at 5 km [dBZ] <sup>a</sup>	-28	-43.5	-40
Nyquist Velocity [ $\pm \text{ms}^{-1}$ ]	78	10.5	1.8-10.2
Range Resolution [m]	36	36	12-36
Temporal Sampling [s]	2	2	3
Lowest clutter-free range [m]	300	400	300
Radome	No	No	Yes

<sup>a</sup> Minimum sensitivities have been derived from the reflectivity histograms shown in [Figure 3.3](#).

<sup>b</sup> Pulse repetition frequency, number of spectral average, Nyquist velocity and range resolution depend on the chirp definition; those values are indicated in [Table 3.2](#).

Table 3.2: Configuration parameters of the chirp sequence of the W-Band (vertically pointing) during the TRIPEX-Pol.

Attributes	Chirp sequence			
	1	2	3	4
Integration Time [s]	0.818	0.595	0.686	0.503
Range Interval [m]	216 – 1482	1482 – 3999	3999 – 8164	8164 – 11997
Range Resolution [m]	36	12.7	12.7	12.7
Nyquist Velocity [ $\pm \text{ms}^{-1}$ ]	10.2	6.8	3.4	1.8
Doppler velocity bins	512	512	256	128
Number of Spectral Average	13	13	15	11
Chirp Repetition Frequency [kHz]	12.8	8.6	4.2	2.2

### 3.2.2 Auxiliary instruments

The JOYCE-CF is equipped with six other ground-based remote sensing instruments and several other auxiliary instruments as described by Löhnert et al., (2015). These instruments continuously operated

during the campaign producing additional information of the atmospheric state, which can be used in combination with observations from the multi-frequency radars.

One of the instruments is the laser disdrometer PARSIVEL (Löffler-Mang and Joss, 2000) manufactured by OTT Hydromet (Germany). Unlike during TRIPEX, the PARSIVEL continuously recorded the drop size distribution of the rainfall events, and it allowed to independently verify the calibration of the radar reflectivities using rainfall events as described in section 3 from Dias Neto et al., (2019). Another auxiliary instrument used in the processing of the TRIPEX-Pol data is the Microwave Radiometer (Humidity and Temperature PROfiler, HATPRO) manufactured by RPG (Rose et al., 2005). The HATPRO continuously retrieved liquid water path (LWP) and integrated water vapour. In particular, the LWP is a variable used during the data quality control to identify periods with large LWP (section 3 from Dias Neto et al., (2019)). In Figure 3.2, one can see how close to the radars PARSIVEL and HATPRO were installed.

In addition to the ground-based measurements, 16 radiosondes DFM-09 manufactured by GRAW Radiosondes GmbH & Co. KG (Germany) were launched to measure the atmospheric state variables (pressure, humidity and temperature). In Section 3.3, the temperature and humidity profiles from Cloudnet are evaluated using the respective profiles measured by the radiosondes.

### 3.2.3 Data processing

The processing of the multi-frequency radar observations from the TRIPEX-Pol follows the procedure developed for processing TRIPEX dataset. Section 3 from Dias Neto et al., (2019) provides a detailed description of the data processing and the generation of the quality flags. Figure 3.3 shows the distribution of Ze measured during the entire TRIPEX-Pol after filtering Ze values from X- and W-Band flagged as errors. Figure 3.3 shows that the Ka-Band is the radar with the highest sensitivity and the largest dynamic range comparing with the X- and W-Band radars. The red curve is the fit of the minimum received power as a function of height, and the fitting equation is the same introduced in section 4.3 from Dias Neto et al., (2019). Table 3.3 lists the retrieved coefficients for each radar.

A direct comparison between the histograms of Ze from both campaigns indicates that the new X-Band radar used during TRIPEX-Pol has much higher sensitivity than the X-Band used during the TRIPEX campaign. (Figure 3.3-a shows that at 7 km the sensitivity and the dynamic range from the new X-Band are  $\approx -24$  dB and 40 dB, while the sensitivity and the dynamic range from the previous X-Band at the same altitude are  $\approx -15$  dB and 20 dB, respectively (Figure 8a from Dias Neto et al., (2019)). Due to higher sensitivity of the new radar, it



was possible to observe clouds up to 10 km during TRIPEX-Pol while the observations from the X-Band during TRIPEX are limited up to 8 km, most of the time (Figure 8 in Dias Neto et al., (2019))

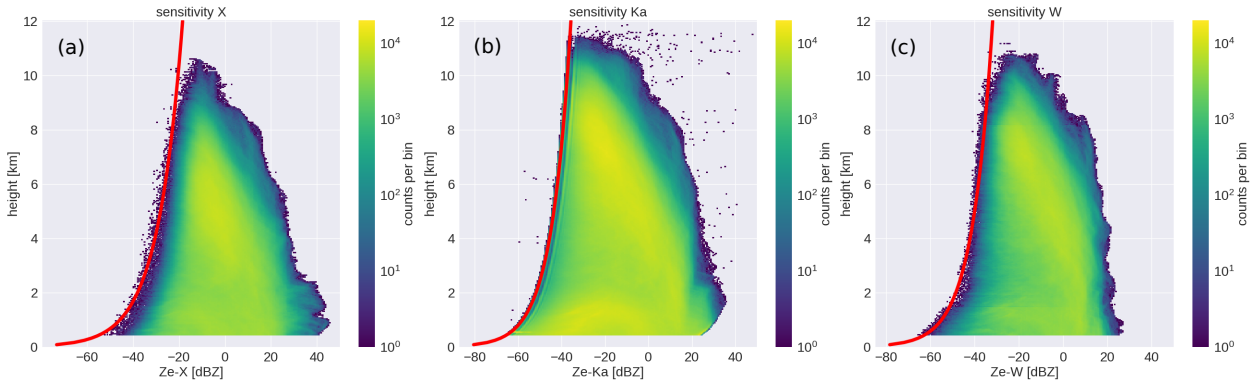


Figure 3.3: Histograms of the Ze from the Level-2 data from the entire TRIPEX-Pol. The red curve is the vertical profile of the minimum measured Ze. Panels a, b and c are the histograms for X-, Ka and W-Band, respectively; all the error flags were applied to filter the data.

Thanks to the continuous operation of the PARSIVEL during TRIPEX-Pol, it was possible to calibrate the Ze from each radar from rain fall events. For the calibration, the Ze lowest usable radar range bins are compared with the Ze derived from the observations from the nearby optical disdrometer (Dias Neto et al., 2019). The result of this calibration revealed that the X-Band has the smallest offset  $-0.1$  dB while the calculate offset from Ka-Band and W-Band were  $-2.8$  and  $2.0$  dB.

Table 3.3: Coefficients  $a$  and  $b$  of the sensitivity equation retrieved for the X-, Ka-, and W-Band using the Level-2 data. All values flagged as error are excluded from the fitting calculation.

Radar	$a$	$b$
X-Band	$7.63 \times 10^{-13}$	2.52
Ka-Band	$1.05 \times 10^{-12}$	2.06
W-Band	$1.22 \times 10^{-12}$	2.13

### 3.2.4 Improved volume matching and pointing

Although the TRIPREX-Pol had similarities with the TRIPEX campaign such as the same observational site, same season, multi-frequency radar observations and other auxiliary observations, two other points differ from the previous campaign.

The first one is the range resolution of the vertically pointing radars. During the TRIPEX, the X-, Ka-, and W-Band radars operated with a vertical resolution of 30, 28.8 and 16-34.1 m, respectively (Table 1

in Dias Neto et al., (2019)). These different resolutions introduced an artificial range mismatch between the volume observed by the different radars, and the magnitude of this mismatch oscillates along the vertical coordinate. Figure 3.4(a-e) illustrates the range mismatch between X- and Ka-Band radars and between Ka- and W-Band radars. Figure 3.4-a shows that the mismatch between X- and Ka-Band is periodically well-defined, while Figure 3.4(b-e) shows that the mismatch between Ka- and W-Band is not periodically well-defined and change for each chirp sequence. During TRIPEX-Pol campaign the vertical range resolution from the X-, Ka- and W-Band radars was defined to minimize the volume mismatch. The X- and Ka-Band radar were operated with a resolution of 36 m. However, due to the characteristic of the W-Band radar controlling software, the definition of the range resolution is not flexible; for this reason, the vertical resolution of the W-Band was set to 36 m for the first chirp sequence and 12.7 m for the second, third and fourth chirp sequences. Figure 3.5(a-e) illustrates the mismatch between X- and Ka-Band radars and between Ka- and W-Band radars during TRIPEX-Pol. One can see in Figure 3.5-a constant mismatch (1.9 m) between X- and Ka-Band, which remains due to the height difference between the antennas from X- and Ka-Band (Figure 3.1). Figure 3.5-b shows that the first chirp sequence from the W-Band radar has a constant mismatch (2.2 m), which is also due to the height difference between Ka- and W-Band antennas (Figure 3.1). Figure 3.5(c-e) shows the mismatch from the second, third and fourth chirp sequences, and one can see that the mismatch remain, but the mismatch periodicity is comparable within those chirps, which was not the case during TRIPEX.

The second one is the verification of the pointing alignment of the radars. During TRIPEX the X-Band radar operated continuously rotating the antenna due to a limitation of the radar software (see section 4.2 from Dias Neto et al., (2019)), which introduced periodic oscillation in the DDV-XKa, limiting the use of this variable without additional post-processing. Although the Ka- and W-Band were operated statically, without rotating the antenna, the DDV-KaW (Figure 3.6) shows a continuous increase of the DDV-KaW from 0 m/s at cloud bottom ( $\approx 2$  km) up to 0.3 m/s at cloud top ( $\approx 10$  km). This continuous increase in DDV-KaW towards cloud top indicates a relative mispointing between Ka- and W-Band radars.

Different from the TRIPEX campaign, the pointing offset between the radars used during TRIPEX-Pol was estimated at the beginning of the campaign. The Sun-tracking method (Muth et al., 2012) was applied to the Ka-Band for evaluating its absolute pointing accuracy; the results indicate that the error is smaller than  $0.1^\circ$  in elevation and azimuth. The zenith pointing of this radar was also verified. The radar was set to perform azimuth scans while the antenna was maintained vertically pointing, and no indication of misalignment



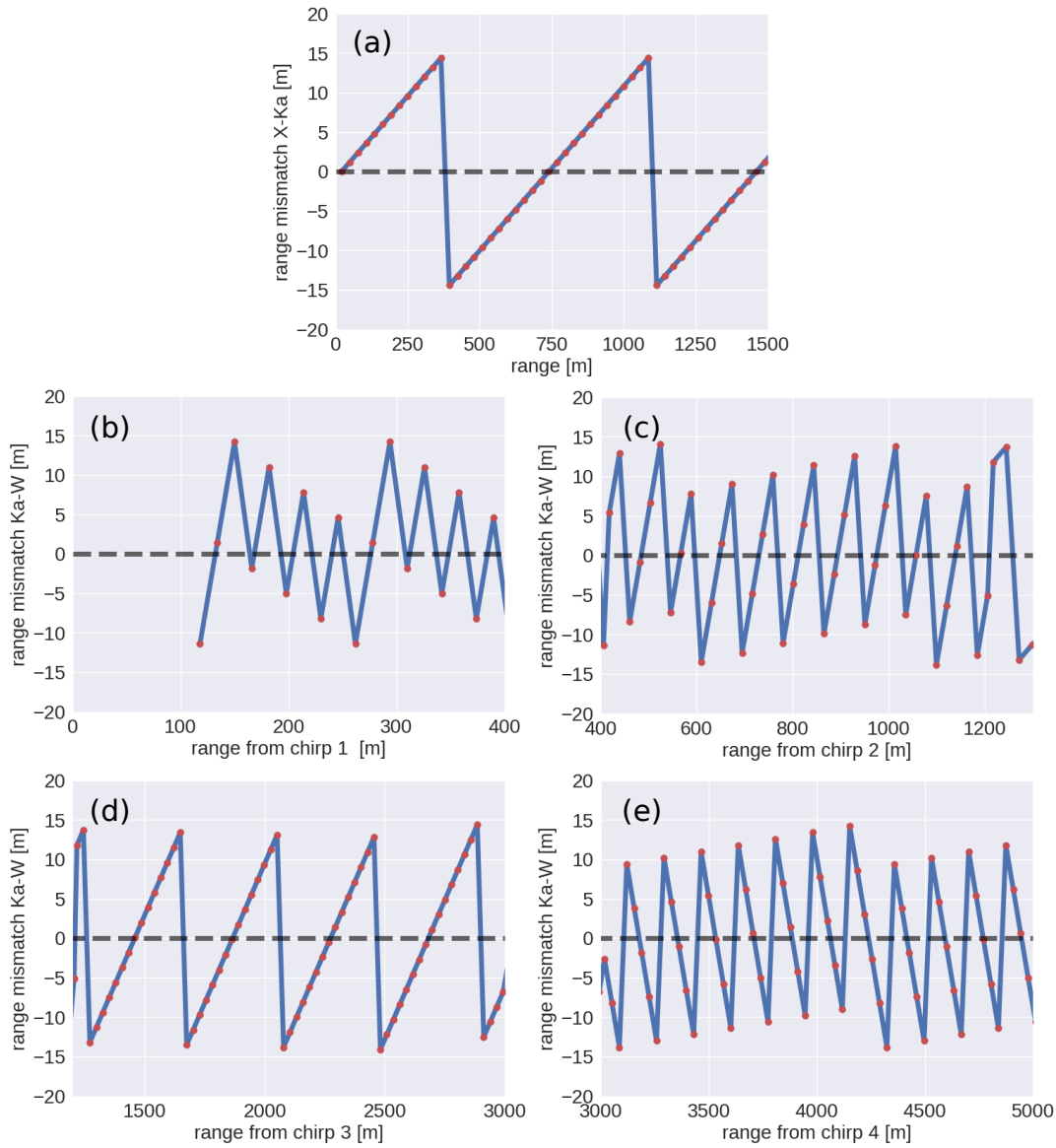


Figure 3.4: Illustration of the vertical mismatch between X- and Ka-Band radars (Panel a) and Ka- and W-Band radars for the different chirp sequence (Panels b-e) during TRIPEX.

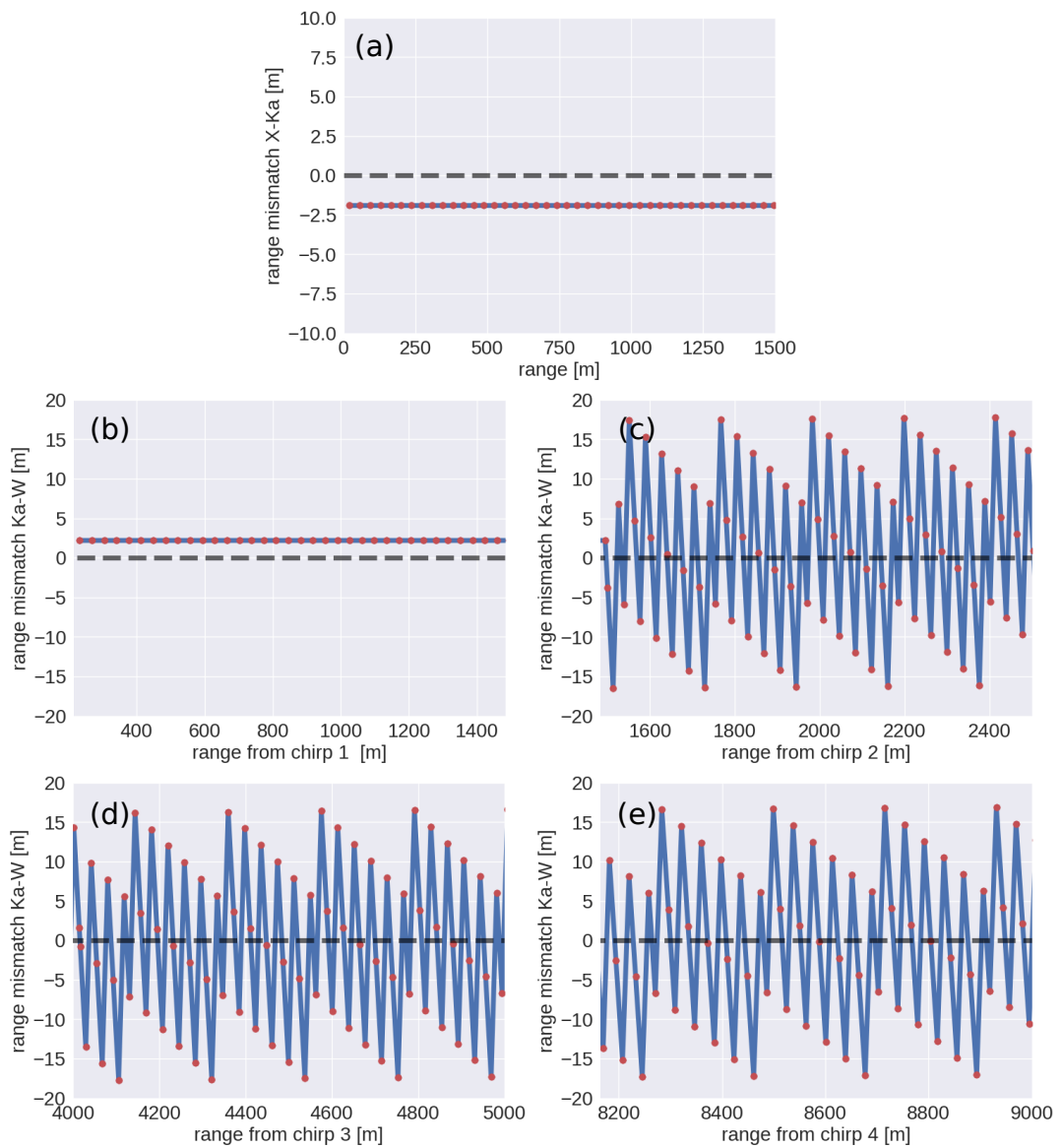


Figure 3.5: As in Figure 3.5, but for TRIPEX-Pol.

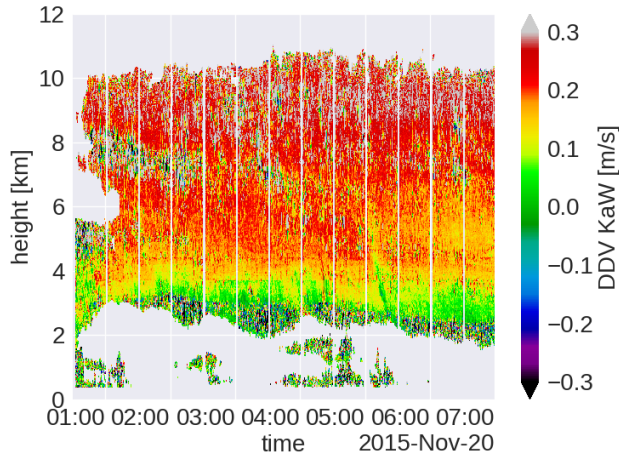


Figure 3.6: Time-height plot of the DDV-KaW from November 20<sup>th</sup>, 2015 (observed during TRIPEX).

was found. A similar approach could not be applied for evaluating the absolute pointing of the X- and W-Band radars; the antenna from these radars are fixed mounted. However, a relative evaluation of the pointing of X- and W-Band using the Ka-Band as reference was possible. The pointing of the X- and W-Band was compared to the Ka-Band in different conditions of wind speed and direction using a similar method applied by Kneifel et al., (2016). The results of this comparison indicate that the misalignment in elevation between the X-, Ka- and W-Band is  $\approx 0.1^\circ$ . Those results are supported by the DDV plots in Figure 3.7(a-b) which show that the DDV-XKa and DDV-KaW are mainly distributed around 0 m/s from the bottom of the cloud to the uppermost regions.

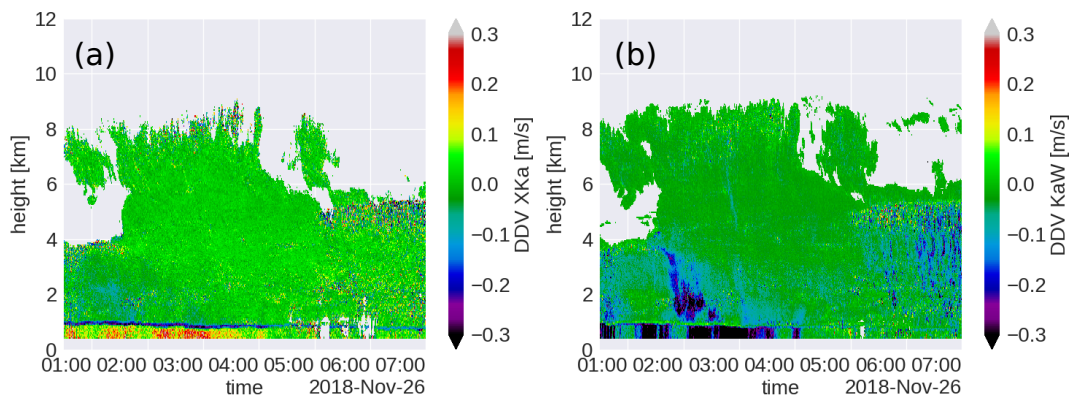


Figure 3.7: Time-height plot of the DDV-XKa (a) and DDV-KaW (b) from November 26<sup>th</sup>, 2018 (TRIPEX-Pol).

The excellent alignment between the three radars combined with the data processing developed for TRIPEX campaign allowed to use the triple-frequency MDV observation to develop a triple-frequency based retrieval (TDV-Method) of the mean mass-weighted equivolume

diameter ( $D_m$ ) of raindrops (Mróz et al., 2020b). The authors also showed that the TDV-Method reduced the bias of  $D_m=2.25$  mm by 15% (20%) when compared with retrieval based on DDV-XW (DDV-KaW)(Liao et al., 2008; Matrosov, 2017; Tian et al., 2007).

### 3.3 EVALUATING TEMPERATURE AND RELATIVE HUMIDITY FROM CLOUDNET

As described in chapter [Chapter 2](#), the development and evolution of the microphysical processes in clouds are closely related to temperature. Therefore, in this thesis, the temperature is often used as vertical coordinate. In total, 27 radiosonde ascents are available, combining the radiosondes from TRIPEX and TRIPEX-Pol. However, this number of radiosonde ascents is not enough to convert the range coordinate from radar profiles from the combined TRIPEX/TRIPEX-Pol dataset into temperature coordinate. Therefore, the temperature profiles from Cloudnet are used for the range-temperature transformation. The temperature and the other atmospheric state variables implemented in Cloudnet are from the European Centre for Medium-Range Weather Forecasts Integrated Forecast System (ECMWF-IFS). This model has a horizontal grid resolution of  $\approx 10$  km and 137 vertical levels. Illingworth et al., (2007) provides a detailed description of the Cloudnet products.

In order to compare the temperature (T-CDN) and the relative humidity over water (RHw-CDN), both from Cloudnet, with the corresponding radiosonde measurements (T-RAD) and (RHw-RAD), the Cloudnet profiles are averaged over two minutes time window centred at the radiosonde launching time. Additionally, the radiosonde profiles are interpolated to the Cloudnet vertical grid, and the measurements from above 8 km are excluded from the comparison. It was noted that for regions above 8 km the RH values reported by the radiosonde were unrealistic; the profiles showed an abrupt change from values close to 100% to 0% suggesting a malfunction of the RH sensor in regions above 8 km. The data laying outside of a radius of 5 km far from JOYCE-CF are excluded as well; it ensures that the radiosonde measurements lay inside of the ECMWF-IFS grid cell which JOYCE-CF is within.

The scatterplot of the T-CDN and the T-RAD ([Figure 3.8-a](#)) shows that the filtered data is mainly distributed between  $-20$  and  $20$  °C; it also suggests a good agreement between both quantities, which is confirmed by the statistical metrics. The bias indicates that the mean difference between the data from Cloudnet and measured by the radiosonde is  $\approx 0.2$  °C. The precision indicates that the standard deviation of the difference between T-CDN and T-RAD is  $\approx 1.1$  °C. The uncertainty shows that the root mean square difference (T-CDN - T-RAD) is  $\approx 1.1$  °C. The calculated correlation between T-CDN and

T-RAD is ( $\approx 0.9$ ). The error distribution over the temperature range observed by the radiosonde (Figure 3.8-b) shows that it is distributed around 0 °C for temperatures between  $-20$  and  $20$  °C and it slightly increases for temperatures colder than  $-20$  °C (indicated by the orange curve). The corresponding uncertainty is mainly distributed around  $\approx 1$  °C for temperatures between  $-20$  and  $20$  °C, and it also increases for temperatures colder than  $-20$  °C (Figure 3.8-b cyano curve). The poor statistical results for temperatures colder  $-20$  °C is related to the small amount of data available at this temperature region.

A similar analysis was applied to the relative humidity RHw. Figure 3.8-c shows that the measurements are mainly distributed between 60 and 100%. The entire population has a small bias ( $\approx 1.1\%$ ), a good correlation ( $\approx 0.7$ ), uncertainty of  $\approx 9.2\%$  and precision of  $\approx 9.2\%$ . Figure 3.8-d shows a detailed analysis of the error over the RHw-RAD range. The uncertainty and the bias vary around 9% (cyano curve) and 0% (orange curve), respectively.

As introduced in chapter Chapter 2, the relative humidity over ice (RHi) is an important variable related to the growth of ice crystals. In order to evaluate RHi, it is calculated using Equation 3.1 where  $e_{sw}(T)$  and  $e_{si}(T)$  are the saturation vapour pressure over water and ice, respectively. T and RHw are the profiles of temperature and relative humidity over water.  $e_{sw}(T)$  and  $e_{si}(T)$  are calculated following Marti and Mauersberger, (1993) and Murphy and Koop, (2005).

$$\text{RHi} = \frac{e_{sw}(T)\text{RHw}}{e_{si}(T)} 100 \quad (3.1)$$

Figure 3.8-e shows the distribution of the RHi values between 60% and 100%. As expected, the statistic metrics are similar to the that from RHw; the uncertainty is  $\approx 9.8\%$ , the bias is 0.96%, the correlation is  $\approx 0.68$ , and the precision is  $\approx 9.7$ . Figure 3.8-f shows the bias distributed around 0%, and the uncertainty is distributed around  $\approx 9\%$ .

Overall, the statistical results suggest that the atmospheric profiles from Cloudnet products are comparable to the profiles measured by the radiosondes and allow using those profiles for data corrections and long term statistics. Table 3.4 summarizes the statistical results.

### 3.4 DOPPLER SPECTRA PROCESSING

In addition to the standard radar moments derived from the spectra (e.g. Ze, MDV, SW), this work uses two other sets of variables derived from the spectra. The information contained in the first set is the classification of the spectra as mono- or multi-mode, the maximum spectral power and the Doppler velocity of each mode. The second set contains the Doppler velocity retrieved from the spectra edges. In this thesis, these two sets of variables are from the Ka-Band spectra only;

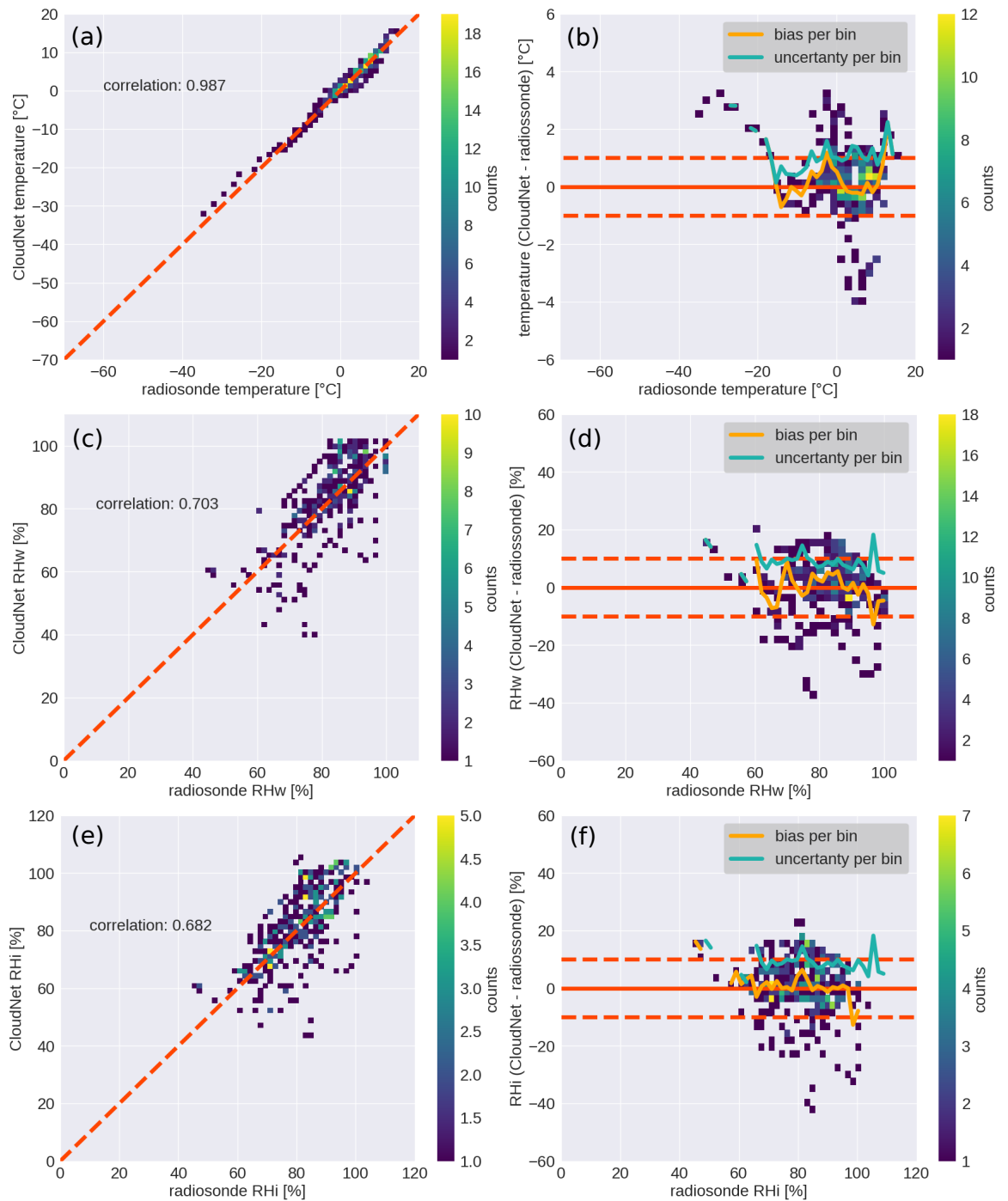


Figure 3.8: Panels a, c, and e are two dimensional histograms of T, RHw and RHl from Cloudnet products versus the corresponding radiosonde measurements. Panels b, d and f are two dimensional histograms of error of the T, RHw and RHl from Cloudnet over the range of values measured by the radiosonde.

Table 3.4: Statistics of the comparison between the T, RHw, and RHi data from Cloudnet products and the corresponding data measured by the radiosonde.

Metrics	T [°C]	RHw [%]	RHi [%]
Precision	1.14	9.26	9.76
Uncertainty	1.16	9.27	9.80
Bias	0.20	1.17	0.96
Correlation	0.98	0.70	0.68

it is because the Ka-Band is the most sensitive radar (see [Section 3.2](#)) and its spectra dataset is available for TRIPEX and TRIPEX-Pol. The following sections describe the retrieval of those additional variables.

### 3.4.1 Spectra classification

There are several approaches currently available for identifying the Doppler spectral modes. One approach is using a polynomial fitting of the Doppler spectra to identify the modes (Kollias et al., 1999, 2003). Another approach is using machine learning to identify the spectral modes (Kalesse et al., 2019); the authors also show that their approach produces similar results to the polynomial fitting. In this thesis, The identification of the spectra modes and their classification as mono- or multi-peak uses the polynomial fitting approach and is performed in three steps.

At the first step, the observed Ka-Band spectra in linear units [ $\text{mm}^6/\text{m}^3$ ] ( $S_O$ ) are normalized by the size of the velocity bin producing spectra with the following units [ $(\text{mm}^6/\text{m}^3)/(\text{m/s})$ ]. This units transformation is applied to interpolate  $S_O$  to smaller velocity bin 0.01 m/s ( $S_{IN}$ ). At this point, the  $S_{IN}$  are still affected by noise, and a moving averaging window of 0.07 m/s is applied over the velocity dimension to reduce it, producing smooth spectra ( $S_{IS}$ ). [Figure 3.10-a](#) shows an example of this first step applied to a bi-modal spectrum from January 22<sup>nd</sup>, 2019, at 15 : 07, from an altitude of  $\approx 3$  km. One can see that the  $S_{IS}$  (orange curve) is similar to the  $S_O$  (green curve).

At the second step, a polynomial function of degree 4 is used to fit the spectrum of each range bin. Then, the fall velocity of each local maximum spectral power is retrieved from the fitted polynomial function, but the power from local maxima is retrieved from the  $S_{IS}$ . This approach minimizes the error that could be introduced using the maxima estimated by the polynomial fit and ensures that the stored maxima are as close as possible to the observed values. Once the velocity-power pairs are retrieved, they are sorted by their velocities. These sorted pairs are then classified according to their spectral power. [Figure 3.9](#) illustrates the methodology developed to



classify the velocity-power pairs, which assign ordering indexes to each peak. As the first step of this identification, an index equal to 0 is assigned to the velocity-power pair with maximum power to identify the main peak (Peak-0). Then, increasing positive indexes are assigned to sorted pairs that have fall velocities slower than the velocity of the Peak-0. Finally, decreasing negative indexes are assigned to sorted pairs that have fall velocities faster than the velocity of the Peak-0. This approach is idealized to allow easy identification of peaks faster than Peak-0 that could be produced by rimed particles and peaks slower than Peak-0 that could be produced by new nucleated particles, secondary ice, and supercooled water.

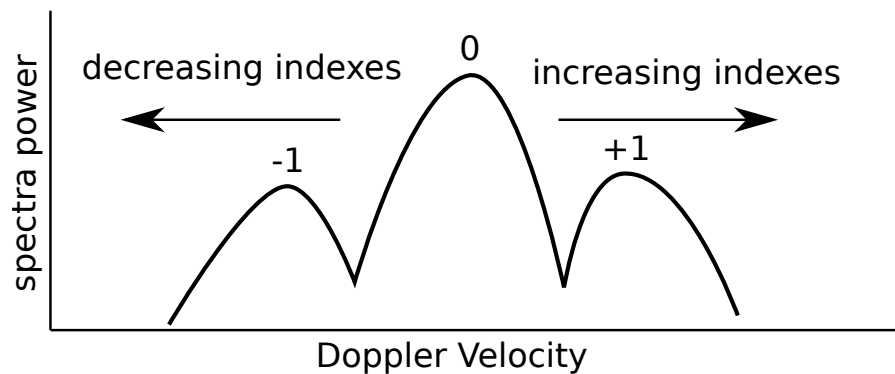


Figure 3.9: Conceptual illustration of the Doppler spectra classification. The numbers on top of each mode are the ordering indexes.

Figure 3.10-a shows an example of the retrieved velocity-power pairs for each local maxima (peaks) and their respective ordering indexes. Figure 3.10-b shows a bi-modal  $S_O$  from January 22<sup>nd</sup>, 2019, at 15 : 07 and the retrieved fall velocity from each peak. The fall velocity from Peak-0 increases from 0 m/s at cloud top to  $\approx 1$  m/s at 2 km, and it remains  $\approx 1$  m/s towards the surface. The Peak-1 appears at  $\approx 3.5$  km with fall velocity  $\approx 0.3$  m/s; its velocity slowly increases down to an altitude of  $\approx 3$  km where the two modes merge.

The last step in the spectra classification is to create a time-height map of the number of the identified peaks (hereafter Peak-Map). This map is created counting all the velocity-power pairs, identified in the previous step, from a given time and height. Figure 3.11 is an example of this map. One can see that, in this case, most of the multi-peaks are distributed in the first 4 km.

The base of the spectra classification is a polynomial fit. Therefore, it is important to mention that there is a scenario where this classification would fail. It happens, for example, when there is no well-defined separation between two spectral peaks. In this case, the polynomial fit would identify one peak. Consequently, the number of retrieved peaks would be smaller than the observed. This scenario is often found where the different modes are merging. Figure 3.10-b shows



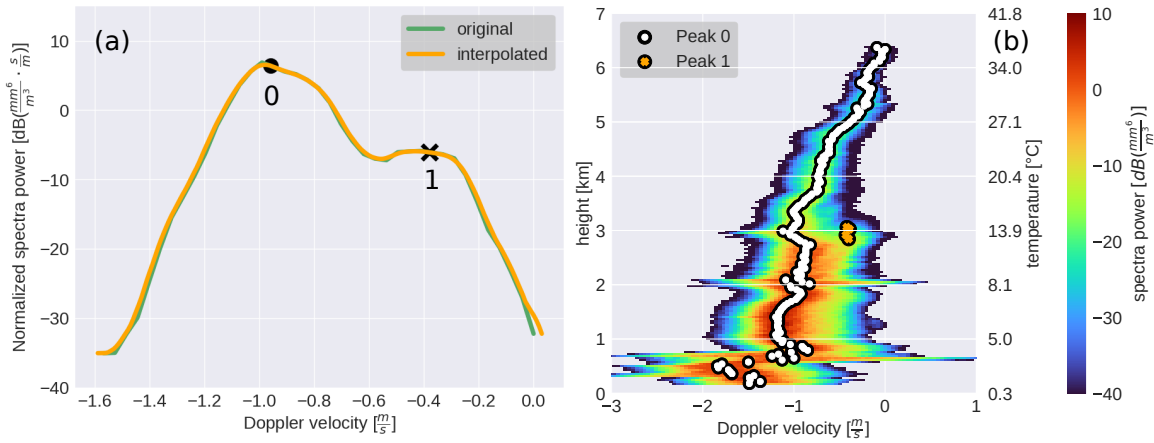


Figure 3.10: Panel a is a bi-modal spectrum from January 22<sup>nd</sup>, 2019, at 15 : 07, from an altitude of  $\approx 3$  km. The measured and the interpolated spectrum are indicated by the green and orange curve, respectively. The dots indicate the retrieved velocity-power pairs for the Peak-0 and Peak-1. Panel b is the spectra from the same day and same time. The circles and crosses indicate Peak-0 and Peak-1, respectively.

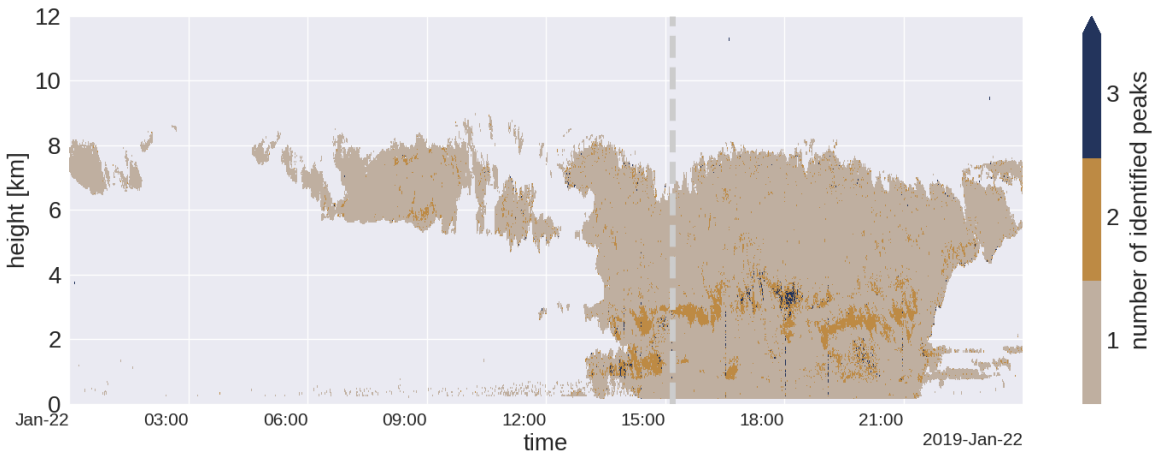


Figure 3.11: Time-height map of the number of identified peaks from January 22<sup>nd</sup>, 2019. The vertical gray dashed line indicates the time of the spectra from [Figure 3.10](#).

an example of this scenario at  $\approx 3$  km; at this height, the two modes merge, and the retrieved velocity of the Peak-1 is not available.

### 3.4.2 Detection of the spectra edges

Several studies showed that exists a relationship between the particle size and its fall velocity (Heymsfield and Westbrook, 2010; Karrer et al., 2020; Mitchell, 1996). However, MDV is weighted by the entire distributions of particles and does not indicate the maximum and minimum fall velocities from the distribution. Here, the spectra edges are introduced as a source of information of the maximum and minimum fall velocities. The spectra edge profiles could provide additional information about the size growth of the particles. These profiles could also provide information about upward motion in case both edges are affected by a slowdown.

The detection of the spectra edges starts by removing the values dominated by noise and preserving the values from the back-scattered signal. The internal processing of the Ka-Band calculates the mean noise level of each spectrum using the method developed by Hildebrand and Sekhon, (1974). For filtering out the noise, a threshold of 3 dB plus the mean noise level is applied and removes all values smaller than the threshold from the spectrum at each height. If some of the noise peaks are higher than the threshold, they are not removed. In this case, the spectra edges would be affected by sharp random broadening. Since the spectra are free of noise, vertical profiles of the spectra edges are retrieved from the faster and slower fall velocities of each spectrum over the height dimension. Figure 3.12 shows an example of an original Ka-Band spectrum from January 22<sup>nd</sup>, 2019 and its retrieved edges. One can see that the edge profiles follow the shape of the spectra very well.

An additional application of the spectra edges is the removal of the spurious signal present in the spectra from the W-Band used during the TRIPEX-Pol. As mentioned in Section 3.2, the operating frequency from the W-Band had to be slightly altered. The chirp generator from both RPG radars is optimized for 94 GHz output frequency. If the output frequency is set to a different value, the output signal from the chirp generator has a slight amplitude modulation. From signal processing theory, it is known that any amplitude-modulated radio-signal has one carrier frequency( $f$ ) and two other components that are symmetrically offset from the carrier ( $f \pm \Omega$ ). In case of a chirp, the amplitude modulation leads to secondary chirps with an instantaneous frequency offset in the order of few MHz (Figure 3.13). When the main chirp is scattered from too close or too distant targets the frequency difference between the transmitted and received signals is out of the frequency range of the band-pass filter in the radar receiver (black dashed line in Figure 3.13). On the other hand, the signals received

*chirp generator:  
printed-circuit-  
board with a direct  
digital synthesizer  
specially-designed  
for generating the  
radar signals*

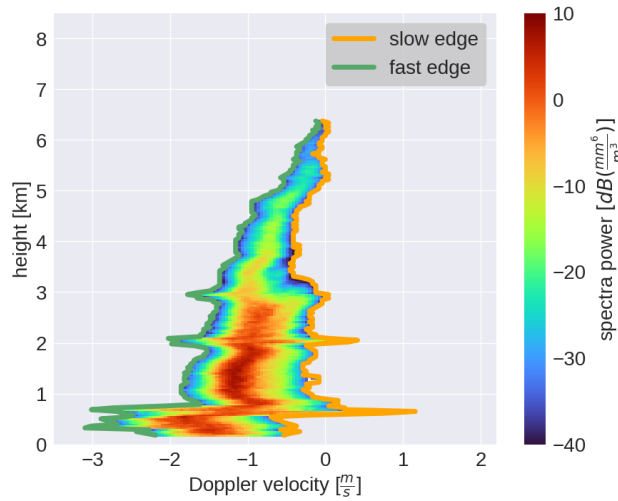


Figure 3.12: Observed Ka-Band spectra from the same time as Figure 3.10. The green and orange curves are the retrieved fast slow edges, respectively.

from the secondary chirps may produce frequency differences within the band-pass range (green dashed line Figure 3.13). In this case the signal from the secondary chirp is erroneously detected.

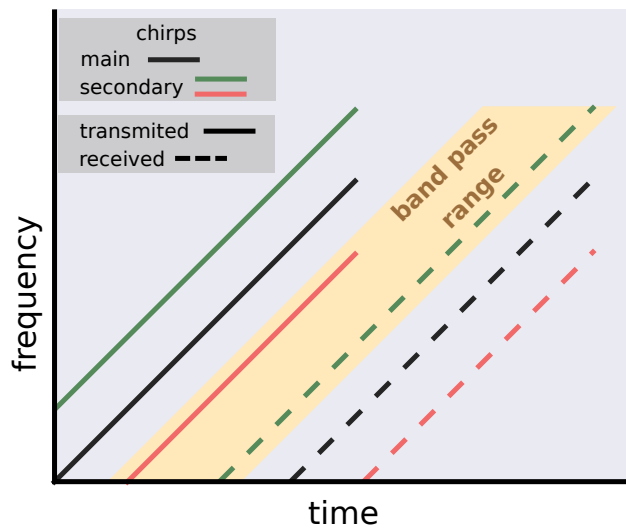


Figure 3.13: Illustration of the main (black) and secondary (green and red) transmitted (continuous) and received chirps (dashed) of a distant target; the yellow region indicates the frequency range of the band-pass filter.

Figure 3.14 shows an example of W-Band spectra observed at the same time as Figure 3.10 and the edges from the Ka-Band spectra as overlapping lines. Figure 3.14 also shows that there are three regions where the W-Band spectra are outside of the Ka-Band spectra edges; one region is at  $\approx 1$  km, and the other two are at  $\approx 3.2$  km and  $\approx 6.5$  km. This figure also shows that using the edges from the Ka-

Band spectra, it is possible to remove most of the spurious signal. However, in case the spurious signal is inside of the retrieved edges, it cannot be removed. Figure 3.15-a shows a time-height plot of the Ze-W of stratiform cloud from January 22<sup>nd</sup>, 2019. The effect of the spurious signal is visible at the same altitudes as showed in Figure 3.14. After applying the edge removal method, the Ze-W has a significant reduction of the spurious signal (Figure 3.15-b).

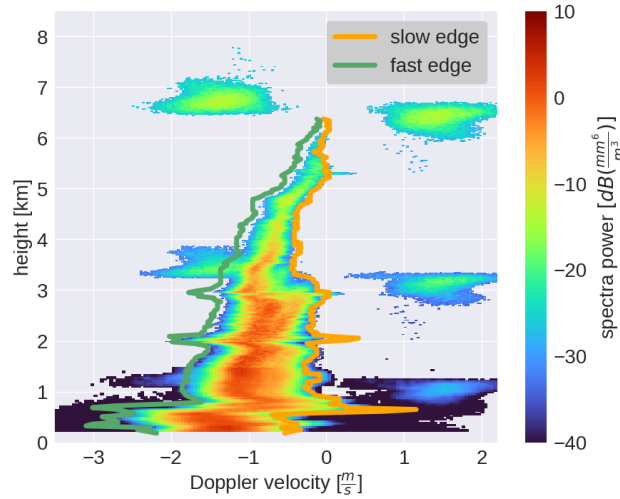


Figure 3.14: Observed W-Band spectra from the same time as Figure 3.10. The fast and slow edges retrieved from the Ka-Band spectra are indicated by the green and orange curves, respectively. The spurious signal are laying outside of the Ka-Band edges at  $\approx 1$ ,  $\approx 3.2$  and  $\approx 6.5$  km.

The spectra edges are also used to remove artefacts from the spectra retrieved by the X-Band radar. It was observed, during TRIPEX-Pol, that some of the X-Band spectra were affected by side lobes. However, these side lobes were far enough from the main spectra mode allowing their removal.

### 3.5 DETECTION OF THE MELTING LAYER

As introduced in Chapter 2, aggregation enhances towards the 0 °C isotherm, and at regions with temperatures higher than 0 °C melting also takes place. This work is focused on aggregation and avoids regions where melting is taking place, commonly denoted as melting layer (ML). Therefore, the altitude where melting starts needs identification to ensure that the data used is from heights above the ML.

There are different methods for detecting the top and the bottom of the ML using data from ground-based radars. Some methods use the changing in Ze curvature profiles, in this region, to detect the ML (Fabry and Zawadzki, 1995; Rico-Ramirez and Cluckie, 2007).

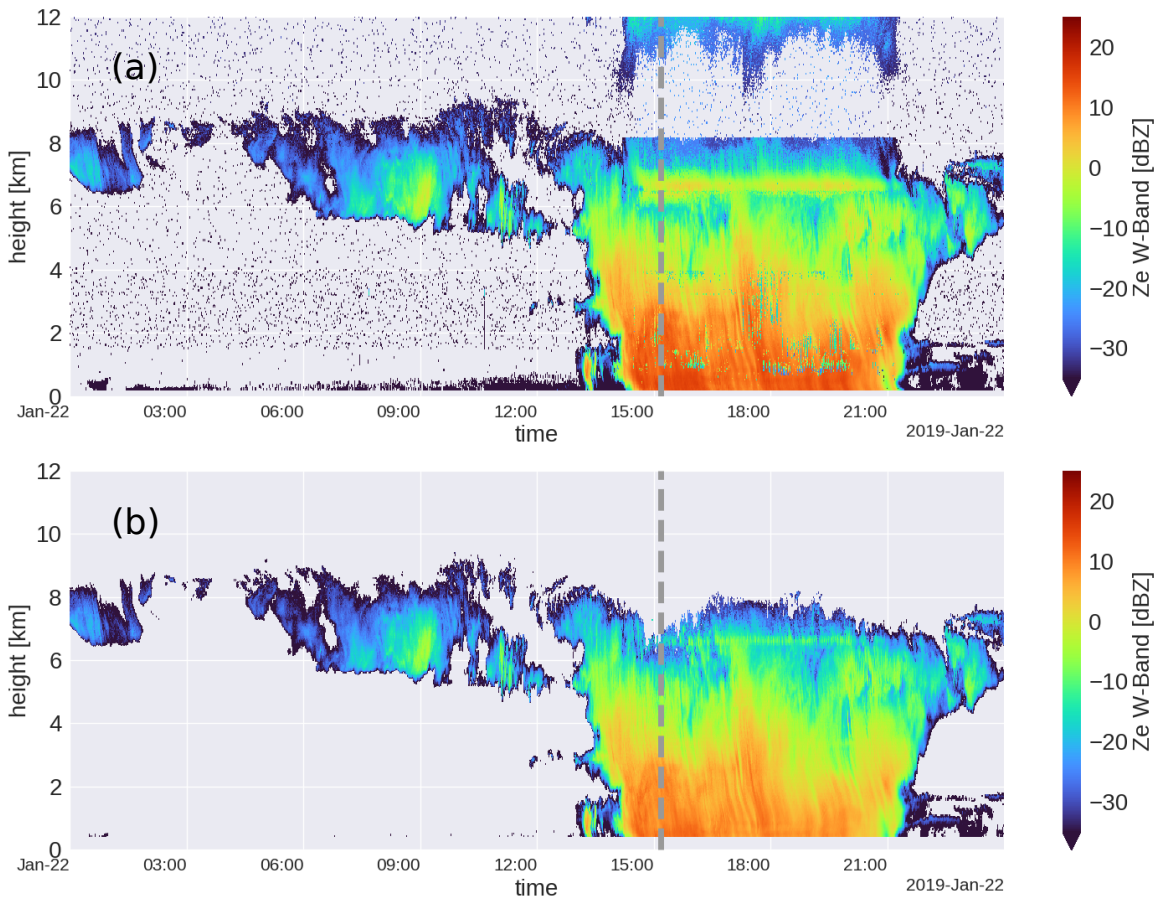


Figure 3.15: Time-height of the Ze from the W-Band from January 22<sup>nd</sup>, 2019. Panel a is the observed data affected by the spurious signal. Panel b is the same data after filtering the spurious data using the retrieved edges from the Ka-Band.

However,  $Z_e$  is not only sensible to phase transition, but it is also sensitive to the particles growth and concentration. Using  $Z_e$  alone could introduce a bias to the detected ML top and bottom. Other methods use the maximum curvature of the MDV profiles during the melting (Baldini and Gorgucci, 2006; Klaassen, 1988; Zrnić et al., 1994) to identify both heights. However, the detection of the ML top could be biased by turbulence. Another detection method uses the enhance of the LDR profiles due to changing in the refractive index of the particles during melting (Bandera et al., 1998; Le and Chandrasekar, 2013), but a fixed threshold is used to identify the ML top and bottom. This fixed threshold could also introduce a bias to the detected top and bottom.

In this thesis, the methodology applied to detect ML top and bottom uses the second-order derivative of the LDR profiles observed by the Ka-Band combined with the temperature profiles provided by Cloudnet. The detection of ML top and bottom is made in three steps. First, a moving average of 5 minutes is applied over the time dimension to minimize the LDR variability due to random noise. Second, the height of the maximum LDR is identified at temperature regions warmer than  $-1$  °C. This temperature threshold is used to minimize the enhance of LDR produced by needles that usually grow around  $-5$  °C. As the last step, the second-order derivative is calculated over the height dimension, and local maxima above and below the height of maximum LDR are assigned to ML top and bottom, respectively. Figure 3.16 shows an example of the retrieved top and bottom of the ML of a frontal system from December 23<sup>rd</sup>, 2018. The top (blue curve) and bottom (orange curve) of the ML well follow the region of enhanced LDR parallel to the isotherm of  $0$  °C (grey dashed curve).

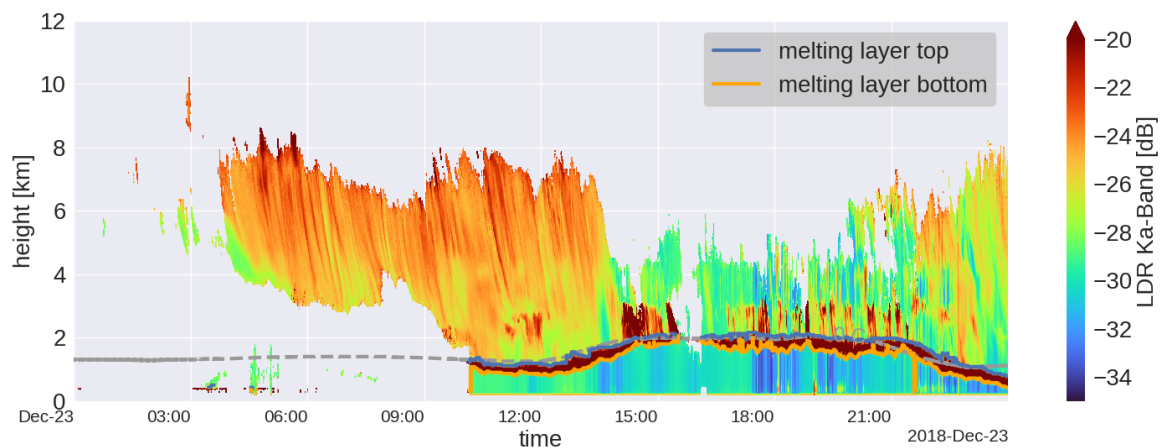


Figure 3.16: Time-height plot of the LDR observed by the Ka-Band on December 23<sup>rd</sup>, 2018. The top and bottom of the ML are indicated by the blue and orange curves, and the isotherm of  $0$  °C is indicated by the grey dashed curve.

The statistical results from the TRIPEX campaign (Figure 9 from Dias Neto et al., (2019)) revealed that the DWR-KaW substantially increases at  $-15\text{ }^{\circ}\text{C}$  coinciding with the DGZ. Based on the results from previous studies (Connolly et al., 2012; Pruppacher and Klett, 1997) aggregation is likely the main reason for this increase. This chapter investigates further aggregation within DGZ using the combined TRIPEX/TRIPEX-Pol dataset, and it addresses the following scientific questions: 1) How is the intensity of aggregation in the DGZ connected to the properties of the particles aloft?; 2) Is the often observed decrease of the MDV (slowdown) in the DGZ caused by dynamical or microphysical processes?; 3) Are the often observed broadening and bimodalities within DGZ related to the intensity of aggregation?. This chapter starts with a brief literature review of studies addressing aggregation in the DGZ (Section 4.1). Section 4.2 introduces a case-study of enhanced DWR-KaW in the DGZ. In Section 4.3, longterm statistics of the combined dataset is used to evaluate if the slowdown is a dynamical or microphysical feature. In Section 4.4 the spectra dataset from the DGZ is used to evaluate if bimodalities intensify aggregation. Section 4.5 investigates if the intensification of aggregation in the DGZ is related to the cloud top temperature. Finally, Section 4.6 provides a summary of the findings and draws some conclusive remarks.

#### 4.1 REVIEW OF RADAR SIGNATURES FOUND IN THE DGZ BY PREVIOUS STUDIES

Several previous studies showed distinct signatures in polarimetric and non-polarimetric variables occurring between  $-20$  and  $-10\text{ }^{\circ}\text{C}$  usually assigned to the DGZ. This section describes the results found by those studies and the interpretation of the observed polarimetric signatures according to the *state of the art* radar science.

Kennedy and Rutledge, (2011) investigated enhanced S-Band KDP signatures of four winter storm events at temperature regions in the vicinity of the  $-15\text{ }^{\circ}\text{C}$ . The authors used T-matrix (Mishchenko and Travis, 1998) to simulate the observed polarimetric variables and investigate the scattering characteristics of the hydrometeors that produced the polarimetric signatures. Their results suggest that the enhanced KDP regions, in the vicinity of  $-15\text{ }^{\circ}\text{C}$ , appear when there is a high concentration of large dendrites with their maximum dimension between  $\approx 0.8 - 1.2\text{ mm}$  with their bulk densities greater than  $\approx 0.3\text{ gcm}^{-3}$ . Additionally, the authors suggested that the formation of these



large particles, at temperatures close to  $-15\text{ }^{\circ}\text{C}$ , needs an extreme depositional growth occurring in a water-supersaturated environment, which requires the presence of upward air motion to provide the needed water vapour.

Andrić et al., (2013) showed a case study where the S-Band polarimetric variables ZDR and  $\rho\text{HV}$  had a maximum and a minimum, respectively, at altitudes coinciding with  $-15\text{ }^{\circ}\text{C}$ . In comparison, KDP had a maximum at altitudes coinciding with  $-8\text{ }^{\circ}\text{C}$  indicating a vertical separation between both ZDR and KDP maxima.  $Ze_{\text{HH}}$  continuously increased from  $-30\text{ }^{\circ}\text{C}$  towards the ground. The authors used a two-moment bulk microphysical model coupled with a scattering model to study those polarimetric signatures. The authors found that the continuous growth of  $Ze_{\text{HH}}$  is a response to deposition and aggregation, and the rapid increase and decrease of the ZDR at  $-15\text{ }^{\circ}\text{C}$  are responses to an intense depositional growth of plate-like crystals followed by aggregation. The authors also suggest that the KDP maximum below the ZDR maximum indicates that a secondary ice process is generating asymmetric ice crystals.

Schrom et al., (2015) presented three case studies where X-Band polarimetric radar variables ( $Ze_{\text{HH}}$ , ZDR, KDP) show different signatures in the DGZ. The authors used the radar observations as inputs of a PSDs retrieval technique assuming a gamma distribution ( $\mu=2$ ) of plates and dendrites to investigate if dendrites could produce the polarimetric signatures. For the case where only ZDR had a maximum, the retrieval indicates the presence of crystals in the initial stage of depositional growth without significant aggregation. For the other two cases where the KDP and  $Ze_{\text{HH}}$  are enhanced, the retrieval suggests the presence of pristine crystals (plates and dendrites) produced the KDP signal while aggregates were responsible for enhancing  $Ze_{\text{HH}}$ . The authors also suggest that upward motion would influence the growth of the ice particles. A weak updraft would lead to a growth regime dominated by deposition and aggregation, while in case of a strong upward motion, riming may also contribute to the snow growth.

Griffin et al., (2018) used the quasi-vertical profile technique (Ryzhkov et al., 2016) to investigate if the polarimetric signatures in the DGZ from five stratiform clouds could be related to isometric (I type) and dendritic (D type) particles. These two classes of particles are defined by Griffin et al., (2018) as follows: "*I-type particles include a broad category of snow aggregates and ice crystals with irregular or nearly spherical shapes and can result in moderate ZDR and significant KDP (if the concentration of isometric ice is sufficiently high). The D-type crystals are composed of highly oblate (dendrites or hexagonal plates) or prolate (needles) hydrometeors that have very anisotropic shape and higher density than I-type ice particles.*" The authors suggest that regions with enhanced ZDR are dominated by D-type particles, supported by in-situ observation, and regions with

enhanced KDP are dominated by I-type particles (due to high concentration of ice), but it does not exclude the presence of D-type. The authors indicate that while the I-type particles fall through the DGZ, the larger ones will continuously grow without significant change in the shape; however, if the I-type particles are small, they can grow as dendrites-like and due to high capacitance of these newly formed particles they grow fast. Additionally, the slower fall velocity of the D-type particles contributes to the growth of large particles with low aspect ratios, leading to high ZDR values.

Moisseev et al., (2015) reported an event of bimodal Doppler spectra, from a C-Band radar, at temperature regions close to  $-15$  °C. For the same region, the authors also observed an enhanced differential reflectivity (ZDR), and differential phase shift (KDP) observed by a C-Band polarimetric radar. The study suggests that this bimodal scenario results from a seeder-feeder effect, where faster ice particles, from the upper part of the cloud, fall into a region of much slower ice particles leading to an enhancement of the collision between the two groups of particles and thus enhancing aggregation. The increased ZDR region observed at the same height of the bimodality indicates that there is no significant riming taking place. Additionally, Moisseev et al., (2015) suggested that enhanced ZDR without significant KDP can be used as an indicator of crystal growth zone. On the other hand, for scenarios where ZDR and KDP are enhanced but with a vertical offset between them (Andrić et al., 2013), the authors hypothesize that early aggregates may be enhancing KDP. The authors also suggest that if bands of enhanced ZDR and KDP are observed, the formation of KDP bands could only take place in regions where seeder-feeder or secondary ice process are supplying the high concentration of dense asymmetric particles.

Barrett et al., 2019 showed a Doppler spectra where two groups of different particles are present at temperatures close to  $-15$  °C. One group of fast-falling particles, from the upper part of the cloud, falls on top of a slower group of particles; similarly to observed by Moisseev et al., (2015). Additionally, Barrett et al., (2019) observed an enhanced DWR-KaW below the region where the two groups merge, which indicates an increase in the mean particle sizes. The authors used spectral DWR to retrieve the PSD at different heights in the cloud and investigate the evolution of the PSD throughout the column. Based on the retrieved PSDs and no evidence of supercooled water combined with the rapid increase of DWR-KaW from 0 to 7 dB within 500 m, the authors excluded the possibility of the enhancement of the DWR-KaW to be a result of riming or deposition and suggested that it is a result of rapid aggregation. This study suggests that at this temperature region, the slow group of particles is composed of dendrite-like particles, and they easily aggregate with each other and with the fast-falling ones leading to an enhancement of the DWR-KaW.

Trömel et al., (2019) presented a statistical analysis of polarimetric variables from 52 stratiform precipitation events. For each event, the authors computed quasi-vertical profiles of  $Z_{e_{HH}}$ , ZDR and KDP from plan position indicators scans (radar keeps a constant elevation and varies its azimuth). The authors found a positive correlation between KDP and  $Z_{e_{HH}}$  in the DGZ, which is regarded as an indicator of the increase in ice particles concentration and intensification of aggregation. Additionally, the authors indicated that the enhanced KDP bands at DGZ correlate with the enhancement of the  $Z_{e_{HH}}$  near the surface, which suggests an intensification of precipitation. In contrast to the results from Griffin et al., (2018), Trömel et al., (2019) did not find a negative correlation between the ZDR in the DGZ and cloud top temperature.

As a summary from these previous studies, Figure 4.1 illustrates the conceptual behaviour of the profiles from the different radar variables as a function of temperature.

Those previous works indicate that two possible scenarios could be responsible for enhancing aggregation. In the first scenario (SCN-1), the occurrence of an updraft in the DGZ would create an environment super-saturated over water that would enhance further the depositional growth and sharply increase the size of dendrite-like particles. Later, those large dendrite-like particles would enhance aggregation. In the second scenario (SCN-2), secondary ice processes would be taking place in the DGZ. These processes would produce ice fragments that would grow as dendrites. Later, these new dendrites would intensify aggregation. The following analysis in this thesis will combine Doppler spectra, DWRs and MDV observations to investigate the signature of potential upward motion, new particle formation and aggregation.

#### 4.2 CASE STUDY OF DGZ OBSERVATIONAL FEATURES

On January 22<sup>th</sup>, 2019 a stratiform cloud system passed over the JOYCE-CF platform between 13:00 and 23:00 UTC, and snow was observed on the ground during the entire event (also recorded by the PARSIVEL). The data from a nearby weather station indicates that the temperature at 2 m above the ground ranged between  $-3$  and  $1$  °C. The data recorded by the radars are presented in Figure 4.2. One can see that around 15:07 UTC,  $Z_e$  (Figure 4.2-a) strongly increases reaching values up to 20 dBZ. The MDV-Ka (Figure 4.2-b) also shows relatively low variability between  $-1$  and  $0$  m/s throughout the entire period. The fall velocities slowly increase toward the ground reaching the typical MDV of snowflakes ( $1$  m/s); however, in some regions close to the  $-15$  °C isotherm, the MDV shows a slowdown of the fall velocities, which, as it was showed before in Figure 3.11, is due to a spectral multi-modality. The DWR-XKa (Figure 4.2-c) is close to

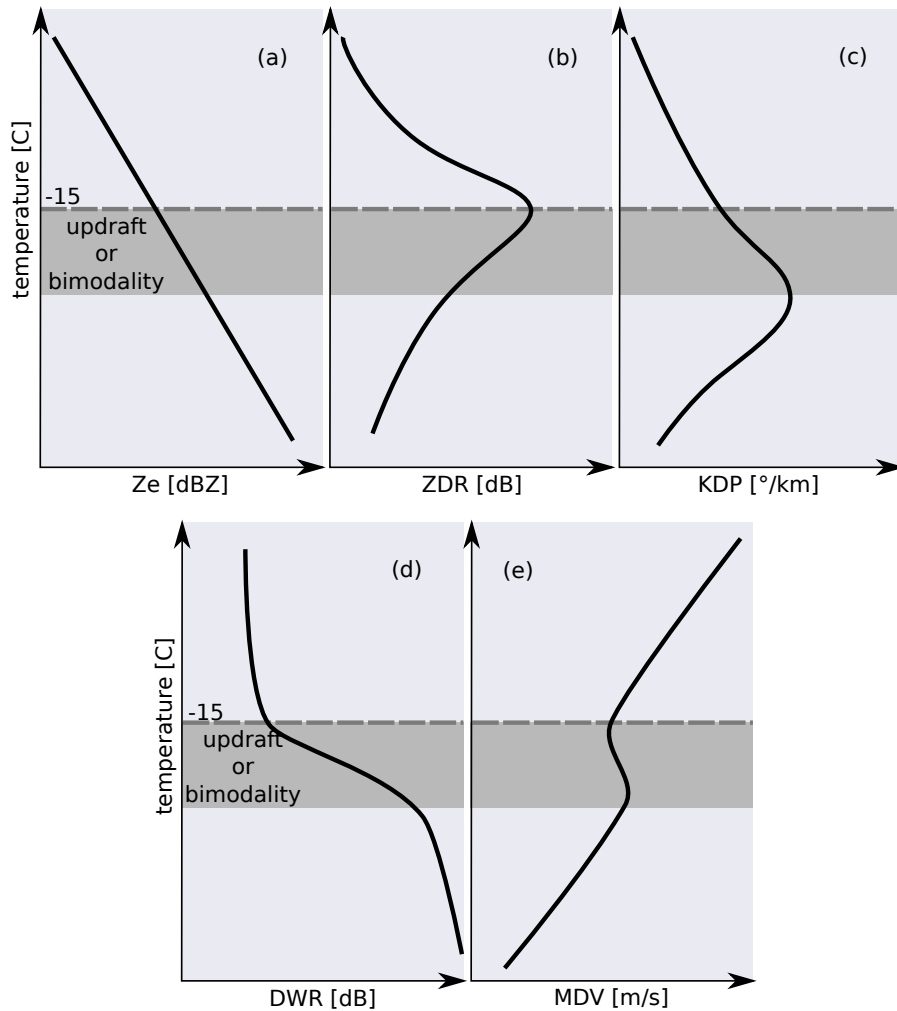


Figure 4.1: Conceptual illustration of the radar signatures within DGZ found by previous studies. Radar reflectivity factor Ze (a), differential reflectivity ZDR (b), specific differential phase KDP (c), dual wavelength ratios DWR (d), mean Doppler velocity MDV (e). The horizontal dashed line indicates the isotherm of  $-15^{\circ}\text{C}$ . The gray strip indicates the region where updraft or bi-modal spectra were observed.

0 dB over almost the entire cloud, and it slightly enhances up to 5 dB at  $\approx 15:07$  and  $\approx 21:00$  suggesting that aggregation is enhanced at those times. In the DWR-KaW field (Figure 4.2-d) is possible to identify two different regimes. One for the cloud regions above the  $-15^\circ\text{C}$  isotherm and another below. In the upper region, the DWR-KaW remains at 0 dB. In the lower section of the cloud, DWR-KaW enhances towards the ground and reaches its maximum value (10 dB), at the same time (15:07 and 21:00) DWR-XKa enhances, which indicates the presence of large snowflakes. Both DWRs are attenuation corrected, as described in Section 3.1. Additionally, both DWRs plots show vertical stripes (e.g. 15:07 UTC), and they result from the high temporal fluctuation of attenuation that was not possible to capture with the method introduced in Section 3.1.

In addition to the data from the non-polarimetric radars, Figure 4.2(e-f) show the differential reflectivity (ZDR) and the specific differential phase (KDP) from W-Pol obtained from constant  $30^\circ$  elevation. Here, the meaning of ZDR and KDP are briefly introduced; a more detailed derivation and discussion can be found in Andronache, (2018), Bringi and Chandrasekar, (2001), and Fabry, (2015). This study does not focus on the polarimetric variables because they were not available during TRIPEX. However, the polarimetric variables are used to corroborate with the interpretation of the multi-frequency and spectral observations. ZDR is defined as the ratio between the  $Z_{e_{HH}}$  and  $Z_{e_{VV}}$  in linear units and is sensitive to the particles aspect ratio. For example, more rounded particles like aggregates produce low ZDR while very flat or elongated crystals such as plates or needles produce very high ZDR (4-6 dB, Kumjian, (2013)). Unlike  $Z_e$ , ZDR is independent of the particle concentration, but it is reflectivity-weighted and thus integrated ZDR reflects the polarimetric signal of the most relevant scatterers. As a result, the low ZDR contribution of a few round aggregates can dominate the total ZDR despite a high ZDR of low-reflectivity small particles. KDP is defined as half of the range derivative of the differential phase shift ( $\phi_{DP}$ ); this last variable,  $\phi_{DP}$ , is the differential propagation phase shift ( $\phi_{HH} - \phi_{VV}$ ). In contrast to  $Z_e$ , KDP is not affected by attenuation or radar miscalibration. As described by Andronache, (2018), Bringi and Chandrasekar, (2001), and Fabry, (2015) KDP is usually low for large snowflakes and enhanced by asymmetric ice crystals. ZDR and KDP provide complementary information; while ZDR is insensitive to concentration, KDP is mainly driven by ZDR producing particles. Not only aspect ratio by also density of particles drives ZDR and KDP (Moisseev et al., 2015). KDP scales with  $\lambda^{-1}$  and hence the KDP at W-Band is expected to be larger than at X-Band. The KDP showed in Figure 4.2-f was calculated by the radar software, and no bias was found in ZDR from drizzles during TRIPEX-Pol.

Figure 4.2-e shows that the majority of the ZDR values are distributed around 2 dB, indicating that there are a significant number of ZDR producing particles in the volume, probably small asymmetric particles. On the other hand, ZDR reduces to values around 0.2 dB in the same region where the DWR-KaW strongly enhances, providing additional support to the interpretation of the presence of aggregates. The time-height plot of KDP (Figure 4.2-f) shows values  $0^\circ/\text{km}$  at regions above the  $-15^\circ\text{C}$  isotherm, while it enhances at regions below. At 15:07 UTC and above  $-15^\circ\text{C}$  ZDR is enhanced (1-2 dB) while KDP is around  $0^\circ/\text{km}$  and both DWRs are around 0 dB, suggesting the presence of small asymmetric particles, but probably with low concentration. However, below  $-15^\circ\text{C}$  this scenario rapid changes, which is similar to the results from previous results (Moisseev et al., 2015; Trömel et al., 2019). The ZDR reduces down to 0 dB while and DWR-KaW increases up to 8 dB supporting the interpretation of enhanced aggregation and formation of large aggregates. Interestingly at the same time and region, KDP also increases up to  $3^\circ/\text{km}$  and remains almost constant towards the ground. This increase in KDP is unexpected since aggregation should reduce the concentration of small asymmetric particles and therefore reduce KDP.

In order to understand further the microphysical processes that are taking place from cloud top down to the ground, the following analyses use ten minutes average profiles of Ze, MDV, DWRs, ZDR, and KDP centred at 15:07 and it is focused in three regions. Region 1 is between 7 and 3 km; region 2 is between 3 and 2 km, and region 3 is between 2 km and the surface. All the averaged profiles are shown in figure Figure 4.3.

In region 1, the reflectivity profiles from X- Ka- and W-Band Figure 4.3-a) continuously increase from  $-20$  to 5 dBZ, with the same gradient, from cloud top down to 3 km ( $\approx -14^\circ\text{C}$ ), as a result both DWRs profiles are almost constant close to 0 dB (Figure 4.3-c). The MDV (Figure 4.3-c) continuously increases from 0 up to 1 m/s (typical fall velocity for aggregated snow). Inside of region 1 yet, ZDR increases from 0 up to 1.2 dB between cloud top and 4.5 km (from  $-40$  to  $-20^\circ\text{C}$ ); the habit diagram (Figure 2.4) indicates that plate-like crystals are likely to grow there. Between 4.5 and 3.5 km, ZDR decreases from 1.2 to 0.7 dB and between 3.5 and 3 km ZDR sharply increases from 0.7 to 0.9 dB. The habit diagram indicates that from the temperature of the last two regions, dendrite-like crystals are expected to grow there. The KDP in region 1 is noisy and does not allow to draw conclusions from it.

This scenario, within region 1, indicates that either the particles are growing continuously, but their mean size appears to be still smaller than can be detected by DWR-KaW ( $\approx 0$  dB), or the concentration of the particles is increasing and producing a continuous increase Zes without increasing DWRs. However, the constant increase of MDV



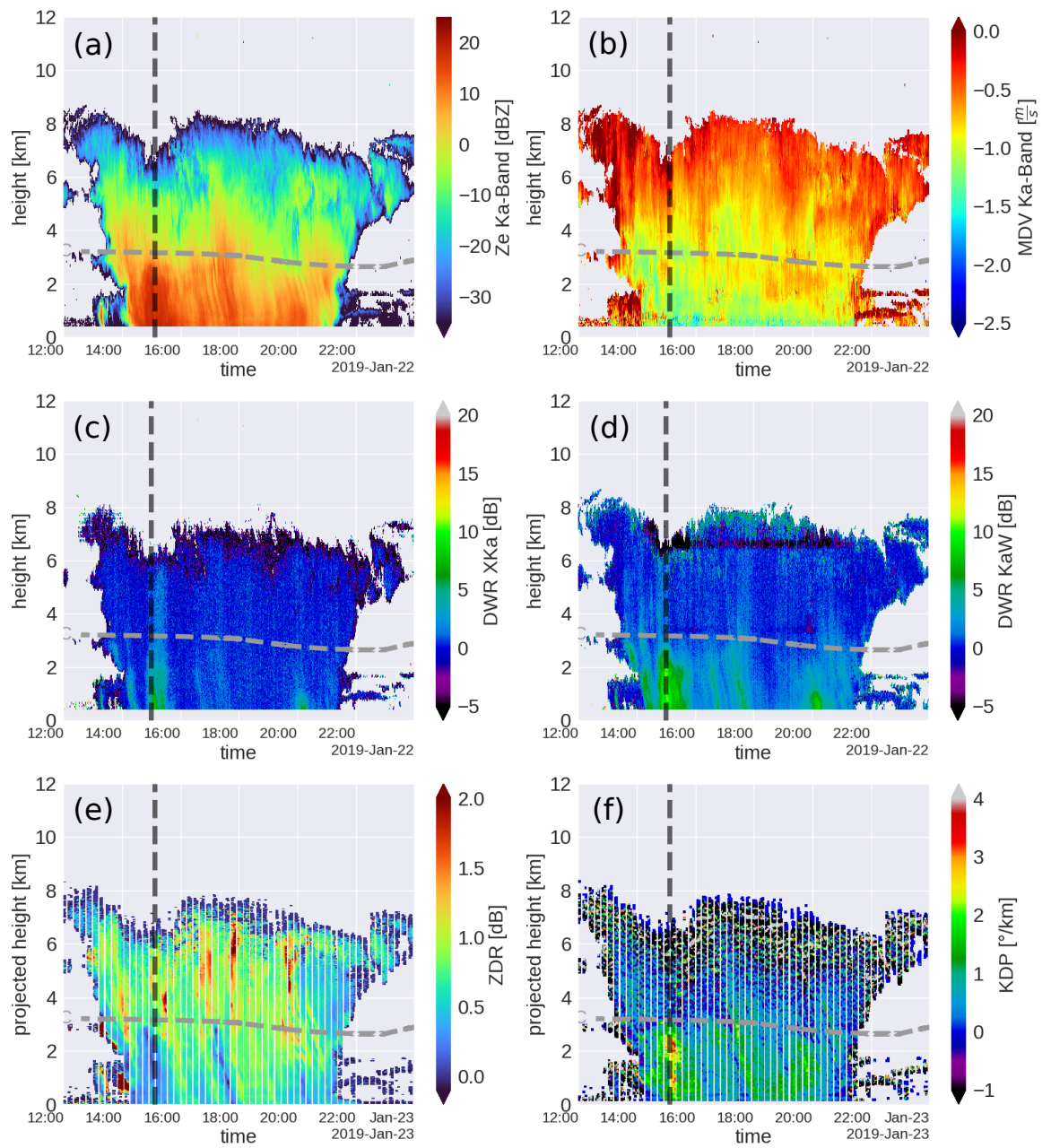


Figure 4.2: Time-height displays of several radar variables obtained at JOYCE on January 22<sup>nd</sup>, 2019: radar reflectivity factor Ze (a), mean Doppler velocity MDV (b) and the negative values indicate downward motion, dual wavelength ratios DWR-XKa (c) and DWR-KaW (d), differential reflectivity ZDR (e), specific differential phase KDP (f). The polarimetric variables are from 30° elevations and projected to the zenith. The vertical dashed gray line indicates 15 : 07 UTC and the horizontal line indicates the -15 °C isotherm.



favours the interpretation of continuous growth of the particles. The reduction of ZDR (between 4.5 and 3 km) coincides with the region where dendrites are formed, which supports the interpretation that aggregation is taking place.

In region 2, Ze-W slightly increases from 3 to 7 dBZ while Ze-X increases from 3 to 20 dBZ. Ze-Ka also increases, but its values remain between X and W (increasing from 3 to 16 dBZ). DWR-XKa slightly increases up to 4 dB while the DWR-KaW sharply increases up to 7 dB. In the same region 2, the MDV profile reveals a slowdown. The MDV first reduces from 1 m/s down to 0.7 m/s between 3 and 2.7 km; in the region below, between 2.7 km and 2 km, the MDV increases from 0.7 to 1.0 m/s. ZDR within region 2 continuously decreases from 0.9 dB down to 0.3 dB while KDP increases from 0 °/km up to 3 °/km.

The continuous increase of Ze-X, while Ze-W remains almost constant, combined with the increase of both DWRs suggest continuous growth of the mean particle sizes. The reduction of ZDR favours the interpretation that the particles are growing by aggregation; due to the temperature region (between  $-14$  and  $-8$  °C) aggregation is like to be intensified by dendritic growth. Surprisingly, KDP continuously increases within region 2, suggesting that the concentration of asymmetric particles is increasing. The sharp reduction of the MDV could be a result of a localised updraft or a new population of small and slow-falling particles. The Doppler spectra (Figure 3.10) shows that there is an additional mode of particles at the same region of the slowdown and due to enhanced KDP it is likely that asymmetric particles form this new spectral mode. This new spectral mode could result from new nucleation or secondary ice processes.

Within region 3, Ze-W and Ze-Ka remain almost constant around 7 and 16 dB respectively while Ze-X still increases from 20 to 23 dBZ. The DWR-KaW slowly increases from 8 to 10 dB, and the DWR-XKa continuously increases from 4 dB up to 7 dB. The MDV shows an additional increase in the fall velocity from 1 m/s to a saturation point around 1.2 m/s. ZDR profile shows an additional reduction from 0.3 to 0.1 dB between 2 and 1.5 km and then ZDR increases up to 0.5 dB towards the ground. Inside of the region 3, KDP reduces from 3 °/km and keep almost constant around 1.6-1.8 °/km.

In this last scenario from region 3, the further increase of Ze-X combined with the increase of both DWRs suggest an additional growth of the mean size of the particles. The almost constant MDV corroborates with the interpretation that those particles are large snowflakes. The additional increase in ZDR suggests the presence of asymmetric particles within the observed volume; the habit diagram (Figure 2.4) indicates that this temperature region favours the formation of needles, and due to their asymmetry, needles could be producing the enhancement of ZDR. The constant KDP combined with the enhancing of both

DWRs could be an indicator of a continuous supply of asymmetric particles and favouring the growth of even larger snowflakes.

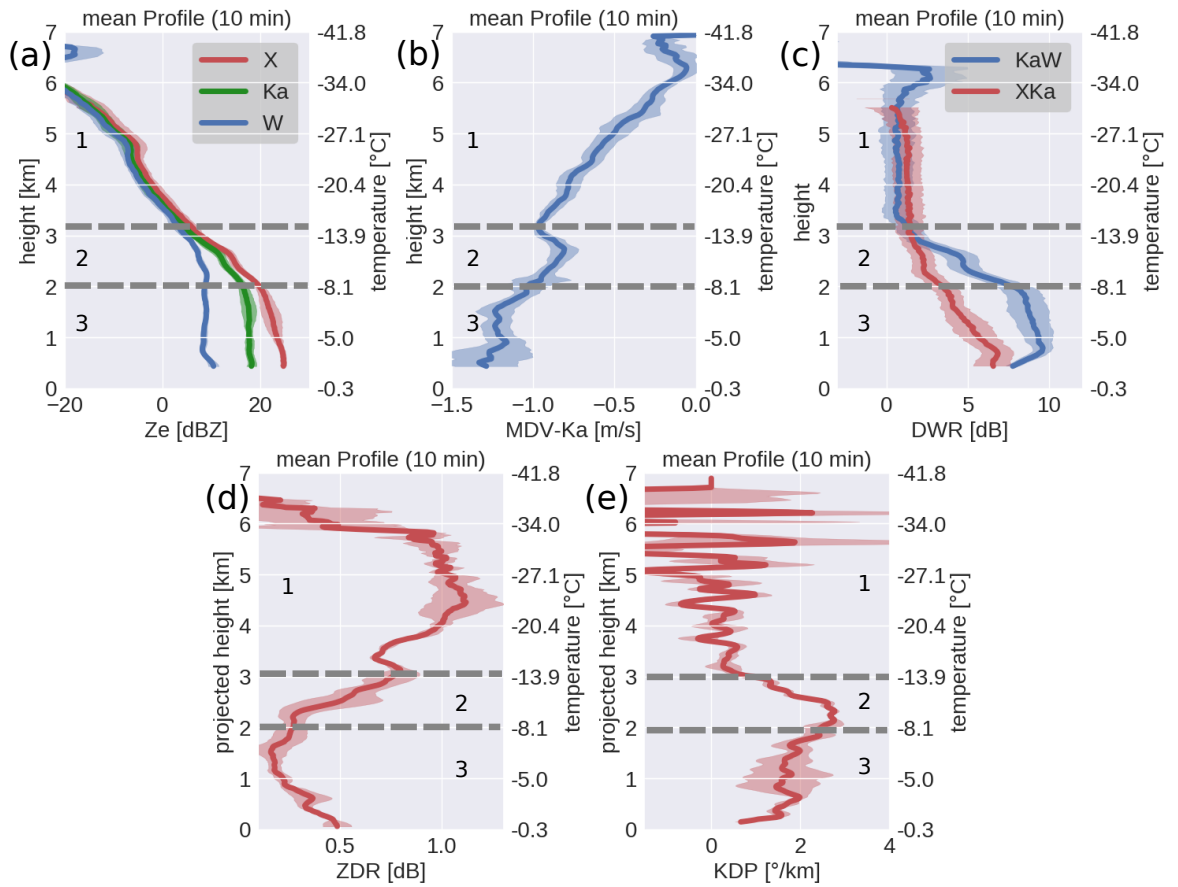


Figure 4.3: Ten minutes averaged profiles of the radar variables on January 22<sup>nd</sup>, 2019 centred at 15 : 07 UTC. In panel (a) the blue, green and red curves are Ze profiles from W-, Ka- and X-Band, respectively. Panel (b) shows the MDV profile from Ka-Band. In Panel (c), the red and blue curves are from the DWR-XKa and DWR-KaW, respectively. Panels (d) and (e) show the ZDR and KDP profiles, respectively. Ze, DWRs, ZDR are average from the profiles in log units. The standard deviation is indicated by the contour along each profile. The horizontal gray dashed lines indicate the separation between the different regions as described in the text.

#### 4.3 STATISTICAL ANALYSES OF RADAR VARIABLES WITHIN DGZ

The long term combined TRIPEX/TRIPEX-Pol dataset gives the possibility to use statistical analysis to evaluate the realism of the different aggregation scenarios in the DGZ, and it also may reveal if any additional process is taking place. As described in [Chapter 2](#), the DWR-KaW is more sensitive to the initial increase of mean size than DWR-XKa, and therefore DWR-KaW is used as an indicator of aggregation in the DGZ. For the current statistical analysis, five

different classes of increasing maximum DWR-KaW (mDWR-KaW) within DGZ are defined [Table 4.1](#). The DWR-KaW usually saturates around 8 dB, but the DWR-KaW can reach values larger than 8 dB in case of rimed particles or particular PSDs. The classes 1 to 4 cover the mDWR-KaW range from 0 up to 8 dB and they are defined to be equally spaced by 2 dB. The class-5 is defined to capture those DWR-KaW values that exceed 8 dB. Those classes are then used to group the vertical profiles of DWR-KaW, DWR-XKa, MDV, and spectra edges according to the mDWR-KaW.

Table 4.1: mDWR-KaW intervals defined to represent aggregates at the different growth stage inside of the DGZ.

mDWR-KaW classes	mDWR-KaW interval	number of profiles
class-1	0-2	44256
class-2	2-4	68890
class-3	4-6	40733
class-4	6-8	20986
class-5	8-20	14608

In order to investigate the initial growth of the ice particles in the DGZ, the following analyses use the DWR-KaW vertical profiles and classify them according to mDWR-KaW classes. [Figure 4.4](#) shows the histograms of DWR-KaW profiles of each class. The different classes of DWR-KaW profiles show the presence of negative values and noise, which are from periods when the offset correction cannot be adequately calculated due to large time window. Note that the histograms of the DWR-KaW profiles, for each class, have a different upper DWR limit in the DGZ, which corresponds to the upper limit of the different classes from [Table 4.1](#). The histograms ([Figure 4.4a-e](#)) show that at temperatures colder than  $-30$  °C the DWR-KaW profiles are mainly distributed at  $\approx 0$  dB. At this temperature regime, the habit diagram ([Figure 2.4](#)) indicates the preferential growth habit of bullet rosettes and assemblages of plates; however, these particles are not large enough to enhance the DWR-KaW. The histograms additionally show that the DWR-KaW starts to increase at  $-30$  °C, and it continuously increases towards the ground; the only exception is the class-1 ([Figure 4.4-a](#)) that remains  $\approx 0$  dB and only increases at temperatures warmer than  $-10$  °C.

The median profiles ([Figure 4.4-f](#)) show that overall the larger maximum of DWR in DGZ (i.e., higher DWR class) seems to be also related to larger DWR values of the entire profile. The initial increase of the DWRs above the DGZ could result from an enhanced depositional growth in case of higher Si (Hallett and Mason, 1958; Kobayashi, 1957; Takahashi, 2014; Takahashi et al., 1991) or initially formed aggregates

(Karrer et al., 2020). Between  $-15$  and  $-10$  °C, the medians indicate a rapid increase of the gradient from each DWR profile and the gradient becomes stronger with increasing class number. For example, the gradient from classes 1 and 5 between  $-30$  and  $-15$  °C are  $0.01$  and  $0.10$  dB/ °C, respectively, while for the same two classes between  $-15$  and  $-10$  °C the gradient increases to  $0.13$  and  $0.85$  dB/ °C, respectively. As introduced in Section 2.1.1, this last temperature region (from  $-15$  to  $-10$  °C) is known for the growth of dendrites, which suggests that this sharp increase could be driven by intensification of aggregation due to an intense growth of dendrites. The enhancement of aggregation in this temperature region is supported by the increase of the aggregation efficiency found by laboratory studies (Connolly et al., 2012; Hosler and Hallgren, 1960). In the temperature region between  $-10$  and  $0$  °C, the lowest three classes show a further increase of the DWR-KaW, while the highest two classes show a decrease followed by a slight increase. In this temperature region, aggregation is favoured by the increase of the sticking efficiency of the ice surface which could explain the observed additional increase of the DWRs towards  $0$  °C; however, the reduction of the DWRs observed for the highest two classes indicates a reduction of the particle sizes. This size reduction could result from fragmentation, sublimation or because the particles were driven away.

The DWR-KaW reaches its maximum value for a distribution of aggregates with  $D_0$  around  $4 - 5$  mm while the DWR-XKa is sensitive to  $D_0$  larger than  $3 - 4$  mm (Figure 2.16). Therefore, the DWR-XKa profiles will only indicate the presence of large aggregates. Figure 4.5 shows the histograms of the DWR-XKa profiles for the same classes as in Figure 4.4. The DWR-XKa histograms (Figure 4.5a-e) show an almost constant spread of the data around  $\approx 0$  dB at temperatures colder than  $-15$  °C, and at temperatures warmer than  $-15$  °C, the spread increases towards large DWR-XKa values. In contrast to DWR-KaW median profiles, the inter-comparison between the DWR-XKa median profiles (Figure 4.5-f) does not show any significant variation at temperatures colder than  $-15$  °C indicating that the growth experienced by the particles is not enough to enhance the DWR-XKa. Between  $-15$  and  $-10$  °C, the lowest two classes remain without a significant increase, while the other classes increase similar to the DWR-KaW medians (Figure 4.4) but less pronounced. This increase of the DWRs profiles corroborates the intensification of aggregation due to the growth of dendritic-like particles. At temperatures warmer than  $-10$  °C, the highest two classes also show a reduction followed by an increase of the DWR values. This reduction suggests that there is an additional process taking place at this temperature region and driving the reduction of the particle sizes.

One can expect that the increase of mean the particle sizes also correlates with the increase of fall velocities (Karrer et al., 2020; Mitchell,

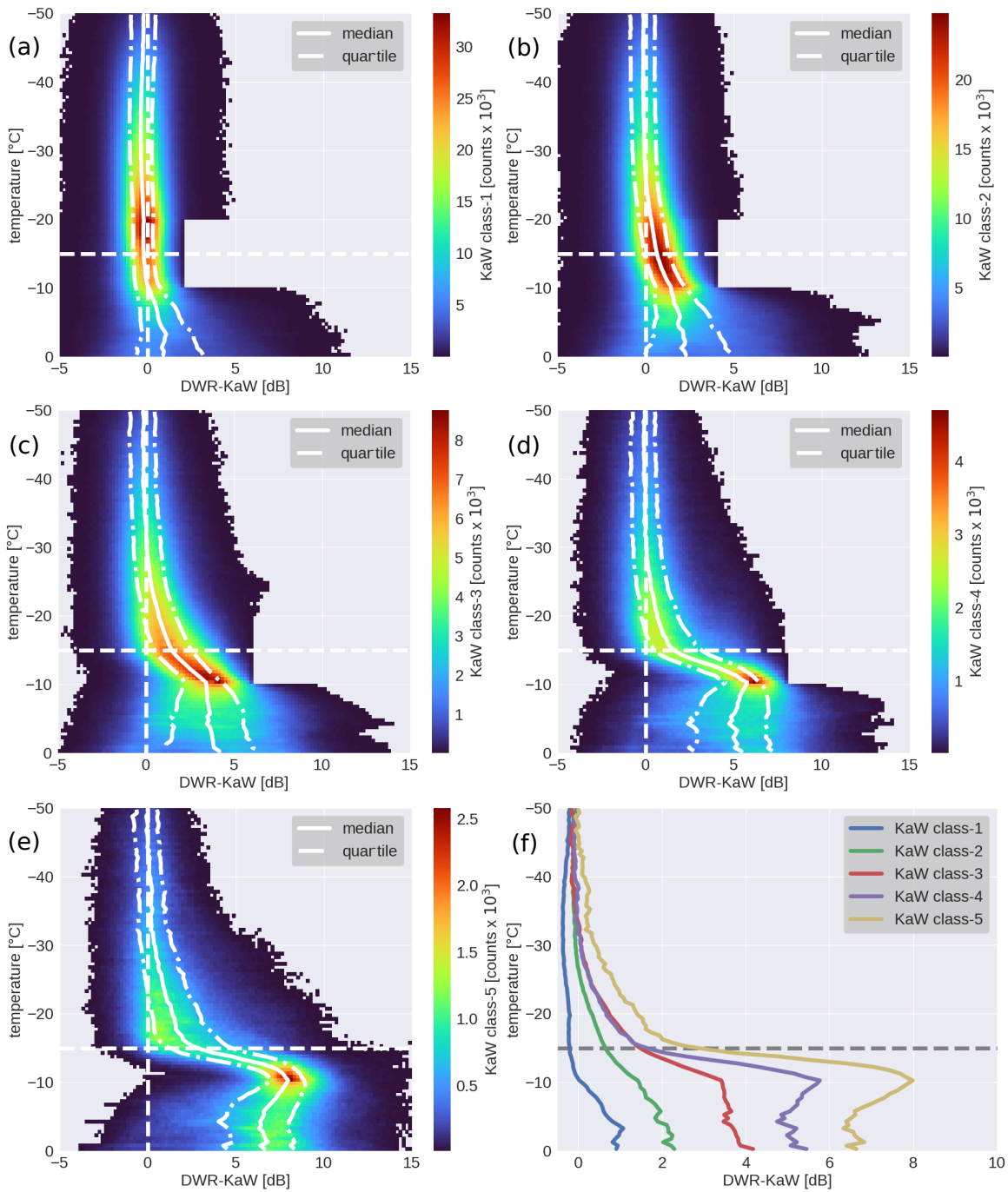


Figure 4.4: Histograms of the DWR-KaW profiles stratified with temperature for the mDWR-KaW classes defined in Table 4.1. Panels a) to e) are for the class-1 to class-5. The continuous and dashed lines are the median and the quartiles of the distribution, respectively. Panel f) is the intercomparison between the median profiles from the different classes. The horizontal and vertical dashed lines indicate the isotherm of  $-15\text{ }^{\circ}\text{C}$  and DWR-KaW equal to 0 dB, respectively.

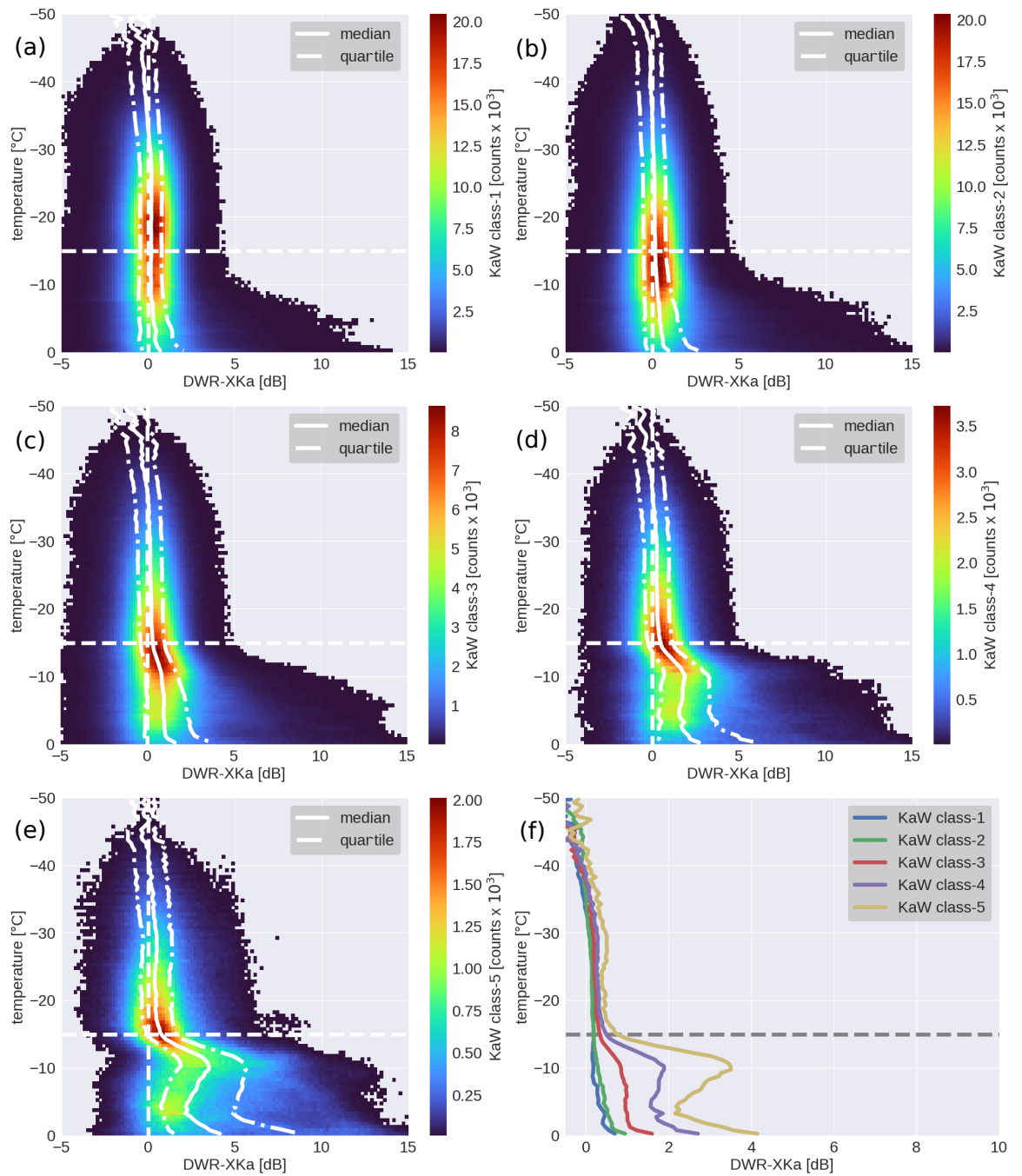


Figure 4.5: Similar as Figure 4.4 but for DWR-XKa profiles.



1996). In order to investigate if the increase in aggregates maximum sizes correlates with the increase in fall velocities, the MDV profiles are classified according to the mDWR-KaW classes. Figure 4.6 shows the histograms of the MDV profiles for each mDWR-KaW class; the MDV profiles are not corrected for air density. Overall, the different classes (Figure 4.6 a-e) indicate an increase in the fall velocity of the ice particles from the top of the clouds towards the ground, which is expected by continuous depositional growth and/or aggregation. However, the different classes show a slowdown taking place within the DGZ, which suggests that either an updraft or an additional mode of slow falling particles is generating this effect.

Figure 4.6-f shows that the different median profiles in temperature regions colder than  $-30\text{ }^{\circ}\text{C}$  have a similar gradient ( $-0.02\frac{\text{m}}{\text{s}^{\circ}\text{C}}$ ). In the region between  $-30$  and  $-20\text{ }^{\circ}\text{C}$ , the MDV median profiles reveal a changing in the gradient compared to the region above. The lowest two classes have a similar gradient ( $-0.024\frac{\text{m}}{\text{s}^{\circ}\text{C}}$ ) between  $-30$  and  $-25\text{ }^{\circ}\text{C}$ ; however, between  $-25$  and  $-15$  the gradient from class-1 reduces to  $-0.01\frac{\text{m}}{\text{s}^{\circ}\text{C}}$  while the gradient from class-2 remains constant. The profiles from the highest three classes have a similar gradient ( $-0.03\frac{\text{m}}{\text{s}^{\circ}\text{C}}$ ) between  $-30$  and  $-20\text{ }^{\circ}\text{C}$ . The general increase of the MDV with increasing DWR class suggests that the particles within this temperature would be experiencing different Si conditions, which could lead to the formation of different types of particles as suggested by Figure 2.4.

Figure 4.6-f also shows that in the DGZ, the increase of the DWR classes suggests a correlation with the magnitude of the slowdown. For example, the magnitude of the slowdown from classes 1, 3 and 5 are 0.05, 0.1 and 0.2 m/s, respectively. If the slowdown within DGZ is caused by updrafts as suggested by SCN-1, the increase of the magnitude of the slowdown would suggest an intensification of the updrafts. On the other hand, if a new mode of particles is growing within DGZ as suggested by SCN-2, the increase of the magnitude of the slowdown would indicate that the velocity difference between different modes is increasing. In the temperature regions between  $-10$  and  $0\text{ }^{\circ}\text{C}$ , the MDV increases to typical aggregate velocities of 1 – 1.2 m/s except for the lowest two mDWR-KaW classes where particles might sublime before reaching the ML.

In order to better understand the possible reason for the slowdown in the MDV profiles around  $-15\text{ }^{\circ}\text{C}$ , the following analysis uses the slow and fast Doppler spectra edges and applies the same mDWR-KaW classification to them. If an updraft is tanking place in the DGZ, both edges will be affected by a slowdown. However, if only the slow edge is affected by a slowdown, it would be an indication of the formation of new particles. Figure 4.7 shows the histograms of the spectra edges profiles grouped by the mDWR-KaW classes as the previous variables. Figure 4.7(a-e) shows an overall increase in the



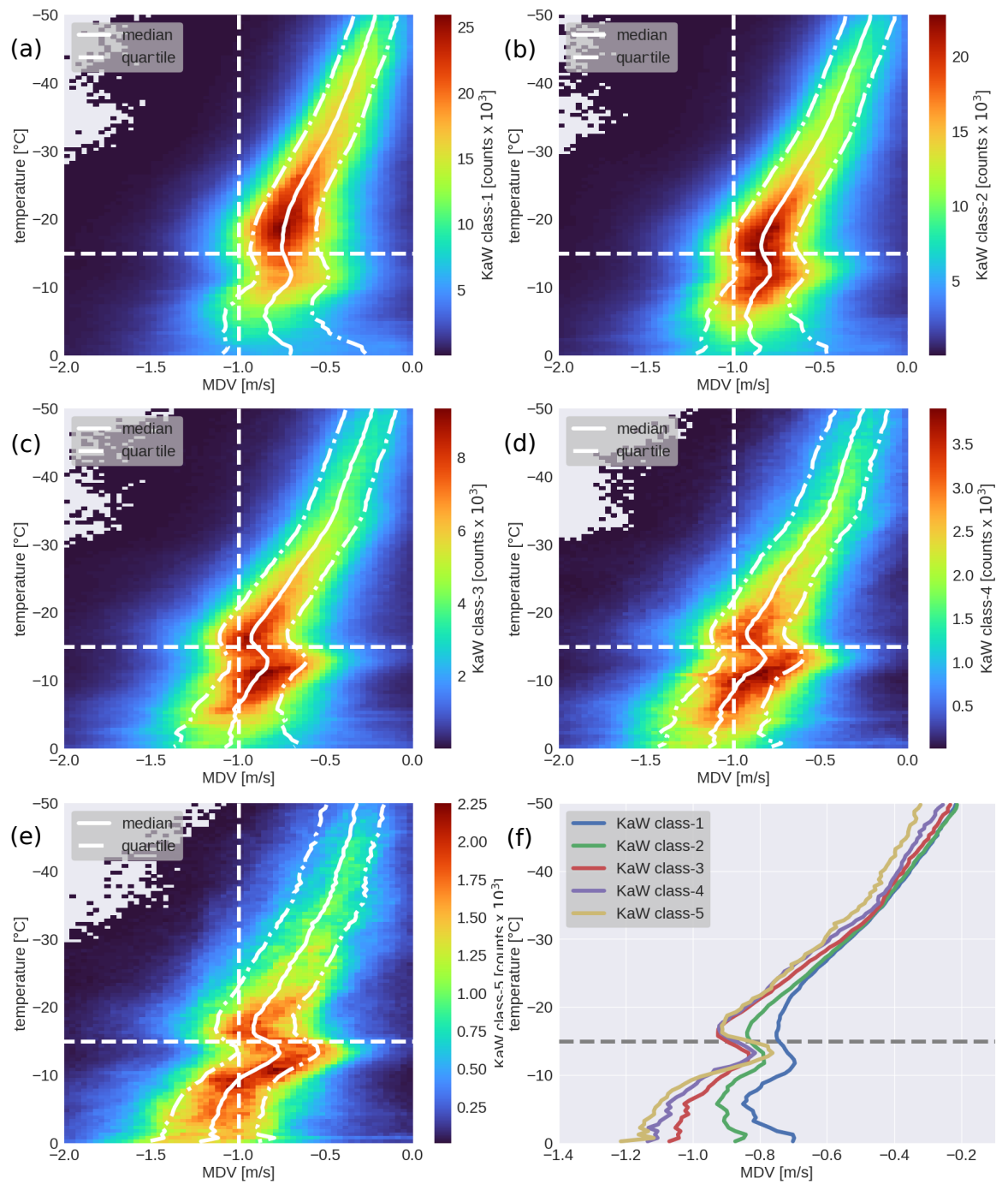


Figure 4.6: Similar as Figure 4.4 but for MDV profiles. The vertical dashed line at  $-1$  m/s indicates the typical fall velocity of snowflakes.

Doppler velocity (DV) of the fast and slow edges throughout the entire profile except in the DGZ where both edges indicate a slowdown.

In temperature regions colder than  $-30\text{ }^{\circ}\text{C}$  (Figure 4.7-f), the median profiles of the fast and slow edges show that the DV is increasing slightly different. The slow edges have a gradient of  $-0.01\frac{\text{m}}{\text{s}^{\circ}\text{C}}$  while the fast edges have a gradient of  $-0.024\frac{\text{m}}{\text{s}^{\circ}\text{C}}$ . Between  $-30$  and  $-20\text{ }^{\circ}\text{C}$ , the slow edges remain with a gradient of  $-0.01\frac{\text{m}}{\text{s}^{\circ}\text{C}}$ , while the fast edges clearly separate. The DV of the fast class-1 continuously increase with the same gradient ( $-0.024\frac{\text{m}}{\text{s}^{\circ}\text{C}}$ ) from the regions above while the class-2 has a gradient of  $-0.035\frac{\text{m}}{\text{s}^{\circ}\text{C}}$  and the higher three classes have a gradient of  $-0.046\frac{\text{m}}{\text{s}^{\circ}\text{C}}$ . The fact that the fast edges have larger gradient than the slow edges combined to the fact that the gradients of the fast edges additionally increase corroborate with the interpretation based on DWRs and MDVs that growth/broadening of the PSD is driving the MDV evolution.

Within the DGZ (Figure 4.7-f), the slow edges show that the magnitude of the slowdown starts to increase around  $-17\text{ }^{\circ}\text{C}$ ; this figure shows that the maximum slowdown happens around  $-12\text{ }^{\circ}\text{C}$  and the magnitude of the maximum slowdown ( $0.1 - 0.3\text{ m/s}$ ) correlates with increasing DWR class. In addition, the highest two classes of the slow edge show positive DV up to  $0.3\text{ m/s}$ , indicating that an updraft is taking place in this region. The fast edges also show a slowdown within DGZ ( $0.1\text{ m/s}$ ), but its magnitude does not correlate so clearly with the increase of the DWR class number as observed for the slow edges. However, the slowdown of the fast edges cannot be explained by bimodalities alone. The slowdown of both spectra edges supports the hypothesis of an updraft in this region as suggested by (Kennedy and Rutledge, 2011; Schrom et al., 2015).

An updraft is expected to affect both spectra edges equally, but Figure 4.7-f shows that the edges are asymmetrically affected by the slowdown suggesting that a microphysical might be affecting one edge more than other. The presence of an updraft within DGZ also increases the ventilation velocity over the ice particles that are falling in this region. Laboratory studies from Keller and Hallett, (1982) and Takahashi et al., (1991) show that an increase of the ventilation at  $\approx -15\text{ }^{\circ}\text{C}$  enhances the mass growth rate of the particles and reduces the water supersaturation level needed for plates grow as dendrites. Additionally, an updraft can enhance aggregation by creating a size-sorting effect. Small particles falling from regions aloft entering the updraft region would remain in this region and grow continuously (e.g. by deposition, aggregation or riming) until reaching a critical point when the weight force overcome the drag force and then the particles leave the updraft region. This effect could explain the enhancement of DWR-KaW and the rapid increase of the Doppler velocity in this region.

At temperatures warmer than  $-10\text{ }^{\circ}\text{C}$  (Figure 4.7-f), the slow edge profiles are equally affected by a slowdown, while the DV of the fast edge continuously increases. A possible reason for this feature is an upward air motion in this region, which would favour the presence of supercooled liquid water (Zawadzki et al., 2001). The supercooled liquid water would lead to the formation of rimed particles, which increases the fall velocities of the particles (Heymsfield and Kajikawa, 1987; Locatelli and Hobbs, 1974; Mitchell et al., 1990; Mosimann, 1995; Zikmunda and Vali, 1972). The presence of riming in this temperature region is supported by the results from Kneifel and Moisseev, (2020), which show that the frequency of riming sharply increases for temperatures warmer than  $-12\text{ }^{\circ}\text{C}$ .

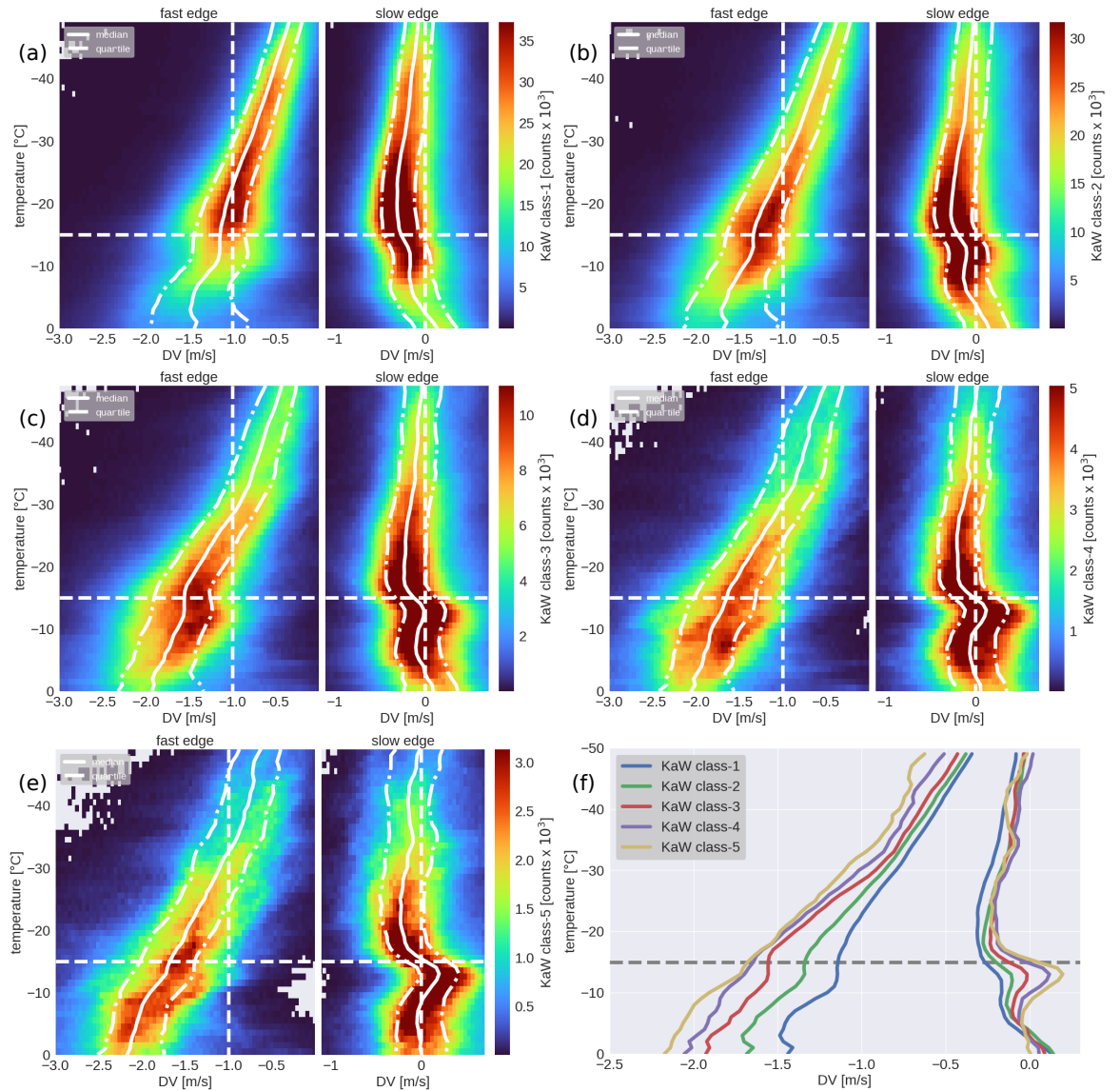


Figure 4.7: Similar as Figure 4.4 but for the slow and fast edges of the Doppler spectra. The vertical dashed lines at the fast and slow edge panels indicate the fall velocities of  $-1\text{ m/s}$  and  $0\text{ m/s}$ , respectively.

In order to evaluate if an updraft in the DGZ could be enhancing depositional growth or even nucleation of new particles and then enhancing aggregation, the following analysis investigates the vertical separation between the region of maximum slowdown and the region where aggregation is enhanced. The maximum slowdown is calculated according to the Equation 4.1.  $DV_{se}(T = -20)$  is the Doppler velocity of the slow edge at  $-20$  °C and  $DV_{se}(DGZ)$  is the Doppler velocity of the slow edge in the DGZ.

$$mSLOW = \max[DV_{se}(T = -20) - DV_{se}(DGZ)] \quad (4.1)$$

Figure 4.8 shows the 2D-histogram of the maximum height difference between the maximum DWR and maximum slowdown as a function of the mDWR-KaW in the DGZ. The analysis shows that there is a broad spread of the height differences for small mDWR-KaW values, and the spread reduces with increasing mDWR-KaW. This increase of the spread towards small mDWR-KaW could result from fluctuations in the DWR-KaW that could cause a misidentification of the height of the mDWR-KaW. The median height difference as a function of the maximum DWR-KaW indicates that for mDWR-KaW smaller than 2 dB the height of the mDWR-KaW is higher than the height of the mSLOW, but for larger values, the height separation reverses and height of the mSLOW becomes higher than the height of the mDWR-KaW. The median difference suggests a stabilization of the height difference  $\approx 400$  m for mDWR-KaW larger than 5 dB. This result suggests that a new mode of small ice particles is forming in the region of the maximum slowdown first and then enhancing aggregation below.

The combined analyses of the MDV, DWRs, and spectral Doppler edges profiles sorted by the maximum DWR-KaW classes suggest an overall increase of the particles sizes starting at  $-30$  °C and that this increase in sizes correlates with the intensification of aggregation in the DGZ. This analyses showed that an updraft is taking place in the DGZ and the intensification of the updraft correlates with the intensification of aggregation in the DGZ. The spectral edges revealed an asymmetric broadening of the Doppler spectra within DGZ suggesting that in addition to the updraft another microphysical process might be taking place in this region and correlating with the intensification of aggregation.

#### 4.4 AGGREGATION WITHIN DGZ AND DOPPLER SPECTRAL BIMODALITIES

Results from previous studies (Section 4.1) and the case study presented in Section 4.2 indicate that bimodalities are often found in the region of the slowdown. The analysis based on the spectra edges

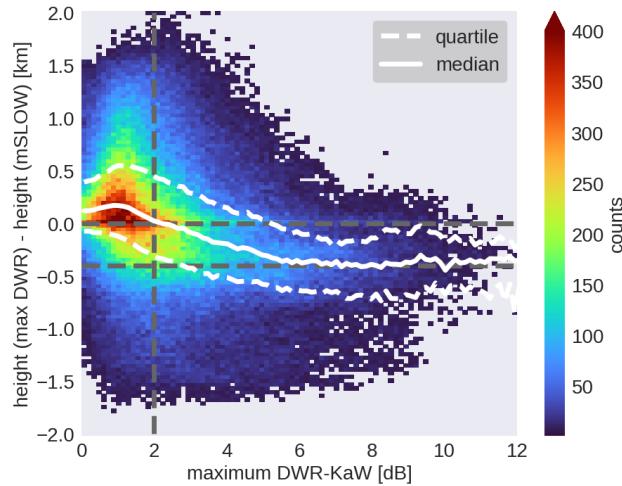


Figure 4.8: Histogram of the height separation between the mDWR-KaW and mSLOW as a function of mDWR-KaW. The continuous and dashed white lines are the median and quartiles of the distribution. The horizontal grey lines indicate the separation height at 0 and 0.4 km. The vertical grey line at 2 dB indicates the point where the median height separation reverses.

revealed an asymmetrical broadening of the spectra in the DGZ, but the spectral edges are including all cases (bimodal and non-bimodal). In order to investigate further if a clear separated spectral mode correlates with the intensification of aggregation in the DGZ, the Peak-Map (see [Section 3.4](#)) and DWR-KaW datasets are used.

For this analysis, only data laying in the DGZ is used, and all DWR-KaW profiles are flagged as mono-peak or multi-peak using the Peak-Map data. A DWR-KaW profile is classified as mono-peak when all data points from the corresponding Peak-Map profile are only mono-peak; otherwise, it is identified as multi-peak. Once the classification has been applied, the mDWR-KaW and its co-located DWR-XKa from each profile are stored.

[Figure 4.9-a](#) shows the probability distribution curves (PDC) of the mDWR-KaW values of the mono-peak and multi-peak profiles. The maximum probability of the mono-peak profiles is found where the mDWR-KaW is  $\approx 1$  dB, and the probability decrease with increasing mDWR-KaW. For the multi-peak profiles, the maximum probability happens at slightly higher mDWR-KaW ( $\approx 2$ ) dB. As the mono-peak profiles, the probability of the multi-peaks rapid decreases with increasing mDWR-KaW. The difference between the mono-peak and multi-peak PDCs ([Figure 4.9-b](#)) shows that there is a higher probability for mDWR-KaW values larger than 2 dB to occur in case of multi-peak profiles. In total, the probability of an mDWR-KaW larger than  $\approx 2$  dB to occur in a multi-peak scenario is  $\approx 25\%$  higher than in a mono-peak scenario. [Figure 4.9-c](#) shows the PDC of the collocated DWR-XKa of both mono- and multi-peak scenarios. One can see that there are no

significant differences between both PDCs, indicating that the larger particles from the multi-peak cases are not large enough ( $D_0$ : 1 – 5 mm) to enhance the DWR-XKa in the DGZ significantly.

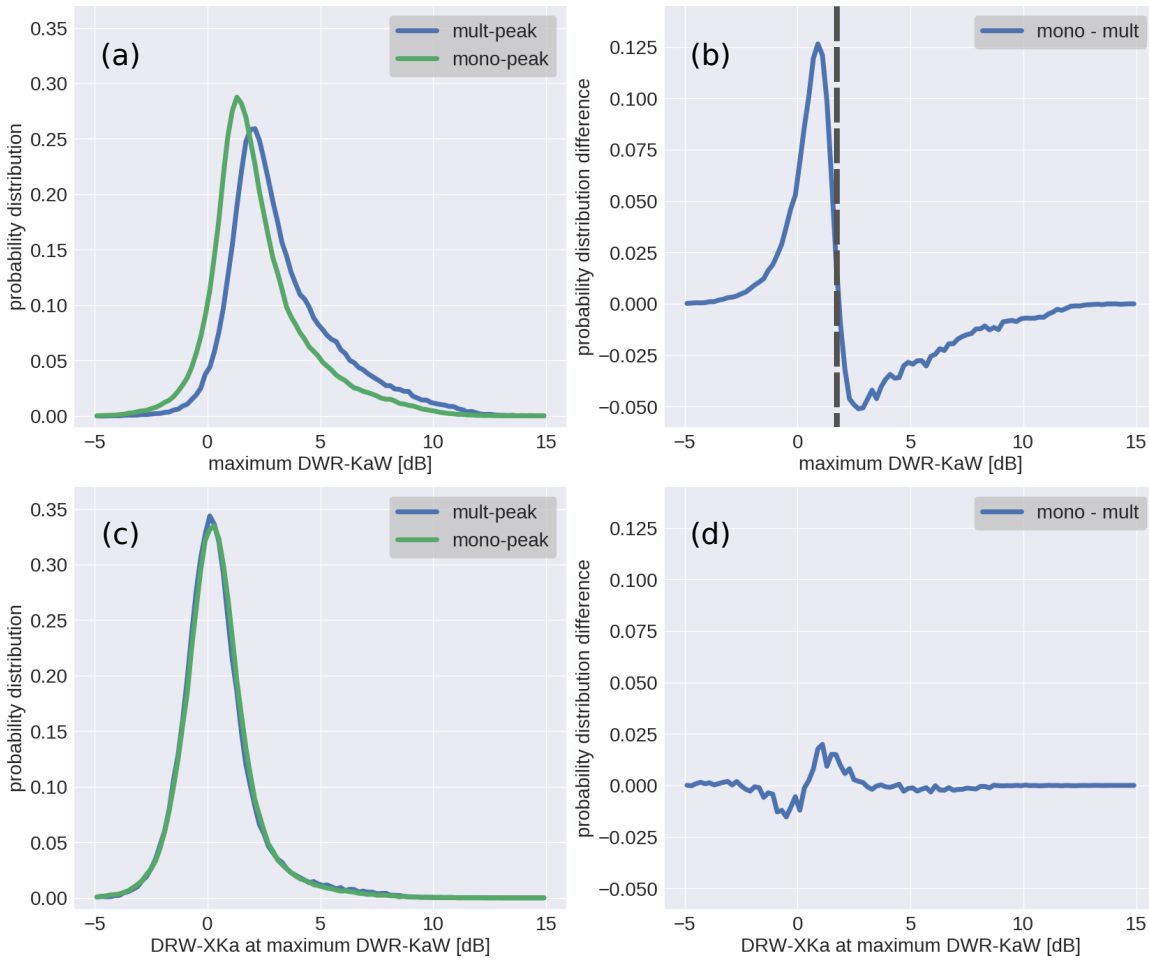


Figure 4.9: Panels a) and c) are the probability distributions of the mDWR-KaW within DGZ and the co-located DWR-XKa of the mono- and multi-peak classes, respectively. Panels b) and d) are the differences between the probability distributions of the mono- and multi-peak classes of the mDWR-KaW and the co-located DWR-XKa, respectively. The vertical dashed grey line in Panel b) indicates the mDWR-KaW of 2 dB.

The bimodalities are often observed in the DGZ, and one could expect that the scenarios of clear bimodalities would have a strong correlation with aggregation in the DGZ. The statistical results indicate that the probability of observing enhanced mDWR-KaW for multi-peak cases is around 25% higher than for mono-peak cases. However, the probabilities of multi-peak cases may be underestimated due to the methodology applied in the identification of the spectral peaks (described in [Section 3.4](#)). Therefore, a detailed analysis using a more robust bimodality detection is needed for providing a better



understanding of the connection between the presence of bimodalities within DGZ and enhancement of aggregation.

#### 4.5 AGGREGATION WITHIN DGZ AND CLOUD TOP TEMPERATURE

Another hypothesis for the enhancement of aggregation in the DGZ suggests that high and cold cloud tops would lead to the formation of a large diversity of ice particles (Kumjian et al., 2014) and high concentration of primary ice (Bailey and Hallett, 2009; DeMott et al., 2010). Those particles would grow by vapour deposition or aggregation while falling in regions above the DGZ. In the DGZ, those particles would rapidly grow by deposition and thus their size would increase fast. The large size of these crystals would enhance aggregation (Griffin et al., 2018). Based on this hypothesis, one can expect a positive correlation between the CTT and the size of the aggregates in the DGZ. Using multi-frequency vertically pointing radars, one could expect that the colder is the CTT, the larger is the DWR-KaW within the DGZ.

In order to evaluate this hypothesis, the CTT is retrieved as the temperature at the same altitude of the highest observed Ze-Ka pixel from each profile. The CTT are grouped into three classes of increasing mDWR-KaW. The first two classes are the class-1 and class-2 (0 – 2 dB and 2 – 4 dB, respectively) introduced in Section 4.3. To account for the reduction of the number of profiles that have CTT > –30 °C with increasing mDWR-KaW, as indicated in Figure 4.9, the last three classes from Table 4.1 are grouped as one new class (mDWR-KaW 4 – 20 dB). Figure 4.10 shows the probability distribution of the CTT for the different classes. One can see that the CTT probability decreases with increasing temperature, and it becomes almost stable between –30 and –20 °C. The PDCs do not reveal any significant difference between the classes, which indicates that, at least for our dataset, there is no correlation between the CTT and mDWR-KaW. This result is similar to the findings of Trömel et al., (2019) where no clear dependence between CTT and ZDR in the DGZ was found, contrasting to the result found by Griffin et al., 2018.

*The statistical results from Griffin et al., 2018 are based on 5 cases, which could explain the difference.*

It is essential to mention that due to the uncertainties in the methodology used to relate the CTT and the mDWR-KaW within DGZ, the correlation between the two quantities might be hidden. This methodology assigns a CTT value from a profile at a particular time to the mDWR-KaW value within DGZ from the same profile. One could expect a large uncertainty since the higher the cloud top, the larger is the time required for ice particles produced at the cloud top to reach the DGZ and thus the higher is the chance that the DWR-KaW signatures within DGZ are not directly connected to the particles close to the cloud top.



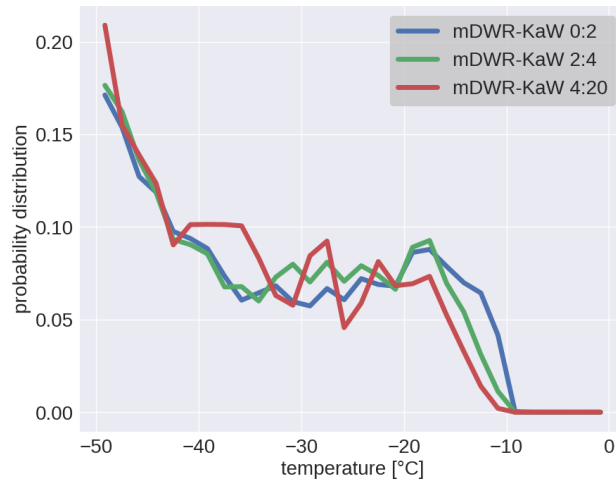


Figure 4.10: Probability distribution curves (PDC) of the CTT grouped according to the mDWR-KaW in the DGZ. Each distribution is normalized by its total number of counts.

#### 4.6 CONCLUSION

In this chapter, the long term combined dataset from TRIPEX and TRIPEX-Pol campaigns was used to investigate if the intensification of aggregation within DGZ is related to an updraft within DGZ (SCN-1) or to a microphysical process (SCN-2). For the investigation of the SCN-1, the vertical profiles of the commonly used radar variables DWR-KaW, DWR-XKa, MDV and the novel dataset of spectra edges profiles were classified according to the maximum DWR-KaW (mDWR-KaW) in the DGZ. For investigating the SCN-2, the dataset of identified spectral modes was used to classify the data according to the occurrence of mono- or multi-modal spectra within DGZ.

The statistical analysis showed that the increase in the maximum size of aggregates in the DGZ correlates with the initial growth of particles at temperature regions above the DGZ. This correlation is indicated by the increase of the gradients from DWR-KaW (from 0.01 to 0.1 dB/°C, Figure 4.4) and the Doppler velocity of the fast edge (from  $-0.024$  to  $-0.046 \frac{\text{m}}{\text{s}^\circ\text{C}}$ , Figure 4.7) with increasing mDWR-KaW suggesting the presence of large and faster particles above the DGZ. The increase in aggregate sizes also correlates with the intensification of the slowdown (0.1 – 0.3 m/s) of the slow edge in the DGZ. The slowdown is found on both edges and the fact that the slow edge even shows upward motion of hydrometeors support the hypothesis of the SCN-1, suggested by previous studies, that an updraft within DGZ increases the supersaturation leading to an intense depositional growth and then favouring the growth of dendritic structure on the ice particles.

The combined analysis between mDWR-KaW and the occurrence of multi-peaks showed that 25% of the mDWR-KaW larger than 2

dB occurred for radar profiles that present multi-modalities in their Doppler spectra (Figure 4.9) suggesting that the presence of multiple particles types contributes to the enhancement of the aggregation. However, it must be noted that the underestimation of multi-modality occurrence, due to the methodology applied, might have compromised the statistics. The technique requires a well-defined separation between the spectral peaks and therefore, a more robust peak-identification method is needed to investigate the connection between the occurrence of multi-modality and the intensification of aggregation.

The results of the statistical analyses did not show a correlation between the CTT and intensification of aggregation within DGZ (Figure 4.10). Again, the weak correlation may result from the methodology applied; which uses the CTT and the mDWR-KaW from the same radar profile. However, those results support the results of Trömel et al., (2019). Additionally, this absence of a clear correlation suggests that another factor is enhancing aggregation in the DGZ. As shown in sections Section 4.3 and Section 4.4, the enhance of aggregation within DZG correlates with the increase of particles sizes and fall velocities in temperature regions between  $-30$  and  $-20$  °C. From the aggregation kernel (Equation 2.3) one could expect that due to the larger range of sizes and velocities aggregation could be enhanced in the DGZ. However, the only way to investigate the impact of the different components is by using model simulations (e.g. McSnow, Brdar and Seifert, (2018)) .

*McSnow is a Monte-Carlo ice microphysics model to simulate the evolution of ice particles due to deposition, aggregation, riming, and sedimentation.*

## INTENSIFICATION OF AGGREGATION NEAR THE MELTING LAYER

---

The initial analysis from the data collected during the TRIPEX campaign (Figure 9 from Dias Neto et al., (2019)) shows that the main increase in DWR-XKa occurs close to the melting layer (ML). This result suggests that even larger aggregates than that found in DGZ are often formed in a second temperature region (from  $-10$  to  $0$  °C). This chapter focuses on the growth of snowflakes by aggregation close to the ML and addresses the following scientific questions: 1) Is the enhancement of aggregation close to the ML top influenced by aggregation that happens aloft in the DGZ? 2) How does aggregation close to the ML change the rain properties below the ML? 3) How much is the assumption that each snowflake melts into a mass equivalent raindrop justified? This chapter is structured as follows. Section 5.1 shows an example case where the DWR-XKa is enhanced close to the ML top. In Section 5.2, a statistical analysis similar to that used in the DGZ (Chapter 4) is applied to the vertical profiles of DWRs, MDV and spectra edges from the combined TRIPEX/TRIPEX-Pol dataset to answer the first question. In Section 5.3 the correlation between the characteristic size of raindrops and DWR-XKa near ML top is studied in order to answer the second question. Section 5.4 correlates Ze flux ratio from ML top and bottom with the DWR-XKa at ML top to answer the third question. Finally, Section 5.5 summarizes the findings and draw conclusions.

### 5.1 CASE STUDY OF INTENSE AGGREGATION CLOSE TO MELTING LAYER TOP

This section shows a case study of exceptionally strong aggregation close to the melting layer top. This case study is used to introduce the radar signatures that later will be analysed statistically. On December 31, 2015, a stratiform rainfall event passed over JOYCE-CF between 4 : 00 and 9 : 00 UTC, which produced approximately 0.5 mm accumulate precipitation. Figure 5.1 shows the time-height plots of Ze, MDV, DWR-XKa, DWR-KaW and LDR recorded by the radars during that period. The Ze-Ka (Figure 5.1-a) generally increases towards the ground, except around 5 : 30 and 6 : 30 UTC closet to ML top where Ze-Ka decreases. The bright band can be identified at  $\approx 2$  km, suggesting that the frozen particles are starting to melt close to this height (Fabry and Zawadzki, 1995; Rico-Ramirez and Cluckie, 2007). At altitudes higher than 8 km, close to the cloud top, the measured MDV-Ka (Figure 5.1-

b) is approximately  $-0.5$  m/s. The MDV-Ka reaches the typical fall velocity of unrimed snowflakes  $\approx 1$  m/s at around 8 km and it keeps constant until reaching the ML top, except around 05 : 30 UTC and between 4 and 2 km where MDV-Ka reaches 2 m/s indicating the presence of rimed particles. At altitudes around 5 km and close to  $-15$  °C isotherm, the MDV plot shows a pronounced slowdown ( $\approx 0.4$  m/s) consistent with statistics discussed in [Section 4.3](#). The analyses in [Section 4.3](#) indicated that it is likely a result of localised updrafts. At around 2 km and coinciding with the bright band, MDV sharply increases and reaches values larger than 2.5 m/s as a result of the conversion of frozen hydrometeors into raindrops. [Figure 5.1-c](#) and [Figure 5.1-d](#) show that the both DWRs remain smaller than 5 dB above the  $-15$  °C isotherm, indicating that the ice particles are not large enough ( $D_0 < 1$  mm) to enhance the DWRs. Below the  $-15$  °C isotherm, DWR-KaW ([Figure 5.1-c](#)) increases and reaches a saturation point around 8 dB while DWR-XKa ([Figure 5.1-d](#)) slowly increases towards the ML, reaching values up to 15 dB. Note that the DWR-XKa generally cannot be reliably computed for altitudes higher than 8 km due to the low sensitivity of the X-Band radar used during the TRIPEX campaign (see [Section 3.1](#)). LDR ([Figure 5.1-e](#)) is almost constant around  $-25$  dB for the entire period from cloud top down to the bright band altitude. Within the bright band, LDR sharply increases to values larger than  $-20$  dB, indicating the presence of partially melted particles (Bandera et al., 1998; Tian et al., 2007). Below the ML, LDR reduces to values around  $-30$  dB which is typical of rainfall (Fabry, 2015; Raghavan, 2003).

A particularly relevant enhancement of the DWR-XKa close to the bright band was observed around 06 : 50 UTC ([Figure 5.1-d](#)). In order to investigate this enhancement of the DWR-XKa, averaged profiles of Ze, MDV, DWR, and LDR for a 10 minutes time window centred at 06 : 50 UTC are calculated and shown in [Figure 5.2](#). The Ze profiles from X-, Ka- and W-Band ([Figure 5.2-a](#)) show different regimes in four distinct altitude regions. The first region is at altitudes above 5 km where the reflectivity profiles are overlapping, indicating that most of the particles are behaving like Rayleigh scatterers at each of the three frequencies. In the second region, between 5 and 3 km, Ze-W shortly increases up to 14 dBZ slightly below 5 km and then the profile remains almost constant around 11 dBZ while Ze-Ka and Ze-X exhibit a sharp peak: a rapid increase of reflectivity (Ze-Ka: from 10 to 18 dBZ and Ze-X: from 10 to 22 dBZ) is followed by a noticeable decrease (Ze-Ka and Ze-X down to 14 dBZ) between 5 and 4 km. It indicates an intense increase and decrease of mean particle sizes within a height region of 1 km. As discussed in details in [Chapter 4](#), the sudden increase in Ze and DWR at  $-15$  °C is most likely caused by intense growth of dendritic-like particles favouring aggregation and then leading to the formation of large aggregates. Due to increase

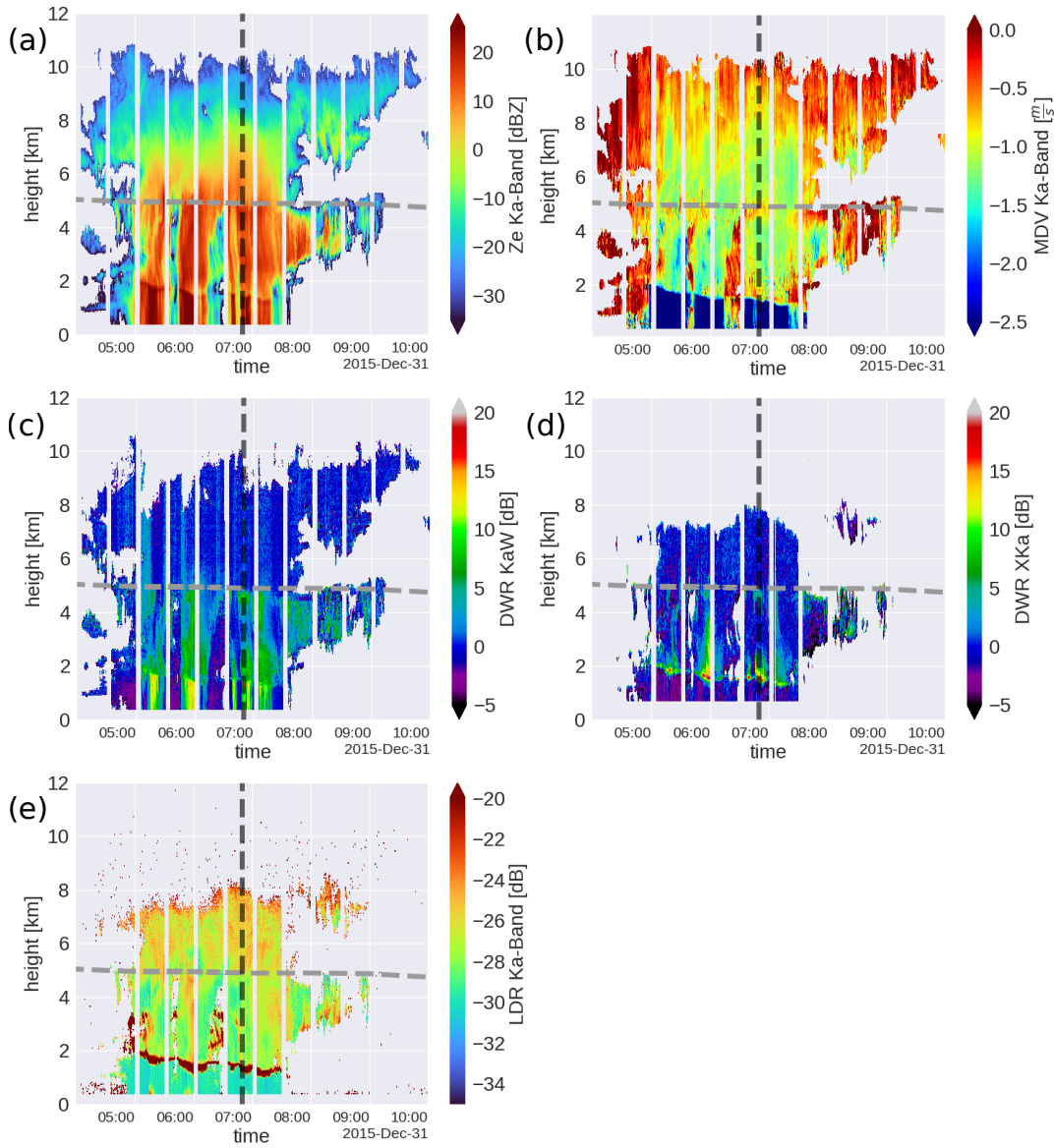


Figure 5.1: Time-height plots of radar reflectivity factor Ze (a), mean Doppler velocity (b) and negative values indicate downward motion, dual wavelength ratios DWR-KaW (c) and DWR-XKa (d), linear depolarization ratio LDR (e). The DWR-XKa is limited to a maximum altitude of 7 km because of less sensitive of the X-Band used during TRIPEX. The vertical dashed grey line indicates 06 : 50 UTC and the horizontal line indicates the  $-15\text{ }^{\circ}\text{C}$  isotherm.

in size, those aggregates transition to non-Rayleigh scattering regime at W-Band. One can speculate that the reduction of particles size below could result from break up of aggregates due to collision or sublimation. However, for investigating the hypothesis of sublimation, it would require detailed information on the humidity profile, which is not available. The third region is between altitudes of 3 km and 1.5 km, where Ze-X slowly increases up to 18 dBZ while Ze-Ka and Ze-W decrease down to 7 and 2 dBZ, respectively. This behaviour suggests that the aggregates are growing to very large sizes and transitioning to non-Rayleigh scattering regime at Ka-Band. The fourth region is between ML top at 1.5 km and the ground, where Ze-X slightly increases up to 22 dBZ and then decreases down to 15 dBZ while Ze-Ka and Ze-W increase up to 17 dBZ. One can see that the lowest part of Ze-Ka and Ze-X profiles have almost the same values, but Ze-W is 7 dB lower than the other two profiles. This difference is likely to result from the non-Rayleigh scattering regime of the droplets and rain attenuation; as described in [Section 2.2.2.1](#), the W-Band signal is the most affected by attenuation when compared to Ka- and X-Band signal.

The interpretation of the Ze profiles becomes clear when adding the DWR profiles ([Figure 5.2-b](#)). One can see that the DWR profiles also show distinct behaviours in the same four regions. In the first region (above 5 km), both DWRs are around 0 dB indicating that most of the particles are scattering in the Rayleigh regime for all the three frequencies. Inside of the second region (between 5 and 3 km), the DWR-KaW and DWR-XKa first increase up to  $\approx 9$  and  $\approx 4$  dB respectively, and decrease down to 2 and 0 dB, respectively. This sharp increase contrasts with the continuous increase of both DWRs shown in [Figure 4.3](#), and it provides an additional indication that the growth by aggregation is very efficient. From DWR- $D_0$  relation ([Figure 2.16](#)), one can estimate the increase of  $D_0$  within this 500 m region from 1 to 4 mm. The sharp reduction of both DWRs suggests that the opposite effect is taking place and reducing the particle sizes. In the third region (between 3 and 1.5 km), DWR-KaW increases up to  $\approx 8$  dB while DWR-XKa continuously increases up to 10 dB, suggesting an intense growth by aggregation. In the fourth region (below 1.5 km), the DWR-XKa slightly increases and then decreases to negatives values  $\approx -1$  dB and remains constant towards the ground. Those slightly negative values may result from the methodology used to correct the reflectivity profiles in the ice part of the clouds (introduced in [Section 3.1](#)). However, negative DWR-XKa values are expected for raindrops with  $D_m$  between 0.5 and 1.5 mm (Battaglia et al., 2020). In the same fourth region, the DWR-KaW increase and then remain constant  $\approx 8$  dB, which could result from non-Rayleigh scattering regime and attenuation.



In continuity with the investigation, the MDV-Ka profiles (Figure 5.2-c) show that at around 6 km (in the first region), the MDV-Ka is approximately  $-1.2$  m/s, which could result from the continuous growth by deposition or initial aggregation (Atlas et al., 1973; Karrer et al., 2020; Pruppacher and Klett, 1997). Between 6 and slightly below 5 km, the MDV-Ka first reduces from  $-1.2$  m/s to about  $-0.7$  m/s. It is likely that this sudden reduction of the MDV-Ka is at least partly caused by an updraft and then contributing to the growth of aggregates as described in Section 4.3. In the second region, between 5 and 4 km, MDV-Ka sharply increases from  $-0.7$  up to  $-1.3$  m/s and between 4 and 3 km MDV-Ka decreases from  $-1.3$  down to  $-1.1$  m/s. This reduction in MDV-Ka continues within the third region where MDV-Ka reaches  $-0.7$  m/s at 1.5 km. Similar to the first region, this last reduction of the fall velocities (within the third region) is likely to result from an updraft because continuous aggregation would result in an almost constant MDV-Ka around  $-1$  m/s. Below 1.5 km and toward the ground, MDV-Ka sharply increases to velocities faster than  $-2$  m/s, which indicates the transition to rain.

LDR (Figure 5.2-d) is constant around  $-25$  dB in the first region and it reduces to  $-27$  dB and remains constant in the second and third region. This reduction in LDR values provides an additional indication that aggregation is taking place below the first region. In the fourth region, LDR sharply increases between 1.5 and 1.0 km indicating the melting layer. Below 1 km, LDR is constant around  $-30$  dB, indicating the presence of raindrops.

In order to investigate further the intensification of aggregation close to ML top and the reduction of the Ze-Ka and Ze-W that starts at 3 km, the triple-frequency plot of the DWR-KaW and DWR-XKa pairs from the region between 3 and 1.5 km and within 10 minutes time window centred at 06 : 50 UTC is shown in Figure 5.3-a. For this investigation, the ML top was identified using LDR as described in Section 3.5, and after that, all data laying between ML top and 120 m above the top was excluded. Figure 5.3-a shows the typical bending-up signature, as found by previous studies (Kneifel et al., 2015), followed by a slightly bending-back signature, which results from a continuous increase of DWR-XKa and an increase of DWR-KaW followed by a decrease with increasing particle sizes (see Section 2.2.2). In fact, as DWR-XKa continuously increases up to 14 dB, with increasing temperature, the DWR-KaW increases up to a saturation point (8 dB) and then slightly decreases to 6 dB. As introduced in Section 2.2.2, this scenario suggests that aggregation was significantly enhanced in this region and led to the formation of large aggregates able to cause a reduction in the DWR-KaW. This enhancement of aggregation could result from a combination of two mechanisms. The first one is the increase of the sticking efficiency with increasing temperature (described in Section 2.1). The second one is the occurrence of an

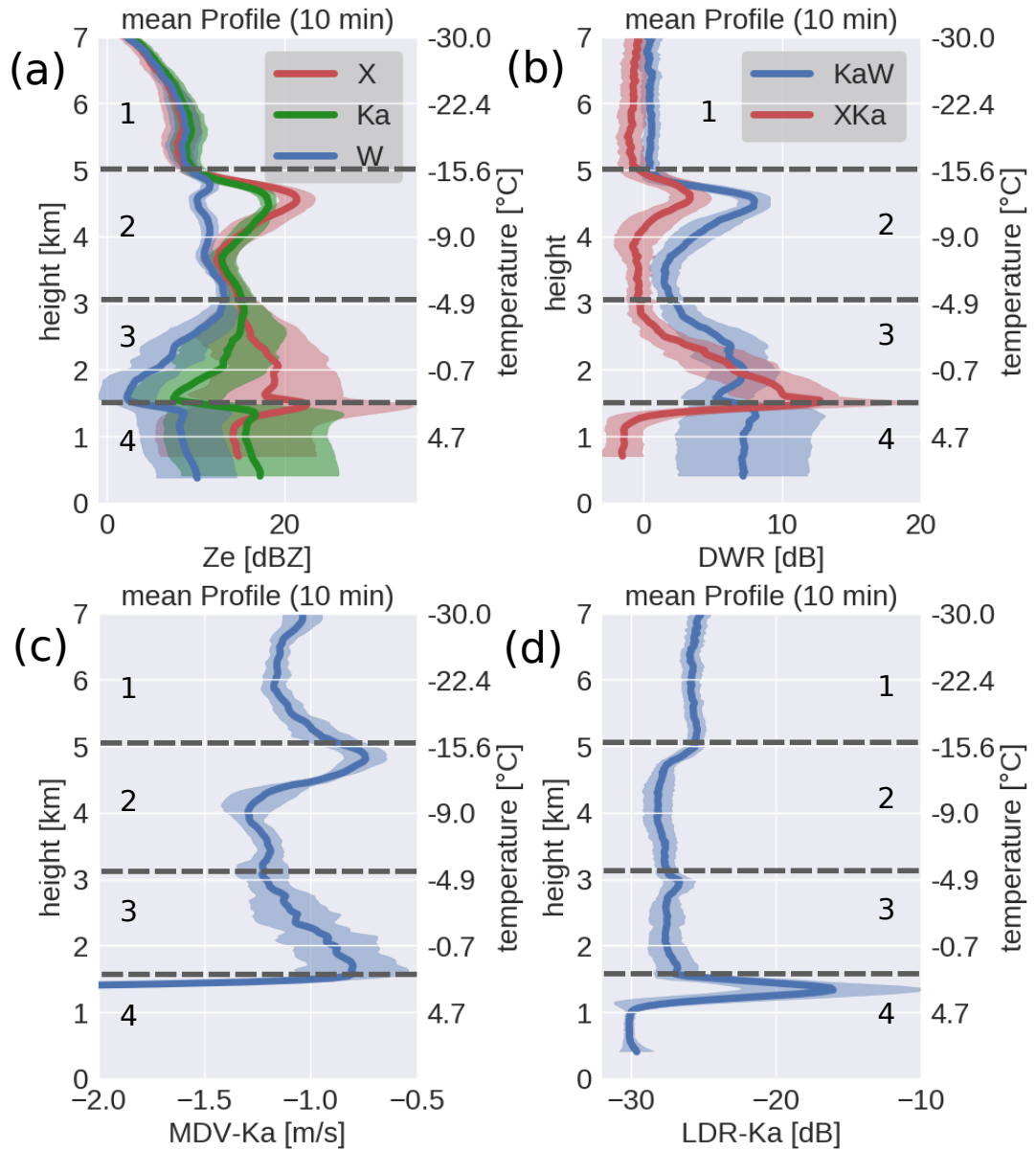


Figure 5.2: Ten minutes averaged profiles of the radar variables on December 31<sup>st</sup>, 2015 centred at 06 : 50 UTC. In panel (a) the blue, green, and red curves are Ze profiles from W-, Ka- and X-Band, respectively. In Panel (b), the red and blue curves denote DWR-XKa and DWR-KaW, respectively. Panels (c) and (d) shows the MDV and LDR profiles from Ka-Band. The standard deviation is indicated by the contour along each profile. The numbers indicate the different defined regions.

updraft, suggested by the reduction of the fall velocity in [Section 5.2-c](#), which would increase saturation and hence depositional growth but also increase the residence time of the particles by reducing their sedimentation velocity; both effects would favour aggregation.

[Figure 5.3-b](#) shows the theoretical evolution of the DWR-KaW and DWR-XKa pairs from four scattering models of non-rimed aggregates ([Table 5.1](#)) ([Leinonen and Szyrmer, 2015](#); [Mróz et al., 2020a](#); [Ori et al., 2014](#)) as a function of the PSD size parameter  $D_0$ . One can see that the different scattering models can reproduce the initial growth of particles (DWR-KaW < 6 dB and DWR-XKa < 3 dB); however, the later growth stage (DWR-KaW > 6 dB and DWR-XKa > 3 dB) is only reproduced for extremely large  $D_0$  (as large as 20 mm). The only exception is the OC model that can reach large DWR-XKa values 14 dB with  $D_0 \approx 10$  mm, but OC has a much higher DWR-KaW saturation point when compared to the other models. The saturation point difference could be related to the methodology used to produce aggregates (e.g. density constrain) and the shape of the PSD. [Figure 5.3](#) also indicates that even with  $\mu$  parameter as high as 4 the simulated DWR-XKa still requires extreme large  $D_0$  (20 mm) in order to reach 14 dB. One can question the realism of this simulation since unrealistic  $D_0$  values are required to reproduce the observations. However, this analysis suggests that the reduction of Ze-Ka and Ze-W and large DWR-XKa (14 dB) close to the ML top are likely to result from the presence of extreme large aggregates.

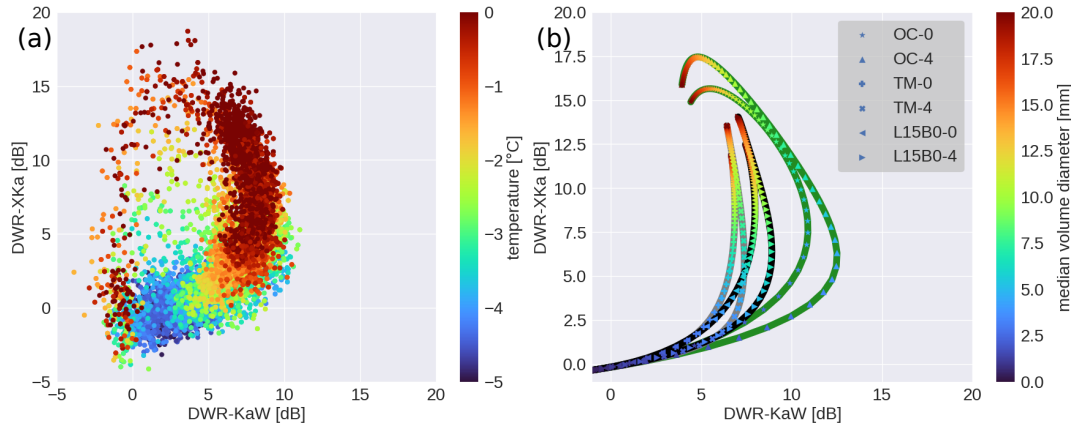


Figure 5.3: Triple-frequency plot of all DWR-XKa and DWR-KaW pairs. Panel (a) is from the observed DWR pairs from the temperature region between  $-5$  and  $0$  °C in [Figure 5.2-b](#), the color code indicates temperature. Panel (b) is from simulated DWR pairs of three unrimed aggregate models using a gamma distribution for  $\mu$  equal to 0 and 4, and the color code indicates  $D_0$ . See [Table 5.1](#) for the list of the used models.

Table 5.1: List of the of the aggregate scattering models used to simulate the DWRs pairs in Figure 5.3-b.

scattering model	short description	$\mu$ parameter
OC-0	aggregates of columns	0
OC-4	(Ori et al., 2014)	4
TM-0	aggregates of columns and	0
TM-4	dendrites (Mróz et al., 2020a; Ori et al., 2020b)	4
L15B0-0	aggregates of dendrites	0
L15B0-4	(Leinonen and Szyrmer, 2015)	4

## 5.2 STATISTICAL ANALYSES OF AGGREGATION SIGNATURES CLOSE TO ML TOP

In order to investigate the growth of aggregates at regions between the DGZ and ML top and search for correlations with particles growing in the DGZ and regions above, a profile classification of the radar recorded variables, similar to the classification used in Section 4.3, is applied to the combined TRIPEX/TRIPEX-Pol dataset. As shown in Figure 9 from Dias Neto et al., (2019), the DWR-KaW reaches its saturation point within the DGZ while the DWR-XKa continuously increases towards the 0 °C isotherm. Therefore, the profiles are classified according to the maximum DWR-XKa (mDWR-XKa) from temperature regions between  $-10$  and  $-1$  °C. The maximum temperature is limited to  $-1$  °C to reduce the potential of identification error of mDWR-XKa due to initially melted particles. Table 5.2 lists the mDWR-XKa intervals used for the classification. For the following analysis, three main temperature regions are defined. The first region is for temperatures colder than  $-20$  °C (above the DGZ). The second region is for temperatures between  $-20$  and  $-10$  °C (DGZ). The third temperature region is between  $-10$  and 0 °C (below the DGZ).

Table 5.2: mDWR-XKa intervals defined to represent aggregates at the different growth stage close to the ML top.

mDWR-XKa classes	mDWR-XKa interval	number of profiles
class-1	0-2	65924
class-2	2-4	100954
class-3	4-6	43254
class-4	6-8	20667
class-5	8-20	24113

As introduced in section [Section 2.2](#), DWR-KaW is sensitive to the initial growth of ice particles. In order to investigate if this initial growth of ice particles above the DGZ correlates with the formation of large aggregates close to the ML top, the DWR-KaW profiles are classified using the mDWR-XKa classes. [Figure 5.4-\(a-e\)](#) shows the histograms of the DWR-KaW classified according to mDWR-XKa.

Above the DGZ, the different histograms show that the DWR-KaW data is distributed around 0 dB, which is also indicated by the 25 and 75 percentiles. The histograms also show that the spread of data towards large DWRs increases with increasing temperature and mDWR-XKa classes. These results suggest that most of the particles above the DGZ are experiencing a slower growth process such as water vapour deposition or initial aggregation. Within DGZ, the histograms show a trend of increasing DWR-KaW with increasing mDWR-XKa classes, suggesting an intensification of aggregation and enhancement of the growth of the ice particles. As described in [Section 2.1](#), dendrite-like crystals grow in this temperature region and this kind of crystal favour aggregation and formation of large particles. Below the DGZ, the histograms indicate that the DWR-KaW is almost constant with temperature, but this constant value increases with increasing mDWR-XKa classes.

[Figure 5.4-f](#) shows the comparison between the median profiles from each mDWR-XKa class. Above the DGZ, in temperature regions colder than  $-30$  °C the median DWR-KaW profiles are close to 0 dB, but between  $-30$  and  $-20$  °C the DWR-KaW profiles show an increasing trend with a gradient of  $0.067$  dB/ °C. In the DGZ, between  $-20$  and  $-15$  °C, the different profiles remain with the same gradient  $0.067$  dB/ °C and the DWR-KaW increases up to  $0.05$  dB. In contrast, between  $-15$  and  $-10$  °C, the gradient increases from  $0.067$  to  $1.1$  dB/°C with increasing mDWR-XKa classes; the class-1 reaches 1 dB while the class-5 reaches 6 dB. This sharp increase of the DWR-KaW profiles with increasing mDWR-XKa suggests an intensification of aggregation within DGZ, which could result from an intense growth of dendritic crystals (Andrić et al., 2013; Kennedy and Rutledge, 2011; Schrom et al., 2015; Trömel et al., 2019) or multimodal distribution of ice crystal scenario (Barrett et al., 2019; Moisseev et al., 2015). However, the results from [Section 4.4](#) do not indicate a significant enhancement of the DWR-KaW in case of multiple Doppler peaks are detected. This intensification of DWR-KaW with increasing mDWR-XKa class suggests a correlation between the intensification of aggregation within DGZ and the growth of larger aggregates found close to the ML top. Below the DGZ, the DWR-KaW from class-1 decreases down to  $\approx 0$  dB while from classes 2, 3 and 4 it increases up to 2, 5 and 6 dB, respectively; the DWR-KaW from class-5 remains constant around 6 dB.

The results showed in [Figure 5.4](#) contrast with the results from [Section 4.3](#), where there is a clear separation between the DWR-KaW profiles from the different classes in regions colder than  $-15\text{ }^{\circ}\text{C}$ . This difference could arise for two possible reasons. The first one is a possible uncorrelation between the initial growth of ice particles in regions above the DGZ and the growth of aggregates close to ML top. The second reason is a possible limitation of the methodology used to correlate aggregation close to ML top with the other temperature regions. It does not take into account the temporal separation needed for particles growing above the DGZ to reach the warmer regions close to ML top.

The DWR-KaW reaches its saturation point for particles sizes larger than  $\approx 6\text{ mm}$  (see [Figure 2.16-b](#)). In order to investigate the additional growth of ice particles into sizes larger than 6 mm in regions close to ML top, the DWR-XKa profiles are classified according to the mDWR-XKa classes. The histograms of the DWR-XKa classified profiles are shown in [Figure 5.5-\(a-e\)](#). Above the DGZ, the data from the different profile classes are distributed around 0 dB. Inside of the DGZ and below the DGZ, the different panels show a trend of increasing DWR-XKa with increasing mDWR-XKa classes. This increasing of DWR-XKa suggests that the particles inside of these last two regions are experiencing more intense growth process than the particles that are above the DGZ. [Figure 5.5-\(a-e\)](#) also shows the effect of the upper limit of the mDWR-XKa for each class similar to that explained for DWR-KaW histograms [Figure 4.4](#).

The comparison between the median profiles ([Figure 5.5-f](#)) shows that there is an almost constant offset among the various classes above the DGZ, and the offset appears to be increasing with mDWR-XKa classes. The averaged offset of class-1 is stable around 0 dB while for class-5 it is around 0.9 dB, and the averaged offset of classes-2, 3, and 4 populate around 0.5 dB. Although a similar effect is not visible in [Figure 4.4](#), [Figure 4.5](#) and [Figure 5.4](#), this constant offset suggests that the methodology used to correct the Ze profiles (described in [Section 3.1](#)), for some cases, under-estimated or over-estimated the correction. In the DGZ, between  $-20$  and  $-15\text{ }^{\circ}\text{C}$ , the different profiles remain with the same offset from the previous regions. However, between  $-15$  and  $-10\text{ }^{\circ}\text{C}$ , the gradient from the different profiles increases with increasing mDWR-XKa classes. The class-1 has a small negative gradient ( $-0.05\text{ dB}/^{\circ}\text{C}$ ) while the class-5 has the largest gradient ( $0.53\text{ dB}/^{\circ}\text{C}$ ); the gradient from the other three classes are 0.05, 0.16 and  $0.34\text{ dB}/^{\circ}\text{C}$ . Below the DGZ, the DWR-XKa profiles remain with the same gradient; the profile from class-1 decreases to  $\approx -0.05\text{ dB}$ , while the profiles from classes 2, 3, 4 and 5 increase up to 1, 3, 5 and 9 dB, respectively. This continuous increase of DWR-XKa from the DGZ towards the ML supports the hypotheses that large aggregates within DGZ would favour the formation of even larger aggregates close to the



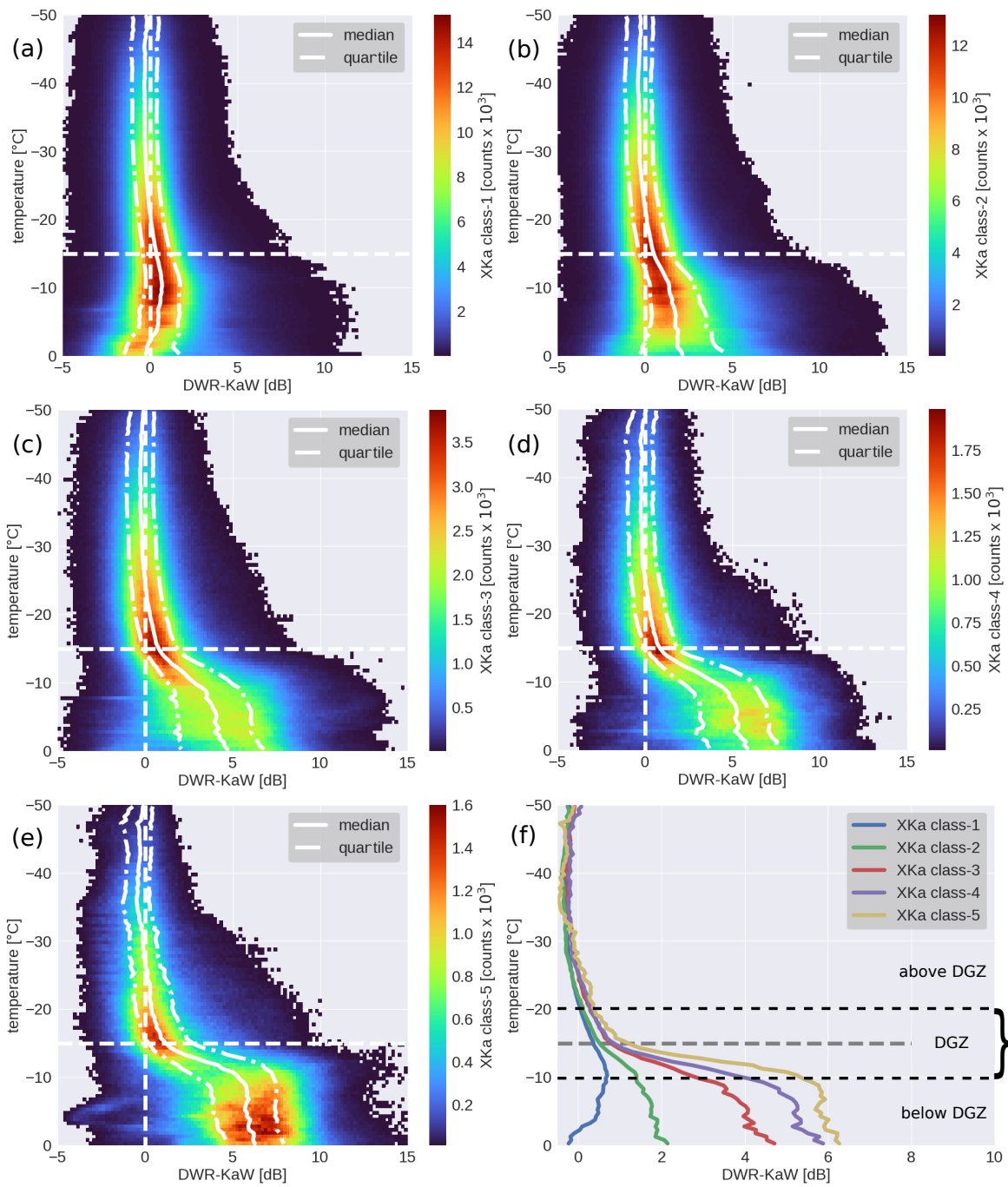


Figure 5.4: Histograms of the DWR-KaW profiles stratified with temperature for the mDWR-XKa classes defined in Table 5.2. Panels a) to e) are for the class-1 to class-5. The continuous and dashed lines are the median and the quartiles of the distribution, respectively. Panel f) is the intercomparison between the median profiles from the different classes. The horizontal and vertical dashed lines indicate the isotherm of  $-15\text{ }^{\circ}\text{C}$  and DWR-KaW equal to 0 dB, respectively.

ML. As described in [Section 2.1](#), the sticking efficiency of ice surfaces increases with increasing temperature; therefore, it would favour the already large aggregates (produced in the DGZ) to grow continuously toward the ML. However, [Figure 4.5](#) in [Section 4.3](#) shows a slightly different result where large aggregates within DGZ could have their size reduced towards the ML. Those results suggest that the presence of large aggregates in the DGZ favour the growth of even bigger snowflakes towards ML, but this is not a necessary condition for that to happen. On the other hand, if big aggregates are found close to ML top, it is likely that the aggregates were already larger within DGZ. [Figure 5.1-b](#) gives an example of this case. One can see that both DWRs sharply decreases below the DGZ and sharply increases towards the ML.

Similarly to the DWR profile classification, the MDV-Ka profiles are classified according to the mDWR-XKa, and the classification results are shown in [Figure 5.6](#)-(a-e). Above the DGZ, the histograms from the different mDWR-XKa classes show a continuous increase of the fall velocity from  $-0.2$  m/s at cloud-top up to  $-0.8$  m/s close to  $-20$  °C isotherm suggesting that the particles are not experiencing an abrupt change of mass, size or vertical air motion in this region. Within DGZ, all classes show the distinctive slowdown region, which is likely to result from upward motion as presented in [Section 4.3](#). Below the DGZ, the fall velocity increases towards the ground.

[Figure 5.6-f](#) shows the MDV-Ka median profiles from each mDWR-XKa class. One can see that, as the DWRs profiles in [Figure 5.4](#) and [Figure 5.5](#), the median MDV-Ka profiles above the DGZ have the same gradient ( $-0.024 \frac{\text{m}}{\text{s}^\circ\text{C}}$ ). This result, based on the classification of the profiles according to mDWR-XKa close to ML top, contrasts with the velocity separation found in the result from the classification based on mDWR-KaW ([Section 4.3](#)). This discrepancy between the results from both classifications provides an additional indication of the limitation of using vertical profiles for the statistical analysis without taking into account for the trajectories (time lagged correlation between upper and lower levels). In the DGZ, between  $-20$  and  $-17$  °C, the different profiles continue with the same gradient ( $-0.024 \frac{\text{m}}{\text{s}^\circ\text{C}}$ ) and MDV-Ka increases up to  $-0.85$  m/s. Between  $-17$  and  $-10$  °C, the gradient from all profiles abruptly changes to  $0.06 \frac{\text{m}}{\text{s}^\circ\text{C}}$  reducing the MDV-Ka to  $-0.75$  m/s and than at around  $-13$  °C the gradient changes again to  $-0.04 \frac{\text{m}}{\text{s}^\circ\text{C}}$  and the MDV-Ka from the different classes increases up to  $-0.85$  m/s except the class-1 that increases up to  $-0.8$  m/s. Below the DGZ, the median profiles show an increasing of separation between the MDV profiles towards the ML top. The class-1 remains almost constant at  $\approx 0.8$  m/s while the class-2 increases up to  $-1$  m/s and the highest three classes reach values up to  $\approx -1.2$  m/s. The overlapping between MDV-Ka profiles of the highest three classes suggest that on average, even though the particles are increasing in

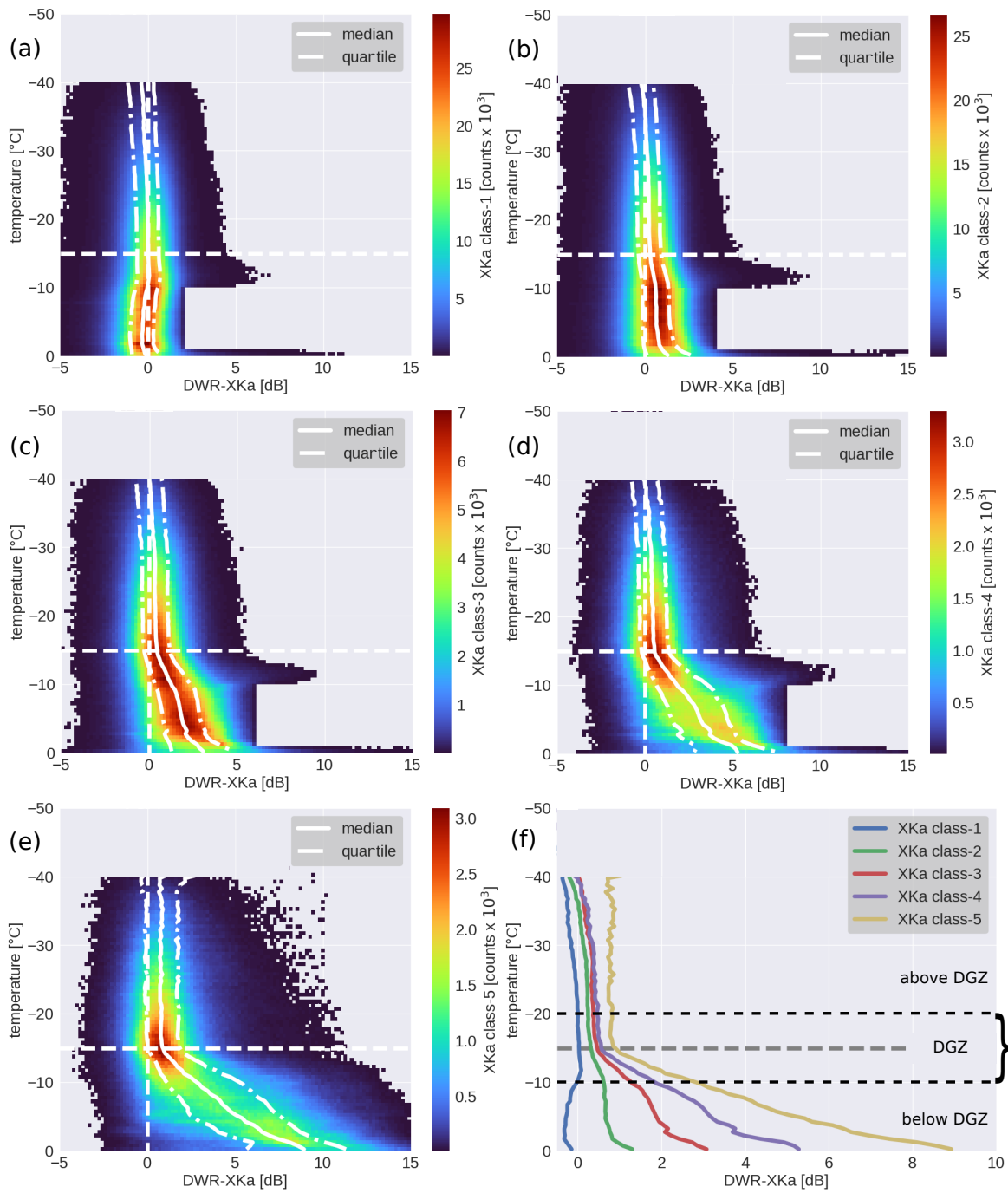


Figure 5.5: Similar as Figure 5.4 but for DWR-XKa profiles. The horizontal line indicates the isotherm of  $-15\text{ }^{\circ}\text{C}$ .

size, their fall velocity remains similar. This result is in accordance to the results of Atlas et al., (1973), Karrer et al., (2020), Locatelli and Hobbs, (1974), and Pruppacher and Klett, (1997) where the terminal velocity of aggregate models is found to increase with their maximum dimension, but after the aggregates grow larger than a critical size, their terminal velocity approaches a constant value.

The spectra edges are also classified according to the mDWR-XKa classes, and Figure 5.7-(a-e) shows the histograms of the classification. Similarly to the MDV profiles, the spectra edges curves also change their behaviour in the same temperature regions. Above the DGZ, both edges indicate a continuous increase in the Doppler velocity (DV). Within the DGZ, all classified spectra edges show a reduction of DV, but the reduction is more intense for the slow edges than for the fast edges. This reduction in DV is similar to the one described in Section 4.3, suggesting that an updraft motion is taking place in this region. Below the DGZ, the slow edge slows down while the fast edge speeds up, as shown in Section 4.3. The histograms of the slow edges also show that the distribution of positive DV enhances with increasing mDWR-XKa. This effect is well demonstrated by the 75 percentile profiles, which reach values up to 0.4 m/s close to 0 °C, which suggest the presence of an updraft in this temperature region (between -10 and 0 °C) (Korolev et al., 2020; Lawson et al., 1998).

The median profiles in figure Figure 5.7-f show that above the DGZ the slow edges overlap each other with the same gradient ( $-0.01 \frac{\text{m}}{\text{s}^\circ\text{C}}$ ) and their DV increase from 0 up to -0.3 m/s. In the same region (above the DGZ), the DV of the fast edges also increase from -0.5 up m/s to -1.5 m/s, but in contrast to the slow edges, the gradient of the fast edges changes around -30 °C and the profiles from classes 1 and 2 are slightly separated from the other three classes. In temperature regions colder than -30 °C the gradient is  $-0.025 \frac{\text{m}}{\text{s}^\circ\text{C}}$  and it changes to  $-0.037 \frac{\text{m}}{\text{s}^\circ\text{C}}$  between -30 and -20 °C. These results are similar to the results obtained in Section 4.3 using the classification based on mDWR-KaW classes. However, the new results do not show a similar change in the gradient of the fast edges with increasing mDWR-XKa classes in temperature regions between -30 and -20 °C, which suggest that there is no clear correlation between the intensification of aggregation close to ML top and the particles from above the DGZ.

Within the DGZ, the separation between the classified edge profiles is enhanced. The slow edges show that the slowdown starts around -17 °C and it intensifies (from 0.1 up to 0.4 m/s) with increasing mDWR-XKa. This intensification suggests a correlation between the increase of aggregate sizes close to the ML top and the intensification the updraft motion within DGZ. The fast edges show that in the DGZ, in contrast to the slow edge, the DV increases from -1.3 up to -1.5 m/s with increasing mDWR-XKa, indicating that the particles are also on average larger. These results are similar to that found in Section 4.3

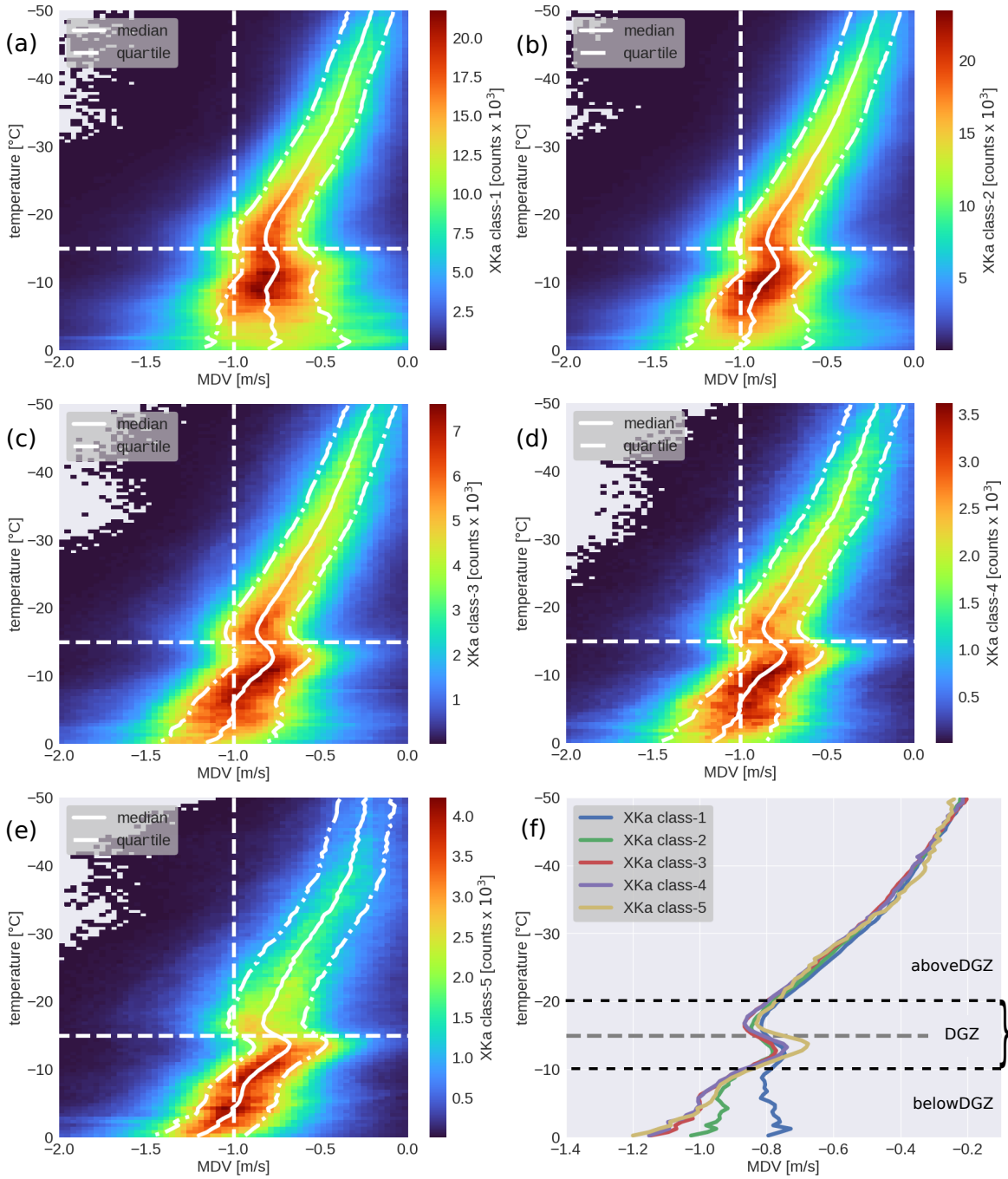


Figure 5.6: Similar as Figure 5.4 but for MDV-Ka profiles. The vertical dashed line at  $-1$  m/s indicates the typical fall velocity of snowflakes and the horizontal line indicates the isotherm of  $-15$  °C.

and favour the hypothesis that an intensification of the updraft in the DGZ would enhance aggregation by increasing the collision rate of the ice particles.

Below the DGZ, the slow edge profiles show a similar reduction of the DV and a switch to positive fall velocities (up to 0.3 m/s at 0 °C) with increasing the mDWR-XKa classes while the fast edges show an enhancement of the separation between them. The DV of the fast edge class-1 increases and reaches its maximum of  $-1.5$  m/s at  $-5$  °C and remains constant between  $-5$  and  $0$  °C. On the other hand, the DV from classes 2, 3, 4 and 5 continuously increases towards  $0$ °C and reaches to  $-1.3$ ,  $-1.7$  and  $-2$  m/s.

As already mentioned, the presence of an updraft in the DGZ can be expected to favour the formation of large aggregates. After those particles leave the DGZ and fall in the region below, they would still grow by aggregation or riming, and in consequence, their DV also would increase; which would be compatible with the overall increase of DV from the fast edges. In contrast, the slow edges suggest that the particles are getting slower and below  $-3$  °C some particles move upwards. A possible reason for the observed spectra broadening is turbulence. One could expect that turbulence would be enhanced due to latent heat release associated with phase transition from ice to water at regions close to the ML (Szyrmer and Zawadzki, 1999). However, turbulence is expected to affect both edges similarly, which is not the behaviour shown by the spectra edges suggesting that another process is taking place. Another possibility that could lead to positive DVs is an updraft. In this case, the small and slow falling particles would have their fall velocity reduced, and at a certain point, these particles would move upward driven by the updraft. At the same time, the fast and large particles would be falling through this region collecting the small and slow falling or upward-moving particles, leading to an increase in size, mass and fall velocity (Lawson et al., 1998). This scenario would be consistent with the slowdown of the slow edges indicated by the medians and the 75 percentile profiles.

The results of the statistical analyses using the mDWR-XKa classes suggest an intensification of aggregation below the DGZ and towards the ML. This region coincides with the temperature region where the sticking efficiency of the ice surface increases with increasing temperature (Connolly et al., 2012; Mitchell, 1988; Phillips et al., 2015), which favour aggregation. Additionally, the statistical results of the spectra edges suggest that at this temperature region an updraft is possibly taking place and contributing to enhancing aggregation due to an increase of the collision rate. These results support the findings from Lawson et al., (1998) where the authors estimated that an updraft of  $\approx 0.5$  m/s close to  $0$  °C would be required to produce the condition to form the observed 5 cm snowflakes.



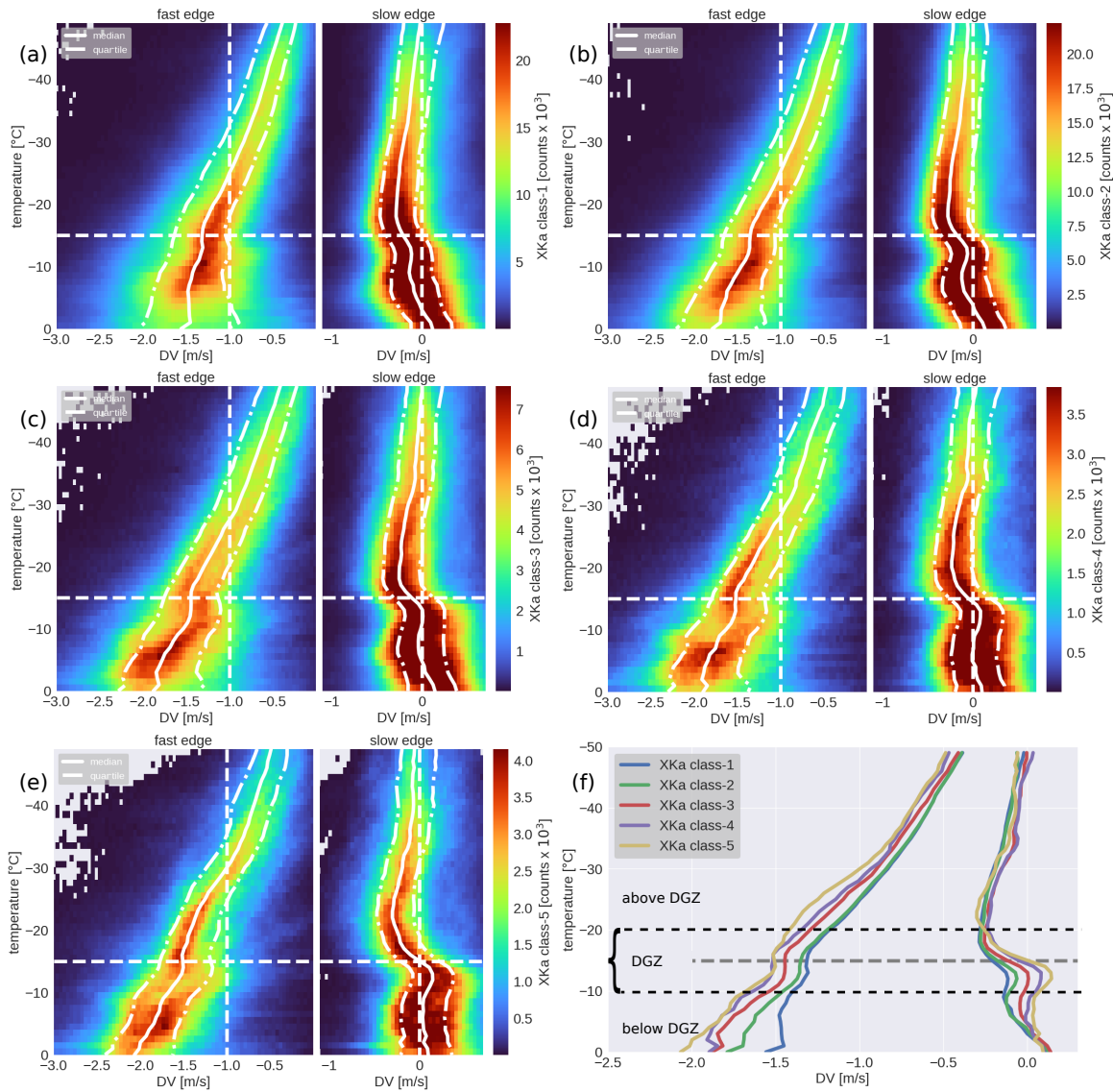


Figure 5.7: Histograms of the slow and fast edges of the spectra as in Figure 5.4. The vertical dashed lines at the fast and slow edge panels indicate the fall velocities of  $-1$  m/s and  $0$  m/s, respectively.

### 5.3 CONNECTING AGGREGATION AT ML TOP AND RAINDROP CHARACTERISTIC SIZE

The statistical results from Fabry and Zawadzki, (1995); Trömel et al., (2019) indicate a positive correlation between  $Z_e$  at ML top and  $Z_e$  at ML bottom, suggesting that an increase in particles size or concentration is correlated with an intensification of rain. The results from the previous Section 5.2 suggest that the size of aggregates is continuously increasing from the DGZ towards the ML top, and in order to verify if an increase of aggregates sizes correlates with a larger raindrops sizes, a statistical analyses of the TRIPEX-Pol dataset is made. For that, the methodology introduced by Mróz et al., (2020b) is used to retrieve the characteristic size of raindrops distributions ( $D_m(\text{rain})$ ) and correlate with the DWR-XKa from aggregates.

The rain  $D_m$  retrieval uses a principle similar to the DWRs such that raindrops can also scatter in different scattering regimes if observed using different frequencies. As introduced in Section 2.2.3, the MDV is weighted by the shape of the distribution of particles, and therefore, the MDV observed by different frequencies can be different. Liao et al., (2008), Matrosov, (2017), Mróz et al., (2020b), and Tian et al., (2007) showed that this difference is proportional to  $D_m(\text{rain})$  and can be used to retrieve it. A variable that quantifies the difference between MDVs is defined by Equation 5.1.

$$\text{DDV} = \text{MDV}_{\lambda_1} - \text{MDV}_{\lambda_2} \quad \lambda_1 > \lambda_2 \quad (5.1)$$

Equation 5.2 describes the approximated relation between  $D_m(\text{rain})$  and DDV for MDV from X- and W-Band proposed by Mróz et al., (2020b). The authors indicate that DDV-XW retrieval is accurate for  $D_m(\text{rain})$  between 0.7 and 2 mm with an uncertainty ranging between 11% and 22%

$$\begin{aligned} D_m(\text{rain}) \approx & 0.009\text{DDV}^5 - 0.097\text{DDV}^4 + 0.353\text{DDV}^3 \\ & - 0.499\text{DDV}^2 + 0.608\text{DDV} + 0.661 \end{aligned} \quad (5.2)$$

In order to correlate DWR-XKa from ice particles and estimate  $D_m(\text{rain})$ , the DWR-XKa at four range gates above the ML top and the DDV-XW from one range gate below the ML bottom are selected. This separation from the ML is used to minimize the influence of partially melted particles on the statistical analyses. The ML top and bottom are detected as described in section Section 3.5. The statistical analysis is limited to the dataset collected during the TRIPEX-Pol campaign because as described in Dias Neto et al., (2019), the MDV collected by the X-Band radar during the TRIPEX campaign is affected by errors induced by the continuous rotation of the antenna.

Figure 5.8-a shows the statistical results of the correlation between the retrieved  $D_m(\text{rain})$  and the DWR-XKa from the entire dataset. One can see that the majority of the retrieved  $D_m(\text{rain})$  values are smaller than 1.2 mm and have DWR-XKa values smaller than 5 dB. The scatter-plot indicates a positive correlation (almost linear) between  $D_m(\text{rain})$  and DWR-XKa, suggesting that an increase in the ice particles size above the ML coincides with the increase in the droplet sizes. The close correlation is expected if one assumes that each snowflake melts into its mass equivalent raindrop as suggested by Drummond et al., (1996), Matrosov, (2017), and Mróz et al., (2020a). Nonetheless, several other processes (e.g. breakup, collision-coalescence, and evaporation) could be taking place in the ML and reducing the droplet sizes. However, the reduction in droplet sizes is not observed, suggesting that some processes might compensate each other.

In addition to the enhanced aggregation close to ML top, it is possible that riming is influencing the raindrops characteristic size due to an increase in the density of the ice particles. An experimental study conducted by Leinonen and Lerber, (2018) using a 3-D model for melting snowflakes indicates that the increase in density due to riming can prevent the particle structural breakup. However, partially and completely melted particles could still shed (Rasmussen and Heymsfield, 1987) or breakup (Kamra et al., 1991) due to aerodynamic effects. Previous studies indicated that particles with MDV faster than  $-1.5$  m/s could be used as a proxy of riming (Barthazy and Schefold, 2006; Kneifel and Moisseev, 2020; Mosimann, 1995), while MDV slower than this value can be associated with unrimed or slightly rimed particles. In order to verify if riming and aggregation would lead to the formation of different regimes of droplet sizes, the dataset is separated into two categories according to the MDV-Ka above ML top. The first category is for MDV-Ka faster than  $-1.5$  m/s (hereafter referred to as the rimed category of particles), which represents rimed ice particles. The second is for MDV-Ka slower than  $-1.5$  m/s (hereafter unrimed category), which correspond to slightly rimed or unrimed particles.

Figure 5.8-(b,c) shows the statistical results from the data classified as unrimed and rimed categories. One can see that the distribution from the unrimed particles (Figure 5.8-b) is comparable to the distribution from the entire dataset (Figure 5.8-a), indicating that the majority of the observations are from potentially unrimed particles. Figure Figure 5.8-c indicates that only a small fraction of the data ( $\approx 14\%$ ) are from rimed particles. This small fraction of rimed particles is similar to the results from the TRIPEX campaign (see Section 3.1) and from the long term statistics of riming for the same site found by Kneifel and Moisseev, (2020) where the authors found that the frequency of rime mass fraction larger than 0.6, corresponding to  $\text{MDV} > 1.5$  m/s, ranges between 1 and 8%.

The statistics of the unrimed particles (Figure 5.8-b) shows that an increase in DWR-XKa correlates with an increase in  $D_m(\text{rain})$ , and for example, the mDWR-XKa class-5 correlates with  $D_m$  between 1.4 and 1.8 mm. The statistics of the rimed particles (Figure 5.8-c) also suggests an almost linear relation between  $D_m(\text{rain})$  and DWR-XKa. The  $D_m(\text{rain})$  values from the rimed particles range almost the same interval as compared to the unrimed ones; however, it happens at a narrower DWR-XKa range. The comparison between the fit of the medians from each category (Figure 5.8-d) highlights the difference between them. It shows that for a given  $D_m(\text{rain})$ , the DWR-XKa from the unrimed category is almost two times larger than the DWR-XKa from the rimed category. This difference suggests that the presence of heavily rimed particles favours the formation of large droplets (due to the higher particle density) when compared to unrimed or slightly rimed aggregates.

The scattering model from Leinonen and Szyrmer, (2015) is used to evaluate the hypothesis that an increasing density of the ice particles also could contribute to the increase of the droplet sizes. This model is used because it includes rimed particles which are need for the sensitivity experiment. For the evaluation, it is assumed that one ice particle generates one raindrop and that the mass is conserved. Processes that could change the mass of the raindrops are not considered (e.g. droplet breakup, evaporation, coalescence). In steady-state condition, this hypothesis results in a constant mass and number flux through the ML (Drummond et al., 1996). It is also assumed that after the ice particles entirely melt, the resulting droplets are spheres, and the diameter  $D_{\text{drop}}$  is given by equation Equation 5.3.  $m_s$  is the mass of the snowflakes and  $\rho_w$  is the density of water.

$$D_{\text{drop}} = 2 \left( \frac{3 m_s}{4\pi \rho_w} \right)^{\frac{1}{3}} \quad (5.3)$$

The distribution of snow sizes is assumed to be an inverse exponential (Equation 2.22,  $\mu = 0$ ) and to mimic the growth of the ice particles lambda ranges from  $10^2$  to  $10^5 \text{ m}^{-1}$ . Figure 5.9 shows  $D_m(\text{rain})$  from the different degree of riming versus the DWR-XKa from the ice particles. The theoretical curves indicate that for a given DWR-XKa, the increase in density leads to the increase of the  $D_m(\text{rain})$ , supporting the results from the observation.

Although an increase in the density of ice particles can contribute to the formation of larger droplets, the statistics indicate that riming did not often happen in JOYCE-CF, suggesting that an increase in the size of unrimed or slightly rimed aggregates are probably the factors that mostly contribute for increasing the droplet sizes over JOYCE-CF.

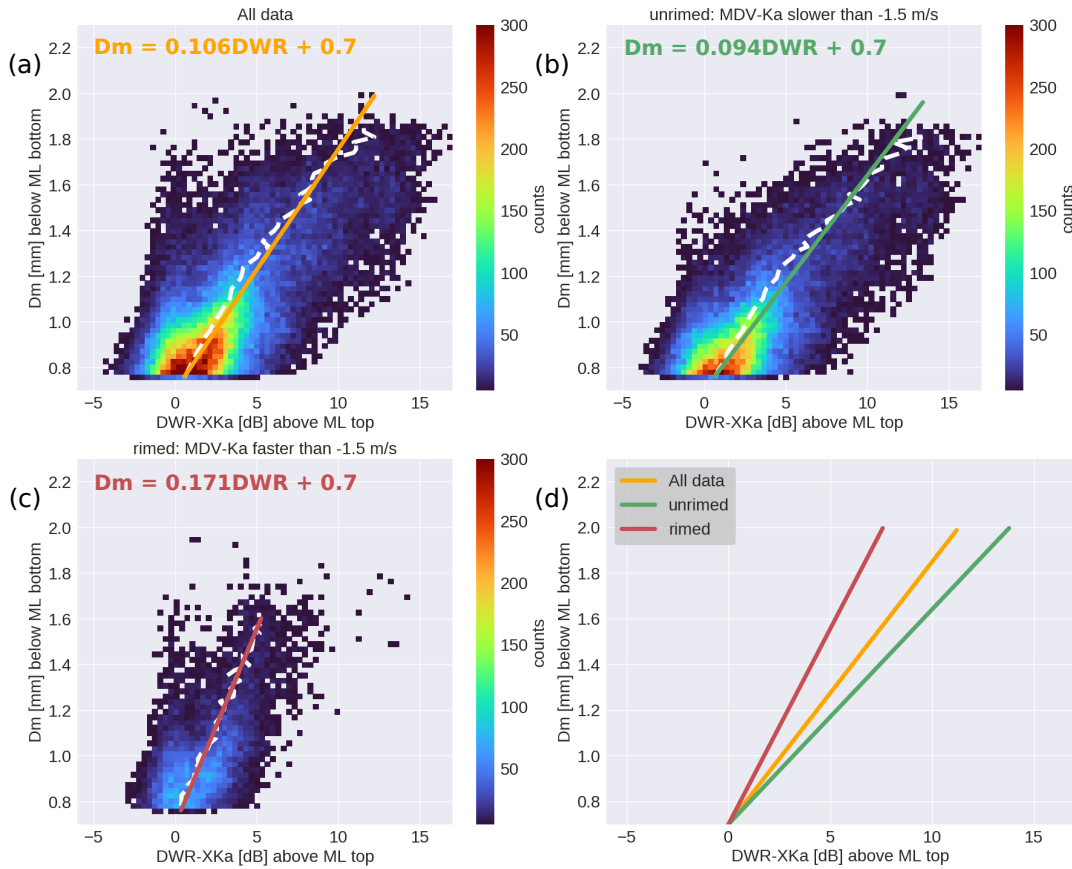


Figure 5.8: Two-dimensional histogram of the pairs rain  $D_m$  and DWR-XKa in the snow aloft.  $D_m$  is from one range gate below the identified ML bottom and DWR-XKa is from four range gates above the identified ML top. Panel (a) is for the entire dataset. Panel (b) is for the data where MDV-Ka four range gates above the ML is slower than  $-1.5$  m/s (unrimed), and Panel (c) is for MDV-Ka faster than  $-1.5$  m/s (rimed). The dashed line and the continuous line are the median and the fit, respectively. The fitting equation is indicated on the top of each Panel. Panel (d) shows the intercomparison between the fits from (a) to (c).

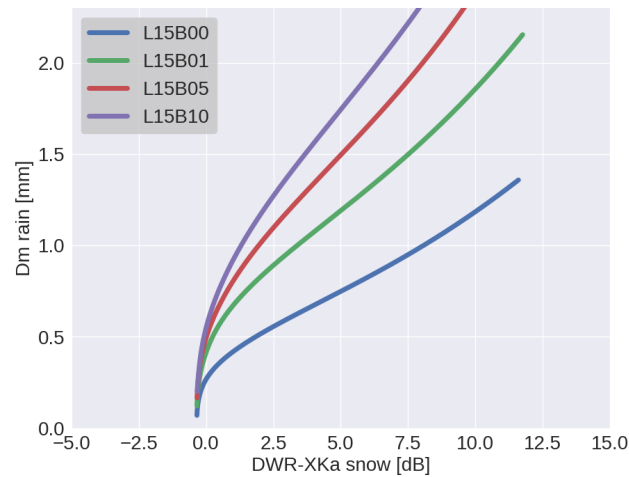


Figure 5.9: Scatter plot of the simulated  $D_m$  from raindrops and the DWR-XKa from snow for increasing riming mass fraction of dendrite aggregates with various degree of riming (Leinonen and Szyrmer, 2015). The blue, green, red, and purple curves are from 0, 0.1, 0.5 and 10  $\text{kg}/\text{m}^2$  effective liquid water path.

#### 5.4 EVALUATING THE ONE-TO-ONE MELTING ASSUMPTION

The results from section [Section 5.3](#) suggest that the presence of large raindrop below the ML bottom correlates with the increase of size and density from the ice particles above ML top. In this section it will be evaluated if it would be possible to grasp additional information about the predominant microphysical process that is taking place inside of the ML, and if this process depends on the microphysical characteristics of the snowflakes aloft (i.e. if they are either large and soft aggregates or rimed particles). Drummond et al., (1996) proposed a methodology that combines Ze and MDV from vertically pointing radars, which indicates the predominance of breakup or aggregation within the ML. This methodology is applied in this section to evaluate how rimed and unrimed particles are correlated with either breakup or coalescence of particles in the ML. A short description of the method and its assumptions is given below.

According to Drummond et al., (1996) under the assumption of a melting-only steady state ML, one snowflake melts into a raindrop of equal mass. If no other microphysical processes are taking place within the ML (e.g. aggregation, accretion, breakup, coalescence) the one-to-one relationship is valid. Another additional assumption is that there is a continuous supply of ice particles above the ML top and continuous flow between the ML top and bottom. Under those conditions, the distribution of ice particles  $N_s(D)$  above the ML can be related to the distribution of raindrops  $N_r(D)$  below the ML through the conservation of mass and number fluxes. Moreover, under the hypothesis of Rayleigh scattering, the number and mass flux conser-



vation also implies a precise ratio between the reflectivity fluxes (ZFR, Equation 5.4) which only depends on the ratio between the dielectric properties of ice and water ( $\mu$ , Equation 5.5). This relation is made explicit by  $ZFR = \mu$ . The subscript  $s$  and  $r$  stand for snow and rain, respectively. For X-Band radar,  $\mu \approx 0.23$  and it varies less than 2% for temperatures between  $-5$  and  $5$  °C.

$$ZFR = \frac{Ze_s MDV_s}{Ze_r MDV_r} \quad (5.4)$$

$$\mu = \frac{|K_s|^2}{|K_r|^2} \quad (5.5)$$

In case aggregation or accretion is taking place inside of the ML, the size of raindrops would increase and lead to an increase in  $Ze$  and  $MDV$  from the raindrops, which would reduce  $ZFR$  and it would be smaller than  $\mu$ . However, if droplet breakup or evaporation are the predominant processes,  $Ze$  and  $MDV$  from raindrops would reduce, and the  $ZFR$  would be larger than  $\mu$ . Drummond et al., (1996) also indicate that vertical air motion would introduce uncertainties in  $ZFR$ . For example, in the case of vertical air motion of  $\pm 0.5$  ( $\pm 1$ ) m/s in the rain (snow) region, the one-to-one assumption would be compatible with  $ZFR$  values between 1.5 and 3.0 (Drummond et al., 1996).

The X-Band pairs ( $Ze$ ,  $MDV$ ) from four range gates (144 m) above ML top and one range gate below (36 m) ML bottom are used as data from snow and rain regions, respectively. Similarly to the previous section, those separations from ML top and bottom are applied to minimize the error introduced by partially melted particles.

For the initial analyses, the dataset is separated into two classes (rimed and unrimed) as used in Section 5.3. Figure 5.10 shows the probability distributions of  $ZFR$  for the rimed and unrimed particles. The mode of both distributions are within the uncertainty interval indicated by Drummond et al., (1996); however, one can see that there is a tendency for the rimed particles have  $ZFR$  larger than  $\mu$ , while the unrimed particles have  $ZFR$  slightly smaller than  $\mu$ . These results suggest that rimed particles are prone to experience breakup while aggregates are prone to experience additional aggregation within the ML. However, the mode from both distributions is within the uncertainty interval estimated by Drummond et al., (1996). In order to minimize the error introduced by vertical air motions, a methodology is still needed. However, one can speculate that due to the high density of rimed particles, these particles would melt into large droplets as indicated in Section 5.3, which could favour the breakup due to enhanced collision rate and increase in the collision kinetic energy according to experimental results from (Low and List, 1982a,b; Warner, 1977) or due to hydrodynamic instability that affects droplets larger

than 6.6 mm as it is well established by laboratory experiments of (Kamra et al., 1991). On the other hand, extremely low ZFR values (close to 0) are 5 times more likely to be associated with unrimed falling particles with respect to the rimed ones. This result suggests that rimed particles are less likely to cause aggregation in the ML, or they enable additional processes that will counteract the effects of aggregation in the ML.

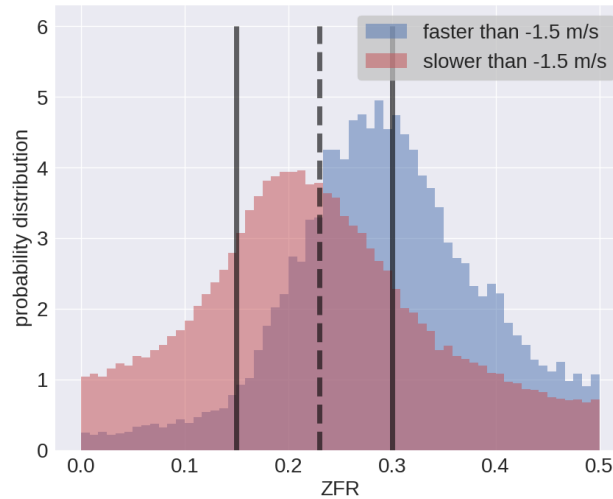


Figure 5.10: Histograms of the Ze flux ratio (ZFR). The blue and red histograms are from the data where the MDV-Ka at four range gates above the ML top is faster and slower than  $-1.5$  m/s, respectively. The vertical dashed line indicates the theoretical ZFR ( $\mu = 0.23$ ), and the vertical continuous lines indicates the uncertainty range in case of vertical air motion of  $\pm 0.5/\pm 1$  m/s in the rain/snow region (Drummond et al., 1996).

As a step further to the previous analysis to obtain additional information about aggregation, the dataset from the unrimed falling particles is further classified using the same mDWR-XKa classes defined in Section 5.2. Figure 5.11(a,b) shows the probability distribution and the corresponding cumulative probability of ZFR for the different mDWR-XKa classes. From these results, one can see that it is more likely to observe a ZFR smaller than  $\mu$  in the profile corresponding to the higher mDWR-XKa classes. This trend suggests that the increase in aggregate sizes is correlated with additional aggregation within the ML. This correlation could be explained by the same mechanism introduced by Trömel et al., (2014), where large and partially melted ice particles collect small droplets (accretion) or another partially melted ice particle (aggregation).

A more detailed study combining in-situ measurements and numerical models of the ML is needed to verify the results from this last analysis. However, the results demonstrate the potential of exploring the combined observations of DWR and colocated Doppler observations.

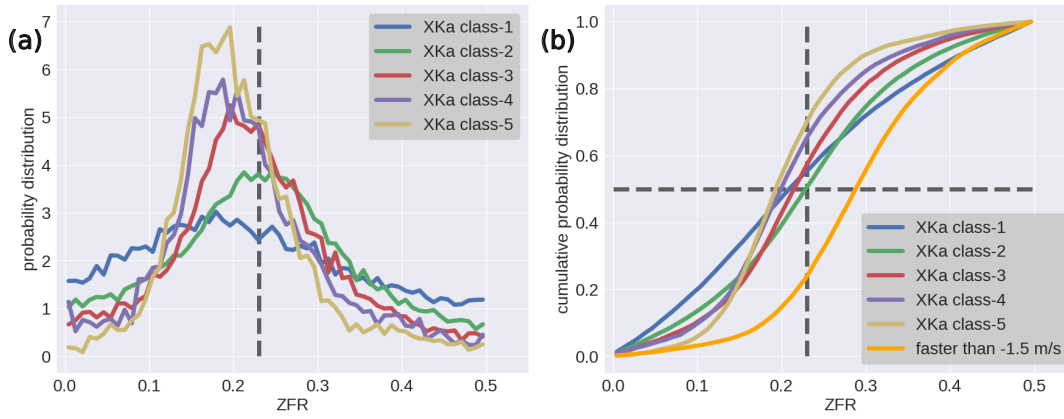


Figure 5.11: Statistical results of the Ze flux ratio from the data where the MDV-Ka at four range gates above the ML top is slower than  $-1.5$  m/s. Panel (a) shows the histograms of ZFR and Panel (b) shows the cumulative probability distribution from the profiles classified according to the mDWR-XKa. Additionally, Panel (b) shows the cumulative probability distribution from the profiles where the MDV-Ka is faster than  $-1.5$  m/s (orange line).

## 5.5 CONCLUSION

In this chapter, the long term radar datasets obtained during the TRIPEX and TRIPEX-Pol were combined and used to investigate the intensification of aggregation that is often observed below the DGZ and close to ML top. The vertical profiles of Ze, MDV, DWRs and the spectra edges were classified according to mDWR-XKa from the region between the DGZ and ML top. These classified profiles were exploited to verify if the enhance of DWR-XKa close to ML top correlates with the enhance of aggregation within DGZ and with larger raindrops characteristic sizes below the ML.

The results from the statistical analyses (Section 5.2) indicate that an enhancement of DWR-XKa and DWR-KaW within DGZ correlates with the augmented mDWR-XKa close to the ML top. Additionally, the DWRs profiles classified according to the mDWR-XKa deviate from each other around  $-15$  °C, and the deviation persists towards the ML top. The slow spectra edge also showed that the intensification of the slowdown correlates with the increase of the mDWR-XKa near ML top. These results suggest that the presence of an updraft within DGZ favours the snowflake growth by aggregation as shown in Section 5.2 and those large aggregates continuously grow towards the ML, leading to the formation of sometimes very large aggregates. However, the statistical results shown in Section 4.3 suggest that some of the large aggregates may not grow continuously towards the ML. The combined results suggest that the presence of large aggregates in the DGZ is a favourable, but not a sufficient condition to ensure the presence of large aggregates close to the ML top.

The combination of long term observations of DWR-XKa and the retrieval of the raindrop characteristic sizes ( $D_m(\text{rain})$ ) based on DDV-XW (Mróz et al., 2020b) showed that the increase of DWR-XKa close to ML top correlates with the increase of  $D_m(\text{rain})$  close to the ML bottom [Section 5.3](#). This correlation suggests that the increase in aggregate sizes favours the increase of raindrop sizes. Using an MDV threshold of  $-1.5$  m/s to separate the data of heavily rimed aggregates from the unrimed and slightly rimed aggregates showed that the occurrence of rimed aggregates close to ML top could favour the formation of large droplets when compared with unrimed or slightly rimed aggregates. This effect can be interpreted as a result of the increased density of rimed snowflakes. Additionally, this separation also showed that the frequency of occurrence of heavily rimed aggregates is much lower than the other aggregates. This result is similar to the results from Kneifel and Moisseev, (2020), which found that observations characterized by a rime mass fraction larger than 0.6 constitute 1 to 8% of the events.

The statistical analysis of the DWR-XKa dataset combined with the Ze flux ratio methodology from above and below the ML (Drummond et al., 1996) to identify preferential aggregation or break up within ML revealed two distinct trends for heavily rimed aggregates and unrimed or slightly rimed aggregates. The results indicate that the heavily rimed aggregates are prone to break up within the ML, while unrimed or slightly rimed aggregates are more likely to continue aggregation within the ML. One could speculate that due to faster fall velocities and higher density of heavily rimed aggregates, their collision rate would be enhanced and the resulting melted particles would grow to a critical size at which they would be hydrodynamic unstable and break up. By analyzing the ZFR distribution for various mDWR-XKa classes related to the slower falling particles it is revealed that the largest classes of aggregates are more likely to cause additional aggregation within the ML.

## CONCLUSIONS AND OUTLOOK

---

Aggregation is the cloud microphysical process that most effectively contributes to the rapid increase of snowflake sizes. From the literature, it is known that aggregation is enhanced at two main temperature regimes. The first temperature region is between  $-20$  and  $-10$  °C, which is well known for the preferential growth of dendritic ice crystals (DGZ). In the DGZ the ice nucleation is favoured leading to large number concentrations of pristine crystals which increase the collision rate. Moreover, the dendritic shape also makes the crystals more likely to interlock with one another after colliding. The second region is between  $-10$  and  $0$  °C, where the stickiness of ice surfaces increase due to the effect of a quasi liquid layer on the ice surface.

This work aims at improving the current understanding of ice aggregation. The analysis takes advantage of the synergistic observation from vertically pointing triple-frequency Doppler radars (moments and spectra) collected during winter campaigns from 2015/2016 (TRIPEX) and 2018/2019 (TRIPEX-Pol). This study aims to address the following main questions: 1) Is the intensification of aggregations in the DGZ related to microphysical or dynamical processes? 2) Is the enhancement of aggregation close to the ML top influenced by aggregation that happens aloft in the DGZ? 3) How does aggregation close to the ML change the raindrop sizes below the ML?

In order to explore the data collected during the triple-frequency campaigns, this work introduced a two-level processing framework for providing a high quality controlled dataset. In the first processing level, the data from each radar is resampled to a common time and range grid. In the second processing level, the data is corrected for atmospheric gases and water vapour attenuation using vertical profiles of the atmospheric state variable (temperature, pressure and humidity) provided by Cloudnet over JOYCE-CF. This second processing level also minimizes attenuation produced by other sources (e.g. snow, supercooled water, wet radome) by matching the Ze from each radar at the uppermost region of the clouds. A set of quality flags are introduced in this processing level to provide identification of regions where the corrections cannot be guaranteed with confidence due to several reasons (e.g. absence of enough data points, non-uniform bin filling). This approach gives flexibility while using the dataset because it allows activating or deactivating specific flags according to the needs. The unique characteristics of the resulting dataset (e.g. easy usability, quality controlled) triggered new other studies: evaluation of cloud microphysical processes in numerical models (Ori et al., 2020a);

development of new methodology based on triple-frequency Doppler velocity for estimating raindrop characteristic sizes (Mróz et al., 2020b), and evaluation a multi-frequency based methodology for estimating the total differential attenuation (Tridon et al., 2020).

This thesis additionally introduced a methodology for filtering the majority of spurious signals affecting the measurements from the W-Band radar during the TRIPEX-Pol campaign. The spurious signals were removed from the W-Band spectra by using the edges from the Ka-Band spectra. The same technique was also applied to the X-Band spectra dataset collected during TRIPEX-Pol campaign to remove noise spikes that were not removed by the radar software. Besides the filtering application, the long term statistics of the spectra edges was introduced by the first time as an additional source of information of particles fall velocities.

The initial statistical analyses from triple-frequency observations of the ice part of the clouds, collected during the TIRPEX campaign, revealed that the DWR-KaW enhances in the DGZ while the DWR-XKa enhances close to the ML top coinciding with the regions where aggregation is most favourable. The results from the TRIPEX campaign also indicated that, in both temperature regions, there are scenarios where aggregation is particularly intense. Those scenarios are indicated by the broadening of the distribution of DWRs in both temperature regions. In the DGZ ( $-20 > T > -10$  °C) the DWR-KaW values range between 0 and 8 dB and below the DGZ ( $-10 > T > 0$  °C) towards ML top the DWR-XKa values range between 0 and 15 dB.

The combination of the data collected during TRIPEX and TRIPEX-Pol campaigns provided the longest quality-controlled triple-frequency dataset ( $\approx 6$  months) allowing to investigate further the conditions that may contribute for intensifying aggregation in the DGZ and close to ML top. For this investigation, the statistical information of the radar moments ( $Z_e$ , MDV, DWRs) and spectra edges was stratified by the atmospheric temperature provide by Cloudnet. The vertical profiles of this new dataset were then classified according to the increasing of the maximum DWR from each temperature region; the maximum DWR was used as an indicator of the mean maximum sizes of the ice particles. Since the DWR-KaW and DWR-XKa are sensitive to the particle growth at different stages, the classification in the DGZ was made using five classes of maximum DWR-KaW and the classification close to the ML top was made using five classes of maximum DWR-XKa.

The statistical results from vertical profiles classified according to the maximum DWR-KaW in the DGZ revealed three main findings. First, the intensification of aggregation in the DGZ correlates with the increase of particle sizes starting around  $-30$  °C, which is indicated by the increase of DWR-KaW gradient ( $0.01 - 0.1$  dB/°C) with increasing mDWR-KaW classes. In contrast, the classification of the



DWR-XKa profiles did not show a similar signature suggesting that those particles were not large enough to enhance the DWR-XKa ( $D_0 < 3$  mm). This initial growth of particles was also confirmed by the increased MDV and the fast spectra edges. Both quantities show an increasing trend for their gradient (MDV: from  $-0.02$  to  $-0.03 \frac{\text{m}}{\text{s}^\circ\text{C}}$ , fast edges: from  $-0.024$  up to  $-0.046 \frac{\text{m}}{\text{s}^\circ\text{C}}$ ), starting around  $-30$  °C, that correlates with the increasing mDWR-KaW class. The second finding is a correlation between the increase of the mean particles sizes with increasing mDWR-KaW classes and the location of the  $-15$  isotherm. The vertical gradients of DWR-KaW ( $0.13 - 0.85$  dB/°C) and DWR-XKa ( $0.06 - 0.6$  dB/°C) increase in this region suggesting an intensification of aggregation in the DGZ. Finally, the third result is that the growth of aggregates within DGZ correlates with the intensification of a slowdown ( $0.1-0.3$  m/s) of the ice particles fall speed within DGZ. This is shown by the classified MDV and spectra edges profiles. The statistical analysis of the slow edge profiles suggested that this slowdown is likely to be the result of an updraft. This hypothesis is supported by positive DV of the slow edges, which reaches up to  $0.3$  m/s. The occurrence of an updraft in the DGZ would increase the supersaturation leading to an enhancement of the depositional growth of dendrite-like crystals and then intensifying aggregation. An updraft would also increase the time of the particles remaining within DGZ, favouring additional growth either by deposition or aggregation.

In order to investigate, if the occurrence multimodalities in the DGZ is connected to the intensification of aggregation, the Ka-Band spectra dataset was used for creating a time-height map of the multimodality occurrence. By restricting the multimodality map to the DGZ it was possible to classify the maximum DWR-KaW values within DGZ according to the occurrence of multimodalities. The results from this classification indicated that the probability of maximum DWR-KaW  $> 2$  dB to happen in a multi-peak scenario is approximately 25% higher than in a single-peak scenario, suggesting that the multi-peak scenario could also contribute to enhancing aggregation in the DGZ. However, the origin of this additional spectral mode remains not well understood. One possibility is the nucleation of new ice crystal by primary ice formation which is favoured in the DGZ. Another possibility is that the new mode of ice particles results from the secondary ice formation. In order to better understand the origin of this additional mode and its role on the intensification of aggregation, it is suggested to use lagrangian models (e.g. McSnow) to simulate aggregation with active SIP under different supersaturation scenarios. In-situ and radar observations could be used as an additional constraint in a dedicated observational campaign.

The statistical analyses of the radar observation classified according to maximum DWR-XKa in regions below the DGZ suggested that an increase of snowflake sizes close to the ML top correlates with

an increase in particles sizes starting around  $-15\text{ }^{\circ}\text{C}$ . Close to ML top, the median DWR-XKa reached values up to 8 dB suggesting that the median volume diameter of those particles is larger than 10  $\mu\text{m}$ . In contrast, the statistics from the classification using the maximum DWR-KaW in the DGZ suggests that the sizes of the large particles can decrease towards the ML top. Those results, combined, indicate that the presence of large aggregates in the DGZ favour the formation of even larger aggregates close ML top, but this condition is not sufficient to guarantee the presence of even larger aggregates close to ML top. The reduction of aggregate sizes could result from fragmentation, sublimation or because the particles were driven away by advection from the horizontal wind.

The statistical result combining the DWR-XKa close to ML top with the retrieved raindrop characteristic sizes ( $D_m(\text{rain})$ ) indicates that the two quantities are strongly correlated with an almost linear relation. Since satellite-based radar observations are affected by attenuation in regions below the ML, this linear relation could be used to estimate  $D_m(\text{rain})$  from satellite-based dual-frequency observations above the ML height.

The observations and the sensitivity study using snowflakes with different amount of riming suggest that rimed particles are more likely to form large raindrops when compared with unrimed aggregates. However, in this study approximately 14% of the radar observed profiles were identified as rimed snowflakes (MDV-Ka faster than  $-1.5\text{ m/s}$ ) suggesting that an increase in  $D_m(\text{rain})$  over JOYCE-CF is likely resulting from the increase of the size of the aggregates. An additional study based on the reflectivity flux ratio from regions above and below the ML indicated that the unrimed aggregates are preferentially experiencing further aggregation within ML, while the rimed, more massive, particles are prone to breakup. This breakup experienced by rimed particles could be a result of hydrodynamic instabilities of already larger raindrops which can grow beyond the stability limiting size due to enhanced collision rate. In order to understand further the role of the riming degree on the microphysical characteristics of raindrops, a more detailed study combining the results from this thesis and melting layer models would be beneficial.

## BIBLIOGRAPHY

---

- Andrić, J., M. R. Kumjian, D. S. Zrnić, J. M. Straka, and V. M. Melnikov (2013). "Polarimetric Signatures above the Melting Layer in Winter Storms: An Observational and Modeling Study." In: *Journal of Applied Meteorology and Climatology* 52.3, pp. 682–700. ISSN: 1558-8424. DOI: [10.1175/JAMC-D-12-028.1](https://doi.org/10.1175/JAMC-D-12-028.1).
- Andronache, C. (2018). *Remote Sensing of Clouds and Precipitation* -. Berlin, Heidelberg: Springer. ISBN: 978-3-319-72583-3.
- Atlas, D., R. C. Srivastava, and R. S. Sekhon (1973). "Doppler radar characteristics of precipitation at vertical incidence." In: *Reviews of Geophysics* 11.1, pp. 1–35. DOI: [10.1029/RG011i001p00001](https://doi.org/10.1029/RG011i001p00001).
- Aufdermaur, A. N. and D. A. Johnson (1972). "Charge separation due to riming in an electric field." In: *Quarterly Journal of the Royal Meteorological Society* 98.416, pp. 369–382. DOI: [10.1002/qj.49709841609](https://doi.org/10.1002/qj.49709841609).
- Bacon, N. J., B. D. Swanson, M. B. Baker, and E. J. Davis (1998). "Breakup of levitated frost particles." In: *J. Geophys. Res.* 103.D12, pp. 13763–13775. DOI: [10.1029/98JD01162](https://doi.org/10.1029/98JD01162).
- Bailey, M. P. and J. Hallett (2009). "A comprehensive habit diagram for atmospheric ice crystals: Confirmation from the laboratory, AIRS II, and other field studies." In: *Journal of the Atmospheric Sciences* 66.9, pp. 2888–2899. DOI: [10.1175/2009JAS2883.1](https://doi.org/10.1175/2009JAS2883.1).
- Baldini, L. and E. Gorgucci (2006). "Identification of the Melting Layer through Dual-Polarization Radar Measurements at Vertical Incidence." In: *Journal of Atmospheric and Oceanic Technology* 23.6, pp. 829–839. ISSN: 0739-0572. DOI: [10.1175/JTECH1884.1](https://doi.org/10.1175/JTECH1884.1).
- Bandera, J., A. D. Papatosoris, P. A. Watson, J. Tan, and J. W. Goddard (1998). "Method for detecting the extent of the melting layer." In: *Electronics Letters* 34.22, pp. 2104–2105.
- Barrett, A. I., C. D. Westbrook, J. C. Nicol, and T. H. M. Stein (2019). "Rapid ice aggregation process revealed through triple-wavelength Doppler spectrum radar analysis." In: *Atmospheric Chemistry and Physics* 19.8, pp. 5753–5769. DOI: [10.5194/acp-19-5753-2019](https://doi.org/10.5194/acp-19-5753-2019).
- Barthazy, E. and R. Schefold (2006). "Fall velocity of snowflakes of different riming degree and crystal types." In: *Atmospheric Research* 82.1-2, pp. 391–398. DOI: [10.1016/j.atmosres.2005.12.009](https://doi.org/10.1016/j.atmosres.2005.12.009).
- Battaglia, A., S. Tanelli, F. Tridon, S. Kneifel, J. Leinonen, and P. Kollias (2020). "Triple-Frequency Radar Retrievals." In: *Satellite Precipitation Measurement: Volume 1*. Springer International Publishing, pp. 211–229. ISBN: 978-3-030-24568-9. DOI: [10.1007/978-3-030-24568-9\\_13](https://doi.org/10.1007/978-3-030-24568-9_13).
- Baumgardner, D., L. Avallone, A. Bansemer, S. Borrmann, P. Brown, U. Bundke, P. Y. Chuang, D. Cziczo, P. Field, M. Gallagher, J. F. Gayet, A. Heymsfield, A. Korolev, M. Krämer, G. McFarquhar, S. Mertes,

- O. Möhler, S. Lance, P. Lawson, D. Petters, K. Pratt, G. Roberts, D. Rogers, O. Stetzer, J. Stith, W. Strapp, C. Twohy, and M. Wendisch (2012). "In situ, airborne instrumentation: Addressing and solving measurement problems in ice clouds." In: *Bulletin of the American Meteorological Society* 93.2, pp. 29–34. DOI: [10.1175/BAMS-D-11-00123.1](https://doi.org/10.1175/BAMS-D-11-00123.1).
- Bechini, R., L. Baldini, and V. Chandrasekar (2013). "Polarimetric radar observations in the ice region of precipitating clouds at C-Band and X-Band radar frequencies." In: *Journal of Applied Meteorology and Climatology* 52.5, pp. 1147–1169. DOI: [10.1175/JAMC-D-12-055.1](https://doi.org/10.1175/JAMC-D-12-055.1).
- Behrangi, A., Y. Tian, B. H. Lambriksen, and G. L. Stephens (2014). "What does CloudSat reveal about global land precipitation detection by other spaceborne sensors?" In: *Water Resources Research* 50.6, pp. 4893–4905. DOI: <https://doi.org/10.1002/2013WR014566>.
- Böhm, J. P. (1992). "A general hydrodynamic theory for mixed-phase microphysics. Part III: Riming and aggregation." In: *Atmospheric Research* 28.2, pp. 103–123. DOI: [10.1016/0169-8095\(92\)90023-4](https://doi.org/10.1016/0169-8095(92)90023-4).
- Boucher, O., D. Randall, P. Artaxo, C. Bretherton, G. Feingold, P. Forster, V. M. Kerminen, Y. Kondo, H. Liao, U. Lohmann, P. Rasch, S. K. Satheesh, S. Sherwood, B. Stevens, and X. Y. Zhang (2013). "Clouds and Aerosols. Chapter 7 Climate Change 2013: The Physical Science Basis. Contribution of Working Group I to the Fifth Assessment Report of the Intergovernmental Panel on Climate Change." In: pp. 571–657. DOI: [10.1017/CB09781107415324.016](https://doi.org/10.1017/CB09781107415324.016).
- Brdar, S. and A. Seifert (2018). "McSnow: A Monte-Carlo Particle Model for Riming and Aggregation of Ice Particles in a Multidimensional Microphysical Phase Space." In: *Journal of Advances in Modeling Earth Systems* 10.1, pp. 187–206. DOI: [10.1002/2017MS001167](https://doi.org/10.1002/2017MS001167).
- Bringi, V. N. and V. Chandrasekar (2001). *Polarimetric Doppler Weather Radar: Principles and Applications*. Cambridge University Press. DOI: [10.1017/CB09780511541094](https://doi.org/10.1017/CB09780511541094).
- Connolly, P. J., C. P. R. Saunders, M. W. Gallagher, K. N. Bower, M. J. Flynn, T. W. Choulaton, J. Whiteway, and R. P. Lawson (2005). "Aircraft observations of the influence of electric fields on the aggregation of ice crystals." In: *Quarterly Journal of the Royal Meteorological Society* 131.608, pp. 1695–1712. DOI: <https://doi.org/10.1256/qj.03.217>.
- Connolly, P. J., C. Emersic, and P. R. Field (2012). "A laboratory investigation into the aggregation efficiency of small ice crystals." In: *Atmospheric Chemistry and Physics* 12.4, pp. 2055–2076. DOI: [10.5194/acp-12-2055-2012](https://doi.org/10.5194/acp-12-2055-2012).
- Crawford, I., K. N. Bower, T. W. Choulaton, C. Dearden, J. Crosier, C. Westbrook, G. Capes, H. Coe, P. J. Connolly, J. R. Dorsey, M. W. Gallagher, P. Williams, J. Trembath, Z. Cui, and A. Blyth (2012). "Ice formation and development in aged, wintertime cumulus over

- the UK: observations and modelling." In: *Atmospheric Chemistry and Physics* 12.11, pp. 4963–4985. DOI: [10.5194/acp-12-4963-2012](https://doi.org/10.5194/acp-12-4963-2012).
- Crosier, J., K. N. Bower, T. W. Choularton, C. D. Westbrook, P. J. Connolly, Z. Q. Cui, I. P. Crawford, G. L. Capes, H. Coe, J. R. Dorsey, P. I. Williams, A. J. Illingworth, M. W. Gallagher, and A. M. Blyth (2011). "Observations of ice multiplication in a weakly convective cell embedded in supercooled mid-level stratus." In: *Atmospheric Chemistry and Physics* 11.1, pp. 257–273. DOI: [10.5194/acp-11-257-2011](https://doi.org/10.5194/acp-11-257-2011).
- DeMott, P. J., A. J. Prenni, X. Liu, S. M. Kreidenweis, M. D. Petters, C. H. Twohy, M. S. Richardson, T. Eidhammer, and D. C. Rogers (2010). "Predicting global atmospheric ice nuclei distributions and their impacts on climate." In: *Proceedings of the National Academy of Sciences of the United States of America* 107.25, pp. 11217–22. DOI: [10.1073/pnas.0910818107](https://doi.org/10.1073/pnas.0910818107).
- Dias Neto, J., S. Kneifel, D. Ori, S. Trömel, J. Handwerker, B. Bohn, N. Hermes, K. Mühlbauer, M. Lenefer, and C. Simmer (2019). "The TRIPLE-frequency and Polarimetric radar Experiment for improving process observations of winter precipitation." In: *Earth System Science Data* 11.2, pp. 845–863. DOI: [10.5194/essd-11-845-2019](https://doi.org/10.5194/essd-11-845-2019).
- Dong, Y., R. G. Oraltay, and J. Hallett (1994). "Ice particle generation during evaporation." In: *Atmospheric Research* 32.1, pp. 45–53. DOI: [10.1016/0169-8095\(94\)90050-7](https://doi.org/10.1016/0169-8095(94)90050-7).
- Doviak, R. J. and D. S. Zrnic (2014). *Doppler Radar & Weather Observations*. Amsterdam, Boston: Academic Press. ISBN: 978-1-483-29482-7.
- Drummond, F. J., R. R. Rogers, S. A. Cohn, W. L. Ecklund, D. A. Carter, and J. S. Wilson (1996). "A New Look at the Melting Layer." In: *Journal of the Atmospheric Sciences* 53.5, pp. 759–769. DOI: [10.1175/1520-0469\(1996\)053<0759:ANLATM>2.0.CO;2](https://doi.org/10.1175/1520-0469(1996)053<0759:ANLATM>2.0.CO;2).
- Dye, J. E. and P. V. Hobbs (1968). "The Influence of Environmental Parameters on the Freezing and Fragmentation of Suspended Water Drops." In: *Journal of the Atmospheric Sciences* 25.1, pp. 82–96. ISSN: 0022-4928. DOI: [10.1175/1520-0469\(1968\)025<0082:TIOEP0>2.0.CO;2](https://doi.org/10.1175/1520-0469(1968)025<0082:TIOEP0>2.0.CO;2).
- Eliasson, S., S. A. Buehler, M. Milz, P. Eriksson, and V. O. John (2011). "Assessing observed and modelled spatial distributions of ice water path using satellite data." In: *Atmospheric Chemistry and Physics* 11.1, pp. 375–391. DOI: [10.5194/acp-11-375-2011](https://doi.org/10.5194/acp-11-375-2011).
- Fabry, F. (2015). *Radar Meteorology - Principles and Practice*. Cambridge: Cambridge University Press. ISBN: 978-1-107-07046-2.
- Fabry, F. and W. Szyrmer (1999). "Modeling of the melting layer. Part II: Electromagnetic." In: *Journal of the Atmospheric Sciences* 56.20, pp. 3593–3600. DOI: [10.1175/1520-0469\(1999\)056<3593:MOTMLP>2.0.CO;2](https://doi.org/10.1175/1520-0469(1999)056<3593:MOTMLP>2.0.CO;2).
- Fabry, F. and I. Zawadzki (1995). "Long-Term Radar Observations of the Melting Layer of Precipitation and Their Interpretation." In:

- Journal of the Atmospheric Sciences* 52.7, pp. 838–851. DOI: [10.1175/1520-0469\(1995\)052<0838:LTR00T>2.0.CO;2](https://doi.org/10.1175/1520-0469(1995)052<0838:LTR00T>2.0.CO;2).
- Field, P. R. and A. J. Heymsfield (2003). "Aggregation and Scaling of Ice Crystal Size Distributions." In: *Journal of the Atmospheric Sciences* 60.3, pp. 544–560. DOI: [10.1175/1520-0469\(2003\)060<0544:AAS0IC>2.0.CO;2](https://doi.org/10.1175/1520-0469(2003)060<0544:AAS0IC>2.0.CO;2).
- (2015). "Importance of snow to global precipitation." In: *Geophysical Research Letters* 42.21, pp. 9512–9520. DOI: <https://doi.org/10.1002/2015GL065497>.
- Field, P. R., R. P. Lawson, P. R. A. Brown, G. Lloyd, C. Westbrook, D. Moisseev, A. Miltenberger, A. Nenes, A. Blyth, T. Choulaton, P. Connolly, J. Buehl, J. Crosier, Z. Cui, C. Dearden, P. DeMott, A. Flossmann, A. Heymsfield, Y. Huang, H. Kalesse, Z. A. Kanji, A. Korolev, A. Kirchgaessner, S. Lasher-Trapp, T. Leisner, G. McFarquhar, V. Phillips, J. Stith, and S. Sullivan (2017). "Chapter 7. Secondary Ice Production - current state of the science and recommendations for the future." In: *Meteorological Monographs*. DOI: [10.1175/AMSMONOGRAPHS-D-16-0014.1](https://doi.org/10.1175/AMSMONOGRAPHS-D-16-0014.1).
- Fukuta, N. (1969). "Experimental Studies on the Growth of Small Ice Crystals." In: *Journal of the Atmospheric Sciences* 26.3, pp. 522–531. DOI: [10.1175/1520-0469\(1969\)026<0522:ES0TGO>2.0.CO;2](https://doi.org/10.1175/1520-0469(1969)026<0522:ES0TGO>2.0.CO;2).
- Fukuta, N. and H. J. Lee (1986). "A Numerical Study of the Supersaturation Field around Growing Graupel." In: *Journal of the Atmospheric Sciences* 43.17, pp. 1833–1843. DOI: [10.1175/1520-0469\(1986\)043<1833:ANS0TS>2.0.CO;2](https://doi.org/10.1175/1520-0469(1986)043<1833:ANS0TS>2.0.CO;2).
- Fukuta, N. and T. Takahashi (1999). "The Growth of Atmospheric Ice Crystals: A Summary of Findings in Vertical Supercooled Cloud Tunnel Studies." In: *Journal of the Atmospheric Sciences* 56.12, pp. 1963–1979. DOI: [10.1175/1520-0469\(1999\)056<1963:TGOAIC>2.0.CO;2](https://doi.org/10.1175/1520-0469(1999)056<1963:TGOAIC>2.0.CO;2).
- Gagin, A. (1972). "Effect of supersaturation on the ice crystal production by natural aerosols." In: *Journal de Recherches Atmosphériques* 6, pp. 175–185.
- Gaussiat, N., H. Sauvageot, and A. J. Illingworth (2003). "Cloud liquid water and ice content retrieval by multiwavelength radar." In: *Journal of Atmospheric and Oceanic Technology* 20.9, pp. 1264–1275. DOI: [10.1175/1520-0426\(2003\)020<1264:CLWAIC>2.0.CO;2](https://doi.org/10.1175/1520-0426(2003)020<1264:CLWAIC>2.0.CO;2).
- Greco, M., W. S. Olson, and E. N. Anagnostou (2004). "Retrieval of precipitation profiles from multiresolution, multifrequency active and passive microwave observations." In: *Journal of Applied Meteorology* 43.4, pp. 562–575. DOI: [10.1175/1520-0450\(2004\)043<0562:ROPPFM>2.0.CO;2](https://doi.org/10.1175/1520-0450(2004)043<0562:ROPPFM>2.0.CO;2).
- Griffin, E. M., T. J. Schuur, and A. V. Ryzhkov (2018). "A polarimetric analysis of ice microphysical processes in snow, using quasi-vertical profiles." In: *Journal of Applied Meteorology and Climatology* 57.1, pp. 31–50. DOI: [10.1175/JAMC-D-17-0033.1](https://doi.org/10.1175/JAMC-D-17-0033.1).



- Hallett, J. and B. J. Mason (1958). "The influence of temperature and supersaturation on the habit of ice crystals grown from the vapour." In: *Proceedings of the Royal Society of London. Series A. Mathematical and Physical Sciences* 247.1251, pp. 440–453. DOI: [10.1098/rspa.1958.0199](https://doi.org/10.1098/rspa.1958.0199).
- Hallett, J. and S. C. Mossop (1974). "Production of secondary ice particles during the riming process." In: *Nature* 249.5452, pp. 26–28. DOI: [10.1038/249026a0](https://doi.org/10.1038/249026a0).
- Harimaya, T. and M. Sato (1989). "Measurement of the Riming Amount on Snowflakes." In: *Journal of the Faculty of Science, Hokkaido University. Series 7, Geophysics* 8, pp. 355–366.
- Heinze, R. et al. (2017). "Large-eddy simulations over Germany using ICON: a comprehensive evaluation." In: *Quarterly Journal of the Royal Meteorological Society* 143.702, pp. 69–100. DOI: <https://doi.org/10.1002/qj.2947>.
- Heymsfield, A. J. (1982). "A Comparative Study of the Rates of Development of Potential Graupel and Hail Embryos in High Plains Storms." In: *Journal of Atmospheric Sciences* 39.12, pp. 2867–2897. DOI: [10.1175/1520-0469\(1982\)039<2867:ACS0TR>2.0.CO;2](https://doi.org/10.1175/1520-0469(1982)039<2867:ACS0TR>2.0.CO;2).
- (1986). "Ice Particle Evolution in the Anvil of a Severe Thunderstorm during CCOPE." In: *Journal of the Atmospheric Sciences* 43.21, pp. 2463–2478. DOI: [10.1175/1520-0469\(1986\)043<2463:IPEITA>2.0.CO;2](https://doi.org/10.1175/1520-0469(1986)043<2463:IPEITA>2.0.CO;2).
- Heymsfield, A. J. and M. Kajikawa (1987). "An Improved Approach to Calculating Terminal Velocities of Plate-like Crystals and Graupel." In: *Journal of the Atmospheric Sciences* 44.7, pp. 1088–1099. DOI: [10.1175/1520-0469\(1987\)044<1088:AIATCT>2.0.CO;2](https://doi.org/10.1175/1520-0469(1987)044<1088:AIATCT>2.0.CO;2).
- Heymsfield, A. J. and S. C. Mossop (1984). "Temperature dependence of secondary ice crystal production during soft hail growth by riming." In: *Quarterly Journal of the Royal Meteorological Society* 110.465, pp. 765–770. DOI: [10.1002/qj.49711046512](https://doi.org/10.1002/qj.49711046512).
- Heymsfield, A. J. and C. D. Westbrook (2010). "Advances in the Estimation of Ice Particle Fall Speeds Using Laboratory and Field Measurements." In: *Journal of the Atmospheric Sciences* 67.8, pp. 2469–2482. DOI: [10.1175/2010JAS3379.1](https://doi.org/10.1175/2010JAS3379.1).
- Heymsfield, A. J. and P. Willis (2014). "Cloud Conditions Favoring Secondary Ice Particle Production in Tropical Maritime Convection." In: *Journal of the Atmospheric Sciences* 71.12, pp. 4500–4526. DOI: [10.1175/JAS-D-14-0093.1](https://doi.org/10.1175/JAS-D-14-0093.1).
- Heymsfield, A. J., A. Bansemer, C. Schmitt, C. Twohy, and M. R. Poellot (2004). "Effective ice particle densities derived from aircraft data." In: *Journal of the Atmospheric Sciences* 61.9, pp. 982–1003. DOI: [10.1175/1520-0469\(2004\)061<0982:EIPDDF>2.0.CO;2](https://doi.org/10.1175/1520-0469(2004)061<0982:EIPDDF>2.0.CO;2).
- Heymsfield, A. J., C. Schmitt, C. C. J. Chen, A. Bansemer, A. Gettelman, P. R. Field, and C. Liu (2020). "Contributions of the Liquid and Ice Phases to Global Surface Precipitation: Observations and

- Global Climate Modeling." In: *Journal of the Atmospheric Sciences* 77.8, pp. 2629–2648. DOI: [10.1175/JAS-D-19-0352.1](https://doi.org/10.1175/JAS-D-19-0352.1).
- Hildebrand, P. H. and R. S. Sekhon (1974). "Objective Determination of the Noise Level in Doppler Spectra." In: *Journal of Applied Meteorology* 13.7, pp. 808–811. DOI: [10.1175/1520-0450\(1974\)013<0808:ODOTNL>2.0.CO;2](https://doi.org/10.1175/1520-0450(1974)013<0808:ODOTNL>2.0.CO;2).
- Hobbs, P. V. and D. A. Burrows (1966). "The Electrification of an Ice Sphere Moving through Natural Clouds." In: *Journal of the Atmospheric Sciences* 23.6, pp. 757–763. DOI: [10.1175/1520-0469\(1966\)023<0757:TEOAIS>2.0.CO;2](https://doi.org/10.1175/1520-0469(1966)023<0757:TEOAIS>2.0.CO;2).
- Hobbs, P. V., S. Chang, and J. D. Locatelli (1974). "The dimensions and aggregation of ice crystals in natural clouds." In: *Journal of Geophysical Research (1896-1977)* 79.15, pp. 2199–2206. DOI: <https://doi.org/10.1029/JC079i015p02199>.
- Hogan, R. J., A. J. Illingworth, and H. Sauvageot (2000). "Measuring crystal size in cirrus using 35- and 94-GHz radars." In: *Journal of Atmospheric and Oceanic Technology* 17.1, pp. 27–37. DOI: [10.1175/1520-0426\(2000\)017<0027:MCSICU>2.0.CO;2](https://doi.org/10.1175/1520-0426(2000)017<0027:MCSICU>2.0.CO;2).
- Hogan, R. J., N. Gaussiat, and A. J. Illingworth (2005). "Stratocumulus Liquid Water Content from Dual-Wavelength Radar." In: *Journal of Atmospheric and Oceanic Technology* 22.8, pp. 1207–1218. DOI: [10.1175/JTECH1768.1](https://doi.org/10.1175/JTECH1768.1).
- Hogan, R. J., M. P. Mittermaier, and A. J. Illingworth (2006). "The retrieval of ice water content from radar reflectivity factor and temperature and its use in evaluating a mesoscale model." In: *Journal of Applied Meteorology and Climatology* 45.2, pp. 301–317. DOI: [10.1175/JAM2340.1](https://doi.org/10.1175/JAM2340.1).
- Hoose, C. and O. Möhler (2012). "Heterogeneous ice nucleation on atmospheric aerosols: a review of results from laboratory experiments." In: *Atmospheric Chemistry and Physics* 12.20, pp. 9817–9854. DOI: [10.5194/acp-12-9817-2012](https://doi.org/10.5194/acp-12-9817-2012).
- Hosler, C. L. and R. E. Hallgren (1960). "The aggregation of small ice crystals." In: *Discussions of the Faraday Society* 30, pp. 200–207. DOI: [10.1039/DF9603000200](https://doi.org/10.1039/DF9603000200).
- Illingworth, A. J., R. J. Hogan, E. J. O'Connor, D. Bouniol, M. E. Brooks, J. Delanoë, D. P. Donovan, J. D. Eastment, N. Gaussiat, J. W F Goddard, M. Haeffelin, H. Klein Baltinik, O. A. Krasnov, J. Pelon, J. M. Piriou, A. Protat, H. W J Russchenberg, A. Seifert, A. M. Tompkins, G. J. van Zadelhoff, F. Vinit, U. Willen, D. R. Wilson, and C. L. Wrench (2007). "Cloudnet: Continuous evaluation of cloud profiles in seven operational models using ground-based observations." In: *Bulletin of the American Meteorological Society* 88.6, pp. 883–898. DOI: [10.1175/BAMS-88-6-883](https://doi.org/10.1175/BAMS-88-6-883).
- Jackson, J. (1999). *Classical electrodynamics*. New York: Wiley. ISBN: 9780471309321.

- Justo, J. E. and H. K. Weickmann (1973). "types of snowfall." In: *Bulletin of the American Meteorological Society* 54.11, pp. 1148–1162. DOI: [10.1175/1520-0477\(1973\)054<1148:TOS>2.0.CO;2](https://doi.org/10.1175/1520-0477(1973)054<1148:TOS>2.0.CO;2).
- Kajikawa, M. and A. J. Heymsfield (1989). "Aggregation of Ice Crystals in Cirrus." In: *J. Atmos. Sci.* 46, pp. 3108–3121. DOI: [https://doi.org/10.1175/1520-0469\(1989\)046<3108:A0ICIC>2.0.CO;2](https://doi.org/10.1175/1520-0469(1989)046<3108:A0ICIC>2.0.CO;2).
- Kalesse, H., T. Vogl, C. Paduraru, and E. Luke (2019). "Development and validation of a supervised machine learning radar Doppler spectra peak-finding algorithm." In: *Atmospheric Measurement Techniques* 12.8, pp. 4591–4617. DOI: [10.5194/amt-12-4591-2019](https://doi.org/10.5194/amt-12-4591-2019).
- Kamra, A K, V Bhalwankar, and A B Sathe (1991). "Spontaneous breakup of charged and uncharged water drops freely suspended in a wind tunnel." In: 96, pp. 159–168. DOI: <https://doi.org/10.1029/91JD01475>.
- Karrer, M. K., S. Kneifel, D. Ori, C. Siewert, A. Seifert, and A. von Lerber (2020). "Ice Particle Properties Inferred from Aggregation Modelling." In: *Earth and Space Science Open Archive*, p. 52. DOI: [10.1002/essoar.10502128.1](https://doi.org/10.1002/essoar.10502128.1).
- Keller, V. W. (1980). "Ice Crystal Growth in a Dynamic Thermal Diffusion Chamber." In: *NASA Technical Paper 1651* May, p. 215.
- Keller, V. W. and J. Hallett (1982). "Influence of air velocity on the habit of ice crystal growth from the vapor." In: *Journal of Crystal Growth* 60.1, pp. 91–106. DOI: [10.1016/0022-0248\(82\)90176-2](https://doi.org/10.1016/0022-0248(82)90176-2).
- Kennedy, P. C. and S. A. Rutledge (2011). "S-band dual-polarization radar observations of winter storms." In: *Journal of Applied Meteorology and Climatology* 50.4, pp. 844–858. DOI: [10.1175/2010JAMC2558.1](https://doi.org/10.1175/2010JAMC2558.1).
- Khain, A. P. and M. Pinsky (2018). *Physical Processes in Clouds and Cloud Modeling*. Cambridge University Press. DOI: [10.1017/9781139049481](https://doi.org/10.1017/9781139049481).
- King, W. D. and N. H. Fletcher (1976a). "Thermal Shock as an Ice Multiplication Mechanism. Part I. Theory." In: *Journal of the Atmospheric Sciences* 33.1, pp. 85–96. ISSN: 0022-4928. DOI: [10.1175/1520-0469\(1976\)033<0085:TSAAIM>2.0.CO;2](https://doi.org/10.1175/1520-0469(1976)033<0085:TSAAIM>2.0.CO;2).
- (1976b). "Thermal Shock as an Ice Multiplication Mechanism. Part II. Experimental." In: *Journal of the Atmospheric Sciences* 33.1, pp. 97–102. ISSN: 0022-4928. DOI: [10.1175/1520-0469\(1976\)033<0097:TSAAIM>2.0.CO;2](https://doi.org/10.1175/1520-0469(1976)033<0097:TSAAIM>2.0.CO;2).
- Klaassen, W. (1988). "Radar observations and simulation of the melting layer of precipitation." In: *Journal of the Atmospheric Sciences* 45.24, pp. 3741–3753. ISSN: 0022-4928. DOI: [10.1175/1520-0469\(1988\)045<3741:ROASOT>2.0.CO;2](https://doi.org/10.1175/1520-0469(1988)045<3741:ROASOT>2.0.CO;2).
- Kneifel, S. and D Moisseev (2020). "Long-term statistics of riming in non-convective clouds derived from ground-based Doppler cloud radar observations." In: *Journal of the Atmospheric Sciences*, pp. 1–47. DOI: [10.1175/JAS-D-20-0007.1](https://doi.org/10.1175/JAS-D-20-0007.1).
- Kneifel, S., M. S. Kulie, and R. Bennartz (2011). "A triple-frequency approach to retrieve microphysical snowfall parameters." In: *Journal*

- of *Geophysical Research Atmospheres* 116.11, pp. 1–15. DOI: [10.1029/2010JD015430](https://doi.org/10.1029/2010JD015430).
- Kneifel, S., A. von Lerber, J. Tiira, D. Moisseev, P. Kollias, and J. Leinonen (2015). “Observed relations between snowfall microphysics and triple-frequency radar measurements.” In: *Journal of Geophysical Research: Atmospheres* 120, pp. 6034–6055. DOI: [10.1002/2015JD023156](https://doi.org/10.1002/2015JD023156).
- Kneifel, S., P. Kollias, A. Battaglia, J. Leinonen, M. Maahn, H. Kalesse, and F. Tridon (2016). “First observations of triple-frequency radar Doppler spectra in snowfall: Interpretation and applications.” In: *Geophysical Research Letters* 43.5, pp. 2225–2233. DOI: [10.1002/2015GL067618](https://doi.org/10.1002/2015GL067618).
- Kobayashi, T. (1957). “Experimental Researches en the Snow Crystal Habit and Growth by Means of a Diffusion Cloud Chamber.” In: *Journal of the Meteorological Society of Japan. Ser. II* 35A.0, pp. 38–47. DOI: [10.2151/jmsj1923.35A.0\\_38](https://doi.org/10.2151/jmsj1923.35A.0_38).
- Koenig, L. R. (1963). “The Glaciating Behavior of Small Cumulonimbus Clouds.” In: *Journal of the Atmospheric Sciences* 20.1, pp. 29–47. DOI: [10.1175/1520-0469\(1963\)020<0029:TGB0SC>2.0.CO;2](https://doi.org/10.1175/1520-0469(1963)020<0029:TGB0SC>2.0.CO;2).
- Kollias, P., R. Lhermitte, and B. A. Albrecht (1999). “Vertical air motion and raindrop size distributions in convective systems using a 94 GHz radar.” In: 26.20, pp. 3109–3112. DOI: <https://doi.org/10.1029/1999GL010838>.
- Kollias, P., B. A. Albrecht, and F. D. Marks (2003). “Cloud radar observations of vertical drafts and microphysics in convective rain.” In: *Journal of Geophysical Research D: Atmospheres* 108.2. DOI: [10.1029/2001jd002033](https://doi.org/10.1029/2001jd002033).
- Korolev, A. (2007). “Limitations of the Wegener–Bergeron–Findeisen Mechanism in the Evolution of Mixed-Phase Clouds.” In: *Journal of the Atmospheric Sciences* 64.9, pp. 3372–3375. DOI: [10.1175/JAS4035.1](https://doi.org/10.1175/JAS4035.1).
- Korolev, A. and T. Leisner (2020). “Review of experimental studies of secondary ice production.” In: *Atmospheric Chemistry and Physics* 20.20, pp. 11767–11797. DOI: [10.5194/acp-20-11767-2020](https://doi.org/10.5194/acp-20-11767-2020).
- Korolev, A., M. P. Bailey, J. Hallett, and G. A. Isaac (2004). “Laboratory and In Situ Observation of Deposition Growth of Frozen Drops.” In: *Journal of Applied Meteorology* 43.4, pp. 612–622. DOI: [10.1175/1520-0450\(2004\)043<0612:LAIS00>2.0.CO;2](https://doi.org/10.1175/1520-0450(2004)043<0612:LAIS00>2.0.CO;2).
- Korolev, A., I. Heckman, M. Wolde, A. S. Ackerman, A. M. Fridlind, L. A. Ladino, R. P. Lawson, J. Milbrandt, and E. Williams (2020). “A new look at the environmental conditions favorable to secondary ice production.” In: *Atmospheric Chemistry and Physics* 20.3, pp. 1391–1429. DOI: [10.5194/acp-20-1391-2020](https://doi.org/10.5194/acp-20-1391-2020).
- Krüger, M. L., S. Mertes, T. Klimach, Y. F. Cheng, H. Su, J. Schneider, M. O. Andreae, U. Pöschl, and D. Rose (2014). “Assessment of cloud supersaturation by size-resolved aerosol particle and cloud conden-

- sation nuclei (CCN) measurements." In: *Atmospheric Measurement Techniques* 7.8, pp. 2615–2629. DOI: [10.5194/amt-7-2615-2014](https://doi.org/10.5194/amt-7-2615-2014).
- Küchler, N., S. Kneifel, U. Löhnert, P. Kollias, H. Czekala, and T. Rose (2017). "A W-band radar-radiometer system for accurate and continuous monitoring of clouds and precipitation." In: *Journal of Atmospheric and Oceanic Technology* 34.11, pp. 2375–2392. DOI: [10.1175/JTECH-D-17-0019.1](https://doi.org/10.1175/JTECH-D-17-0019.1).
- Kumjian, M. R. (2013). "Principles and Applications of Dual-Polarization Weather Radar. Part I: Description of the Polarimetric Radar Variables." In: *Journal of Operational Meteorology* 1.19, pp. 226–242. DOI: [10.15191/nwajom.2013.0119](https://doi.org/10.15191/nwajom.2013.0119).
- Kumjian, M. R., S. A. Rutledge, R. M. Rasmussen, P. C. Kennedy, and M. Dixon (2014). "High-resolution polarimetric radar observations of snow-generating cells." In: *Journal of Applied Meteorology and Climatology* 53.6, pp. 1636–1658. DOI: [10.1175/JAMC-D-13-0312.1](https://doi.org/10.1175/JAMC-D-13-0312.1).
- Lawson, R. P., R. E. Stewart, J. W. Strapp, and G. A. Isaac (1993). "Aircraft observations of the origin and growth of very large snowflakes." In: *Geophysical Research Letters* 20.1, pp. 53–56. DOI: <https://doi.org/10.1029/92GL02917>.
- Lawson, R. P., R. E. Stewart, and L. J. Angus (1998). "Observations and Numerical Simulations of the Origin and Development of Very Large Snowflakes." In: *Journal of the Atmospheric Sciences* 55.21, pp. 3209–3229. DOI: [10.1175/1520-0469\(1998\)055<3209:OANSOT>2.0.CO;2](https://doi.org/10.1175/1520-0469(1998)055<3209:OANSOT>2.0.CO;2).
- Lawson, R. P., C. Gurganus, S. Woods, and R. Brientjes (2017). "Aircraft Observations of Cumulus Microphysics Ranging from the Tropics to Midlatitudes: Implications for a "New" Secondary Ice Process." In: *Journal of the Atmospheric Sciences* 74.9, pp. 2899–2920. DOI: [10.1175/JAS-D-17-0033.1](https://doi.org/10.1175/JAS-D-17-0033.1).
- Le, M. and V. Chandrasekar (2013). "Hydrometeor profile characterization method for dual-frequency precipitation radar onboard the GPM." In: *IEEE Transactions on Geoscience and Remote Sensing* 51.6, pp. 3648–3658. DOI: [10.1109/TGRS.2012.2224352](https://doi.org/10.1109/TGRS.2012.2224352).
- Leinonen, J. and A. von Lerber (2018). "Snowflake Melting Simulation Using Smoothed Particle Hydrodynamics." In: *Journal of Geophysical Research: Atmospheres* 123.3, pp. 1811–1825. DOI: [10.1002/2017JD027909](https://doi.org/10.1002/2017JD027909).
- Leinonen, J. and W. Szyrmer (2015). "Radar signatures of snowflake riming: a modeling study." In: *Earth and Space Science*, 2015EA000102. DOI: [10.1002/2015EA000102](https://doi.org/10.1002/2015EA000102).
- Leisner, T., T. Pander, P. Handmann, and A. Kiselev (2014). "Secondary ice processes upon heterogeneous freezing of cloud droplets." In: *14th Conf. on Cloud Physics and Atmospheric Radiation*. Boston, MA: Amer. Meteor. Soc.
- Li, Y. and G. A. Somorjai (2007). "Surface Premelting of Ice." In: *The Journal of Physical Chemistry C* 111.27, pp. 9631–9637. DOI: [10.1021/jp071102f](https://doi.org/10.1021/jp071102f).



- Liao, L., R. Meneghini, L. Tian, and G. M. Heymsfield (2008). "Retrieval of Snow and Rain From Combined X- and W-Band Airborne Radar Measurements." In: *IEEE Transactions on Geoscience and Remote Sensing* 46.5, pp. 1514–1524. DOI: [10.1109/TGRS.2008.916079](https://doi.org/10.1109/TGRS.2008.916079).
- Libbrecht, K. G. (2005). "The physics of snow crystals." In: *Reports on Progress in Physics* 68.4, pp. 855–895. DOI: [10.1088/0034-4885/68/4/r03](https://doi.org/10.1088/0034-4885/68/4/r03).
- Liou, K. N. (2002). *An Introduction to Atmospheric Radiation*. Elsevier. ISBN: 9780080491677.
- Lobl, E. S., K. Aonashi, B. Griffith, C. Kummerow, G. Liu, M. Murakami, and T. Wilheit (2007). "Wakasa Bay: An AMSR Precipitation Validation Campaign." In: *Bulletin of the American Meteorological Society* 88.4, pp. 551–558. DOI: [10.1175/BAMS-88-4-551](https://doi.org/10.1175/BAMS-88-4-551).
- Locatelli, J. D. and P. V. Hobbs (1974). "Fall speeds and masses of solid precipitation particles." In: *Journal of Geophysical Research (1896-1977)* 79.15, pp. 2185–2197. DOI: [10.1029/JC079i015p02185](https://doi.org/10.1029/JC079i015p02185).
- Löffler-Mang, Martin and Jürg Joss (2000). "An optical disdrometer for measuring size and velocity of hydrometeors." In: *Journal of Atmospheric and Oceanic Technology* 17.2, pp. 130–139. ISSN: 07390572. DOI: [10.1175/1520-0426\(2000\)017<0130:AODFMS>2.0.CO;2](https://doi.org/10.1175/1520-0426(2000)017<0130:AODFMS>2.0.CO;2).
- Lohmann, U. (2016). *An introduction to clouds : from the microscale to climate*. Cambridge: Cambridge University Press. ISBN: 9781107018228.
- Löhnert, U., S. Kneifel, A. Battaglia, M. Hagen, L. Hirsch, and S. Crewell (2011). "A Multisensor Approach Toward a Better Understanding of Snowfall Microphysics: The TOSCA Project." In: *Bulletin of the American Meteorological Society* 92.5, pp. 613–628. DOI: [10.1175/2010BAMS2909.1](https://doi.org/10.1175/2010BAMS2909.1).
- Löhnert, U., J. H. Schween, C. Acquistapace, K. Ebell, M. Maahn, M. Barrera-Verdejo, A. Hirsikko, B. Bohn, A. Knaps, E. O'Connor, C. Simmer, A. Wahner, and S. Crewell (2015). "JOYCE: Jülich Observatory for Cloud Evolution." In: *Bulletin of the American Meteorological Society* 96.7, pp. 1157–1174. DOI: [10.1175/BAMS-D-14-00105.1](https://doi.org/10.1175/BAMS-D-14-00105.1).
- Low, T. B. and Roland List (1982a). "Collision, Coalescence and Breakup of Raindrops. Part I: Experimentally Established Coalescence Efficiencies and Fragment Size Distributions in Breakup." In: *Journal of the Atmospheric Sciences* 39.7, pp. 1591–1606. ISSN: 0022-4928. DOI: [10.1175/1520-0469\(1982\)039<1591:CCABOR>2.0.CO;2](https://doi.org/10.1175/1520-0469(1982)039<1591:CCABOR>2.0.CO;2).
- (1982b). "Collision, Coalescence and Breakup of Raindrops. Part II: Parameterization of Fragment Size Distributions." In: *Journal of the Atmospheric Sciences* 39.7, pp. 1607–1619. ISSN: 0022-4928. DOI: [10.1175/1520-0469\(1982\)039<1607:CCABOR>2.0.CO;2](https://doi.org/10.1175/1520-0469(1982)039<1607:CCABOR>2.0.CO;2).
- Lubin, D., D. Zhang, I. Silber, R. C. Scott, P. Kalogeras, A. Battaglia, D. H. Bromwich, M. Cadeddu, E. Eloranta, A. Fridlind, A. Frossard, K. M. Hines, S. Kneifel, W. R. Leitch, W. Lin, J. Nicolas, H. Powers, P. K. Quinn, P. Rowe, L. M. Russell, S. Sharma, J. Verlinde, and A. M. Vogelmann (2020). "AWARE: The Atmospheric Radiation



- Measurement (ARM) West Antarctic Radiation Experiment." In: *Bulletin of the American Meteorological Society* 101.7, E1069–E1091. DOI: [10.1175/BAMS-D-18-0278.1](https://doi.org/10.1175/BAMS-D-18-0278.1).
- Macke, A., P. Seifert, H. Baars, C. Barthlott, C. Beekmans, A. Behrendt, B. Bohn, M. Brueck, J. Bühl, S. Crewell, T. Damian, H. Deneke, S. Düsing, A. Foth, P. Di Girolamo, E. Hammann, R. Heinze, A. Hirsikko, J. Kalisch, N. Kalthoff, S. Kinne, M. Kohler, U. Löhnert, B. L. Madhavan, V. Maurer, S. K. Muppa, J. Schween, I. Serikov, H. Siebert, C. Simmer, F. Späth, S. Steinke, K. Träumner, S. Trömel, B. Wehner, A. Wieser, V. Wulfmeyer, and X. Xie (2017). "The HD(CP)<sup>2</sup> Observational Prototype Experiment (HOPE) – an overview." In: *Atmospheric Chemistry and Physics* 17.7, pp. 4887–4914. DOI: [10.5194/acp-17-4887-2017](https://doi.org/10.5194/acp-17-4887-2017).
- Marshall, J. S., R. C. Langille, and W. Mc K. Palmer (1947). "Measurement of rainfall by radar." In: *Journal of Meteorology* 4.6, pp. 186–192. DOI: [10.1175/1520-0469\(1947\)004<0186:MORBR>2.0.CO;2](https://doi.org/10.1175/1520-0469(1947)004<0186:MORBR>2.0.CO;2).
- Marti, J. and K. Mauersberger (1993). "A survey and new measurements of ice vapor pressure at temperatures between 170 and 250K." In: *Geophysical Research Letters* 20.5, pp. 363–366. DOI: <https://doi.org/10.1029/93GL00105>.
- Mason, B. J. and J. Maybank (1960). "The fragmentation and electrification of freezing water drops." In: *Quarterly Journal of the Royal Meteorological Society* 86.368, pp. 176–185. DOI: [10.1002/qj.49708636806](https://doi.org/10.1002/qj.49708636806).
- Mason, S. L., R. J. Hogan, C. D. Westbrook, S. Kneifel, and D. Moisseev (2019). "The importance of particle size distribution shape for triple-frequency radar retrievals of the morphology of snow." In: *Atmospheric Measurement Techniques Discussions*, pp. 1–30. DOI: [10.5194/amt-2019-100](https://doi.org/10.5194/amt-2019-100).
- Matrosov, S. Y. (1992). "Radar Reflectivity in Snowfall." In: *IEEE Transactions on Geoscience and Remote Sensing* 30.3, pp. 454–461. DOI: [10.1109/36.142923](https://doi.org/10.1109/36.142923).
- (1998). "A Dual-Wavelength Radar Method to Measure Snowfall Rate." In: *Journal of Applied Meteorology (1988-2005)* 37.11, pp. 1510–1521. DOI: [10.1175/1520-0450\(1998\)037<1510:ADWRMT>2.0.CO;2](https://doi.org/10.1175/1520-0450(1998)037<1510:ADWRMT>2.0.CO;2).
- (2017). "Characteristic Raindrop Size Retrievals from Measurements of Differences in Vertical Doppler Velocities at Ka- and W-Band Radar Frequencies." In: *Journal of Atmospheric and Oceanic Technology* 34.1, pp. 65–71. DOI: [10.1175/JTECH-D-16-0181.1](https://doi.org/10.1175/JTECH-D-16-0181.1).
- Matrosov, S. Y., R. F. Reinking, R. A. Kropfli, B. E. Martner, and B. W. Bartram (2001). "On the Use of Radar Depolarization Ratios for Estimating Shapes of Ice Hydrometeors in Winter Clouds." In: *Journal of Applied Meteorology* 40.3, pp. 479–490. DOI: [10.1175/1520-0450\(2001\)040<0479:OTUORD>2.0.CO;2](https://doi.org/10.1175/1520-0450(2001)040<0479:OTUORD>2.0.CO;2).
- McFarquhar, G. M., S. Ghan, J. Verlinde, A. Korolev, J. W. Strapp, B. Schmid, J. M. Tomlinson, M. Wolde, S. D. Brooks, D. Cziczo, M. K. Dubey, J. Fan, C. Flynn, I. Gultepe, J. Hubbe, M. K. Gilles, A. Laskin,

- P. Lawson, W. R. Leaitch, P. Liu, X. Liu, D. Lubin, C. Mazzoleni, A.-M. Macdonald, R. C. Moffet, H. Morrison, M. Ovchinnikov, M. D. Shupe, D. D. Turner, S. Xie, A. Zelenyuk, K. Bae, M. Freer, and A. Glen (2011). "Indirect and Semi-direct Aerosol Campaign: The Impact of Arctic Aerosols on Clouds." In: *Bulletin of the American Meteorological Society* 92.2, pp. 183–201. DOI: [10.1175/2010BAMS2935.1](https://doi.org/10.1175/2010BAMS2935.1).
- Mech, M., M. Maahn, S. Kneifel, D. Ori, E. Orlandi, P. Kollias, V. Schemann, and S. Crewell (2020). "PAMTRA 1.0: A Passive and Active Microwave radiative TRAnsfer tool for simulating radiometer and radar measurements of the cloudy atmosphere." In: *Geoscientific Model Development Discussions* 2020, pp. 1–34. DOI: [10.5194/gmd-2019-356](https://doi.org/10.5194/gmd-2019-356).
- Mignani, C., J. M. Creamean, L. Zimmermann, C. Alewell, and F. Conen (2019). "New type of evidence for secondary ice formation at around -15 °C in mixed-phase clouds." In: *Atmospheric Chemistry and Physics* 19.2, pp. 877–886. DOI: [10.5194/acp-19-877-2019](https://doi.org/10.5194/acp-19-877-2019).
- Mishchenko, Michael I and Larry D Travis (1998). "Capabilities and limitations of a current FORTRAN implementation of the T-matrix method for randomly oriented, rotationally symmetric scatterers." In: *Journal of Quantitative Spectroscopy and Radiative Transfer* 60.3, pp. 309–324. DOI: [https://doi.org/10.1016/S0022-4073\(98\)00008-9](https://doi.org/10.1016/S0022-4073(98)00008-9).
- Mitchell, D. L. (1988). "Evolution of Snow-Size Spectra in Cyclonic Storms. Part I: Snow Growth by Vapor Deposition and Aggregation." In: *J. Atmos. Sci* 45, pp. 3431–3451. DOI: [https://doi.org/10.1175/1520-0469\(1988\)045<3431:E0SSSI>2.0.CO;2](https://doi.org/10.1175/1520-0469(1988)045<3431:E0SSSI>2.0.CO;2).
- (1996). "Use of Mass- and Area-Dimensional Power Laws for Determining Precipitation Particle Terminal Velocities." In: *Journal of the Atmospheric Sciences* 53.12, pp. 1710–1723. DOI: [10.1175/1520-0469\(1996\)053<1710:U0MAAD>2.0.CO;2](https://doi.org/10.1175/1520-0469(1996)053<1710:U0MAAD>2.0.CO;2).
- (2002). "Effective diameter in radiation transfer: General definition, applications, and limitations." In: *Journal of the Atmospheric Sciences* 59.15, pp. 2330–2346. DOI: [10.1175/1520-0469\(2002\)059<2330:EDIRTG>2.0.CO;2](https://doi.org/10.1175/1520-0469(2002)059<2330:EDIRTG>2.0.CO;2).
- Mitchell, D. L., R. Zhang, and R. L. Pitter (1990). "Mass-Dimensional Relationships for Ice Particles and the Influence of Riming on Snowfall Rates." In: *Journal of Applied Meteorology* 29.2, pp. 153–163. DOI: [10.1175/1520-0450\(1990\)029<0153:MDRFIP>2.0.CO;2](https://doi.org/10.1175/1520-0450(1990)029<0153:MDRFIP>2.0.CO;2).
- Moisseev, D. N., S. Lautaportti, J. Tyynela, and S. Lim (2015). "Dual-polarization radar signatures in snowstorms: Role of snowflake aggregation." In: *Journal of Geophysical Research* 120.24, pp. 12,644–12,665. DOI: [10.1002/2015JD023884](https://doi.org/10.1002/2015JD023884).
- Morrison, H., M. van Lier-Walqui, A. M. Fridlind, W. W. Grabowski, J. Y. Harrington, C. Hoose, A. Korolev, M. R. Kumjian, J. A. Milbrandt, H. Pawlowska, D. J. Posselt, O. P. Prat, K. J. Reimel, S.-I. Shima,

- B. van Dierenhoven, and L. Xue (2020). "Confronting the Challenge of Modeling Cloud and Precipitation Microphysics." In: *Journal of Advances in Modeling Earth Systems* 12.8. DOI: <https://doi.org/10.1029/2019MS001689>.
- Mosimann, L. (1995). "An improved method for determining the degree of snow crystal riming by vertical Doppler radar." In: *Atmospheric Research* 37.4, pp. 305–323. DOI: [10.1016/0169-8095\(94\)00050-N](https://doi.org/10.1016/0169-8095(94)00050-N).
- Mossop, S. C. (1985). "Secondary ice particle production during rime growth: The effect of drop size distribution and rimer velocity." In: *Quarterly Journal of the Royal Meteorological Society* 111.470, pp. 1113–1124. DOI: [10.1002/qj.49711147012](https://doi.org/10.1002/qj.49711147012).
- Mossop, S. C. and J. Hallett (1974). "Ice Crystal Concentration in Cumulus Clouds: Influence of the Drop Spectrum." In: *Science* 186.4164, pp. 632–634. DOI: [10.1126/science.186.4164.632](https://doi.org/10.1126/science.186.4164.632).
- Mróz, K., A. Battaglia, S. Kneifel, L. von Terzi, M. Karrer, and D. Ori (2020a). "Linking rain into ice microphysics across the melting layer in stratiform rain: a closure study." In: *Atmospheric Measurement Techniques Discussions* 2020, pp. 1–31. DOI: [10.5194/amt-2020-272](https://doi.org/10.5194/amt-2020-272).
- Mróz, K., A. Battaglia, S. Kneifel, L. P. D'Adderio, and J. Dias Neto (2020b). "Triple-Frequency Doppler Retrieval of Characteristic Rain-drop Size." In: *Earth and Space Science* 7.3. DOI: [10.1029/2019EA000789](https://doi.org/10.1029/2019EA000789).
- Mülmenstädt, J., O. Sourdeval, J. Delanoë, and J. Quaas (2015). "Frequency of occurrence of rain from liquid-, mixed-, and ice-phase clouds derived from A-Train satellite retrievals." In: *Geophysical Research Letters* 42.15, pp. 6502–6509. DOI: [10.1002/2015GL064604](https://doi.org/10.1002/2015GL064604).
- Murphy, D. M. and T. Koop (2005). "Review of the vapour pressures of ice and supercooled water for atmospheric applications." In: *Quarterly Journal of the Royal Meteorological Society* 131.608, pp. 1539–1565. DOI: <https://doi.org/10.1256/qj.04.94>.
- Muth, X., M. Schneebeli, and A. Berne (2012). "A sun-tracking method to improve the pointing accuracy of weather radar." In: *Atmospheric Measurement Techniques* 5.3, pp. 547–555. DOI: [10.5194/amt-5-547-2012](https://doi.org/10.5194/amt-5-547-2012). URL: <https://www.atmos-meas-tech.net/5/547/2012/>.
- Oraltay, R.G. and J. Hallett (1989). "Evaporation and melting of ice crystals: A laboratory study." In: *Atmospheric Research* 24.1, pp. 169–189. ISSN: 0169-8095. DOI: [https://doi.org/10.1016/0169-8095\(89\)90044-6](https://doi.org/10.1016/0169-8095(89)90044-6).
- Ori, D., T. Maestri, R. Rizzi, D. Cimini, M. Montopoli, and F. S. Marzano (2014). "Scattering properties of modeled complex snowflakes and mixed-phase particles at microwave and millimeter frequencies." In: *Journal of Geophysical Research: Atmospheres* 119.16, pp. 9931–9947. DOI: [10.1002/2014JD021616](https://doi.org/10.1002/2014JD021616).
- Ori, D., V. Schemann, M. Karrer, J. Dias Neto, L. Terzi, A. Seifert, and S. Kneifel (2020a). "Evaluation of ice particle growth in ICON using statistics of multi-frequency Doppler cloud radar observations." In:

- Quarterly Journal of the Royal Meteorological Society*. DOI: [10.1002/qj.3875](https://doi.org/10.1002/qj.3875).
- Ori, D., L. von Terzi, M. Karrer, and S. Kneifel (2020b). "snowScatt 1.0: Consistent model of microphysical and scattering properties of rimed and unrimed snowflakes based on the self-similar Rayleigh-Gans Approximation." In: *Geoscientific Model Development Discussions* 2020, pp. 1–33. DOI: [10.5194/gmd-2020-359](https://doi.org/10.5194/gmd-2020-359).
- Petty, Grant W., Wei Huang, Grant W. Petty, and Wei Huang (2011). "The Modified Gamma Size Distribution Applied to Inhomogeneous and Nonspherical Particles: Key Relationships and Conversions." In: 68.7, pp. 1460–1473. DOI: [10.1175/2011JAS3645.1](https://doi.org/10.1175/2011JAS3645.1).
- Petäjä, T., E. J. O'Connor, D. Moisseev, V. A. Sinclair, A. J. Manninen, R. Väänänen, A. von Lerber, J. A. Thornton, K. Nicoll, W. Petersen, V. Chandrasekar, J. N. Smith, P. M. Winkler, O. Krüger, H. Hakola, H. Timonen, D. Brus, T. Laurila, E. Asmi, M.-L. Riekkola, L. Mona, P. Massoli, R. Engelmann, M. Komppula, J. Wang, C. Kuang, J. Bäck, A. Virtanen, J. Levula, M. Ritsche, and N. Hickmon (2016). "BAECC: A Field Campaign to Elucidate the Impact of Biogenic Aerosols on Clouds and Climate." In: *Bulletin of the American Meteorological Society* 97.10, pp. 1909–1928. DOI: [10.1175/BAMS-D-14-00199.1](https://doi.org/10.1175/BAMS-D-14-00199.1).
- Phillips, V. T.J., M. Formenton, A. Bansemmer, I. Kudzotsa, and B. Lienert (2015). "A parameterization of sticking efficiency for collisions of snow and graupel with ice crystals: Theory and comparison with observations." In: *Journal of the Atmospheric Sciences* 72.12, pp. 4885–4902. DOI: [10.1175/JAS-D-14-0096.1](https://doi.org/10.1175/JAS-D-14-0096.1).
- Pruppacher, H. R. and J. D. Klett (1997). *Microphysics of Clouds and Precipitation*. Dordrecht: Kluwer Academic Publishers. ISBN: 0792342119.
- Raghavan, S. (2003). *Radar Meteorology*. Kluwer Academic Publishers. ISBN: 9781402016042.
- Rangno, A. L. (2008). "Fragmentation of Freezing Drops in Shallow Maritime Frontal Clouds." In: *Journal of the Atmospheric Sciences* 65.4, pp. 1455–1466. DOI: [10.1175/2007JAS2295.1](https://doi.org/10.1175/2007JAS2295.1).
- Rasmussen, R. M. and A. J. Heymsfield (1987). "Melting and Shedding of Graupel and Hail. Part I: Model Physics." In: *Journal of the Atmospheric Sciences* 44.19, pp. 2754–2763. DOI: [10.1175/1520-0469\(1987\)044<2754:MASOGA>2.0.CO;2](https://doi.org/10.1175/1520-0469(1987)044<2754:MASOGA>2.0.CO;2).
- Rico-Ramirez, M. A. and I. D. Cluckie (2007). "Bright-band detection from radar vertical reflectivity profiles." In: *International Journal of Remote Sensing* 28.18, pp. 4013–4025. DOI: [10.1080/01431160601047797](https://doi.org/10.1080/01431160601047797).
- Rose, C. R. and V. Chandrasekar (2006). "A GPM Dual-Frequency Retrieval Algorithm: DSD Profile-Optimization Method." In: *Journal of Atmospheric and Oceanic Technology* 23.10, pp. 1372–1383. ISSN: 0739-0572. DOI: [10.1175/JTECH1921.1](https://doi.org/10.1175/JTECH1921.1).
- Rose, T., S. Crewell, U. Löhnert, and C. Simmer (2005). "A network suitable microwave radiometer for operational monitoring of the

- cloudy atmosphere." In: *Atmospheric Research* 75.3, pp. 183–200. DOI: <https://doi.org/10.1016/j.atmosres.2004.12.005>.
- Ryzhkov, A. V. and D. S. Zrnich (1998). "Discrimination between rain and snow with a polarimetric radar." In: *Journal of Applied Meteorology* 37.10 PART II, pp. 1228–1240. ISSN: 08948763. DOI: [10.1175/1520-0450\(1998\)037<1228:dbrasw>2.0.co;2](https://doi.org/10.1175/1520-0450(1998)037<1228:dbrasw>2.0.co;2).
- Ryzhkov, A., P. Zhang, H. Reeves, M. Kumjian, T. Tschallener, S. Trömel, and C. Simmer (2016). "Quasi-Vertical Profiles—A New Way to Look at Polarimetric Radar Data." In: *Journal of Atmospheric and Oceanic Technology* 33.3, pp. 551–562. DOI: [10.1175/JTECH-D-15-0020.1](https://doi.org/10.1175/JTECH-D-15-0020.1).
- Saunders, C. P. R. and A. S. Hosseini (2001). "A laboratory study of the effect of velocity on Hallett–Mossop ice crystal multiplication." In: *Atmospheric Research* 59-60. 13th International Conference on Clouds and Precipitation, pp. 3–14. ISSN: 0169-8095. DOI: [https://doi.org/10.1016/S0169-8095\(01\)00106-5](https://doi.org/10.1016/S0169-8095(01)00106-5).
- Schrom, R. S., M. R. Kumjian, and Y. Lu (2015). "Polarimetric radar signatures of dendritic growth zones within Colorado winter storms." In: *Journal of Applied Meteorology and Climatology* 54.12, pp. 2365–2388. DOI: [10.1175/JAMC-D-15-0004.1](https://doi.org/10.1175/JAMC-D-15-0004.1).
- Schwarzenboeck, A., V. Shcherbakov, R. Lefevre, J. F. Gayet, Y. Pointin, and C. Duroure (2009). "Indications for stellar-crystal fragmentation in Arctic clouds." In: *Atmospheric Research* 92.2, pp. 220–228. DOI: [10.1016/j.atmosres.2008.10.002](https://doi.org/10.1016/j.atmosres.2008.10.002).
- Seifert, A. (2008). "On the Parameterization of Evaporation of Raindrops as Simulated by a One-Dimensional Rainshaft Model." In: *Journal of the Atmospheric Sciences* 65.11, pp. 3608–3619. DOI: [10.1175/2008JAS2586.1](https://doi.org/10.1175/2008JAS2586.1).
- Sekelsky, S. M., W. L. Ecklund, J. M. Firda, K. S. Gage, and R. E. McIntosh (1999). "Particle size estimation in ice-phase clouds using multifrequency radar reflectivity measurements at 95, 33, and 2.8 GHz." In: *Journal of Applied Meteorology* 38.1, pp. 5–28. DOI: [10.1175/1520-0450\(1999\)038<0005:PSEIIP>2.0.CO;2](https://doi.org/10.1175/1520-0450(1999)038<0005:PSEIIP>2.0.CO;2).
- Sinclair, G. (1950). "The Transmission and Reception of Elliptically Polarized Waves." In: *Proceedings of the IRE* 38.2, pp. 148–151. DOI: [10.1109/JRPROC.1950.230106](https://doi.org/10.1109/JRPROC.1950.230106).
- Slater, B. and A. Michaelides (2019). "Surface premelting of water ice." In: *Nature Reviews Chemistry* 3.3, pp. 172–188. DOI: [10.1038/s41570-019-0080-8](https://doi.org/10.1038/s41570-019-0080-8).
- Stein, T. H. M., C. D. Westbrook, and J. C. Nicol (2015). "Fractal geometry of aggregate snowflakes revealed by triple-wavelength radar measurements." In: *Geophysical Research Letters* 42.1, pp. 176–183. DOI: [10.1002/2014GL062170](https://doi.org/10.1002/2014GL062170).
- Stephens, G. L. (2005). "Cloud Feedbacks in the Climate System: A Critical Review." In: *Journal of Climate* 18.2, pp. 237–273. DOI: [10.1175/JCLI-3243.1](https://doi.org/10.1175/JCLI-3243.1).



- Stewart, R. E. (1992). "Precipitation Types in the Transition Region of Winter Storms." In: *Bulletin of the American Meteorological Society* 73.3, pp. 287–296. DOI: [10.1175/1520-0477\(1992\)073<0287:PTITTR>2.0.CO;2](https://doi.org/10.1175/1520-0477(1992)073<0287:PTITTR>2.0.CO;2).
- Stubenrauch, C. J., W. B. Rossow, S. Kinne, S. Ackerman, G. Cesana, H. Chepfer, L. Di Girolamo, B. Getzewich, A. Guignard, A. Heidinger, B. C. Maddux, W. P. Menzel, P. Minnis, C. Pearl, S. Platnick, C. Poulsen, J. Riedi, S. Sun-Mack, A. Walther, D. Winker, S. Zeng, and G. Zhao (2013). "Assessment of global cloud datasets from satellites: Project and database initiated by the GEWEX radiation panel." In: *Bulletin of the American Meteorological Society* 94.7, pp. 1031–1049. DOI: [10.1175/BAMS-D-12-00117.1](https://doi.org/10.1175/BAMS-D-12-00117.1).
- Szyrmer, W. and I. Zawadzki (1999). "Modeling of the melting layer. Part I: Dynamics and microphysics." In: *Journal of the Atmospheric Sciences* 56.20, pp. 3573–3592. DOI: [10.1175/1520-0469\(1999\)056<3573:MOTMLP>2.0.CO;2](https://doi.org/10.1175/1520-0469(1999)056<3573:MOTMLP>2.0.CO;2).
- Sölch, I. and B. Kärcher (2011). "Process-oriented large-eddy simulations of a midlatitude cirrus cloud system based on observations." In: *Quarterly Journal of the Royal Meteorological Society* 137.655, pp. 374–393. DOI: <https://doi.org/10.1002/qj.764>.
- Takahashi, T. (1993). "High ice crystal production in winter cumuli over the Japan Sea." In: *Geophysical Research Letters* 20.6, pp. 451–454. DOI: [10.1029/93GL00613](https://doi.org/10.1029/93GL00613).
- (2014). "Influence of Liquid Water Content and Temperature on the Form and Growth of Branched Planar Snow Crystals in a Cloud." In: *Journal of the Atmospheric Sciences* 71.11, pp. 4127–4142. DOI: [10.1175/JAS-D-14-0043.1](https://doi.org/10.1175/JAS-D-14-0043.1).
- Takahashi, T. and N. Fukuta (1988). "Supercooled Cloud Tunnel Studies on the Growth of Snow Crystals between -4 and -20 °C." In: *Journal of the Meteorological Society of Japan. Ser. II* 66.6, pp. 841–855. DOI: [10.2151/jmsj1965.66.6\\_841](https://doi.org/10.2151/jmsj1965.66.6_841).
- Takahashi, T., T. Endoh, G. Wakahama, and N. Fukuta (1991). "Vapor Diffusional Growth of Free-Falling Snow Crystals between -3 and -23 °C." In: *Journal of the Meteorological Society of Japan. Ser. II* 69.1, pp. 15–30. DOI: [10.2151/jmsj1965.69.1\\_15](https://doi.org/10.2151/jmsj1965.69.1_15).
- Takahashi, T., Y. Nagao, and Y. Kushiyama (1995). "Possible High Ice Particle Production during Graupel–Graupel Collisions." In: *Journal of the Atmospheric Sciences* 52.24, pp. 4523–4527. DOI: [10.1175/1520-0469\(1995\)052<4523:PHIPPD>2.0.CO;2](https://doi.org/10.1175/1520-0469(1995)052<4523:PHIPPD>2.0.CO;2).
- Tian, L., G. M. Heymsfield, L. Li, and R. C. Srivastava (2007). "Properties of light stratiform rain derived from 10- and 94-GHz airborne Doppler radars measurements." In: *Journal of Geophysical Research: Atmospheres* 112.D11. DOI: [10.1029/2006JD008144](https://doi.org/10.1029/2006JD008144).
- Tridon, F., A. Battaglia, and P. Kollias (2013). "Disentangling Mie and attenuation effects in rain using a Ka-W dual-wavelength



- Doppler spectral ratio technique." In: *Geophysical Research Letters* 40.20, pp. 5548–5552. DOI: [10.1002/2013GL057454](https://doi.org/10.1002/2013GL057454).
- Tridon, F., A. Battaglia, and S. Kneifel (2020). "Estimating total attenuation using Rayleigh targets at cloud top: applications in multilayer and mixed-phase clouds observed by ground-based multifrequency radars." In: *Atmospheric Measurement Techniques* 13.9, pp. 5065–5085. DOI: [10.5194/amt-13-5065-2020](https://doi.org/10.5194/amt-13-5065-2020).
- Trömel, S., M. R. Kumjian, A. V. Ryzhkov, C. Simmer, and M. Diederich (2013). "Backscatter Differential Phase Estimation and Variability." In: *Journal of Applied Meteorology and Climatology* 52.11, pp. 2529–2548. DOI: [10.1175/JAMC-D-13-0124.1](https://doi.org/10.1175/JAMC-D-13-0124.1).
- Trömel, S., A. V. Ryzhkov, P. Zhang, and C. Simmer (2014). "Investigations of backscatter differential phase in the melting layer." In: *Journal of Applied Meteorology and Climatology* 53.10, pp. 2344–2359. DOI: [10.1175/JAMC-D-14-0050.1](https://doi.org/10.1175/JAMC-D-14-0050.1).
- Trömel, S., A. V. Ryzhkov, B. Hickman, K. A. I. Mühlbauer, and C. Simmer (2019). "Polarimetric radar variables in the layers of melting and dendritic growth at X band—Implications for a nowcasting strategy in stratiform rain." In: *Journal of Applied Meteorology and Climatology* 58.11, pp. 2497–2522. DOI: [10.1175/JAMC-D-19-0056.1](https://doi.org/10.1175/JAMC-D-19-0056.1).
- Vardiman, Larry (1978). "The Generation of Secondary Ice Particles in Clouds by Crystal–Crystal Collision." In: *Journal of Atmospheric Sciences* 35, pp. 2168–2180. ISSN: 0022-4928. DOI: [10.1175/1520-0469\(1978\)035<2168:TGOSIP>2.0.CO;2](https://doi.org/10.1175/1520-0469(1978)035<2168:TGOSIP>2.0.CO;2).
- Verlinde, J., J. Y. Harrington, G. M. McFarquhar, V. T. Yannuzzi, A. Avramov, S. Greenberg, N. Johnson, G. Zhang, M. R. Poellot, J. H. Mather, D. D. Turner, E. W. Eloranta, B. D. Zak, A. J. Prenni, J. S. Daniel, G. L. Kok, D. C. Tobin, R. Holz, K. Sassen, D. Spangenberg, P. Minnis, T. P. Tooman, M. D. Ivey, S. J. Richardson, C. P. Bahrman, M. Shupe, P. J. DeMott, A. J. Heymsfield, and R. Schofield (2007). "The Mixed-Phase Arctic Cloud Experiment." In: *Bulletin of the American Meteorological Society* 88.2, pp. 205–222. DOI: [10.1175/BAMS-88-2-205](https://doi.org/10.1175/BAMS-88-2-205).
- Wallace, J. and P. V. Hobbs (2006). *Atmospheric science : an introductory survey*. Amsterdam Boston: Elsevier Academic Press. ISBN: 978-0-12-732951-2.
- Warner, C. (1977). "Collision Frequencies of Raindrops." In: *IEEE Transactions on Antennas and Propagation* 25.4, pp. 583–585. DOI: [10.1109/TAP.1977.1141638](https://doi.org/10.1109/TAP.1977.1141638).
- Wolde, M. and G. Vali (2001a). "Polarimetric Signatures from Ice Crystals Observed at 95 GHz in Winter Clouds. Part I: Dependence on Crystal Form." In: *Journal of the Atmospheric Sciences* 58.8, pp. 828–841. DOI: [10.1175/1520-0469\(2001\)058<0828:PSFIC0>2.0.CO;2](https://doi.org/10.1175/1520-0469(2001)058<0828:PSFIC0>2.0.CO;2).
- (2001b). "Polarimetric Signatures from Ice Crystals Observed at 95 GHz in Winter Clouds. Part II: Frequencies of Occurrence." In:

- Journal of the Atmospheric Sciences* 58.8, pp. 842–849. DOI: [10.1175/1520-0469\(2001\)058<0842:PSFICO>2.0.CO;2](https://doi.org/10.1175/1520-0469(2001)058<0842:PSFICO>2.0.CO;2).
- Yoshida, Y., S. Asano, and K. Iwanami (2006). “Retrieval of microphysical properties of water, ice, and mixed-phase clouds using a triple-wavelength radar and microwave radiometer.” In: *Journal of the Meteorological Society of Japan* 84.6, pp. 1005–1031. DOI: [10.2151/jmsj.84.1005](https://doi.org/10.2151/jmsj.84.1005).
- Zawadzki, I., F. Fabry, and W. Szyrmer (2001). “Observations of supercooled water and secondary ice generation by a vertically pointing X-band Doppler radar.” In: *Atmospheric Research* 59-60, pp. 343–359. DOI: [10.1016/S0169-8095\(01\)00124-7](https://doi.org/10.1016/S0169-8095(01)00124-7).
- Zawadzki, I., W. Szyrmer, C. Bell, and F. Fabry (2005). “Modeling of the melting layer. Part III: The density effect.” In: *Journal of the Atmospheric Sciences* 62.10, pp. 3705–3723. DOI: [10.1175/JAS3563.1](https://doi.org/10.1175/JAS3563.1).
- Zelinka, M. D., D. A. Randall, M. J. Webb, and S. A. Klein (2017). “Clearing clouds of uncertainty.” In: *Nature Climate Change* 7.10, pp. 674–678. DOI: <https://doi.org/10.1038/nclimate3402>.
- Zikmunda, J. and G. Vali (1972). “Fall Patterns and Fall Velocities of Rimed Ice Crystals.” In: *Journal of the Atmospheric Sciences* 29.7, pp. 1334–1347. DOI: [10.1175/1520-0469\(1972\)029<1334:FPAFV0>2.0.CO;2](https://doi.org/10.1175/1520-0469(1972)029<1334:FPAFV0>2.0.CO;2).
- Zrnić, D. S., R. Raghavan, and V. Chandrasekar (1994). “Observations of Copolar Correlation Coefficient through a Bright Band at Vertical Incidence.” In: *Journal of Applied Meteorology* 33.1, pp. 45–52. DOI: [10.1175/1520-0450\(1994\)033<0045:00CCCT>2.0.CO;2](https://doi.org/10.1175/1520-0450(1994)033<0045:00CCCT>2.0.CO;2).
- Zängl, G., D. Reinert, P. Rípodas, and M. Baldauf (2015). “The ICON (ICOsahedral Non-hydrostatic) modelling framework of DWD and MPI-M: Description of the non-hydrostatic dynamical core.” In: *Quarterly Journal of the Royal Meteorological Society* 141.687, pp. 563–579. DOI: <https://doi.org/10.1002/qj.2378>.

## ACKNOWLEDGMENTS

---

I thank the German Research Foundation (DFG) for funding this work under grant KN 1112/2-1 as part of the Emmy-Noether Group OPTIMIce.

I thank the Graduate School of Geosciences of the University of Cologne for supporting me as PhD candidate funding my participation in scientific conferences and promoting several workshops.

I thank my supervisors Prof. Dr. Ulrich Löhnert, Dr. Silke Trömel and Dr. Stefan Kneifel, for guiding me through this process. I immensely thank Dr. Stefan Kneifel for giving me the opportunity to be a PhD candidate and be a member of his research group (OPTIMIce). During the time I worked in the OPTIMIce (4 years), I had the opportunity to learn a lot about cloud microphysical processes and radar remote sensing. I also thank Dr. Stefan Kneifel for all valuable comments, discussions and time that helped me to improve this thesis.

I thank Dr. Davide Ori for his very illustrative explanation about the scattering of ice particles. I also thank Dr. Davide Ori for reading several parts of this thesis and for his precious comments and time that helped me to express my ideas clearly. I additionally thank him for helping with python and with the development of the multi-frequency data processing. I also thank Dr. Davide Ori for picking me up at the airport when I arrived in Germany for the first time.

I thank Prof. Dr. Roel Neggers for accepting my invitation to be reviewer of this thesis.

I thank Dr. Marek Jacob for providing the codes that I used for the detection of Doppler spectral peaks applied in [Section 3.4](#).

I thank Dr. Rosa Tuulia Gierens for reading and commenting parts of this thesis. Those comments were constructive and helped me to improve the structure of the thesis.

I thank Dr. Alexander Myagkov for answering all my questions about the operation of the W-Band.

I thank Judith Blockland for reading parts of this thesis and for suggesting improvements. I also thank her for the fun time.

I thank the "Mensa crew group" Markus Karrer, Konstantin Klein, Leonie Von Terzi, 江聰(Jian Cong) and 殷欣(Yin Xin) for our chats during lunchtime/dinner and fun time along these four years. In particular, Markus Karrer for reading parts of this thesis and providing suggestions for improving the final text.

I thank my family: Nananel Nilton Dias (father), Marlizete Ricardo de Moraes Dias (mother) and Débora Suzana de Moraes Dias (sister) for helping and supporting me when I was moving from Brazil to Germany.

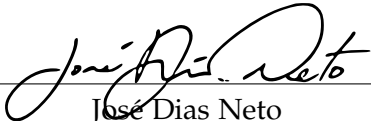


## ERKLÄRUNG

---

Hiermit versichere ich an Eides statt, dass ich die vorliegende Dissertation selbstständig und ohne die Benutzung anderer als der angegebenen Hilfsmittel und Literatur angefertigt habe. Alle Stellen, die wörtlich oder sinngemäß aus veröffentlichten und nicht veröffentlichten Werken dem Wortlaut oder dem Sinn nach entnommen wurden, sind als solche kenntlich gemacht. Ich versichere an Eides statt, dass diese Dissertation noch keiner anderen Fakultät oder Universität zur Prüfung vorgelegen hat; dass sie - abgesehen von unten angegebenen Teilpublikationen und eingebundenen Artikeln und Manuskripten - noch nicht veröffentlicht worden ist sowie, dass ich eine Veröffentlichung der Dissertation vor Abschluss der Promotion nicht ohne Genehmigung des Promotionsausschusses vornehmen werde. Die Bestimmungen dieser Ordnung sind mir bekannt. Darüber hinaus erkläre ich hiermit, dass ich die Ordnung zur Sicherung guter wissenschaftlicher Praxis und zum Umgang mit wissenschaftlichem Fehlverhalten der Universität zu Köln gelesen und sie bei der Durchführung der Dissertation zugrundeliegenden Arbeiten und der schriftlich verfassten Dissertation beachtet habe und verpflichte mich hiermit, die dort genannten Vorgaben bei allen wissenschaftlichen Tätigkeiten zu beachten und umzusetzen. Ich versichere, dass die eingereichte elektronische Fassung der eingereichten Druckfassung vollständig entspricht.

Köln, 21 December 2020

  
José Dias Neto

## TEILPUBLIKATIONEN

Mróz, K., Battaglia, A., Kneifel, S., D'Adderio, L. P., **Dias Neto, J.**, (2020). **Triple-frequency Doppler retrieval of characteristic raindrop size**, *Earth and Space Science*, <https://doi.org/10.1029/2019EA000789>.

**Dias Neto, J.**, Kneifel, S., Ori, D., Trömel, S., Handwerker, J., Bohn, B., Hermes, N., Mühlbauer, K., Lenefer, M., and Simmer, C., (2019). **The TRIPLE-frequency and Polarimetric radar Experiment for improving process observations of winter precipitation**, *Earth System Science Data*, 2019, 11, pp.845-863. <https://doi.org/10.5194/essd-11-845-2019>.





## COLOPHON

This document was typeset using the typographical look-and-feel `classicthesis` developed by André Miede and Ivo Pletikosić. The style was inspired by Robert Bringhurst's seminal book on typography "*The Elements of Typographic Style*". `classicthesis` is available for both L<sup>A</sup>T<sub>E</sub>X and L<sup>Y</sup>X:

<https://bitbucket.org/amiede/classicthesis/>

Happy users of `classicthesis` usually send a real postcard to the author, a collection of postcards received so far is featured here:

<http://postcards.miede.de/>

*Final Version* as of 29. August 2021 (`classicthesis` v4.6).